Faculty of Maritime Studies
University of Rijeka, Croatia

Royal Institute of Navigation
Science Technology Practice

7th GNSS

Vulnerabilities and Solutions Conference

PROCEEDINGS

Baška, Krk Island, Croatia
18 – 20 April 2013

Faculty of Maritime Studies
University of Rijeka, Croatia

Royal Institute of Navigation
Science Technology Practice

7th GNSS
Vulnerabilities and Solutions Conference

PROCEEDINGS

Baška, Krk Island, Croatia
18 – 20 April 2013

Published by:
University of Rijeka, Faculty of Maritime Studies Rijeka, Rijeka, Croatia
The Royal Institute of Navigation, London, UK

For the Publisher:
Full Professor Serdjo Kos, Ph. D., FRIN, Faculty of Maritime Studies Rijeka

Publishing Associates:
Colin Beatty, President, The Royal Institute of Navigation
Capt. Peter Chapman-Andrews, LVO MBE RN, Director, The Royal Institute of Navigation

Editor-in-Chief:
Full Professor Serdjo Kos, Ph. D., FRIN, Faculty of Maritime Studies Rijeka
Associate Professor Renato Filjar, Ph. D., FRIN, Faculty of Maritime Studies, Rijeka

Associate Editor:
Full Professor Axel Luttenberger, Ph. D., Faculty of Maritime Studies Rijeka

Executive Editor:
Marija Šimić Hlača B. Sc., Faculty of Maritime Studies Rijeka

Front-page photo credits:
Associate Professor Renato Filjar, Ph. D., FRIN, Faculty of Maritime Studies, Rijeka

Text Formatting:
Tempora, Rijeka

Print:
AKD d.o.o. Zagreb

Address:
Faculty of Maritime Studies Rijeka
Studentska 2
51000 Rijeka
Croatia
Tel: ++3895 (0)51 338411
Fax: ++385 (0)51 336755
URL: http://www.pfri.uniri.hr/
E-mail: dekanat@pfri.hr

CIP zapis dostupan u računalnom katalogu Sveučilišne knjižnice Rijeka pod brojem 30411074.
ISBN 978-953-165-113-4

CONTENTS

Faculty of Maritime Studies
University of Rijeka, Croatia

Royal Institute of Navigation
Science Technology Practice

7th GNSS
Vulnerabilities and Solutions Conference

PROCEEDINGS

Faculty of Maritime Studies
University of Rijeka, Croatia

Royal Institute of Navigation
Science Technology Practice

7th GNSS
Vulnerabilities and Solutions Conference

CALIBRA: MITIGATING THE IMPACT OF IONOSPHERIC SCINTILLATION ON PRECISE POINT POSITIONING IN BRAZIL

B. Bougard[1], A. Simsky[1], Jihye Park[2], M. Aquino[2], L. Spogli[3], M. Mendonga[4], J. F. Galera Monico[4]

[1] J.-M. Sleewaegen, Septentrio, Belgium
E-mail: Bruno.Bougard@septentrio.com

[2] University of Nottingham, UK

[3] V. Romano Istituto Nazionale di Geofisica e Vulcanologia, Italy

[4] Universidade Estadual Paulista, Brazil

ABSTRACT. *The current increase in solar activity occurs at a time when our reliance on high-precision GNSS applications has reached unprecedented proportions. The perturbations caused in the ionosphere by such solar activity pose a major threat to these applications, in particular in equatorial regions such as Brazil where high exposure to solar-induced disturbances comes with a high reliance on precise GNSS applications in a number of key areas such as in the oil and gas industry. Mitigating the impact of severe ionosphere disturbance on high-precision positioning is the main goal of the FP7 CALIBRA project, which first results are discussed in this paper. We focus on the impact of scintillations, one of the most forthcoming disturbances, on real time precise point positioning (PPP). A simple and effective mitigation approach is discussed and shown to significantly increase the resilience of PPP applications to scintillations.*

1 INTRODUCTION

GNSS has become essential to governmental and industrial sectors in support of activities such as precision agriculture, offshore operations, land management, construction, mining, as well as safety-critical operations, including those related to maritime, land and air transportation. The perturbations caused in the ionosphere by the current increasing solar activity, corresponding to the impending maximum of cycle 24, pose a major threat to these applications, in particular in equatorial regions where high exposure to solar-induced disturbances comes together with high reliance on high-precision GNSS. Brazil is one of the most affected countries. In particular, ionospheric scintillation is a daily issue impacting both the availability and accuracy of high-precision GNSS-based positioning techniques, such as Real-Time-Kinematic (RTK) and Precise Point Positioning (PPP).

Mitigating the impact of severe scintillation on high-precision positioning is the main goal of CALIBRA, a project funded by the European Commission in the framework of the FP7-GALILEO-2011-GSA activity.

In this paper, we present the first results of the CALIBRA project, with as main focus the assessment of the impact of scintillation on Precise Point Positioning (PPP) and its mitigation. The remainder of this paper is organized as follows. First the context, scope and main objectives of the CALIBRA project are described. Next, we discuss the on-going monitoring of ionospheric scintillation in the region of interest, endeavored in the previous CIGALA project, and the resulting climatology results that are instrumental to assess the threat. Then, we zoom on the impact of scintillation on PPP, exploiting data collected during strong scintillation events. Finally, we discuss simple and effective mitigations at positioning algorithm level.

2 THE FP7 CALIBRA PROJECT

CALIBRA (Countering GNSS high Accuracy applications Limitations due to Ionospheric disturbances in BRAzil), a project funded under the Seventh Framework Program (FP7) by the European GNSS Agency (GSA) and coordinated by the Nottingham Geospatial Institute (NGI) at the University of Nottingham, deals with these ionospheric disturbances and their effect on GNSS high accuracy techniques. CALIBRA's partners are the Centre for Atmospheric Research (CAR) at the University of Nova Gorica (UNG) in Slovenia, the Upper Atmospheric Physics group of Istituto Nazionale di Geofisica e Vulcanologia (INGV) in Italy, Septentrio Satellite Navigation NV (SSN) in Belgium, Sao Paulo State University (UNESP) and ConsultGEL (CSG) in Brazil.

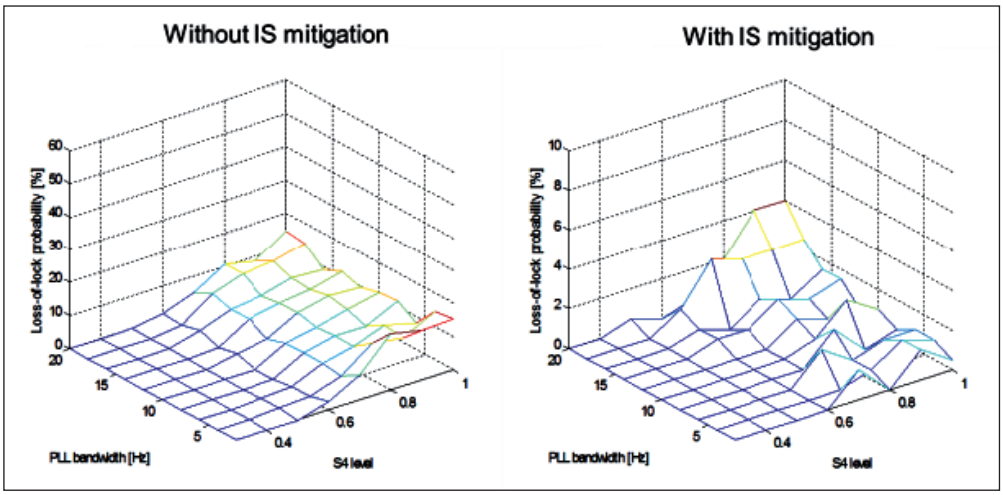

Figure 1 Tracking level mitigation of ionospheric scintillation

CALIBRA builds on the outcomes of the CIGALA project where it was demonstrated that signal tracking under ionospheric scintillation can be effectively mitigated by new algorithms and tracking loop configuration within the receiver signal tracking engine [14]. This is illustrated in Figure 1, which show the achieved loss-of-lock probability as a function of S4 (amplitude scintillation index) and user configurable loop bandwidth. The improved tracking robustness achieved in CIGALA, results in increased availability of the code and phase observables and, consequently, of the position solution (PVT) during moderate to strong scintillation.

CIGALA however also demonstrated that the carrier phase based PVT solution, although available during periods of moderate to strong scintillation thanks to the increased tracking robustness, may be significantly affected, with large error, which in all likelihood is related to the underlying degradation caused by ionospheric scintillation. This is shown in Figure 2, where the time series of the height component of a PPP (Precise Point Positioning) solution is shown during a period of moderate to strong scintillation at a station located in Presidente Prudente in Brazil (22.1 °S, 51.4 °W). The height component is normally the PVT component most affected by the ionosphere.

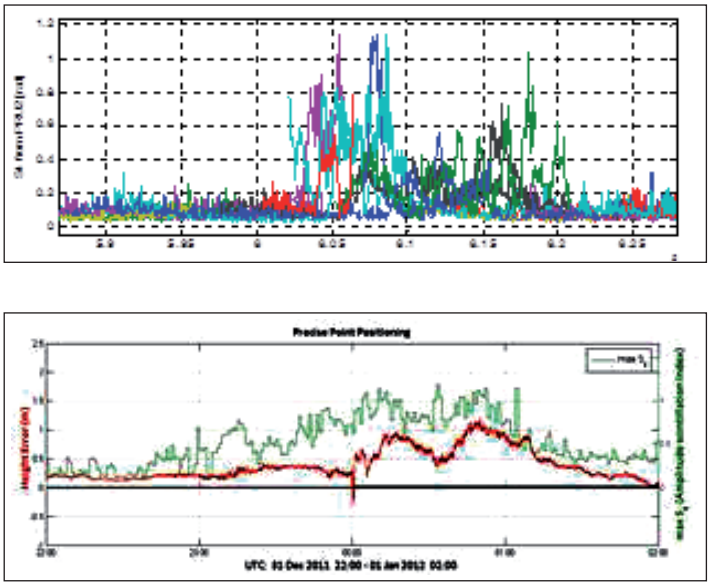

Figure 2 PPP Error during strong scintillation events

The increase in positioning error during scintillation as seen in Figure 2 is a major concern for high precision applications, which may experience accuracy degradation several times over the specification. Resolving this issue is the main goal of CALIBRA with respect to the state of the art. CALIBRA's specific aim is to develop and implement algorithms at receiver level in order to tackle the effects of ionospheric disturbances on high precision phase-based positioning (RTK and PPP). This paper focuses on initial progress in the project with regards to mitigation of scintillation on PPP.

3 MONITORING GNSS SCINTILLATION

The PolaRxS Receiver

Scintillation effects are characterised by a set of indices, where the most important are the amplitude scintillation index S_4 (the standard deviation of the received power normalized by its mean value) and the phase scintillation index σ_ϕ (the standard deviation of the de-trended carrier phase). In particular its 60s version, herein termed *Phi60*, is commonly used. Scintillation strength is typically qualified as *weak* ($S_4 < 0.25$), *moderate* ($0.25 \leq S_4 < 0.6$) or *strong* ($S_4 \geq 0.6$).

An ionospheric scintillation monitor (ISM) is expected to measure these quantities next to more commonly used slant Total Electron Count (TEC) and the rate thereof (RTEC). Scintillation indices can effectively be monitored using GNSS signals as originally proposed in [12] and further in [5]. The GNSS signals from the different satellites are exploited to "sample" the ionosphere parameters at the points where they pierce it.

Using GPS only, 4 to 14 points can be sampled depending on time and location. The recent development of additional GNSS constellations (modernized GLONASS, GALILEO, BEIDOU) and the introduction of new civilian signals in the L2 and/or L5 band in each of them significantly increase the observability of the ionospheric parameters in space, time and frequency.

The PolaRxS™ (Figure 3), which specifications were worked out in close collaboration with the project partners, extends the capabilities of state-of-the-art ISM solutions by incorporating a modern triple-frequency receiver engine capable of tracking simultaneously GPS, GLONASS, GALILEO, BEIDOU, SBAS and QZSS signals. The tracking engine, which is coupled with an ultra-low noise OCXO frequency reference (phase standard deviation *Phi60* less than 0.03 rad), can generate and store raw high rate data (post-correlation I and Q samples) at up to 100 Hz in hourly files which can be processed in real-time or in post-processing to furnish 60s scintillation indices S4 and σ_{ϕ}, along with other parameters like Total Electron Content (TEC), lock-time and the scintillation spectral parameters p (spectral slope of the phase Power Spectral Density, PSD) and T (spectral strength of the phase PSD at 1 Hz) for all visible satellites and frequencies. The signals that can be tracked include: GPS L1CA, L1P, L2C, L2P, L5; GLONASS L1CA, L2CA; Galileo E1, E5a, E5b, E5AltBoc; BEIDOU B1, B2; SBAS L1, L5; QZSS L1, L5.

Figure 3 Septentrio PolaRxS™

The PolaRxS™ has been tested independently by Septentrio and the University of Nottingham in their respective laboratories for interoperability with already installed ISM equipment such as the GSV4004, which used to be the reference.

Since its release and installation in the CIGALA network in 2010, the PolaRxS has been tested and adopted by an increasing number of groups and installed in networks all around the world.

Another important feature of the PolaRxS is the very low noise floor of the σ_ϕ measurement. This is illustrated in Figure 4 which depicts the *Phi60* for the L1 frequency obtained during a 24h long simulation using a Spirent GSS8000 GNSS simulator configured to generate perfect GPS signals.

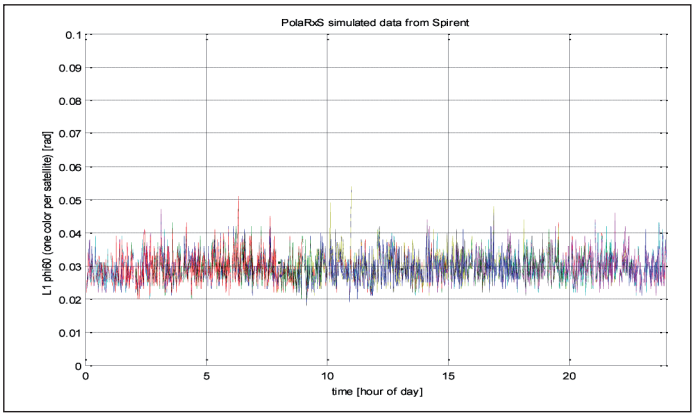

Figure 4 Characterization of the PolaRxS™ noise floor using Spirent GPS simulator

The PolaRxS™ benefits from tracking level scintillation mitigation as described in [14]. This maximizes the availability of code and phase observables, scintillation indices and minimizes the occurrence of cycle slips and loss of lock, even in strong scintillation events.

The CIGALA/CALIBRA ISM network in Brazil

During the years of 2011 and 2012, 8 GNSS stations were deployed in strategic locations over the Brazilian territory. Their localization is represented on Figure 5.

Figure 5 Geographical distribution of the CIGALA ISM Network

Each of those stations is equipped with a Septentrio PolaRxS PRO receiver (Figure 3), capable of logging measurements at a rate up to 100 Hz, a GNSS AERO AT1639 antenna, and PCs with high-end processors and power supply redundancy. In this scope, this network is capable of calculating, sending and storing data in two data mainframes located at Presidente Prudente – SP. Those mainframes run FTP/SSH servers, providing easy access to the collected observations and also an easy environment to work with data analysis tools. Each one of the CIGALA/CALIBRA stations is monitored by local partners. For instance, in Porto Alegre – RS (POAL receiver) the installation site is in a building inside the Federal University of Rio Grande do Sul (UFRGS), in Palmas – TO (PALM station), the receiver is located at a research site of the Federal Institute of Technology (IFT-TO) and in Sao Jose dos Campos – SP (SJCI/SJCE receivers), the equipment is installed in the premise of the National Institute for Spatial Research (INPE) in the Aeronomy department. Figure 5 shows some of the installation sites. This station deployment provides the project with an easy way to control the equipment and to solve issues related to receiver and computer configuration. All the stations have shown more than 90% availabilities in two years of operation.

Also in the mainframes, besides RAW and ISMR files, a data access tool is running on a PHP/SQL environment, providing a suitable solution to data visualization and filtering. In this system, named ISMR Query Tool[1], the registered user can insert queries to the scintillation database, and get the answer in a chart or in a customizable ASCII file. Figure 6 an example page of ISMR Query Tool.

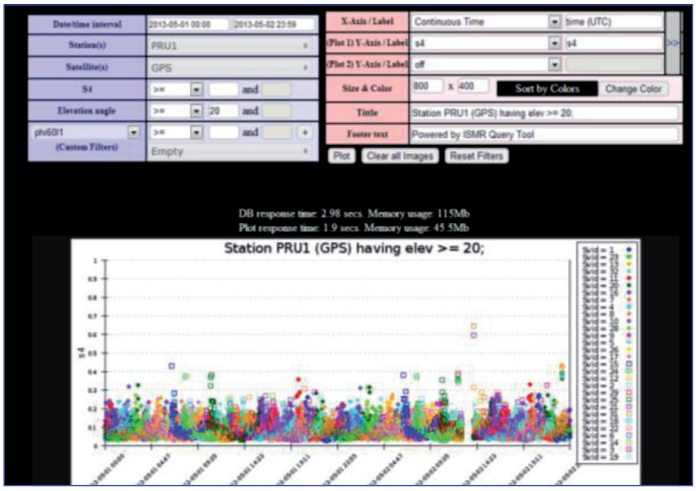

Figure 6 ISMR Query Tool

As the last development of the network, in the beginning of 2013 three new PolaRxS receivers arrived at Unesp, and are ready to be installed to further strengthen geographical coverage. Two places are already defined, as being in Fortaleza – CE and Salvador – BA, both in the northeast region of Brazil and market as green triangles in Figure 5.

More receivers are to come, and more sites are being analyzed to serve the network densification in the context of the CALIBRA project.

[1] Available at http://is-cigala-calibra.fct.unesp.br

Figure 7 CIGALA ISM sites

Ionospheric Scintillation Climatology in Brazil

Using the ISMR data collected by the CIGALA network during the two last years, the climatology of ionospheric scintillation over the region of interest has been studied, allowing us to assess the risk of disruption of high precision positioning services, in particular PPP.

Only data acquired between 2200 and 0400 UTC has been considered, in order to focus on the post sunset period when the scintillation is more likely to occur (see Figure 8 as example).

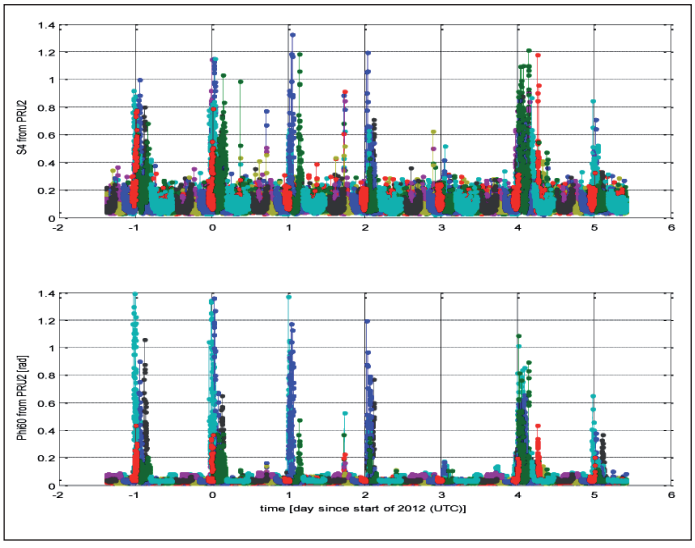

Figure 8 Example of daily scintillation during a period of high solar activity

Analyzing the rate of occurrence of scintillation above a given S4 threshold in the collected data, one can draw a map showing the probability of such scintillation to occur under a given latitude and longitude. Figure 9 depicts such a map for a S4 > 0.25. It is possible to see the enhancement of scintillation probability under the northern crest of the EIA, mainly covered by the MANA observations. This enhancement is for geographic latitudes greater than 0°N and is localized in a band nearly parallel to the geomagnetic equator (red line). The probability of postsunset scintillation with S4 > 0.25 in that area reaches 6%.

On the other hand, the southern crest of the EIA shows its effect in terms of amplitude scintillation occurrence in the band of enhanced scintillation nearly parallel to the geomagnetic equator (red line) and reaching a probability of about 16%. The enhancement over POAL is also meaningful and possibly due to the presence of the particle precipitation occurring in the borders of the SAMA [11].

Positioning applications in these regions will be affected quite significantly. Specific impact is discussed further in the next sections.

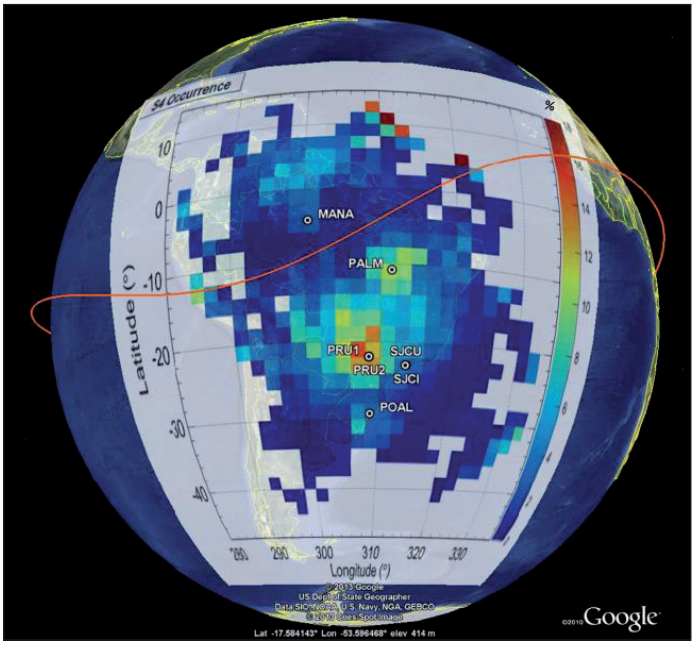

Figure 9 Probabilities of S4>0.25 over the Brazilian territory during post sunset period (2200 to 0400 UTC).

4 IMPACT OF IONOSPHERIC SCINTILLATION ON PRECISE POINT POSITIONING

Being non-differentiated and based on an iono-free combination, one would expect PPP not to be affected by ionospheric delays provided that the delays obey the standard $1/f^2$ rule and that no cycle slip occurs. As it turns out, this is not the case during scintillations. Figure 2 depicts the PPP error measured at station PRU1 during a strong scintillation event. The height error reaches more than 1 m (compared to 12 cm nominal) at periods when 3 satellites show S4 between 0.6 and 1.

To investigate the effect of scintillation on the GNSS measurements used for PPP, we compared the instantaneous signal power and carrier phase of GPS L1 and L2 signals during strong scintillations. It has been observed that, although the time series of the amplitude for the L1 and L2 signals are correlated, the perturbations caused by scintillations do not occur simultaneously on both frequencies. Figure 10 illustrates the delay between L1 and L2 deep fades and the effect of these fades on the carrier phase. The figure shows real data measured for PRN15 at station PRU1. The upper panel shows the instantaneous signal amplitude and the lower panel shows the difference between L1-C/A and L2C carrier phase observables. Four occurrences of so-called "canonical fades" [9] consisting of deep fades associated with half-cycle phase jumps (about 10 cm) are clearly visible and are marked by the red lines. In the case shown in Figure 10, the L2 fades are first to occur, shortly followed by the L1 fades.

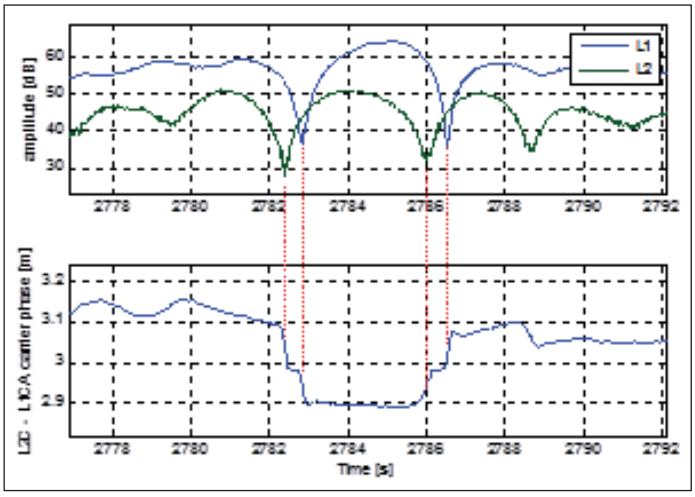

Figure 10 Evolution of signal power and of carrier phase on L1 and L2 frequencies during a scintillation event.

This actually means that the scintillations on L1 and L2 physically occur at different times, the time difference being a fraction of a second. In Figure 10, the L2 fade occurred before the L1 fade, but the value and the sign of the time difference vary from case to case. Figure 11, for example, shows a case where the L1 fade occurred before the L2 fade.

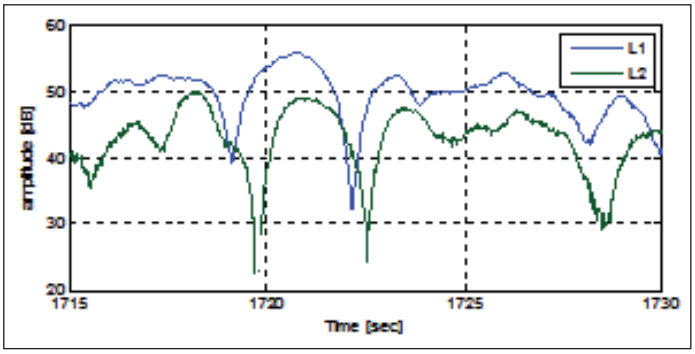

Figure 11 Another example of signal power on L1 and L2 frequencies during a scintillation event

One possible mechanism that could explain the time delay between the L1 and L2 fades is related to the ray path bending of GNSS signals due to the beam refraction in ionosphere coupled with the movement of "ionospheric bubbles". Due to the different path curvature of the L1 and L2 signals, the trajectories of L1 and L2 signals are spatially separated and travelling small-scale disturbances, which cause scintillation, may 'hit' the L1 beam a little later or a little earlier than the L2 beam.

Because the fades are not synchronous between L1 and L2, the iono-free combination cannot remove the associated ranging errors and these errors are directly translated into noise in the PPP solution.

Moreover, because the deep fades can be associated with sudden phase changes, they are likely to cause cycle slips. The presence of cycle slips is evidenced in Figure 11, which shows the L1-L2 phase difference compared to the L2-L1 pseudorange difference over the whole duration of a scintillation event. In the absence of cycle slips, these two quantities should remain parallel. As shown in the lower panel of the figure, this is not the case: the L1-L2 phase has a bias of about 1m with respect to the L2-L1 code after the scintillation. Such cycle slips also contribute to a significant degradation of the PPP accuracy.

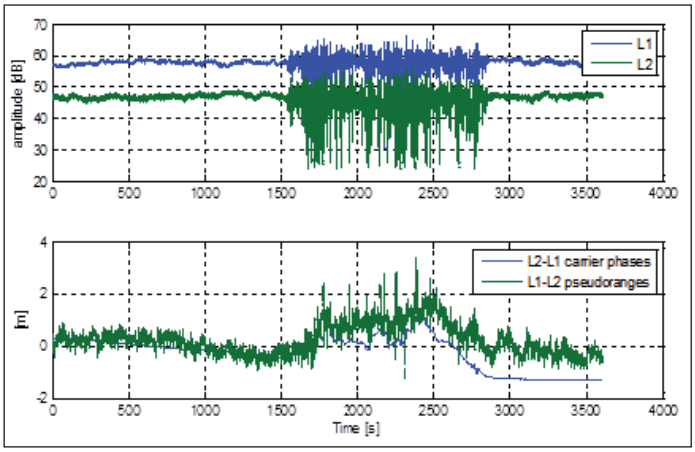

Figure 12 Cycle slips caused by the scintillation. Upper panel shows the L1 and L2 amplitude, where the scintillation time interval is clearly visible. Lower panel illustrates the code-phase divergence due to the cycle slipping during scintillations.

5 MITIGATING IMPACT OF SCINTILLATION ON PPP

In order to investigate possible mitigation at positioning level, the phase residuals for the satellites affected by scintillation were analyzed. Figure 13 shows that such residuals are significantly higher during the scintillation periods, indicating that traditional receiver autonomous integrity monitoring (RAIM) methods may be effective at detecting and removing the scintillating satellites from the positioning solution.

This was confirmed by the analysis of the so-called w-test values where w_i, is defined as the residual ε_i normalized with its estimated standard deviation σ_i. Such values are typically compared in magnitude with a threshold $k_\alpha^{1/2}$ prescribed by the probability of false alarm:

$$-k_\alpha^{1/2} < w_i = \frac{\varepsilon_i}{\sigma_i} < +k_\alpha^{1/2}$$

Most of the time the w_i is within the threshold (as in the above formula), so the w-test is passed and the measurement is used in the solution. If the w-test fails, the measurement is treated as an outlier and is excluded from the solution.

Figure 14 depicts the w-test value for the affected satellites during the scintillation period in question. A threshold of 10 is sufficient to exclude the affected satellites.

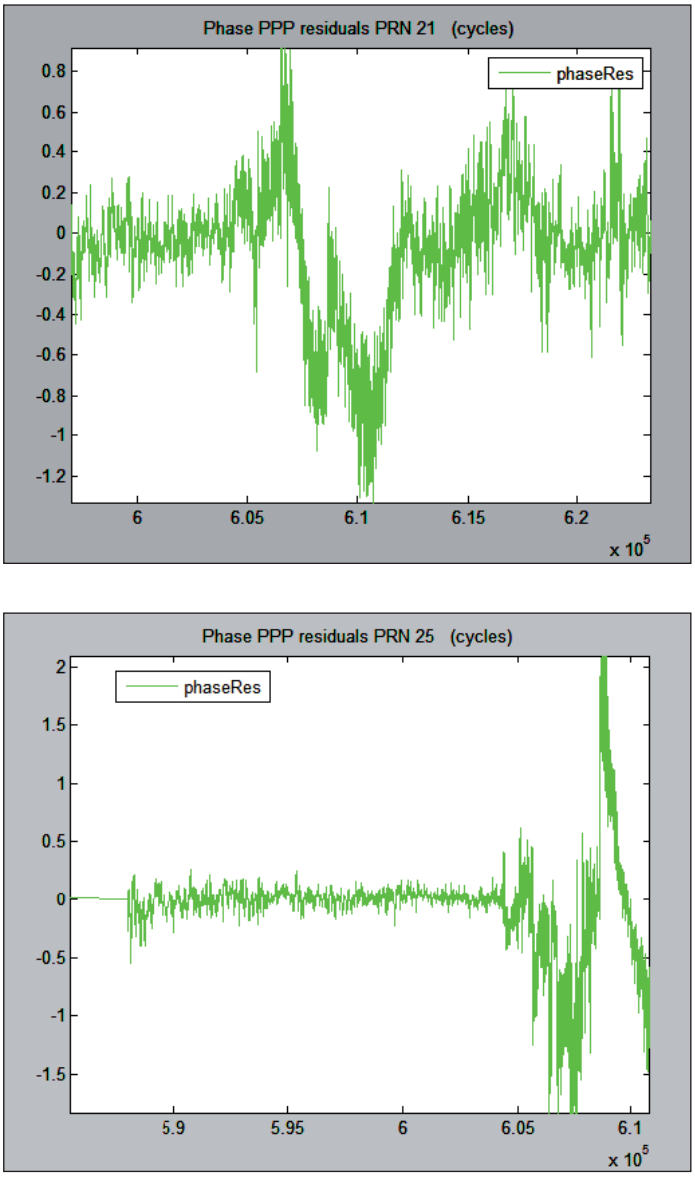

Figure 13 Phase residuals for satellites affected by scintillation

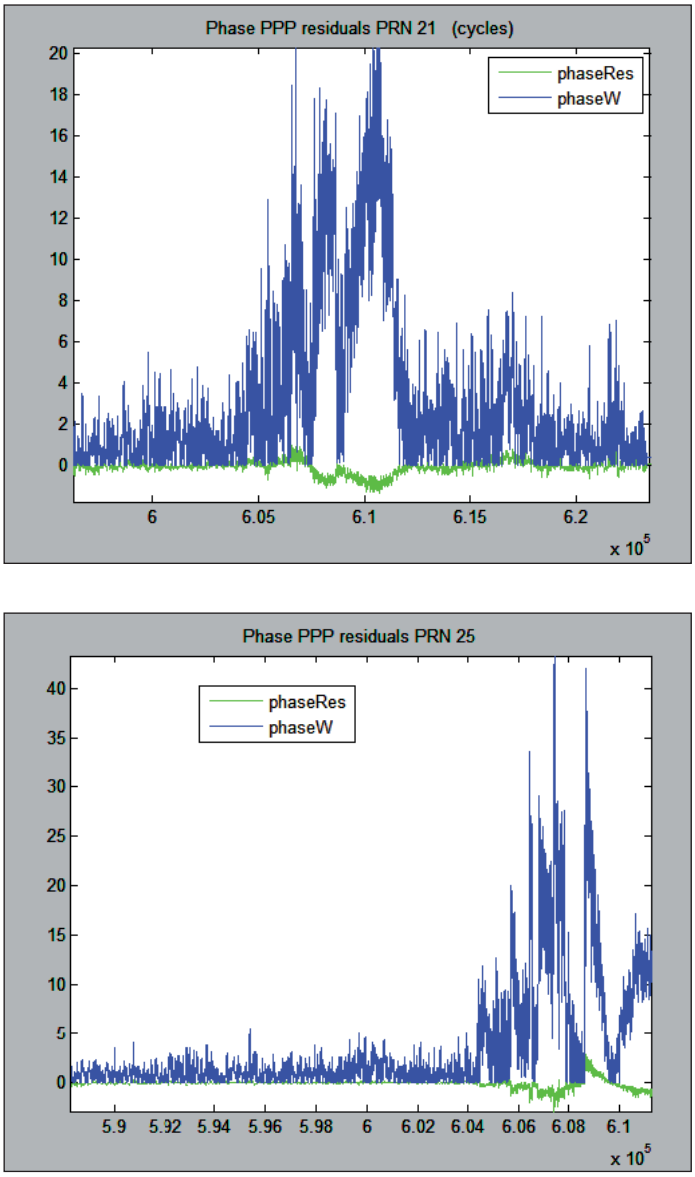

Figure 14 w-test values (blue) and phase residuals (green) for the satellites affected by scintillation

The proposed detection and exclusion method has been prototyped and the measurements reprocessed. As illustrated in Figure 15, the method is effective at restoring the PPP accuracy within its nominal specification during the whole scintillation event.

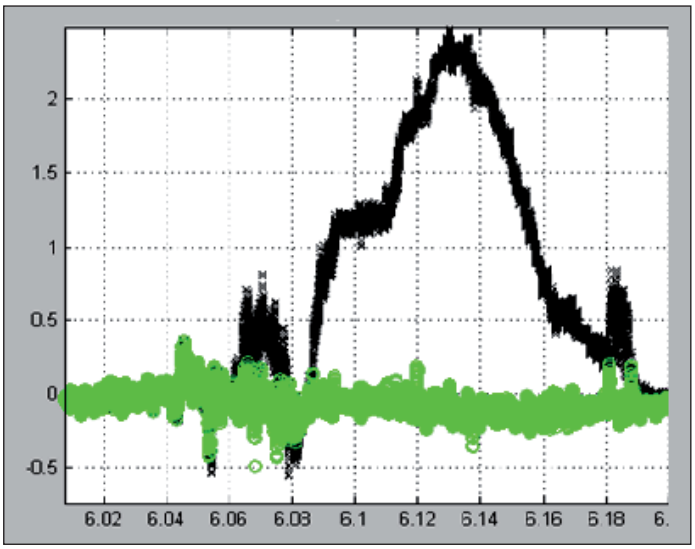

Figure 15 PPP solution with w-test-based integrity monitoring

6 CONCLUSION

The perturbations in the ionosphere resulting from the increasing solar activity pose a major threat to high precision GNSS applications in equatorial regions. This is particularly the case in Brazil where high exposure to solar-induced disturbances comes with a high reliance on precise GNSS applications in a number of key areas such as in the oil and gas industry.

In this paper, we reviewed the first results of the FP7 CALIBRA project, which principal aim is to mitigate the impact of severe ionosphere disturbance on high-precision positioning.

Capitalizing on the asset of previous CIGALA project, notably the ISM network and data archive, the climatology of ionospheric scintillation, the most forthcoming disturbances, was discussed, highlighting the regions most exposed to degradations due to scintillation. Further, we discussed the impact of said scintillations to Precise Point Positioning solutions. It has been found that scintillations cause a disturbance of the iono-free phase observables, which ripple down to the positioning solution with error up to 1m (10x the nominal specification).

Finally, a first mitigation approach, making use of standard RAIM procedures based on statistical tests of residuals, was discussed and demonstrated to significantly increase the resilience of PPP applications to scintillations.

ACKNOWLEDGEMENT

The CALIBRA project is funded under the EU Seventh Framework Program, and is carried out in the context of the Galileo FP7 R&D program supervised by the GSA.

REFERENCES

1. Aarons J., Global morphology of ionospheric scintillations, Proc. IEEE, 70, pp. 360–378, 1982.
2. Aarons J., Construction of a model of equatorial scintillation intensity, Radio Sci., 463(20), pp. 397–402, 1985.
3. Abdu M. A., J. A. Bittencourt, and I. S. Batista, Magnetic declination of the 466 equatorial F region dynamo electric field development and spread F, J. Geophys. Res., 86(467), pp. 11443–11446, 1981.
4. Alfonsi, L., L. Spogli, G. De Franceschi, V. Romano, M. Aquino, A. Dodson, and C. N. Mitchell (2011), Bipolar climatology of GPS ionospheric scintillation at solar minimum, Radio Sci., 46, RS0D05, doi: 10.1029/2010RS004571.
5. Beach T.L. and P.M. Kintner, Development and use of a GPS ionospheric scintillation monitor, IEEE Trans Geosci Remote Sens (USA), 39, pp. 918–928, 2001.
6. Beniguel, Y., Global Ionospheric Propagation Model (GIM): a propagation model for scintillations of transmitted signals, Radio Sci., 37(3), 2002.
7. Humphreys, T. E., M. L. Psiaki, J. C. Hinks, B. O'Hanlon, and P. M. Kintner, Jr., Simulating Ionosphere-Induced Scintillation for Testing GPS Receiver Phase Tracking Loops, IEEE Journal of Selected Topics in Signal Processing, 3, pp. 707–715, 2009.
8. Kelley M.C., The earth's ionosphere: Plasma physics and electrodynamics, Academic Press, San Diego, Calif, 1989.
9. Kintner P. M., H. Kil, T. L. Beach and E. R. de Paula, Fading Timescales Associated with GPS Signals andPotential Consequences, Radio Sci., 36(4), pp. 731–743, 2001.
10. Prieto-Cerdeira R. And Orus-Perez R., Testing Ionospheric Scintillation Monitors based on GNSS using Spirent Constellation Simulator, Proc. International Ionospheric Effects Symposium (IES2011), Alexandria, Virginia, May 2011.
11. Spogli, L., L. Alfonsi, G. De Franceschi, V. Romano, M. H. O. Aquino and A. Dodson, Climatology of GPS ionospheric scintillations over high and mid-latitude European regions, Ann. Geophys, 27, pp. 3429–3437, 2009.
12. Van Dierendonck, A. J., Klobuchar, J., and Hua Q., Ionospheric Scintillation Monitoring Using Commercial Single Frequency C/A Receivers, Proc. IONGPS-93, Salt Lake City, UT, Sept. 1993.
13. Wernik, A. W., and C. H. Liu (1974), Ionospheric irregularities causing scintillations of GHz frequency radio signals. J. Atmos. Terr. Phys., 36, pp. 871–879, 1974.
14. Bougard, B. et al., CIGALA: Challenging the Solar Maximum in Brazil with PolaRxS, Proc. ION GNSS Conference, Portland, Sept. 2011.

Faculty of Maritime Studies
University of Rijeka, Croatia

Royal Institute of Navigation
Science Technology Practice

7th GNSS
Vulnerabilities and Solutions Conference

SPECTRAL AND SPATIAL CHARACTERIZATION OF GNSS JAMMERS

Daniele Borio, Joaquim Fortuny-Guasch, Cillian O'Driscoll

EC Joint Research Centre, Institute for the Protection and Security of the Citizen
E-mail: daniele.borio@jrc.ec.europa.eu

ABSTRACT. *GNSS jammers are small electronic devices able to transmit powerful signals in the GNSS bands and prevent a GNSS receiver to determine its position. Risks connected to jamming are due to the fact that the transmitted power is unconstrained, i.e. no measures are taken to limit the signal transmission in small geographical areas. Jamming signals can propagate for several kilometres and affect GNSS services in a wide area around the jammer.*

The main focus of this paper is the spectral and spatial characterization of GNSS jammers with specific emphasis on multi-frequency wideband jammers which are able to simultaneously jam up to three frequencies. The paper extends previous analysis to jammers also operating in the L2 and L5 bands.

The second contribution of the paper is the spatial characterization of jamming signals. It is noted that jammers are usually used inside cars and other vehicles. The structure of the vehicle interacts with the signal transmitted and some propagation directions are favoured. Two vehicles equipped with in-car jammers were considered and, from the analysis, it emerged that each vehicle has a characteristic signature determined by specific directions favouring or impeding the propagation of the jamming signal.

KEY WORDS: *GNSS, GNSS Jammers, GNSS Vulnerability*

1 INTRODUCTION

Global Navigation Satellite Systems (GNSSs) are able to provide precise location and timing information which find use in several applications. The usage of GNSSs is not limited to personal and car navigation but, for example, they can be employed for the tracking of goods and animals, to locate trains, navigate ships and for sport applications. In addition to this, precise synchronization can be achieved using relatively cheap Global Positioning System (GPS) clocks: telecommunication networks can be precisely synchronized using the common time scale provided by a GNSS.

In addition to this, new GNSS applications are currently under development or consolidation. For example, GPS boxes can be used by insurance companies to monitor the behaviour of a driver and adjust the insurance premium accordingly. GPS and GNSSs in general enable 'pay-as-you-drive' applications which also require the monitoring of the user behaviour. This type of application inevitably introduces privacy issues since GNSSs are used to collect information on GNSS users. This motivates the development and use of devices which can deny GNSS signal reception (Pullen and Gao, 2012).

GNSS jammers are small portable devices able to broadcast disruptive signals in the GNSS bands. A jammer can overpower the much weaker GNSS signals and disrupt GNSS-based services in a geographical area with a radius of several kilometres (Mitch et al. 2011). Despite the fact that the use of such devices is illegal in most countries, jammers can be easily purchased on the internet and their rapid diffusion is becoming a serious threat to satellite navigation.

Clear examples of the risks associated with the usage of GNSS were recently reported in the international press (The Economist, 2011). The case of a truck driver periodically passing close to the Newark Liberty International Airport is described by The Economist (2011). The driver was using a GNSS jammer (or so-called Personal Privacy Device (PPD)) to prevent his company from tracking his position. The jammer was however so powerful that problems were caused to the reception of Wide Area Augmentation System (WAAS) and GNSS signals. Eventually, after three months of investigation, the authorities were able to identify the problem, locate the jammer and fine the truck driver.

From this discussion, it emerges that GNSS jammers are expected to become a serious threat for GNSS operations and countermeasures should be developed to reduce the associated risks. A proper characterization of jamming signals has been recognized as the first step towards the development of appropriate jamming countermeasures (Mitch et al., 2011). Only accurate jamming signal models enable the design of effective detection, mitigation and location strategies.

The main focus of this paper is thus the spectral and spatial characterization of GNSS jammers with specific emphasis on multi-frequency wideband jammers which are able to simultaneously jam up to three frequencies. The paper extends previous analysis to jammers also operating in the L2 and L5 bands.

The characterization of the signals emitted by GNSS jammers was performed in terms of signal spectral features and spatial propagation. The signals transmitted by jammers are frequency modulated chirps which span one or more bands centred on the GNSS frequencies. For each jammer, parameters such as the sweep period, the maximum and minimum swept frequencies and the transmitted power were determined. The spatial characteristics of jammer signals have also been analysed. In particular, it is recognized that the majority of the GNSS denial events reported in the literature originated from in-car jammers. Thus, the effect of the vehicle in which the jammer is located should be taken into account. For this reason, the spatial distribution of the power transmitted by a jammer was analysed accounting for the vehicle presence. The analysis was repeated for two different vehicles: a small car (Fiat Panda) and a van (Fiat Ducato). From the analysis, it emerges that the structure of the vehicle favours specific propagation directions, usually corresponding to the windows. This type of analysis can be useful for the design of sophisticated jammer detection/location algorithms.

The remainder of this paper is organized as follows. In Section 2, a thorough literature review is provided whereas results obtained for the spectral characterization of jamming signals are detailed in Section 3. Section 4 discusses the findings obtained measuring the spatial power distribution of jammer signals located inside vehicles. Conclusions are finally drawn in Section 5.

2 LITERATURE REVIEW

In this section, the literature available on GNSS jammers is briefly reviewed. Particular attention is devoted to jammer classification.

Several classifications for jammers are available in the literature (Graham, 20011), (Brown et al., 1999), (Mitch et al., 2011), (Kraus et al., 2011). Graham (2011) provides a general classification of communications jammers whereas the analyses provided by Brown et al. (1999), Mitch et al. (2011) and Kraus et al. (2011) are specific to GNSS applications. It is noted that GNSS jammers are a special type of communication jammers. Thus, the classification provided by Graham (2011) is reviewed first.

Communications jammers can be divided into the following classes (Graham, 2011):

- *'jam on tune' jammers:* in this case, the centre frequency and bandwidth of the enemy transmission are estimated and the jammer signal is tuned to match the spectral characteristics of the enemy signal. The jammer is on only when the enemy signal is on. A special type of 'jam on tune' jammer is the so called *follower jammer* designed for frequency hopped signals. In this latter case, the jammer is designed to follow the frequency variations of the enemy signal that is assumed to be frequency hopped.
- *swept jammers*: the jammer transmits a frequency modulated signal. The signal is instantaneously narrow band and its centre frequency sweeps a large bandwidth. In this way, a wide portion of the enemy spectrum is affected by the jammer. In this case, the jammer instantaneous frequency assumes a saw-tooth shape. This type of behaviour is typical since it can be easily achieved by slaving a Voltage Controlled Oscillator (VCO) to a progressively increasing voltage source. When a maximum voltage is reached, the process is reset. The vast majority of GNSS jammers belong to this class.
- *barrage jammer*: this type of jammer is able to simultaneously jam a broad portion of the spectrum. Pseudo-random sequences can be used to obtain wide-band jamming signals. Barrage jammers require very high power to be effective over the whole part of the spectrum under attack.
- *adaptive jammer*: this type of device is designed to simultaneously affect signals on several bands. The power available for jamming is split into the required number of channels.
- *smart jammer*: this is a special form or jamming which exploits a priori knowledge of the victim system. If, for example, the system uses a synchronization channel then it is possible to jam only this channel to deny the services associated to the whole system.

The literature available on GNSS jammers (Mitch et al., 2011), (Kuusniemi et al., 2012) and (Kraus et al., 2011) shows that essentially all civilian GNSS jammers are *swept*. This fact is confirmed by the results presented in Section 3 where the characteristics of seven GNSS jammers are analyzed: all the jammers are swept. In (Rash, 1997), a brief review of military GNSS jammers is performed and it is highlighted that *barrage jammers* can also be used. In particular, pseudo-random sequences spectrally matched to the victim GNSS signal can be used. It is noted that although examples of smart jammers have not been reported in the GNSS literature, this type of device could be used to prevent the proper functioning of specific classes of GNSS receivers. For example, jamming the Coarse/Acquisition (C/A) signal alone can be sufficient to prevent

military receivers to acquire and process the encrypted Precision (P) code (P(Y) signal). Multi-frequency GNSS receivers can exploit the timing relationship between signals at different frequencies. For example, codeless processing of GPS L2 P(Y) signals often relies on the successful acquisition and tracking of the C/A L1 component. If the L1 signal is jammed the processing of the L2 P(Y) signal is also impeded.

The classification presented above is general and applies to communications jammers in general. More specific classifications have been suggested in the GNSS community, for example Rash (1997) divided GNSS jammers into

- *Continuous Wave (CW) jammers*: the bandwidth of the transmitted signal is less than 100 kHz.
- *Narrow-band jammers*: the bandwidth of the transmitted signal is greater than 1 MHz but less than 2 MHz that is the width of the main lobe of the GPS C/A signal.
- *Wide-band jammers*: the bandwidth is greater than 2 MHz.

This classification was based on the characteristics of the GPS L1 signal which was the only civil signal available in the late 90s. Moreover, the only form of jamming was military in nature and devices for civil use were not considered. More appropriate classifications have been recently proposed (Mitch et al., 2011), (Kraus et al., 2011). The classification suggested by Mitch et al. (2011) is based on the characteristics of the device used for jamming. In particular, the jammers analysed by Mitch et al. (2011) were divided into three groups:

- *Group I: cigarette lighter jammers*, the device is designed to be plugged into an automotive cigarette lighter 12 Volt power supply.
- *Group II: SMA battery jammers*, the device is powered by a battery and it is connected to an external antenna through an SubMiniature version A (SMA) connector.
- *Group III: non-SMA battery jammers*, the device is powered by a battery and uses an integrated antenna for transmission.

The classification suggested by Kraus et al. (2011) is based on the characteristics of the transmitted signal and divides jammers according to the following classes:

- *Class I: CW signals*, the device transmits a CW signal.
- *Class II: single saw-tooth chirp signals*, the device transmits a frequency modulated signal with a saw-tooth time-frequency characteristics.

- *Class III, multi saw-tooth chirp signals*, the device transmits a frequency modulated signal but its time-frequency evolution is more complex and determined by the combination of several saw-tooth functions.
- *Class IV, chirp with signal frequency bursts*, the device transmits a frequency modulated signal and frequency bursts are used to enlarge the frequency band affected by the disturbing signal.

The two classifications consider different aspects of jamming devices and can be combined as in Figure 1. In this way, a composite jammer classification able to capture both aspects is obtained.

Although the two classifications considered above are able to capture most jammer characteristics, the following aspects should be also considered:

- single vs. multi-frequency jammers: several jammers can simultaneously affect several GNSS bands.
- single vs. multi-antenna jammers

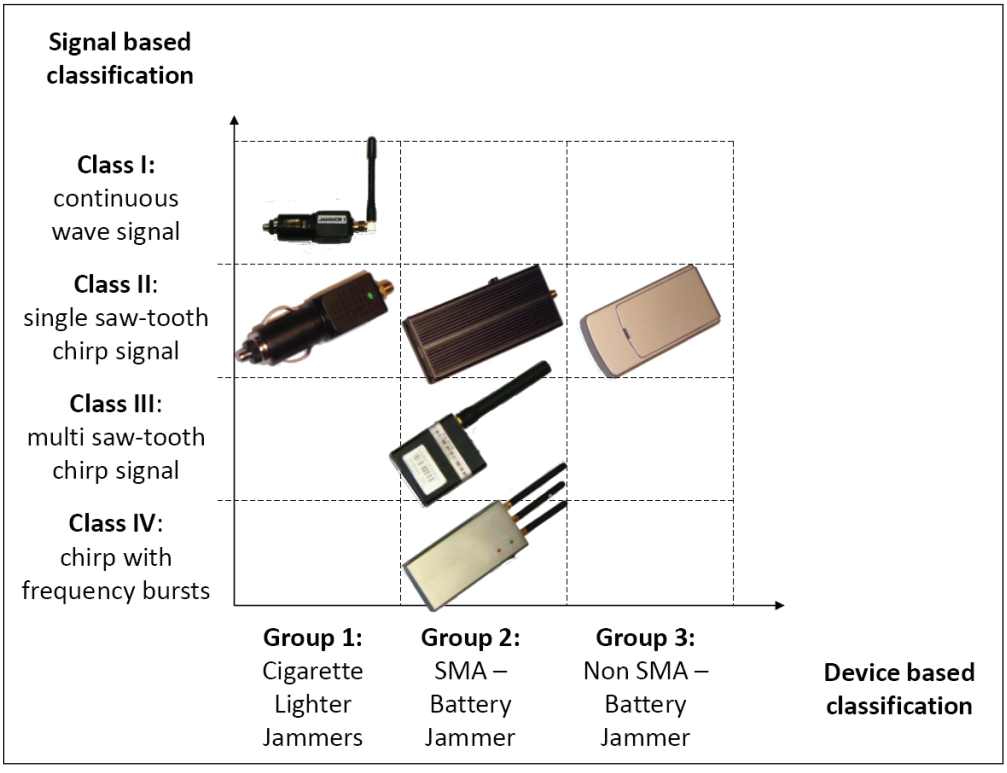

Figure 1 Composite jammer classification accounting for both signal and device characteristics.

- single vs. multi-system jammers: some jammers simultaneously affect GNSS and other communications systems such as Global System for Mobile Communications (GSM) and Universal Mobile Telecommunications System (UMTS).

These aspects are particularly relevant for the design of mitigation and location techniques. For example, several location techniques are based on Time Difference Of Arrival (TDOA) which requires precise synchronization. When GNSS services are denied, other communications signals could be used to achieve precise synchronization.

3 MULTI-FREQUENCY JAMMER CHARACTERIZATION.

In this section, the spectral characteristics of 7 GNSS jammers are described. The jammers used for the analysis were provided by Nottingham Scientific Ltd. (NSL), the coordinator of the FP7 project DETECTOR (http://www.gnss-detector.eu/) which focuses on the "detection, evaluation and characterization of threats to road applications". NSL kindly made the jammers available to the JRC for the tests reported on herein.

The jammers used for the analysis were labeled from 1 to 7 and can be classified as follows. Jammers 1 and 2 belong to group 2 (SMA-battery jammers) of the classification proposed by Mitch et al. (2011) whereas jammers from 4 to 7 are cigarette lighter jammers (group 1). Jammer 3 requires an external 12 Volt power supply and although it came without a dedicated connection for the cigarette lighter it can be powered in this way. All the jammers transmit a single saw-tooth chirp signal and thus belong to class 1 of the classification suggested by Kraus et al. (2011). The spectral characteristics of the 7 jammers used for this project were determined using the experimental setup depicted in Figure 2. The tests were conducted inside the JRC anechoic chamber where it is possible to transmit signals without interfering with other systems. The jammer under test was mounted on a tripod and used to transmit the jamming signal which was received by a calibrated double ridge horn antenna. The receiving antenna was connected to a Tektronix RSA6114a, a wide-band real-time spectrum analyzer able to collect In-phase/Quadrature (I&Q) samples with a sampling frequency up to 150 MHz. Several short datasets of 1 ms duration were collected and used for the characterization of the jamming signals. A Rohde & Schwarz (RS) SMB100A RF and microwave signal generator was used to calibrate the transmission chain and determine the calibration factors used to measure the absolute power transmitted by each jammer.

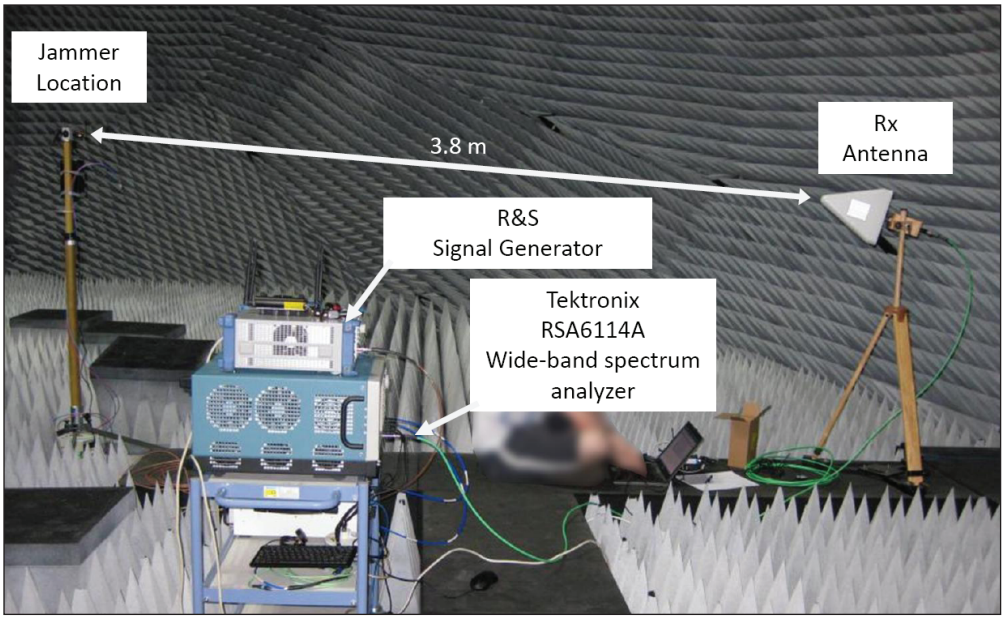

Figure 2 Experimental setup adopted for the characterization of seven GNSS jammers.

The analysis of the jammers follows the approach employed by Mitch et al. (2011) and provides the sweep and power parameters of the signals emitted by the devices considered. The sweep parameters of the seven jammers are provided in Table 1 which also considers signals transmitted in non-GNSS bands. A significant variability among the sweep parameters is observed: for example, the sweep period in the L1 band varies from about 5 to 37 μs. This variability is observable not only among jammers of different models but also among devices of the same type. This phenomenon is consistent with the results discussed by Mitch et al. (2011).

Non-cigarette lighter jammers (J01, J02 and J03) are able to jam very wide frequency ranges (about 50 MHz) in the L1 frequency. In this case, the military P(Y) and Galileo Public Regulated Service (PRS) signals will also be severely affected.

Multi-frequency jammers transmit signals characterized by the same sweep period in each frequency band. This indicates that a single local oscillator is used for the generation of all the signals. Consider for example, jammer J01: the sweep period for the L1 signals is about 5.34 μs whereas for the L2 and L5 components is 5.54 μs. The difference between the two periods is explained by the fact that two different datasets were used for the analysis. The jammer local clock is affected by biases and drifts which explain the variability between

Table 1 Sweep parameters measured for a set of seven GNSSS jammers. Signals transmitted in the non-GNSS bands are also considered.

Jammer	Centre Frequency	f_{min} MHz	f_{max} MHz	Sweep Range MHz	Sweep Period µs
1	GPS L1	20.8	28.4	49.2	5.34
1	GPS L2	10.7	11.2	21.9	5.54
1	GPS L5	11.8	12.2	24	5.54
2	GPS L1	24.6	26.2	50.8	5.15
2	GPS L2	8.5	8.6	17.1	5.24
2	GPS L5	11.6	11.6	23.2	5.24
3	GPS L1	27	29	56	6.83
3	GPS L2	16.1	16.4	32.5	6.83
3	945 MHz	21	21	42	41.9
3	846.5 MHz	42.2	42.2	84.4	41.9
4	GPS L1	7	4.5	11.5	9.47
5	GPS L1	6.6	4	10.6	8.64
6	GPS L1	6	5.5	11.5	9.09
7	GPS L1	7.4	26.5	33.9	36.7

measurements taken at different times. Since the spectrum analyzer used for the analysis is able to capture an instantaneous bandwidth of about 150 MHz, it was possible to jointly collect signals in the L2 and L5 bands. The spectrogram of the signals transmitted by jammer J02 in L2 and L5 is shown in Figure 3. The L2 and L5 jamming signals have a similar pattern although the L5 component is more powerful and spans a larger frequency range.

The two signals have the same sweep period even if there is a relatively small offset between the instants at which a frequency reset occurs. Signals transmitted in non-GNSS bands are characterized by much slower sweep periods. In particular, the signals transmitted in the GSM bands by jammer J03 are characterized by sweep periods about six times slower than those of the signals emitted in the GNSS frequencies.

The results obtained are combined with those of (Mitch et al., 2011) in Figure 4 which provides some indication of the distribution of the sweep periods of jammers available on the market. From the figure, it emerges that cigarette lighter jammers currently operate only in the L1 frequency. Moreover most of these jammers have a sweep period of about 9 µs even if significant deviations

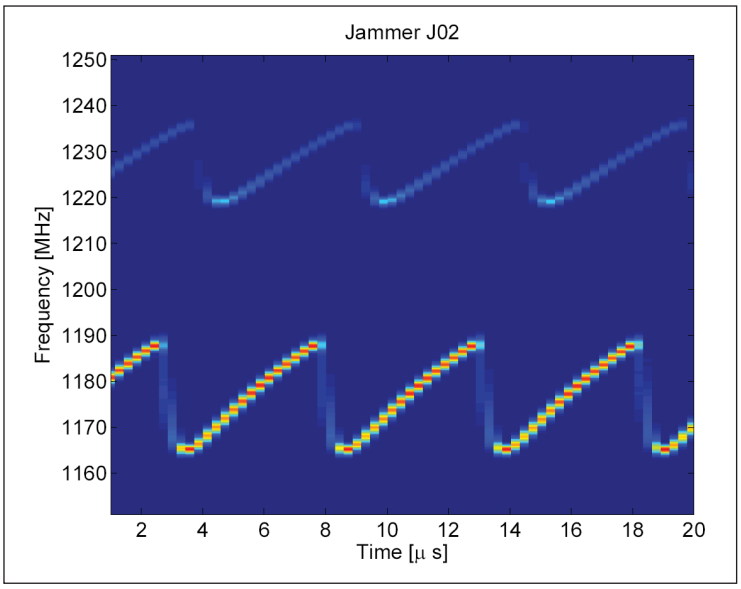

Figure 3 Spectrogram of the signals transmitted by jammer J02 in the GNSS L2 and L5 bands.

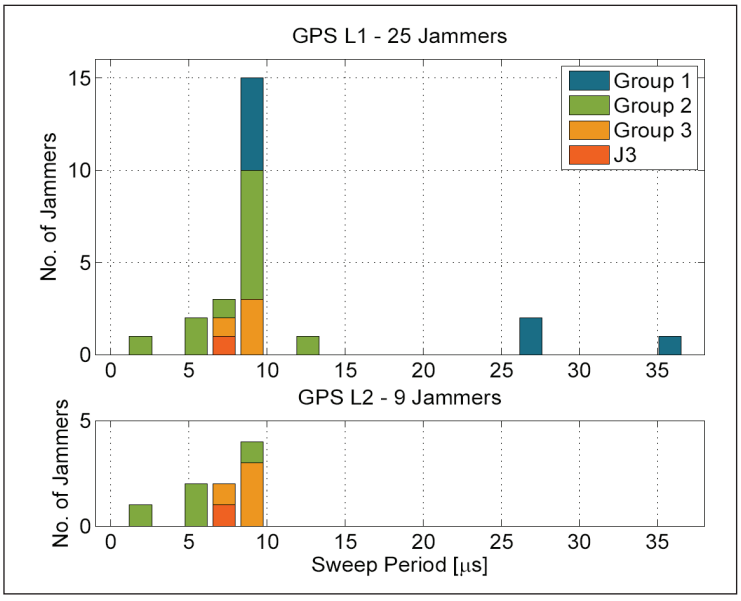

Figure 4 Distribution of the sweep times obtained combining the results obtained with those from (Mitch et al., 2011).

can be found. This is the case of jammer J07 which has a sweep period equal to 36.7 µs. When considering the totality of the jammers, it clearly emerges that 9 µs is the most common value for the sweep period. In Figure 4, jammer J03 is considered separately given its architecture and power consumption.

Table 2 Power parameters measured for a set of seven GNSS jammers. Signals broadcast in non-GNSS bands are also considered.

Jammer	Centre Frequency	Power (2 MHz) mW	Total Power mW
1	GPS L1	0.9	14.5
1	GPS L2	2.3	14
1	GPS L5	1.4	10.5
2	GPS L1	1.2	17.8
2	GPS L2	1.5	9.8
2	GPS L5	7.5	48.9
3	GPS L1	55	1122
3	GPS L2	148	1479
3	945 MHz	398	4266
3	846.5 MHz	74	1698
4	GPS L1	5	15.8
5	GPS L1	1.4	4
6	GPS L1	2.6	7.8
7	GPS L1	0.06	0.5

The power parameters measured for the seven jammers are provided in Table 2. Also in this case, the results obtained are consistent with the findings of Mitch et al. (2011). In particular, the total transmitted power varies depending on the type of jammer and even among jammers of the same type. In general, cigarette lighter jammers are characterized by lower power levels than multi-frequency battery jammers. Moreover, extremely high powers are transmitted in the non-GNSS bands. This is likely due to the fact that communications signals are much more powerful than those of GNSS and thus more power is required to disrupt non-GNSS services.

The results in Table 2 are further analysed in Figure 5 along with the findings reported by Mitch et al. (2011). GNSS jammers can broadcast powers from less than -10 to more than +30 dBm. In particular, jammer J03 can transmit more than 1 W: this amount of power can affect GNSS services for several kilometres.

It is also noted that a strong variability is observed in the total transmit power: these values are also expected to vary over time and depend, for example, on the charge level in the case of battery jammers.

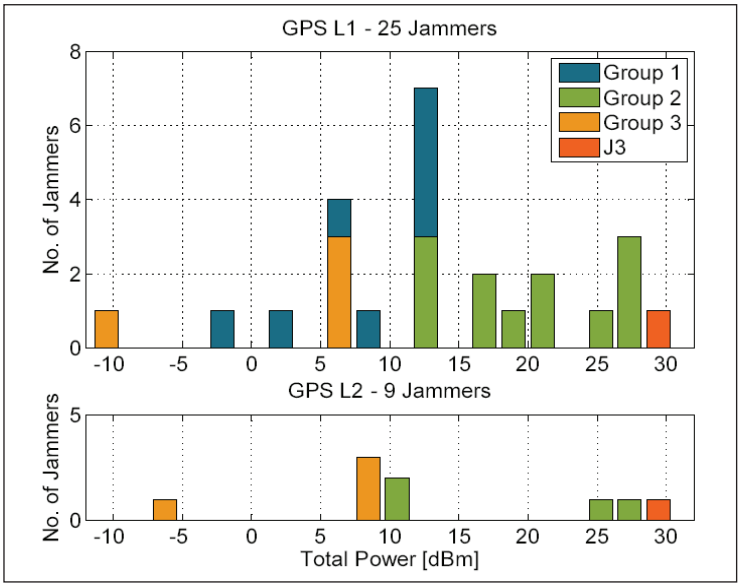

Figure 5 Distribution of the total powers obtained combining the results obtained with those from (Mitch et al., 2011).

4 JAMMER SPATIAL CHARACTERIZATION

Most jammer events detected "in the wild" have arisen from low-cost in-vehicle jammers. For this reason, several tests were performed in the JRC anechoic chamber with the final goal of investigating the impact of the vehicle type and antenna location on the jamming signal.

Two types of tests were conducted:

- *Network analyzer based tests*: the JRC anechoic chamber is equipped with a Vector Network Analyzer (VNA) which allows one to characterize an RF channel as a function of the azimuth and elevation of the receive antenna. Several signal centre frequencies were considered. In this case, the jammer is replaced by a signal source emitting signals with known properties, i.e. CW signals with known power. The measurements with the VNA were conducted using three monopole antennas (those that came with jammers 4, 5, and 6) and a 3-port electromechanical RF switch. At each receiver position (azimuth and elevation), the RF channel associated with each of the three monopole

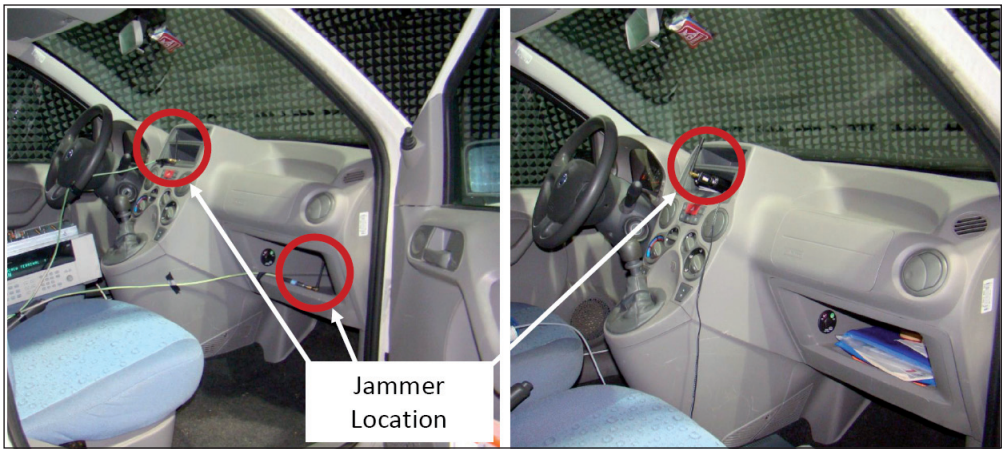

Figure 6 Location of the jammer for the tests conducted on a small car. Left: network analyzer case. Right: Spectrum analyzer case.

antennas was measured. The total measurement procedure over all azimuth and elevation angles took a total of just over 9 hours.

- *Spectrum analyzer based tests*: measurements with a real jammer placed inside a vehicle were conducted. In this case, the Tektronix spectrum analyzer mentioned above was connected to the probe antenna placed on one of the sleds of the anechoic chamber. The JRC anechoic chamber is equipped with two sleds allowing one to scan different elevation angles.

Both the VNA and spectrum analyzer were driven by an external rubidium standard oscillator.

An example of a measurement setup using the network and spectrum analyzer is shown in Figure 6. In this case, a small car, a Fiat Panda, was placed inside the anechoic chamber and three different jammer locations were considered for the network analyzer case (left part of Figure 6). In the spectrum analyzer case, a single jammer position was considered.

The three positions considered for the network analyzer tests are:

- the *dashboard* of the vehicle. This position represents the case of a jammer inserted in the cigarette lighter plug.
- the *glove box* of the vehicle. This position corresponds to the case of a battery jammer left in the glove box.
- in the *boot* of the vehicle. Although this is a less realistic location, it was selected because it was expected to provide significantly different results with respect to the previous cases.

For the spectrum analyzer based tests, the following approach was used. At each position of the probe antenna two measurements were performed and I&Q samples were collected for both Right Hand Circular Polarization (RHCP) and Left Hand Circular Polarization (LHCP) polarizations. The length of each dataset collected was 1 ms, and a sampling frequency f_s = 150 MHz was used. From the signal samples, it was possible to determine different parameters such as the received power in different bandwidths.

Results: Network Analyzer Tests

The calibrated transmission/reception chain of the JRC anechoic chamber was used to determine the composite loss,

$$L_c(\theta,\phi) = L_v(\theta,\phi) + G_{Tx}(\theta,\phi) + L_m, \quad (1)$$

given by the loss caused by the vehicle, L_v, the jammer antenna gain and other mismatch losses, L_m. Quantities in (1) are expressed in dB and the same sign convention is used for losses and gains. This implies that negative quantities in (1) imply a reduction of the signal power. Note that the quantities in (1) are a function of the elevation and azimuth of the receive antenna, θ and ϕ, respectively. Mismatch losses account, for example, for polarization mismatches between the receive and transmit antennas.

The composite loss, L_c, allows one to determine the impact of a vehicle on the signal transmitted by a jammer a function of the jammer direction of arrival. In particular, the jammer power received at a distance r can be computed as

$$P_{Rx}(\theta,\phi)\big|_{dBm} = P_{Tx}\big|_{dBm} + L_c(\theta,\phi) - 20\log_{10}\left(\frac{4\pi r}{\lambda}\right) \quad (2)$$

where λ is wavelength associated to the received signal centre frequency.

Measurements were conducted considering a 5 degree resolution in both the azimuth and elevation domains. Moreover, L_c was obtained by transmitting a CW at a specific frequency. During the tests, the [0.8-2.4] GHz frequency range was swept with a 1 MHz step. The results presented in the following were obtained by averaging the channel losses measured over the 1.570-1.580 GHz frequency range. This range is approximately centered around the GPS L1 centre frequency and has a width comparable to the bandwidths of commercial GNSS receivers.

Two vehicles, a small car (Fiat Panda) and a van (Fiat Ducato) were used and the three jammer positions described above were adopted. In this way, a total of six

cases were considered. The results obtained from the network analyzer tests are shown in Figure 7 and Figure 8. In the figures, L_c is depicted as a function of θ and ϕ. The vehicle was aligned with respect to the horizontal axis of the plot and oriented according to the arrow labelled 'driving direction'. In this way, the front of the car corresponds to the right hemisphere of the plot. From the figures, it emerges that the interaction between the jammer and the vehicle favours specific propagation directions.

For example, when the jammer is placed in the dashboard, the transmitted signal is amplified when received from directions corresponding to the vehicle windscreen. The glass of the windscreen does not significantly attenuate the signal. On the contrary, directions corresponding to the rear of the car are less favoured. By comparing LHCP and RHCP plots, it emerges that there is not a favoured polarization. This is expected since, given the low cost, it is likely that no optimization was implemented in the design of the jammer antenna. Although GNSSs use RHCP signals, no effort is expected for mainly affecting this polarization. When considering the glove box position, no specific propagation direction seems to be favoured in the small car case. When the jammer antenna is placed in this position, the signal emitted interacts with the different elements of the car and several reflections occur. Moreover, the Fiat Panda has wide windows through which the jammer signal can easily propagate.

This phenomenon does not occur for the van. The Fiat Ducato does not have rear windows and the jammer signal can propagate only through the front windows. This effect clearly appears in Figure 8: L_c assumes higher values (in some cases amplification occurs) in correspondence with the front of the vehicle. When the jammer antenna is placed in the rear of the vehicle two situations occur. In the small car case, angles corresponding to the rear windows seem to favour signal propagation. This fact is particularly evident in right part of Figure 7 where L_c assumes positive values in the [150-240] degree azimuth range. The asymmetry in the plot is due to the location of the jammer antenna: the antenna was taped to the flatbed placed over the boot of the car. The antenna was on the right side of the flatbed and hence the maximum L_c was observed on the right part of Figure 7.

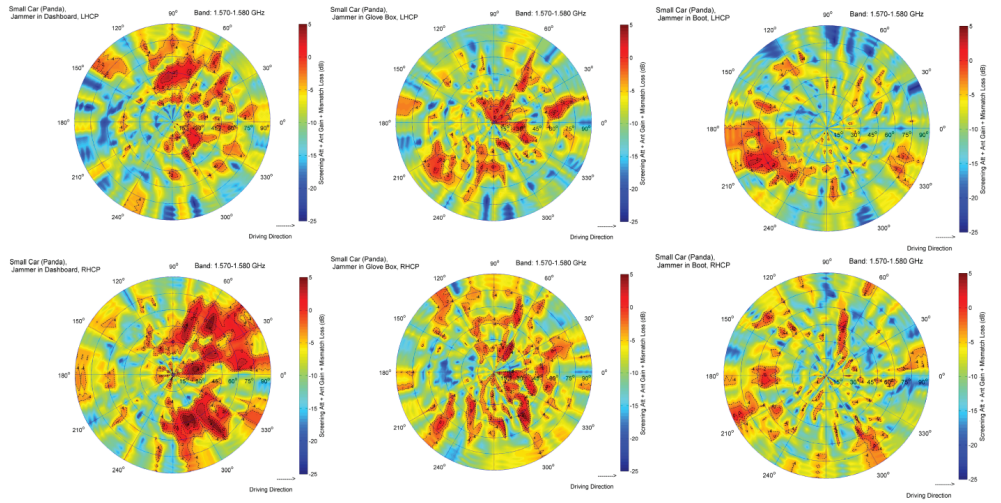

Figure 7 Composite loss accounting for vehicle attenuation, jammer antenna gain and other mismatch losses in the case of a small car (Fiat Panda). The loss was obtained by averaging network analyzer measurements in the 1.570-1.580 GHz frequency range. Different jammer locations and antenna polarizations are considered.

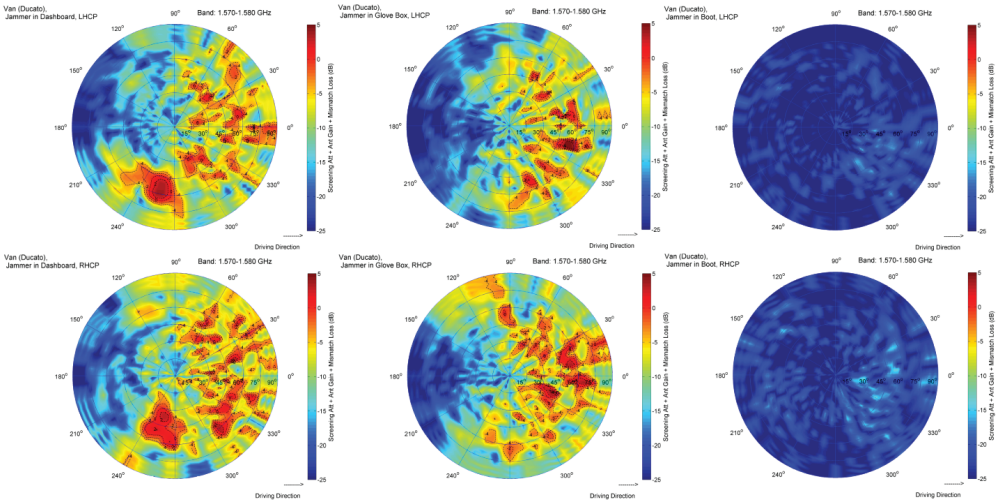

Figure 8 Composite loss accounting for vehicle attenuation, jammer antenna gain and other mismatch losses in the case of a van (Fiat Ducato). The loss was obtained by averaging network analyzer measurements in the 1.570-1.580 GHz frequency range. Different jammer locations and antenna polarizations are considered.

The results obtained for the van are substantially different from those observed during the small car experiments. There are no windows in the rear of the van which essentially behaves as a metal cage. For this reason, the jammer signal is strongly attenuated and L_c assumes values lower than -15 dB. From these results, it emerges that vehicles equipped with GNSS jammers show clear RF signatures which may be used for identifying the vehicle type.

Results: Spectrum Analyzer Tests

In this section, the results obtained using the spectrum analyzer are briefly summarized. In this case, only one case was considered. The jammer was placed in the cigarette lighter of the Fiat Panda described in the previous section. The analysis was limited to one case due to the complexity of the setup and the time required for a single scan: the whole test lasted 7.4 hours.

The total received power is shown in Figure 9a as a function of the direction of arrival (azimuth and elevation angles). The received power is shown in order to provide an indication of the signal strength as seen by a receiver placed at a distance of about 9.5 m from a vehicle equipped with a jammer (the radius of the anechoic chamber is about 9.5 m).

Note that the transmit power can be calculated for the received power using (2). In this, case the free space loss is given by

$$L_{fp} = 20\log_{10}\left(\frac{4\pi r}{\lambda}\right)\Bigg|_{r=9.5} = 56 \text{ dB}. \tag{3}$$

The maximum L_c value observed in Figure 7 is about 5 dB, whereas the maximum received power reported in Figure 9a is about -42 dBm. Using these results, the following transmitted power is obtained

$$P_{Tx}\big|_{dBm} = -42\big|_{dBm} + 56\big|_{dB} - 5\big|_{dB} = 9 \text{ dBm}. \tag{4}$$

This result is in agreement with the power measured for jammer J06 which was used for the test.

The diagrams reported in Figure 9 are in agreement with the results reported in Section 4.1. In particular, patterns similar to those observed in Figure 7 are found: the jammer power mainly propagates through the windscreen of the car whereas other propagation directions are more attenuated. Differences between Figure 9 and Figure 7 are justified by the different way the received power was measured. In the network analyzer case, CWs were transmitted at different

frequencies and the channel attenuation was determined by averaging power measurements obtained at discrete frequencies. In the spectrum analyzer case, the jammer signal continuously scans a wide frequency range and the transmitted power also varies as a function of frequency. When the jammer received power is measured, the different frequency components are weighted differently according to the properties of the transmitted signal and the channel attenuation which also varies as a function of frequency. For this reason, it is not possible to obtain a perfect agreement between the results obtained during the two types of tests. The agreement should be however considered satisfactory since both tests clearly show that specific propagation directions, which reflect the structure of the vehicle, are favoured.

In order to investigate the impact of the measurement bandwidth, the power measured in a 2 MHz one-sided bandwidth centred on the GPS L1 frequency was computed and is shown in Figure 9c and 9d for the LHCP and RHCP

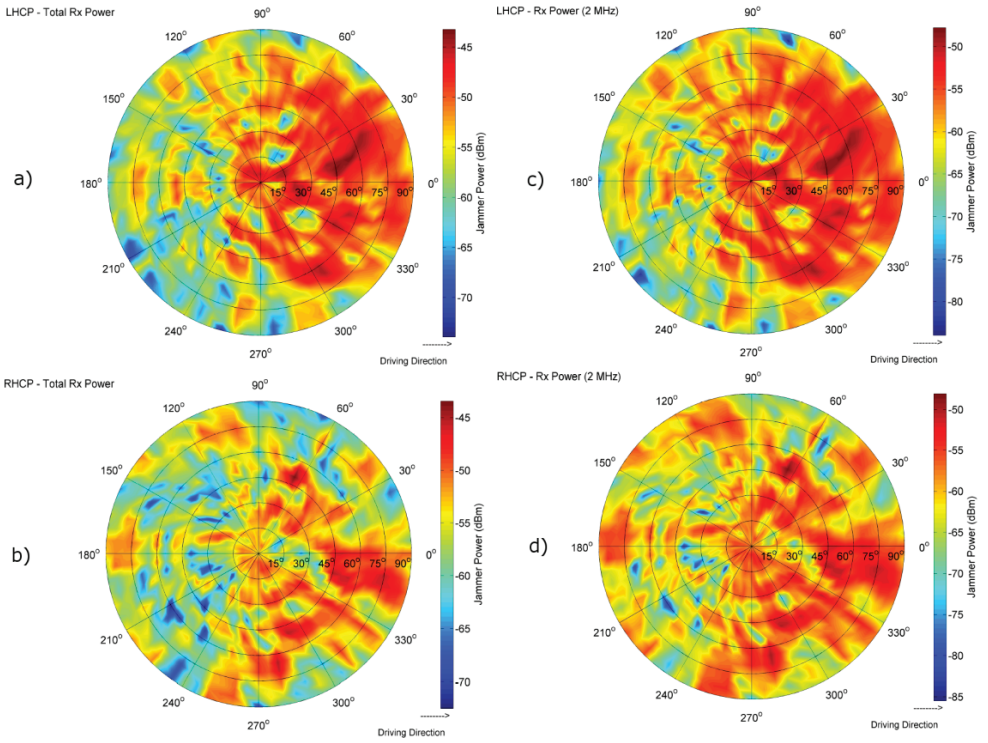

Figure 9 Received power as a function of the direction of arrival measured using a wide-band spectrum analyzer. Two different polarizations (LHCP and RHCP) were considered. Jammer J06, Fiat Panda

polarizations, respectively. The power in the 2 MHz bandwidth was computed using the same approach adopted in Section 3 and the results shown here can be compared with those reported in Table 2.

When the received signal is band-limited the power distribution changes showing the impact of the method used for the computation of received jammer power and further justifying the differences observed between network analyzer and spectrum analyzer tests.

5 CONCLUSIONS

In this paper, signals emitted by several GNSS jammers have been analyzed and spectral and spatial characterizations of jamming signals have been provided. From the signal characterization it emerges that jamming signals can sweep large frequency ranges in short time periods. In particular, it was found that the smallest frequency range covered by a jammer is about 10.5 MHz with a sweep period of about 9 μs. The transmitted power varies significantly depending on the jammer type. Combining results from the literature and experimental findings, it was shown that the transmitted power can vary from about -10 to more than 30 dBm. This variability is due to the availability of different jammer models. When battery jammers are considered the transmitted power is also impacted by the charge level. Despite the large variability, the power levels measured are extremely high compared to the strength of GNSS signals. For this reason, jammers can create serious problems for GNSS operations in large geographical areas.

A spatial characterization of the signals transmitted by jammers was also performed since it has been recognized that most of the jamming events reported in the literature originated from vehicles such as trucks and cars. Thus, the propagation of jamming signals is strongly impacted by the structure of the vehicle which hosts it. The jamming propagation channel was characterized considering the impact of different vehicles and jammer positions. Two vehicles, a small car and a van, were used for the measurements and the attenuation due to the jammer antenna gain pattern and the vehicle structure was determined for different reception angles.

From the analysis, it emerges that the structure of the vehicle favours specific propagation directions which usually correspond to windows. Metal parts of the vehicle strongly attenuate the jamming signals. Each vehicle has a specific RF frequency signature which identifies the vehicle type and may be used to improve jammer detection and location.

ACKNOWLEDGMENTS

The authors would like to express their thanks to the partners of the FP7 project DETECTOR for the support provided in this measurement campaign, in particular for the loan of the jammer used for the tests. Special thanks for the support provided during the measurement campaign are also due to Messrs. Jean-Marc Chareau, Philippe Viaud and Marco Basso, all in Unit G06 of the Institute for the Protection and Security of the Citizen, EC Joint Research Centre.

REFERENCES

1. Brown, A., Reynolds, D., Roberts, D., and Serie S. (1999) Jammer and interference location system design and initial test results. *Proceedings of the 12th International Technical Meeting of the Satellite Division of The Institute of Navigation ION/GPS*, pp. 137–142, Nashville, TN.
2. Graham A. (2011) *Communications, Radar and Electronic Warfare*. John Wiley & Sons, January.
3. Kuusniemi, H., Airos, E., Zahidul, M. and Kröger T. (2012). Effects of GNSS jammers on consumer grade satellite navigation receivers. *Proceedings of the European Navigation Conference (ENC)*, Gdansk, Poland.
4. Kraus, T., Bauernfeind R. and Eissfeller B. (2011). Survey of in-car jammers – analysis and modeling of the RF signals and IF samples (suitable for active signal cancelation). *Proceedings. of the 24th International Technical Meeting of The Satellite Division of the Institute of Navigation ION/GNSS*, pp. 430–435, Portland, OR.
5. Mitch, R. H., Dougherty, R. C., Psiaki, M. L., Powell, S. P., O'Hanlon, B. W., Bhatti, B. W. and Humphreys T. E. (2011). Signal characteristics of civil GPS jammers. *Proceedings of the 24th International Technical Meeting of The Satellite Division of the Institute of Navigation (ION/GNSS)*, pp. 1907–1919, Portland, OR.
6. Pullen, S. and Gao G. (2012). GNSS jamming in the name of privacy. *Inside GNSS*, pp. 34–43.
7. Rash, G. D. (1997). GPS jamming in a laboratory environment. *Proceedings of the 53rd Annual Meeting of The Institute of Navigation*, pp. 389–398, Albuquerque, NM.
8. The Economist (2011). GPS jamming: No jamming tomorrow. *Technology Quartely*, March.

Faculty of Maritime Studies
University of Rijeka, Croatia

Royal Institute of Navigation
Science Technology Practice

7th GNSS
Vulnerabilities and Solutions Conference

ON TESTING THE FUZZY LOGIC APPROACH IN ANTI-COLLISION AT SEA DECISION MAKING

Tanja Brcko, Franc Dimc, Jelenko Svetak

Faculty of Maritime Studies and Transport, University of Ljubljana,
Pot pomorscakov 4, 6320 Portoroz, Slovenia
E-mail: tanja.brcko@fpp.uni-lj.si

ABSTRACT. *Safe navigation is a basic task of each navigator while conducting a vessel. To achieve this goal he/she has to possess different skills such as the ability to identify moving targets, gather various information to assess navigational situations, navigate according to the rules of the road and be able to control the vessel's movement by using the helm and main engine. Although navigational technologies are improving there are still many accidents caused by human error. Some scientists have claimed that human error can be limited by involving artificial techniques in decision support systems, which are already part of the vessel's integrated bridge system, but the question remains: Is it possible to conduct a vessel with only a good computer program? In this paper we will test whether some part of the decision making process may be made using fuzzy reasoning. This is prepared using a data base which was made with an old collision avoidance method – manual radar plotting. Results were obtained using fuzzy logic and radar plotting and compared with the Receiver Operating Characteristic (ROC) analysis.*

KEY WORDS: *Collision avoidance, COLREG, Fuzzy logic, Manual radar plotting, ROC*

1 INTRODUCTION

Collision avoidance is one of the prime skills an Officer of the Watch (OOW) must obtain. It is also a basic technique achieved by knowledge of the rules of the road (COLREG – Convention on the International Regulations for Preventing Collisions at Sea), communication and manoeuvring. Unlike disasters such as grounding, fire or flooding of vessels collisions at sea are rarely caused by *acts of god* or technical error. Based on accident analysis the reasons for collisions are mostly human errors: insufficient lookout (visual or by radar); insufficient adjustment of the radar due to weather conditions, inadequate speed of the vessel according to the navigational situation; lack of bridge team and bridge resource management; superficial communication among bridge team members and/or with a pilot; excessive reliance on the navigational equipment; lack of available crew on the bridge; incorrect interpretation of navigational situations (situation awareness); disregard and ignorance of the rules of the road. (Diestel, 2005; Gale, 2007).

Bridge automation has brought a new aspect to marine navigation. And although it is primarily designed to optimize navigation, at the same time, of course, it creates new training procedures, as well as new risks. Lützhöft (2002) pointed out that automation changes the nature of human error. She has highlighted the importance of training of seafarers to work on integrated navigational bridges; in particular, she focused on the problem of the navigator relying on automation (Lützhöft 2002, Schager 2008). Schager suggested maintaining an attitude of scepticism towards technology and stressed that human error in maritime accidents is also hidden in regard to the manufacturers of navigation devices, which often do not think of system ergonomics (how a device provides information, how information is made visible to the user, what the user must do to extract important information, etc.).

In the case of collision, reliance on devices primarily reflects an exaggerated confidence in information obtained by ARPA radar (Automatic Radar Plotting Aid). ARPA radar is the main part of a vessels‘ collision avoidance system, since information such as CPA (Closest Point of Approach) and TCPA (Time to Closest Point of Approach) provides the navigator essential information for assessing navigational situations, or, rather, indicates the degree of danger of approaching vessels or objects in the vicinity of the vessels. The disadvantages of the CPA data are that they do not take into account the dimensions of the own vessel and target vessel or object, which means that the distance (from the own vessel to the CPA) specified by the data is only indicative, and therefore insufficiently accurate for a full evaluation of the situation. Another problem arose with the

introduction of AIS (Automatic Identification System). Instead of reduction of radio traffic due to static and dynamic exchange of information between vessels, the system has actually increased communication between vessels since it is now easier to identify the target vessel and easier to negotiate the avoidance manoeuvre. Consequently, this presents a number of COLREG rule abuses, as officers, rather than acts according to rules, conduct their vessels in agreement with others. Such manoeuvres are often contrary to the rules and cause confusion at sea (Harati-Mokhtari, 2007).

All these facts lead to reflection regarding whether the future provision of maritime safety lies in the autonomic conduct of vessels. Should the subjective decision-making of OOW be replaced by the computer?

Many researchers around the world are engaged in the development of an autonomic Collision Avoidance System (CAS). Models of research may be divided into three categories: mathematical models and algorithms, soft computing (the evolutionary algorithms, neural networks, fuzzy logic and expert systems), and a combination of all – a hybrid navigation system (Statheros, 2008).

Navigation decision support systems are a newer approach to the development of vessel information systems. Besides their information function, their task is to supply solutions – determination of safe vessels‘ trajectories in the process of their mutual avoidance (Pietrzykowski, 2010).

Perera, et al. (2011) proposed a decision making system based on fuzzy logic in which he highlighted situations that occur when the “stand on” vessel must make a manoeuvre to avoid collision. The stand on vessel is that with the right of way and should maintain her course and speed, while the “give way” vessel is obligated to yield to the stand on vessel. Simulation was performed in Matlab by Fuzzy logic Toolbox.

These same authors followed with an advance created by combining fuzzy logic and the Bayesian network, which works as an inference medium between collision avoidance decisions and collision avoidance actions (Perera, 2012). Smierzchalski (2005) also tried to combine two computer techniques: evolutionary algorithms for the determination of the optimal path of passages and fuzzy logic to control the vessel after a set path of passage (fuzzy logic working as a fuzzy control of course and speed). Pietrzykowski *et al.* (2005, 2010) presented a collision avoidance trajectory with solutions determined by the method of multistage control in a fuzzy environment. In their paper (Pietrzykowski, 2005) they also presented a prototype of a navigational decision support system which utilizes knowledge of experienced navigators using artificial intelligence methods and tools including fuzzy logic.

In discussing the hybrid systems for collision avoidance, it is necessary to mention Hwang et al. (2002), who combined fuzzy logic and expert systems, integrated with the H ∞ autopilot system. The latter system is presented as a robust system; stable in keeping the vessel in the desired direction in bad weather conditions. More complex hybrid systems for autonomous navigation were presented by Lee (2004), where in addition to fuzzy logic, a Virtual Force Field from the field of mobile robotics was proposed.

A support decision system which would suggest a correct time of avoidance and is based on an adaptive fuzzy-neural inference system was introduced by Zhuo et al. (2008). Likewise Liu et al. (2005) used combination of fuzzy logic and neural networks in his inference system, where he divided a network into three subsets, each having the task of processing data and providing the final information for the navigator.

Research results of vessels‘ autonomy with the use of fuzzy logic techniques obviously yield optimistic results. The autonomy of the vessels will be achieved by addressing the underlying problems, one of which is exposed in this article – How to determine the appropriate course of avoidance, using fuzzy reasoning.

2 MANUAL RADAR PLOTTING AND ARPA CALCULATOR

The collision avoidance problem was in the past solved by the method of manual radar plotting, which was in use by seafarers until the implementation of the ARPA calculator on marine radar. Manual radar plotting is a method using vector algebra for calculating parameters such as CPA and TCPA. These are the main parameters for collision probability assessment with the target vessel or fixed object. And although this method is no longer in use by navigators, it is part of the STCW model course for seafarer certification. Based on this method, the ARPA calculator was developed. Almost all marine radar nowadays are ARPA, which on the basis of vessels’ movements calculate the essential navigational parameters:

- Relative and true course of the target vessel.
- Relative and true speed of the target vessel.
- CPA.
- TCPA.
- Distance to the target vessel, etc.

With manual radar plotting the position of the target vessel (distance and bearing) was transferred (in time intervals) on the radar diagram (Manoeuvring Board).

With two positions of the target vessel in 3, 6 or 12 minutes, OOW has been able to determine the relative course of the vessels approach; based on the own and the relative course the navigator obtains the true course of the target vessel (vector velocity triangle), her speed, CPA and TCPA. If the CPA were less than the desired vessel safety domain, the OOW began to design the path of collision avoidance. In everyday navigation, three ways to avoid the target vessel are known:

- Avoidance with change of course (used in this paper).
- Avoidance with change of speed.
- Avoidance with change of speed and course.

When the OOW has determined the size of a vessel's safety domain[1], which must satisfy safety requirements (defined by the Master or Company), he/she must determine at what distance from the target vessel a change the course will begin (in accordance with the COLREG rules). This distance is called the Action Point (AP) from which the tangent line is dragged to the circle of a safe vessel's domain (e.g. 1 NM). Then the tangent line is transferred parallel to a 6th minute position of the observation of the relative vector and thus produces a new relative movement of the vessels, and a new avoidance course to the starboard (Figure 1). Svetak

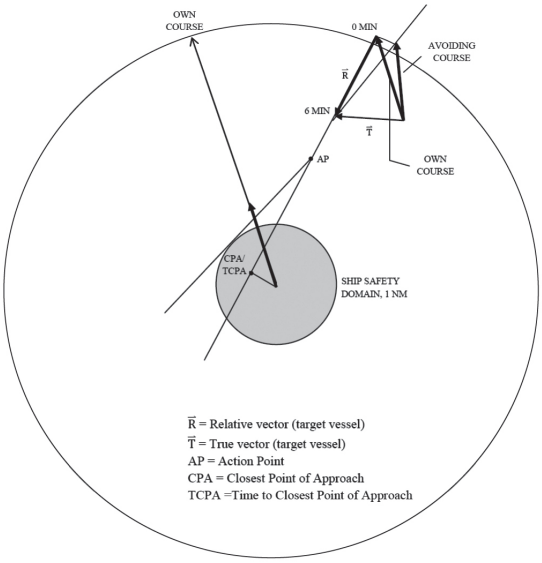

Figure 1 Manual radar plotting

[1] Vessel's safety domain" was explained by Goodwin (1975), who said that the vessel's domain is a sea area around the vessel which should be kept free from other vessels and fixed structures.

(2005) estimated that in the open sea, with good visibility, the CPA_{limit} shall not be less than 1 NM during the day and not less than 2 NM during the night or in heavy seas. In restricted visibility the CPA must be greater than 2 NM. In this article a vessel's safety domain (CPA_{limit}) is subjectively determined by the author and it is at least one nautical mile:

$$CPA_{limit} \geq 1 \text{ NM}. \quad (1)$$

Collision avoidance in crossing situations

The authors focused on a dangerous crossing situation between two power-driven vessels. COLREG rule 15 says: "When two power-driven vessels are crossing so as to involve risk of collision the vessel which has the other on her own starboard side shall keep out of the way and shall, if the circumstances of the case admit, avoid crossing ahead of the other vessel" (COLREG, 1972). This requirement only applies in the event where there is a risk of collision and not if the distances between vessels are great or in cases where the bearing between vessels changes clearly. Also this rule does not apply in narrow channels and excludes the right-hand rule when one of the vessels is a fishing boat or any other vessel restricted in her ability to manoeuvre (and is properly marked according to the rules). Change of course to the starboard of the "give way" vessel is also the best and recommended way of avoidance (Cockcroft, 2001). A new, avoiding, course obtained by manual radar plotting represents the smallest possible change of the course, which satisfies two criteria: the vessel's safety domain and the smallest deviation from the planned track.

3 FROM VECTOR ALGEBRA TO FUZZY LOGIC

Today ARPA radar is part of a vessel's collision avoidance system which automatically calculates the necessary parameters that the OOW must assess in a navigational situation. ARPA radar also provides a function called "Trial Manoeuvre", which simulates a postponed navigational situation within a time interval. With the input data (change of speed and course within the time delay) the OOW receives a picture of the target vessel's trajectory. The problem is that the OOW must preliminarily establish the course (or/and speed) change of the own vessel and estimate the adequate time of the change, which would fulfil two safety criteria mentioned before.

One way to limit the subjective OOW decision making is to introduce decision models that use techniques of artificial intelligence (AI), which include fuzzy

logic, which greatly reduces the computation time and the decision-making process due to its simplicity.

Fuzzy logic was first introduced by Lotfi A. Zadeh, who wrote that human decisions are based on imprecise information (Teodorović, 1998). The advantage of fuzzy logic is in its processing of inaccurate data to create precise solutions, which is especially valuable in the case of complex systems, where it is difficult to apply a different, more complex mathematical model (Virant, 2003).

As an example, let's watch the OOW, who visually observes the surrounding area of the vessel. He/she uses linguistic terms to describe the distance to other vessels, such as: the vessel is far away, the vessel is at medium-distance or the vessel is at a short distance. At the same time the OOW assesses the risk of collision (no risk, medium risk, high risk). In short, the navigator describes situations inaccurately (instead of 9.1 nautical miles (NM) the vessel is far away and the risk of collision is minor or does not exist), and so develop the so-called fuzzy sets, which do not have clear boundaries. We say the statement belongs to a set of statements with a certain grade of membership. Statements about the distance of the vessel can be illustrated graphically, with a fuzzy membership function (Figure 2), where N means that the observed vessel is near, M means middle distance and F means far away.

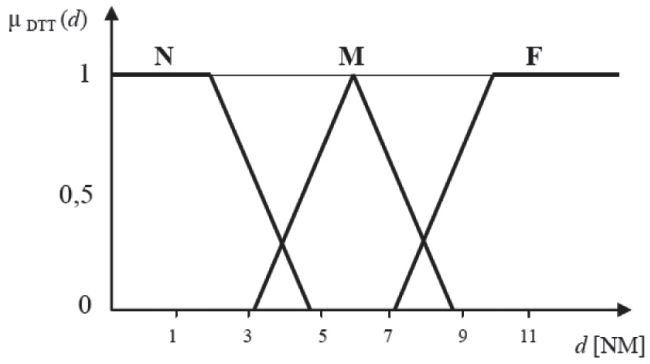

Figure 2 Example of fuzzy membership function

The horizontal axis of a two-dimensional Cartesian coordinate system presents the distance in nautical miles; the vertical axis shows the grade of membership of elements in a fuzzy set. The theory of classical logic assumes only the correct and incorrect statements, so that the statement belongs to a set (true or 1), or does not belongs to a set (false or 0). In the case of fuzzy logic, however, the element belongs to a set with a certain grade of membership depending on the

truth of the statement. For example, if the distance to a target vessel is d = 4.5 NM, it means that it belongs to both sets N and M, but with varying grades of membership:$\mu_N(d)$ = 0.1 and $\mu_M(d)$ = 0.5 (Figure 2). This means that due to the grade of membership in fuzzy set M the vessel is at the middle distance rather than near. The shape of a fuzzy set can also be defined mathematically. As an example, let us look at the definition of fuzzy set M:

$$\mu_{DTT} = \begin{cases} 0 & d \le 3 \\ \left(\frac{d-3}{3}\right) & 3 < d \le 6 \\ \left(\frac{9-d}{3}\right) & 6 < d \le 9 \\ 0 & d > 9 \end{cases} \tag{2}$$

The form of the set is determined by an expert, thus we have known sets in the form of a triangle (the most commonly used form of the sets in the literature), a trapezoid, a Gaussian curve, etc. The procedure by which a certain number or parameter (input) is appointed to an appropriate set and grade of membership is determined (a subjective determination by an expert) is called fuzzification. The fuzzy inference system (FIS), also known as the fuzzy rule-based system, is the process of formulating the mapping from a given input to an output, using fuzzy logic (Figure 3).

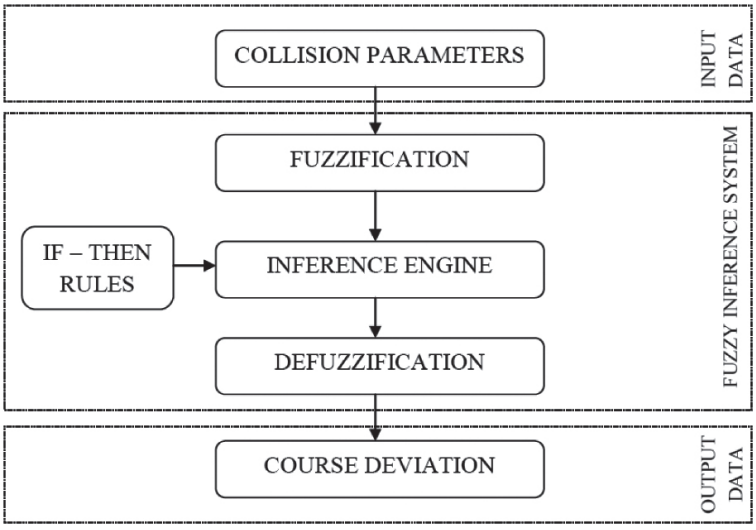

Figure 3 Fuzzy Inference System

This is one of the main elements of the fuzzy logic system. The fuzzy rules are drawn by an expert, taking into account all relevant COLREG rules. The FIS type in this paper is "Mamdani", which is the most commonly used fuzzy methodology. The use of the IF-THEN rules is organized with the "and (min)" and "or (max)" operators. Defuzzification is the last step in FIS and is a conversion of fuzzy output quantities into a crisp output quantity (Fig. 4).

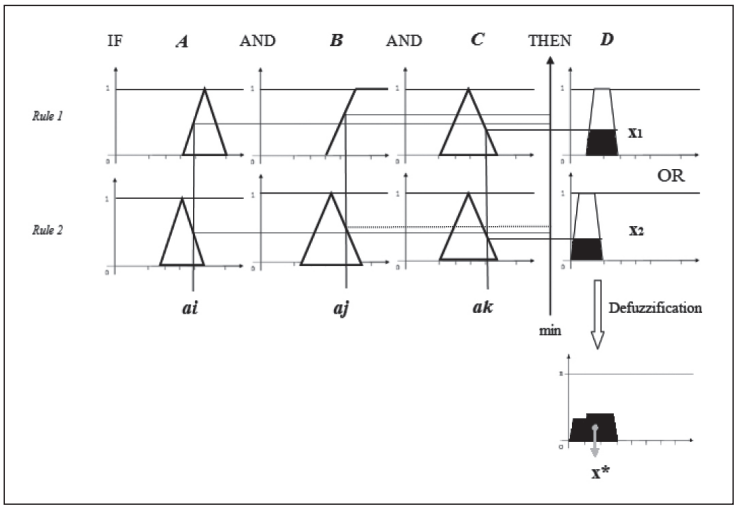

Figure 4 Graphical interpretation of fuzzy inference under minimum rule

In this paper, we explored the method of obtaining the appropriate changes of course of a give-way vessel and we used the principles of fuzzy logic. In order to present the objective knowledge of an expert, we used methods of manual radar plotting to create a database of relevant, minimal changes of course of avoidance in crossing situations (section 2.1). In doing so, we focused on three important parameters that affect the magnitude of the course change: relative bearing (RB) to the target vessel, the distance to the target vessel (DTTV) and CPA with target vessels. TCPA has been neglected because it is assumed that a system decides "in real time".

RB is an angle between the course line of the own vessel, and the bearing line to the target vessel. According to COLREG rules 13, 14, 15, 16, and 17 (in part) the give-way vessel in the crossing situation of two power-driven vessels is a vessel which has another vessel in its own green side light sector. In other words, the angle from her course line to the relative bearing line is 112.5° (Figure 5). If the vessel is observed outside this sector, right of way (Rule 13 and 15) is changed.

As mentioned before, the vessel which has the other vessel on its starboard has to change her heading (course) or speed to avoid the opposite vessel. Composing the expert database (solutions), we divided the "green side light" sector into 12 parts: 0º, 10º, 20º, 30º, 40º, 50º, 60º, 70º, 80º, 90º, 100º and 110º; and distance into 4 sectors: 2 NM, 4 NM, 6 NM and 8 NM (Figure 5).

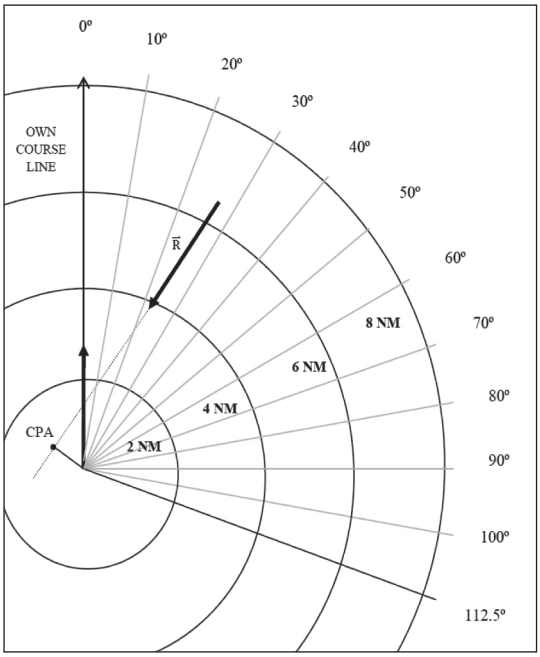

Figure 5 Relative bearing and distance to target

The third parameter, which in our opinion has a strong influence on the change of course, is the CPA. There are three options. If the bearing to the target vessel doesn't changes, the CPA is in the area between 0 – 0.5 NM, which clearly means there is a risk of collision. However, because we have to take into account the different size of the vessels, and the direction of approach (to the bow/stern), we have determined that there is a risk of collision even in cases when the ARPA radar shows the CPA from 0.5 to 0.9 NM. The meeting point on the port or starboard side also has an impact on the change of course, so we have to take into account: + 0.5 NM means that CPA is on the starboard side or stern of our vessel; – 0.5 NM, however, that the CPA is on a port side (bow) of our vessel (Figure 6).

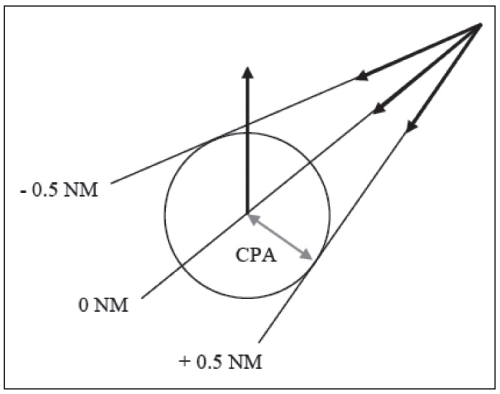

Figure 6 CPA parameter

Ultimately, the minimum safety domain of the vessel was determined, which is a symbolic circle of 1 NM (Figure 1).

With respect to all three parameters and the minimum vessel's domain a data base of 144 solutions has been composed, whereby the intermediate values of the parameters (for example, for RB = 34º, DTTV = 6.3 NM and CPA = 0.4 NM) could be obtained simply by interpolation of the computed results. Finally, after completion of the data base, the process of determination of fuzzy sets for each parameter and the composition of 84 IF – THEN rules has begun.

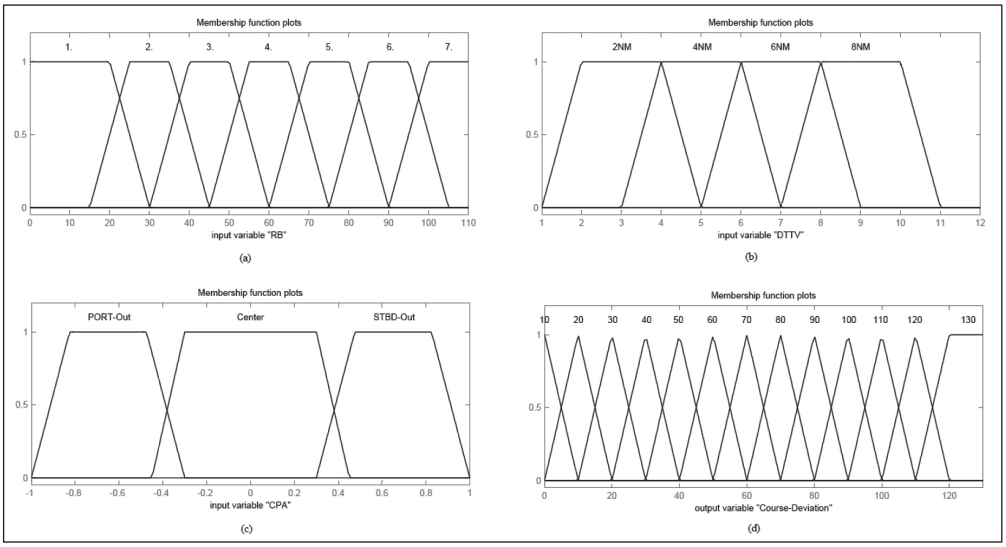

Figure 7 Fuzzy membership functions; Input: (a) RB, (b) DTTV, (c) CPA and Output: (d) course deviation.

Simulations were performed with the Matlab Fuzzy Logic Toolbox Graphical User Interface. Input data are RB (Fig. 7a), DTTV (Fig. 7b) and CPA (Fig. 7c). Output data (decision) is course deviation (Fig. 7d). The relative speed of convergence in the composition of rules and the sets was 20 NM/ h. The speed of the give way vessel was also 20 NM/ h.

4 THE EVALUATION OF THE FUZZY METHOD BY ROC

The evaluation by the receiver operating characteristics (ROC) is made for the fuzzy method and with the use of the manual graphical method. The time of getting the course is not evaluated due to the obvious advantage of the fuzzy approach. The evaluation is based on risk assumption of the commanded course deviation as being performed by two types of evaluators, not knowing the ground truth (GT) results. The method under test is examined at different RB (between 0 and 110 degrees.) and at different CPA (either -0.5 NM or 0 NM or + 0.5 NM); no extra attention was paid to DTTV (between 2 and 8 NM) since at the preliminary stage DTTV was treated as not influencing the evaluation. Since the GT is not known the reliable approximation is obtained by polynomially fitting the results of the manual graphical method at all relevant RBs and CPAs. According to the ROC scheme, the course change acquisition attempts need to be classified into true classes based on the GT data and the division into hypothetical classes which is based on the results from both methods.

A working hypothesis for the risk evaluation of the graphical method is that at all attempts the results are assumed as ‘hypothetically safe’ and thus all results are dedicated to the hyp.class = 1. Two hypothetical persons evaluate the fuzzy method. A hypothesis for the fuzzy method at the moment is two-fold for either the first evaluator is a ‘greenhorn’ (all attempts are ‘hyp.safe’; i.e., all results are dedicated to the hyp.class = 1), and the second evaluator is a ‘sceptical technician’, who has enough computer time to compare the result with the results of the neighbouring RB (all attempts which yield a negative derivation are assumed as ‘hyp.dangerous’ and dedicated to the hyp.class = 0). In the future an evaluation of the third person – the ‘navigational expert’ is planned to evaluate the results of the fuzzy method on the nautical simulator or even at a real deck.

Classification of the results into true classes (‘truly safe’ equals ‘true positive’, ‘truly dangerous’ equals ‘true negative’) is made according to the observed error between the result derived from using a certain method and the ground truth value for the present RB and CPA. For vessel safety reasons the ‘true positive’ i.e. safe attempt results are allowed to be down-to 5 degrees lower than GT.

Thus: *test results* > *GT* – 5 *degs.* which leads to an *error* = *testResult* – *GT* > – 5 *degs*. So all attempts' results are dedicated into a *true.class* = 1 if an *error* < – 5 *degs.* or *true.class* = 0 at other error values (for example CPA = -0.5 NM, see Fig. 8).

It is obvious from the comparison of results, that at DTTV = 4 NM the fuzzy method was not tuned well but the un-tuning status gracefully degraded the fuzzy method results towards the non-dangerous commanded course deviation zone.

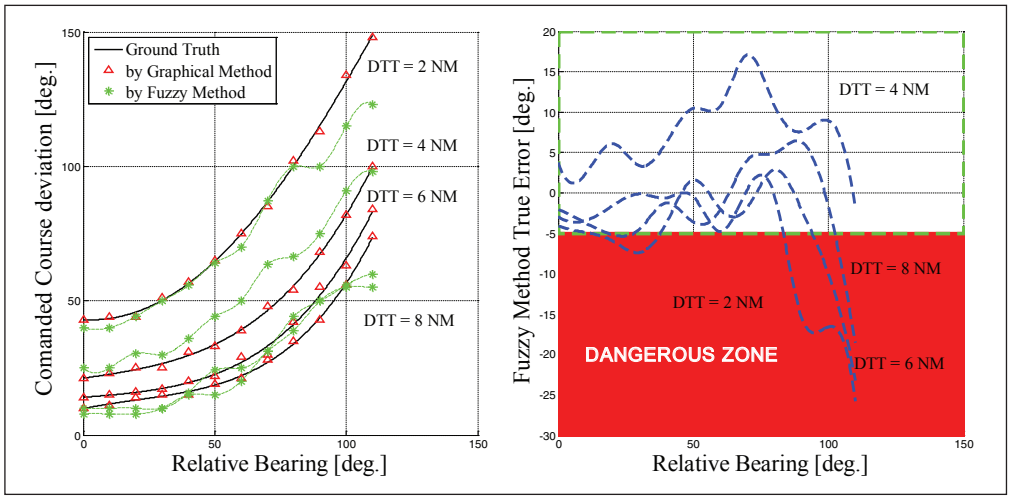

Figure 8 Results with CPA = -0.5 NM
a) Course deviation as get by both methods, b) True error after fuzzy method.

It was expected that the manual method's performance would be close to perfection. Within the confusion matrix no negatives were expected, neither true nor false (TN = 0, FN = 0). On the other hand fuzzy method performance is tuning dependent and thus expectations were much lower. The area under curve (AUC) presents the class of the risk prediction potential of each of the fuzzy method evaluator: the bigger AUC the better is the prediction whether the result is safe or dangerous. For the greenhorn no attempts are dangerous and thus he does not proclaim truly safe attempts as dangerous whereas technician does.

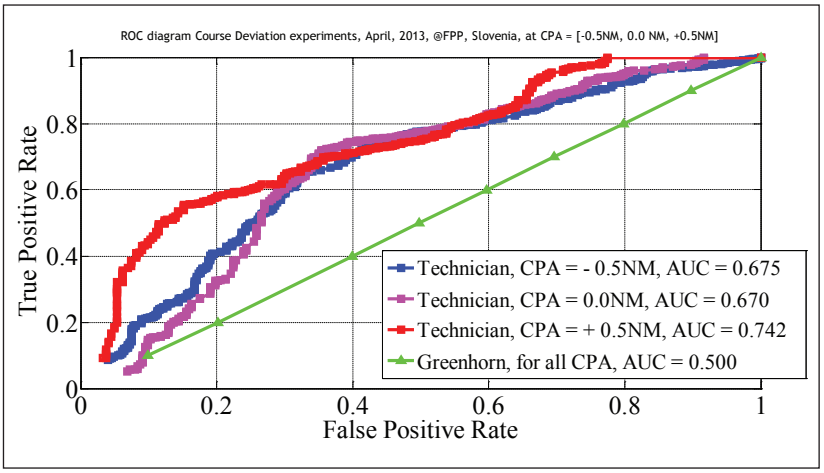

Figure 9 The classifications of the risk prediction at all three CPAs.

The experimental classification accuracies were achieved by 10-fold cross validation whereas for the ROC curves design the random forest machine learning algorithm in Weka was applied. The comparison of the experimental classification accuracies get by technician at all CPAs expresses a slight dependence on CPA. ROC curves together with the AUCs get by greenhorn represent purely random prediction i.e. the greenhorn is not capable to distinguish between safe and dangerous results get by the fuzzy method. Additional knowledge however purely mathematical improves the classification capability over the fuzzy method results. It seems interesting to subject the experienced persons upon such type of the evaluation tests.

As shown by the threshold curves – true positives vs. false positives for each CPA (see Fig. 9) – the performance of the fuzzy method greatly depends on the evaluator. If the evaluator is not exacting, so to speak, with the results, the use of fuzzy method is dangerous, especially if the parameters are tuned badly and they critically degrade the commanded course deviations.

5 CONCLUSIONS

Looking at the results obtained by the ROC, fuzzy logic could be simply just one of the techniques used in an extensive decision making process for collision avoidance. In tuning the fuzzy sets and fuzzy rules, some improvements could be made, but unfortunately self-standing fuzzy logic for collision avoidance is for now still a risky venture and should be combined with other decision

methods. On the other hand it is a method that is easy to work with and has a very short data processing time. A quick response to the input data is also one of the goals of modern technology. Compiling a data base using the results of the graphical radar plotting method provides reliable data for modelling fuzzy sets and fuzzy rules but COLREG rules must be included, and should be the basis for solving every collision avoidance problem. Any solutions that do not take into consideration those rules should be ignored.

Basic parameters used for fuzzy reasoning are enough for a simple inference system. But for further research other parameters should be considered, since movement of vessels also depends on traffic area (narrow channel, traffic separation scheme), state of traffic (multi-encounter situations), state of weather and sea, etc. Automation of vessels is likely in the near future, but we are not yet near the point of knowing which method will be both punctual and accurate enough to replace human decision making. At the moment it is still meaningful how rigorously the expert accepts the commanded course deviations. Testing the expert's level of acceptance based on the relatively trivial evaluation test remains a future work. Similarly to the lengthy process of EGNOS implementation in aircraft navigation as a service on which human lives and goods depend on its accuracy, a certain reluctance exists regarding the penetration of novel methods into widely used nautical systems such as navigation radar and AIS in collision avoidance.

REFERENCES

1. Cockcroft, A. N., Lameijer, J. N.F. (2001). *A guide to collision avoidance rules, 6th edition*, Oxford: Butterworth-Heinemann Ltd.
2. Diestel, H. H. (2005). *Compendium on Seamanship and Sea Accidents – A practical guide to improve Seamanship and to prevent Sea Accidents*. Hamburg: Seehafen Verlag GmbH.
3. Fawcett, T. (2006). An introduction to ROC analysis, *Pattern Recognition Letters*, vol. 27, pp. 861–874.
4. Gale, H., Patraiko, D. (2007). Improving navigational safety. The role of e – navigation. *Seaways*, July 2007.
5. Goodwin, E.M. (1975). A statistical study of vessel domains. *The Journal of Navigation*, 28, pp. 329–341.
6. Harati-Mokhtari, A., Wall, A., Brooks, P., Wang, J. (2007). Automatic Identification System (AIS): Data Reliability and Human Error Implications. *The Journal of Navigation*, 60, pp. 373–389.
7. Hwang, C. N. (2002). The intergrated design of fuzzy collision – avoidance and H_∞ – autopilots on vessels. *The Journal of Navigation*, Vol. 55, pp. 117–136.

8. IMO (1972) *Convention on the international regulations for preventing collisions at sea* (COLREGs).
9. Kobayashi, H. (2005). Use of Simulators in Assessment, Learning and Teaching of Mariners. *WMU Journal of Maritime Affairs*, Vol. 4, No. 1, pp. 57–75.
10. Lee, S., Kwon, K., Joh, J. (2004). A Fuzzy Logic for Autonomous Navigation of Marine Vehicles Satisfying COLREGS Guidelines. *International Journal of Control, Automation and Systems,* Vol. 2, No. 2, pp. 171–181.
11. Liu, Y., Shi, C. (2005). A Fuzzy-Neural Inference Network for Ship Collision Avoidance. *Proceedings of the Fourth International Conference on Machine Learning and Cybernetics*, pp. 4754–4759.
12. Lützhöft, M. H., Dekker, S. W. A. (2002). On Your Watch: Automation on the Bridge. *The Journal of Navigation*. 55, pp. 83–96.
13. Perera, L. P., Carvalho, J. P., Guedes Soares, C. (2011). Fuzzy logic based decision making system for collision avoidance of ocean navigation under critical collision conditions. *Journal of Marine Science and Technology,* Vol. 16, pp. 84–99.
14. Perera, L. P., Carvalho, J. P., Guedes Soares, C. (2012). Intelligent Ocean Navigation and Fuzzy – Bayesian Decision/ Action Formulation. *Journal of Oceanic Engineering*, Vol. 37, No. 2, pp. 204–218.
15. Pietrzykowski, Z. (2005). Multi-stage vessel control in a fuzzy environment. *Methods of artificial intelligence and intelligent agents. Enhanced methods in computer security, biometric and artificial intelligence systems.* Chapter 3, pp. 285–299.
16. Pietrzykowski, Z., Magaj, J., Wolejsza, P. and Chomski, J. (2010). Fuzzy logic in the navigational decision support process onboard a sea – going vessel. *ICAISC 2010*, Part I, pp. 185–193.
17. Schager, B. (2008). When Technology Leads Us Astray: A Broadened View of Human Error. *The Journal of Navigation*, 61, pp. 63–70.
18. Smierzchalski, R. (2005). Evolutionary-Fuzzy System of Safe Ship Steering in a Collision Situation at Sea. *CIMCA-IAWTIC '05*, Vol. 1, pp. 893–898.
19. Statheros, T., Howells, G., McDonald-Maier, K. (2008). Autonomous Vessel Collision Avoidance Navigation Concepts, Technologies and Techniques. *The Journal of Navigation*, 61, pp. 129–142.
20. Svetak, J., Jakomin, L. (2005): Model of Optimal Collision Aviodance Manouevre on the Basis of Electronic Data Collection, *Promet-Traffic-Traffico*, Vol. 17, No. 6, pp. 295–302.
21. Teodorovic, D., Vukadinovic, K. (1998). *Traffic Control and Transport Planning: A Fuzzy Sets and Neural Networks Approach.* Kluwer Academic Publishers, Boston-Dordrecht-London.
22. Virant, J. (2003). *Svet mehkega racunanja, sklepanja in delovanja*. Didakta, Radovljica (in Slovene).
23. Zhuo, Y., Tang, T. (2008). An Intelligent Decision Support System to Ship Anti-Collision in Multi-Ship Encounter. *Proceedings of the 7th World Congress on Intelligent Control and Automation,* pp. 1066–1071.

Faculty of Maritime Studies
University of Rijeka, Croatia

Royal Institute of Navigation
Science Technology Practice

7th GNSS
Vulnerabilities and Solutions Conference

AN ASSESSMENT OF GEOMAGNETIC ACTIVITY--RELATED TECHNOLOGY FAILURE RISK BASED ON PATTERNS OF KP INDEX DYNAMICS IN 2012

David Brčić, Serdjo Kos, Renato Filjar

Navigational GNSS Space Weather Laboratory, Faculty of Maritime Studies, University of Rijeka, Rijeka, Croatia
E-mail: brcic@pfri.hr

ABSTRACT. *Geomagnetic activity proved to be relevant indicator of the impact of space weather effects. The origin and development of solar events include various forms of manifestation in terms of energy and matter transfer to the near-Earth environment. These complex events may manifest as disturbances in the Earth's magnetic field, further encompassing other types of disturbances, posing risks on various Earth's technological and other systems.*

In the proposed paper, geomagnetic activity for the year 2012 has been elaborated, employing Kp geomagnetic index. Using the Kp dynamics pattern and considering possible geomagnetic impacts, assessment of potential risks on technology has been made. Satellite navigation system's performance has been analyzed during events of increased geomagnetic activity through the year. The study showed that geomagnetic activity affected GNSS positioning performance in a measurable amount, preparing in this way the ground for further research.

KEY WORDS: *Risk assessment, GNSS, Space weather, Geomagnetic activity*

1 INTRODUCTION

Space weather effects are today recognized as considerably influential on numerous technical, technological, and socio-economic systems, but also on everyday life. Energy and matter impact originating from the Sun can have adverse effect on terrestrial infrastructure, space systems, transportation and other technologies. Not only the basic technologies are affected, but also all other applications relying on them, e.g. services and applications relying on satellite navigation technologies. The more systems are sophisticated; more they are susceptible to outer influences.

Space weather effects are described in Chapter 2, with the possible affectation on all related systems. Here, authors focused on two subjects: on (i) specific solar impact influencing the Earth's magnetic field and the magnetosphere, and on (ii) GNSS performance in periods of these disturbances. In Chapter 3 origins, development and manifestation of magnetic disturbances were explained and presented. Here, the Kp index was introduced as relevant parameter describing the state and the level of geomagnetic activity. Kp index dynamics through the year 2012 have been elaborated and presented in Chapter 4, giving an overview of geomagnetic activity through the year. In Chapter 5, the most significant geomagnetic activity events have been singled out, aiming on their potential technological impact. Here, the performance of satellite navigation systems in time of geomagnetic events has been studied and the results have been presented.

In last chapters, the assessment of technology failure risk related to geomagnetic disturbances has been discussed, always considering elaborated parameter and studied period, but also documented events which took place since the observation era. The paper concludes with the short overview of geomagnetic activity in 2012.

2 SPACE WEATHER-BASED TECHNOLOGY FAILURE RISKS

2.1 Manifestation of space weather effects

Defining the term in the appropriate context, *space weather* represents occurrence of conditions in the space that affect Earth in general and performance of Earth's technological systems. These conditions have their origin on the Sun, in the solar wind, magnetosphere and ionosphere [9, 12]. Major phenomena producing space weather effects include the solar wind (magnetic flux and charged particles), solar flares (strong eruptions from the Sun's surface) and coronal mass ejections – CMEs (emissions of hot plasma, magnetic field and energetic particles) [13]. Radiation and particles ejected from the Sun, their

nature, intensity and disposition affect the Earth in several forms, and each of them is manifested in their own way. Although complex and often incorporated, these effects can basically be divided in three categories. First, s*olar radiation storms* occur when levels of radiation elevate due to the increased number of energetic particles. Second, the effect caused by the *emission of solar x-ray flux* will result in disturbances of the ionospheric layers. These disturbances manifest on Earth shortly after energy emissions from the Sun. The third manifestation are disturbances of the Earth's magnetosphere, resulting from plasma emission from the Sun. Closely associated with solar flares, CMEs and other solar eruptive events, these emissions can have embedded strong magnetic fields and energetic particles within and, reaching the Earth and its magnetosphere/geomagnetic field, they can disrupt it and cause *geomagnetic storms* [15,21].

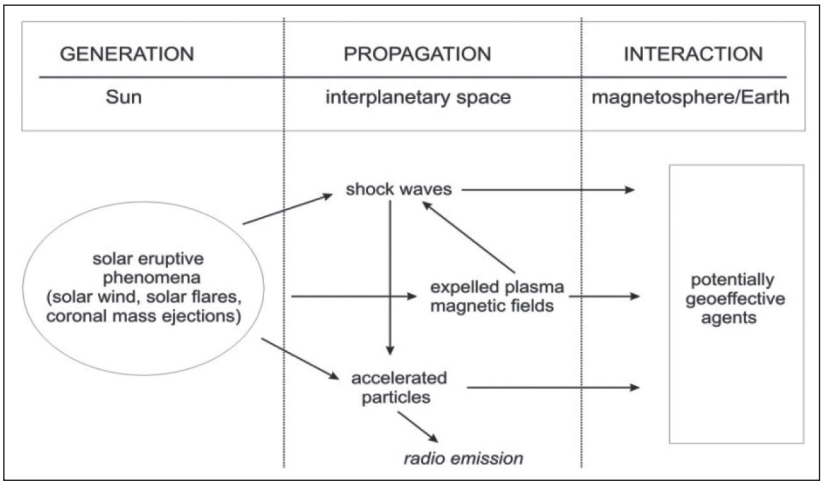

Figure 1 Generation, propagation and interaction scheme of space weather-magnetic component drivers.

Source: Made by the authors according to [26].

Phenomena generated on the Sun propagate through the interplanetary space and interact with the Earth's magnetosphere, causing disturbances in the magnetosphere, ionosphere and the surface of the Earth[1] (Figure 1) [26].

[1] On Figure 1, disturbances such as solar radiation and solar x-ray flux are not shown and, besides description of space weather effects in general, phenomena other than geomagnetic-related will not be elaborated.

Depending on the nature of the specific solar event, categories of effects may manifest individually, however they can be all comprised at once, always in relation to the occurrence which followed.

2.2 Risks of technology failures arising from the effects of space weather

The severity of space weather effects will take place in greater or lesser extent, depending on the type, duration and intensity of the event. These effects will reflect on variety of Earth and near-Earth systems and infrastructure, but also on the space between them. The areas of impact can be divided in terrestrial infrastructure and ground-based systems, avionics, space-borne systems and satellite constellations (including astronauts), and communication, navigation and surveillance systems which are using radio signals.

Rapid variations in the strength and direction of the geomagnetic field (Earth's magnetic field – EMF) can induce an electric field in the surface of the Earth, which further induces electrical currents (Geomagnetically Induced Currents – GIC) at or near the surface of the Earth [25]. The impact of GIC reflects on electrical power grids and other grounded long electrical conductors. Since GICs are destabilizing parts of electric grids, they can cause power transmission network instabilities and burnout of power grid components (e.g. transformers). The impact of GICs can also be manifested in enhanced corrosion of pipelines, interruption or damage of railroad signals and other electric systems, including power cables [23, 13, 25].

Significant satellite losses and outages involving all orbits (geostationary, medium and low) have been attributed to space weather effects, specifically fast solar wind stream and CME-driven storms [23]. Solar energetic particles (protons, ions and electrons) can cause deteriorating effects on satellites and operations performed by spacecrafts. The major causes of anomalies on satellites are electrostatic discharges caused by electron accumulation. They can result in data upsets, false commands and component damage of electronics onboard satellites and satellite vehicles.

Electrons may also cause potential satellite outages and burnouts due to ionizing damage to satellite's microelectronic devices, ranging from correctable to permanent errors. The ionization effect is present in fluxes of solar energetic particles (direct ionization) and in nuclear interactions [23]. Gamma-rays and fast particles can cause damage of satellite electronics, but they are also serious threat to astronauts exposed to these emissions. Atmospheric drag is prevalent in LEO (Low Earth Orbit) satellites where, in case of extreme disruptions, expansion of Earth's atmosphere disturbs LEO satellite's orbits and degrades predictions of satellite positions [23].

The ionizing radiation of particles generated by high energy cosmic rays and solar particles reaches the Earth's ground in their most penetrating component only. However, the ionizing radiation is approximately 300 times higher at aircraft altitudes than at sea level, and risk of radiation on aircraft passengers and crew appears. Moreover, during severe space weather events, polar-operating air traffic is redirected to lower latitudes to avoid disturbed and active auroral regions.

Impact on radio communication systems manifests in number of ways. Radiation of particles and electromagnetic waves, but also CMEs spreads out in wide frequency spectrum, thus affecting various parts of frequency bands. Regarding the nature of the specific solar event and its manifestation, the effects of space weather may be prompt or delayed, always causing communication disruptions and anomalies [23]. Affected parts of the frequency spectrum are ranging from extremely low (ELF) to extremely high (ELF) frequencies, thus affecting variety of radio systems. For instance, systems operating on High Frequency (HF) band can experience signal absorption, fadeout and radio interference in general. Very High Frequency signals can experience overrange or fadeout of propagating signals and other anomalies which take place when, usually ionosphere-penetrating, propagation signal reflects back to Earth [23, 21, 6, 9, 5].

The part of the frequency spectrum at which GNSS systems are operating (Ultra High Frequency band – UHF) is affected in a specific way. Generally, GNSS positioning, navigation and timing systems can be affected through several effects/manifestations [8] such as:

- GNSS positioning degradation
- temporal satellite outages and complete (component) failure, including loss of lock
- GNSS timing accuracy degradation.

Solar radio bursts (SRBs – defined by NOAA SWPC as Radio Blackouts) are events caused by solar flares and other eruptive prominences. Among other parts of the frequency spectrum (especially HF), they are detected at GNSS frequencies, causing radio noise interferences. Depending on the duration and severity of specific solar event, SRBs can affect GNSS performance in a way that they are degrading the receiver's operation, with the possible complete loss of lock [23, 13, 4].

Unlike the SRB – energy transfer, particles, plasma and interplanetary magnetic field reaches the Earth hours or days after eruptions, usually in form of CMEs. These impacts can indirectly cause perturbations to the ionospheric electron

density over large areas and cause gradients in the ionosphere [23]. Small scale generated structures are causing irregularities – scintillation of satellite signals, that are rapid fluctuations of radio-signal's amplitude and phase [11], resulting in signal's intensity decrease, reduced accuracy, loss of lock and GNSS positioning degradation in general.

3 KP INDEX AS AN INDICATOR OF GEOMAGNETIC ACTIVITY

3.1 Disturbances of the geomagnetic field

In previous chapter space weather effects have been generally described. Since the paper elaborates the effects of geomagnetic activity, there appears the need to explain further origins and formation of geomagnetic disturbances emerging from the Sun and Sun-Earth environment.

Interplanetary magnetic field (IMF) is a constant flow embedded, among other particles, in the solar wind, flowing from the Sun's visible surface (photosphere) and its outer atmosphere (corona). Substances of the solar wind are flowing outward along open magnetic field lines [13]. In case of sudden or extreme solar events, the solar wind accelerates. The solar events can be explained as disturbances in its magnetic field, which are associated with sunspots. The latter are caused by complex magnetic activity processes, where magnetic field at

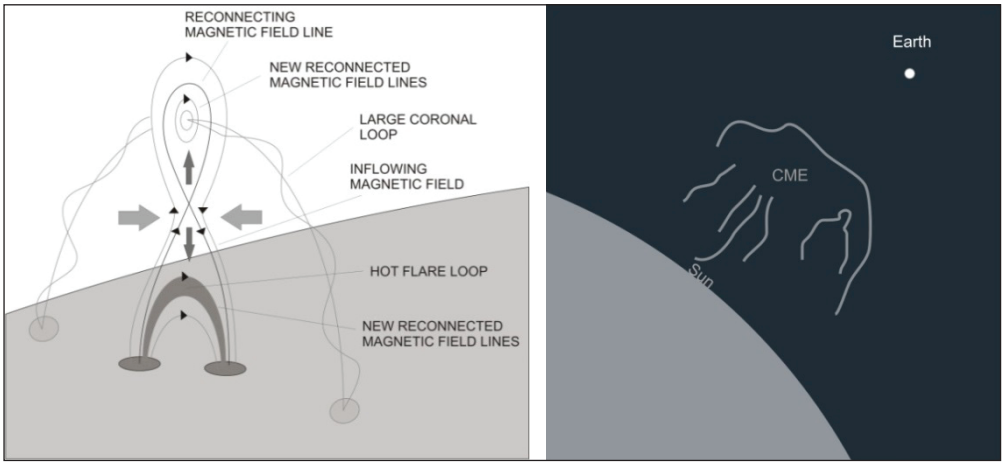

Figure 2 Left – Coronal Mass Ejection (CME) formation caused by magnetic reconnection. Right – Earth-directed CME. Size of the Sun, Earth and the CME are in relative scale.

Source: Made by the authors according to [22] (left) and [2] (right).

certain areas on the Sun's surface has opposite polarity than in the surrounding. In certain cases, oppositely directed magnetic field lines (roughly vertical relative to the solar surface) reconnect and form new field lines that snap both upward and downward, away from the reconnection region – magnetic loops break, ejecting the IMF into space. Outward expansion of magnetic loops is illustrated on Figure 1. This newly created, upward moving field lines are forming a large coronal loops that can develop in CMEs [22] – clouds of ejected magnetic plasma and energetic particles, which can reach tens of Earth's radii in size (Figure 1).

In brief and simplified, solar eruptive events are creating magnetic disturbances – interplanetary magnetic field (IMF) which travels through the interplanetary space and, if directed towards Earth, it may eventually interact with and influencing the Earth's magnetosphere-ionosphere. Under certain conditions, these disturbances can develop in geomagnetic storms [23, 21]; the orientation of the Earth-directed IMF has an important role on the impact on the magnetosphere. The Earth's magnetic field (geomagnetic field) normally protects the Earth from cosmic rays, solar radiation and particles, and from the solar wind in general. It points north at the magnetopause (the boundary region between the magnetosphere and the surrounding solar wind). If the upcoming IMF has the same direction – if the field vector (V) is parallel to Earth's field vector – the magnetosphere reflects the solar wind's bow wave, with electromagnetic disturbances compressing the magnetosphere [23, 15, 13, 25].

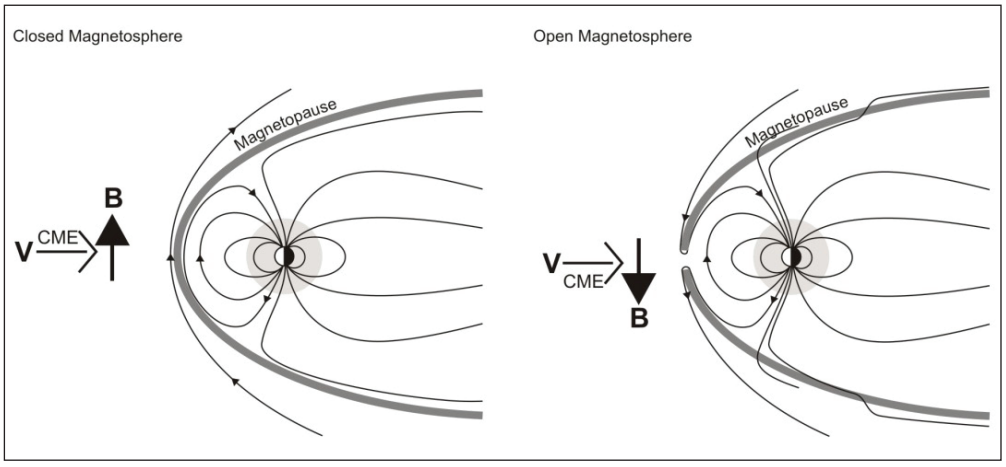

Figure 3 Schematic of CME impacting the magnetosphere with parallel (left) and opposite IMF & EMF magnetic field vectors.

Source: Made by the authors according to [13]

However, if the IMF has an opposite pointing southward component (*southward* B_Z) compared to the EMF (Figure 3), two fields will merge, disrupting and opening the geomagnetic field. The solar wind energy will enter the magnetosphere reaching the sunlit side of the Earth and it will disturb its magnetic field. The more negative the southward component value, the associated geomagnetic disturbance will be stronger [23, 15, 13, 20, 25].

This *geoeffective* event can develop another geomagnetic activity-related component. The solar wind energy which flows by the Earth is transferred to the night side of the Earth and it is stored in the tail of the magnetosphere [23]. After reaching certain critical level, this energy is abruptly released by magnetic reconnection, part of which is pointing back towards Earth.

This occurrence, the substorm, usually lasting one of two hours, will be repeated as long as solar wind enters the magnetosphere. Thus, the geomagnetic storm can contain a series of substorms, so the manifestation of the impact will come in a series of pulses rather than as a continuous high magnetic activity period [23].

3.2 Kp as an indicator of geomagnetic activity

The Kp index is used for describing the geomagnetic disturbances on a global basis. The 'p' stands for 'planetary', meaning that Kp is compound from K-indices – separate 3-hour interval measurements collected from reference stations/ground magnetometers around the globe (Figure 4).

Each geomagnetic observatory measures the relative intensity of magnetic disturbance – maximum fluctuations of Earth's magnetic field horizontal component relative to a quiet day, expressed in nanoteslas (nT) [8, 17]. The final K-indices are determined after the end of three-hours intervals within one day. The maximum positive and negative deviations during the 3-hour period are added together to determine the total maximum fluctuation. The planetary Kp index is derived by calculating a weighted average of collected K-indices network [17].

The scale of the geomagnetic disturbances ranges from 0 to 9, or from very quiet to very disturbed geomagnetic conditions, respectively. The relation between K/Kp index and the strength of the geomagnetic disturbance is presented in Table 1.

Figure 4 Global network of ground-based magnetometers providing 3-hour interval K-indices: Boulder, Colorado, USA; Chambon la Foret, France; Fredericksburg, Virginia, USA; Fresno, California, USA; Hartland, UK; Newport, Washington, USA; Sitka, Alaska, USA; Jeju, Korea; Canberra, Australia; Ottawa, Canada; Meanook, Canada; Niemek, Germany and Wingst, Germany. Transparent circle points are representing new and developing magnetometer reference stations.

Source: Made by the authors according to [15].

Table 1 Relation of the K/Kp index and the geomagnetic activity

K	nT	Geomagnetic intensity/ storm level	Kp
0	0-5	Quiet geomagnetic conditions	0
1	5-10	Quiet geomagnetic conditions	1
2	10-20	Quiet geomagnetic conditions	2
3	20-40	Quiet to active geomagnetic conditions	3
4	40-70	Unsettled geomagnetic conditions	4
5	70-120	G1 (minor geomagnetic storm)	5
6	120-200	G2 (moderate/large geomagnetic storm)	6
7	200-330	G3 (strong/severe geomagnetic storm)	7
8	330-500	G4 (very intense/ extreme geomagnetic storm)	8
9	>500	G5 (very intense/ extreme geomagnetic storm)	9

Source: Based on [8, 17, 18]

Kp values of 5 and higher indicate active geomagnetic activity levels. Those are ranging from minor to extreme geomagnetic disturbance conditions. The Kp-scale is quasi-logarithmic, meaning that the strength of the disturbance increases exponentially with each greater number on the scale. In the following chapter, Kp dynamics pattern through year 2012 has been presented, and the detailed overview of geomagnetic activity through the year has been described.

4 KP INDEX DYNAMICS PATTERNS IN 2012

In this chapter Kp dynamics are presented and described. The estimated Kp data have been retrieved from the NOAA SWPC 2012 [16] official website, with 3-hour interval values per day taken in consideration. An overview of Kp values in 2012 is shown on Figure 5.

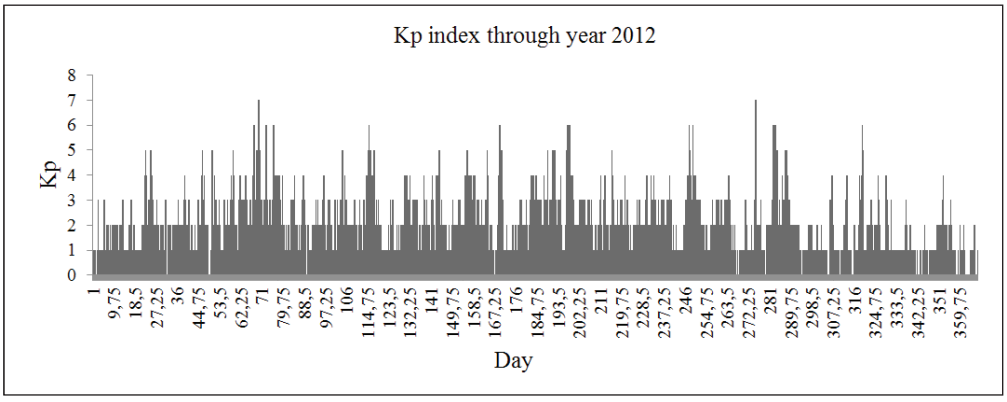

Figure 5 Kp index through year 2012.

Source: NOAA [16]

Of 366 days in the year, number of days when Kp observables were equal or greater than 4, or the geomagnetic activity was at unsettled to active levels, respectively, was 92. In other words, quiet geomagnetic conditions were prevailing through the year, making 75% of the entire period.

From day 1 to 21 Kp value has not exceeded the value of 3. Between day 26 and 44 the Kp value reached level 4 once on day 38, making the 18-day quiet period. The next quiet period (27 days) has been observed between days 76 and 103, with occasional unsettled values. Under the same conditions – Kp value not exceeding the value of 3, with occasional unsettled (4) values – the observed quiet periods have occurred from day 118 to 143 (25-day period), day 216 to 246 (30-day period), day 250 to 274 (24-day period), and day 289 to 318 (29-day

period), respectively. From day 330 to 366 Kp value reached unsettled level once on the day 352, after which it entered well into 2013 again with quiet values, making the quiet Kp period for over 60 days.

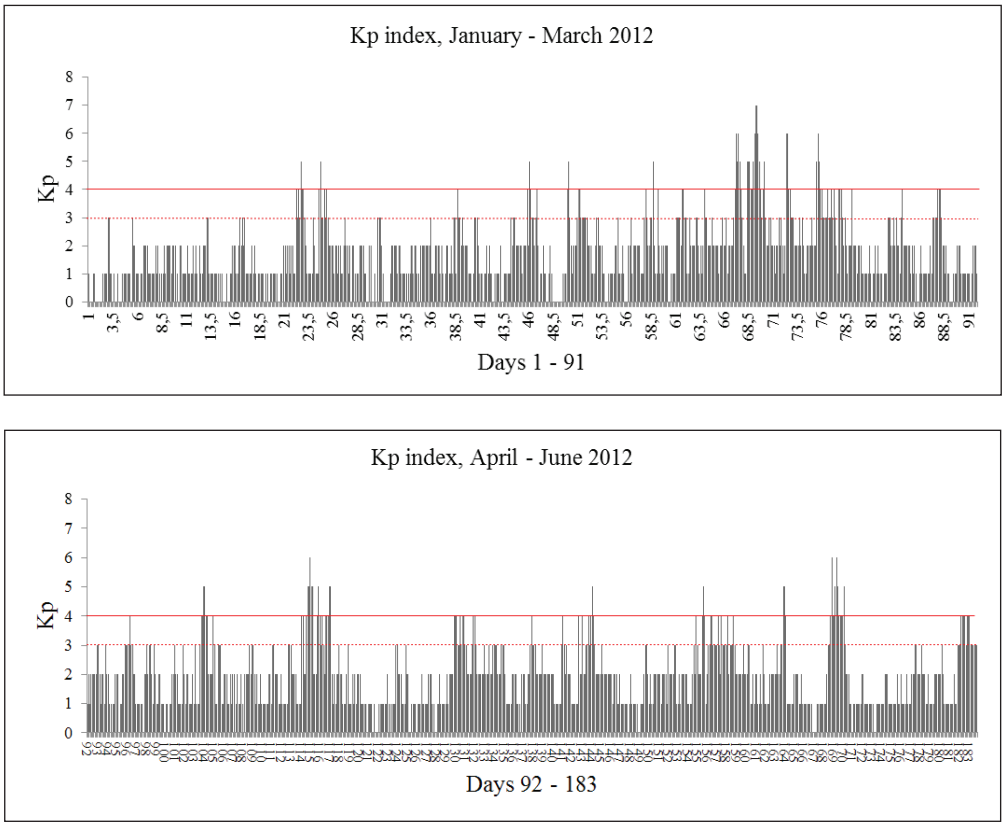

Figure 6 Kp index dynamics from January to March (days 1 to 91), and from April to June 2012 (days 92 to 183), respectively.

Source: NOAA [16]

The Figure 6 represents Kp patterns from January to March (upper graph), and from April to June (lower graph), respectively. The first geomagnetic storm in 2012 occurred on January 22nd, to be repeated two days later. During this geomagnetic event, the Kp index reached its maximum value of 5. Similar event occurred on February 15th.

High Kp values began on March 7th, lasting for several days (until March 10th). Kp index reached the maximum value of 7 (strong geomagnetic disturbance conditions) on March 9th. This is also a highest value Kp reached in 2012. Event

of March 9th was the greatest geomagnetic storm in 2012. It was one of few events when geomagnetic disturbances lasted for relatively long period (36 hours – days 68 and 69). Further geomagnetic activity took place on March 12th and March 15th, with Kp values reaching level 6 (moderate geomagnetic disturbance conditions). The period between three storms in March was marked by pronounced solar activity, resulting in disturbances of the geomagnetic field, but also in solar radiation storms and radio blackouts impact.

Minor storm was recorded on April 13th, with Kp reaching value of 5 for the 6-hours period. The more prolonged geomagnetic disturbances occurred on April 23rd-24th, when Kp reached the value of 6, returning to quiet to unsettled conditions and became active once again on April 26th. In May, besides the 23rd day with Kp = 5 during one 3-hour interval, there were not unsettled/active levels recorded.

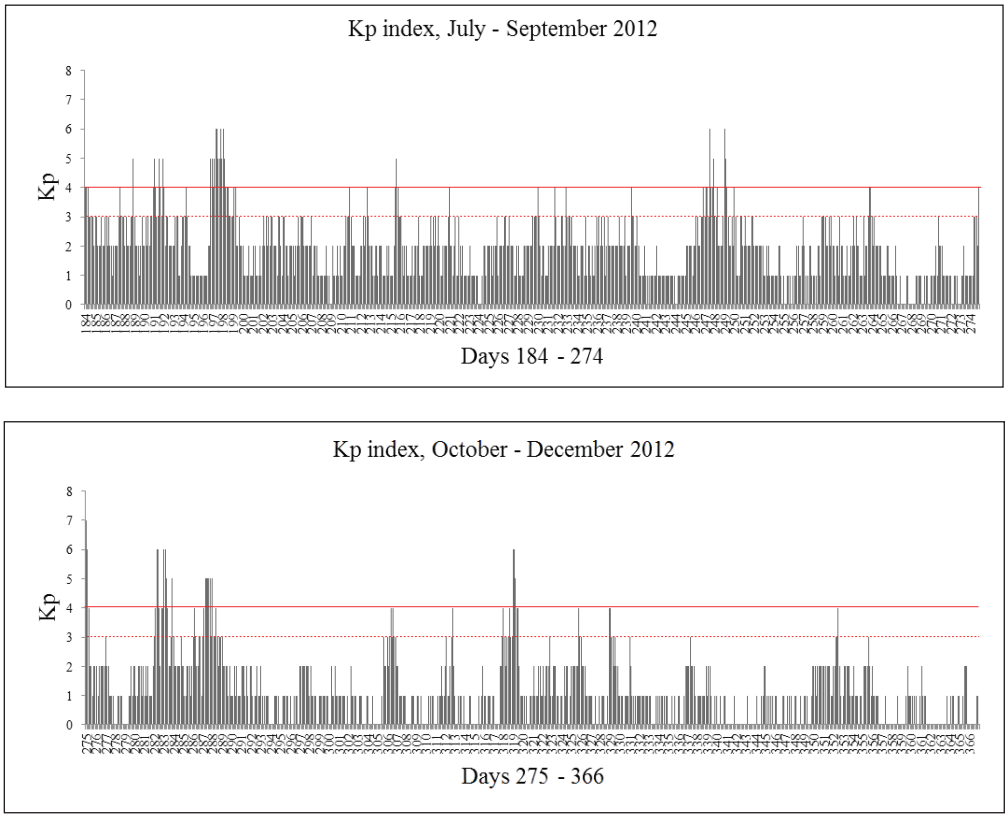

Figure 7 Kp index dynamics from July to September (days 184 to 274), and from October to November 2012 (days 275 to 366), respectively.

Source: NOAA [16]

During June, two geomagnetic storms took place; minor storm on June 12th and moderate (with Kp = 6) geomagnetic storm on June 16th. In the latter, disturbed geomagnetic conditions lasted for 36 hours. June 17th was characterized by all-day active Kp, ranging from unsettled (Kp = 4) to moderate (Kp = 6) disturbance levels.

In 2012, the longest geomagnetic disturbance was recorded during days 196-197-198, where Kp value remained at unsettled to moderate levels for 45 hours. The most intense activity was observed during July 15th (day 197). Short-term disturbance (Kp = 5) occurred on August 2nd within a relatively quiet geomagnetic period, which continued until the September 3rd; geomagnetic disturbance reached moderate levels and remained unsettled to active until September 5th, when Kp returned to lower levels until the end of the month.

On October 1st, strong geomagnetic storm occurred. Together with March 9th event, this was the highest Kp value reached in 2012, however in shorter terms. Longer impact was recorded on October 8th and 9th, with Kp value reaching levels 5 to 6 during 48-hours period. The last storm in October occurred at minor geomagnetic disturbance levels for 15 hours continuously and, after early hours of October 16th it subsided.

The last recorded geomagnetic storm in 2012 was recorded on November 14th, with Kp values reaching moderate levels. After this date, Kp values remained mainly quiet (0-3) until the end of the year.

5 GNSS POSITIONING PERFORMANCE IN TIMES OF PRONOUNCED GEOMAGNETIC ACTIVITY

Regarding effects of space weather, GNSS systems are subject of special attention because they are embedded in a variety of systems and applications used, ranging from standard navigation to precise positioning, timing services and safety of life applications. Position, navigation and timing provision is used in various sectors on individual, regional, national and global level [3]. Impacts on GNSS performance will lead to affectation and vulnerabilities of all applications engaged. Depending on the required level of accuracy, integrity and/or reliability, appears the greater need for risk assessment for performance degradation. In applications demanding high precision degree/precise positioning or highly stabilized timing integrity, high degree of risks assessment that may occur will be required. As for positioning/accuracy requirements, it comes to centimeter-accuracy order of magnitude (e.g. critical applications as high precision approach in aviation, dredging, dive support vessel operations, etc)[2].

[2] For a detailed list of standard and critical applications and their required accuracies, the reader is referred to additional sources [24, 1, 19]

Considering the impact of geomagnetic disturbances on technology, the analysis has been made in terms of the impact on satellite navigation, selecting most pronounced Kp events in 2012. GNSS performance as a space-weather related manifestation on satellite navigation has been taken into consideration, representing one among numerous technologies possibly affected.

For this purpose, mid-latitude GNSS reference station Padua (Italy) has been selected (Figure 8). The performance of satellite positioning was analyzed in terms of positioning pattern response to geomagnetic activities. Padua forms part of the International GNSS Service – the IGS Tracking network. Data have been retrieved in RINEX format from the official IGS website [10], after which they were processed using ©RTKLIB open-source program package for GNSS positioning.

Figure 8 IGS station Padua, Italy: 45.411166146˚ N; 011.896064765˚ E

Comparing obtained results, a day with quiet geomagnetic activity has been chosen for the reference to disturbed days. On Figure 9 Padua GNSS positioning performance is presented for the 24-hour period on March 19th, 2012 (day 79). During the day low Kp values were prevailing, while the day was preceded with quiet geomagnetic period, with unsettled levels, although occasionally.

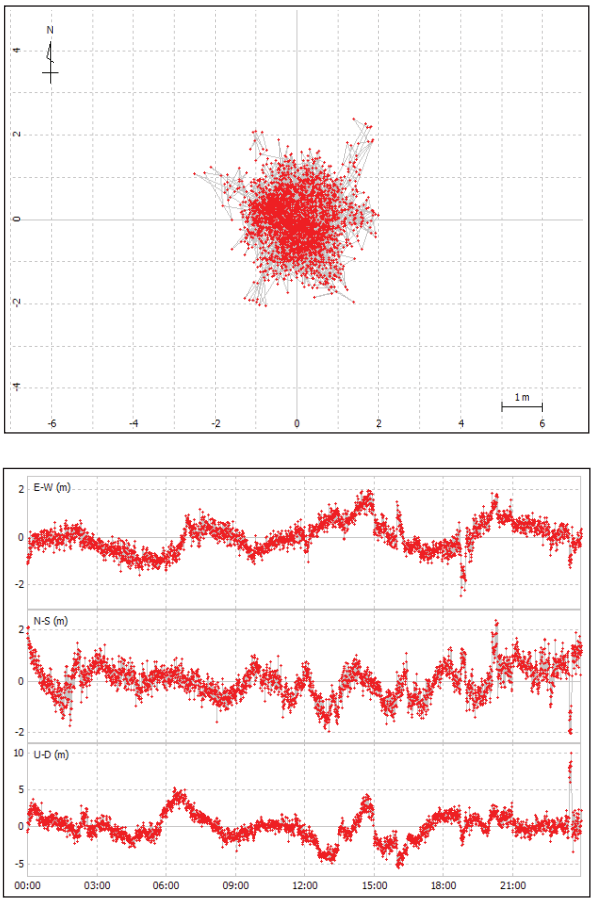

Figure 9 Ground track (horizontal pattern) and positioning plot in all three axes (easting, northing and height). Padua GNSS reference station, March 19th, 2012.

Source: Made by the authors using ©RTKLIB software and IGS data [10]

For the purpose of the study, four most significant Kp events in 2012 have been taken for analysis: days when Kp reached its highest value in 2012, and days when Kp retained high values (unsettled and higher) through entire 24-hour period, i.e. days with the longest disturbed magnetic activity, thus making total of four events.

Days 69 (March 9th) and 275 (October 1st) are the only two days in 2012 with Kp reaching highest value of 7, causing severe geomagnetic storms. Beside the Kp = 7, on March 9th geomagnetic disturbance was present in almost all day. Kp, ground track and positioning pattern for days 69 and 275 are presented on Figure 10.

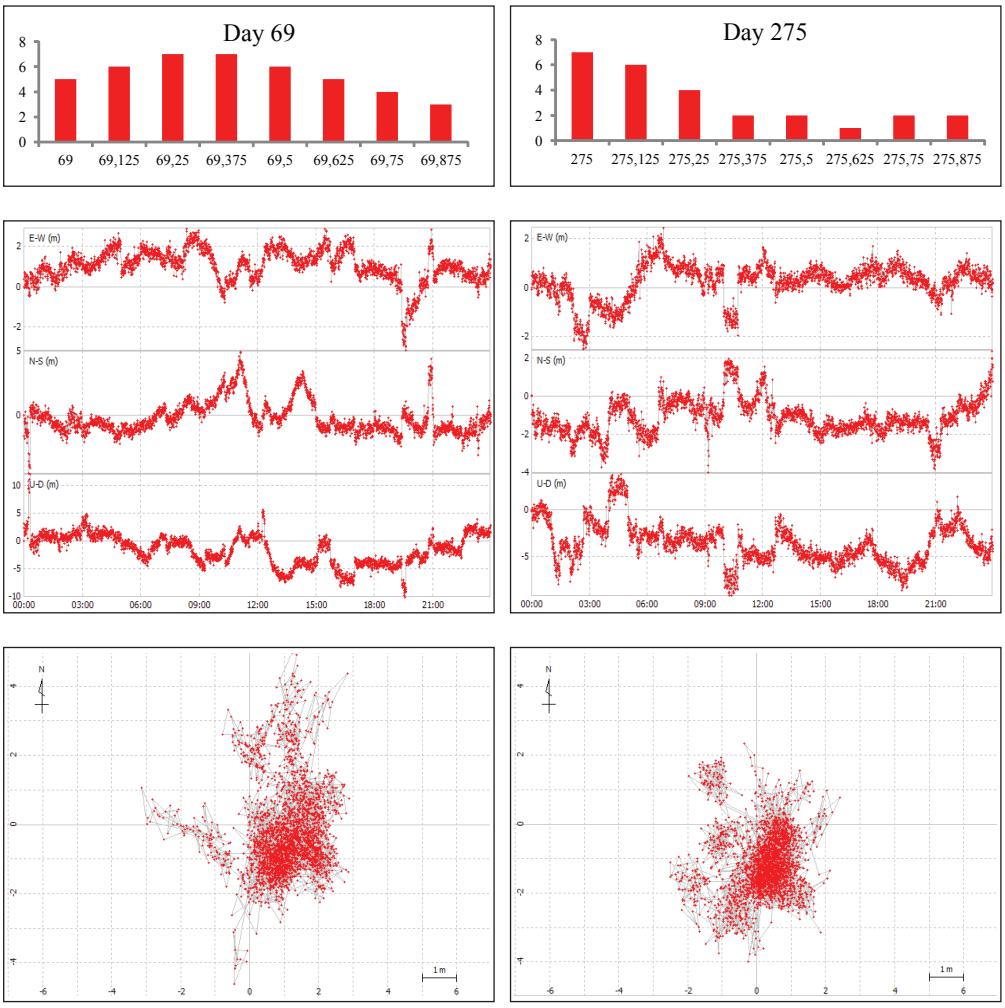

Figure 10: Kp dynamics (uppermost), positioning (middle) and ground track (lowest) pattern plots for day 69 (left) and day 275 (right), respectively.

Source: Made by the authors using ©RTKLIB software and IGS & NOAA SWPC data [10, 16]

In days 169 (June 17th) and 197 (July 15th) Kp value was 4 or higher during entire 24-hour period. Unsettled and upward (max. 6) conditions were present for 36 hours surrounding day 169 (period 168-169-170), and 45 hours surrounding day 197 (period 196-197-198). Kp, ground track and positioning pattern for days 169 and 197 are presented on Figure 10.

Figure 11 Kp dynamics (uppermost), positioning (middle) and ground track (lowest) pattern plots for day 169 (left) and day 197 (right), respectively.

Source: Made by the authors using ©RTKLIB software and IGS & NOAA SWPC data [10, 16]

Table 2 Values of statistical parameters for days 69, 79, 169, 197 and 275, respectively.

Day	Statistical parameters [m]					
	STD East	STD North	STD Up	RMS East	RMS North	RMS Up
Day 79 (quiet)	0,6383	0,6449	1,7870	0,6382	0,6448	1,7866
Day 169 (24-hour)	0,7044	1,0187	2,8112	0,7043	1,0186	2,8107
Day 275 (Kp=7)	0,7428	0,9155	2,1886	0,7427	0,9154	2,1882
Day 69 (Kp=7)	0,8025	1,2659	2,7626	0,8024	1,2657	2,7621
Day 197 (24-hour)	0,9444	1,2270	2,2486	0,9443	1,2268	202482

During selected events GNSS positioning error was more pronounced than it was in the time of low geomagnetic activity, as can be seen on corresponding Figures. In Table 2 statistic parameters (standard deviation and root mean square error) are presented for each of four days, including quiet March 19th.

6 DISCUSSION

Compared to other years, and considering the predicted upcoming solar maximum in 2013, 2012 geomagnetic activity was relatively low. The quiet and disturbed geomagnetic activity periods were described in Chapter 4. On Table 3, Kp estimations of level 4 and upward are presented, with total number of 3-hour interval and number of days affected, respectively.

Table 3 Number of Kp ≥ 4 estimations through 2012

Kp	3-hours estimations	Days affected
4	148	87
5	52	32
6	23	14
7	3	2
8	0	0
9	0	0

Source: NOAA

Minor geomagnetic activity (NOAA level G1) was present in 52 Kp estimations or 32 days, respectively. This is the activity level when weak power grid fluctuations can occur and minor impacts on satellite operations are possible,

depending on the duration of event. Moderate geomagnetic storm conditions (with Kp reaching level 6) were present in 23 estimations or 32 days, respectively. In these conditions geomagnetic effect becomes pronounced at higher latitudes: risk of HF radio propagation fadeout appears, and the drag can affect satellite predictions. In case of long duration of G2 (moderate) storms, voltage increase in power systems may occur, and transformers can experience temporary or permanent damage [18]. Extreme geomagnetic conditions (Kp level 8 and 9) have not occurred during the year. Geomagnetic activity and storm development remained within level 7, and disturbed periods, duration if which stands as an important factor in terms of influence of severity of effects, did not exceed 45 hours in total. The two most significant events with Kp reaching maximum value of 7 (and producing severe geomagnetic conditions – level G3) occurred twice – on March 9th and October 1st (Kp = 7) was estimated in three 3-hours intervals). This is the Kp level when power companies begin monitoring the geomagnetic activity [13]. At this stage, emerging geomagnetic storms can trigger false alarms on some protection devices, and voltage corrections may be required. Drag and surface charging effects on satellites are more pronounced, the need for orientation correction appears, and satellite and low frequency radio navigation may become intermittent [17].

Extreme geomagnetic conditions (Kp level 9) can cause far greater effects than it was the case in 2012. According to [18], the risks of geomagnetic disturbances at extreme levels include widespread voltage control problems, permanent transformer damages and complete collapse of power grid systems. Example for such impact was extreme geomagnetic storm that occurred in March 1989, which produced power blackout in Quebec, Canada, and transformer damage in countries all over the world. In the Quebec case, entire grid collapsed within a minute, leaving the entire province without power for many hours [23, 13, 2]. During the same event, GIC affected transatlantic optical fibre cable, which experienced significant potential changes [23].

Besides the impact on power grids and long conducting wires, this (and similar) geomagnetic storm caused damage on other systems. In series of geomagnetic events of July 14th, 2000 and October, 2003, CME-driven storms resulted in damage of several satellites, ranging from temporary shut-downs to total losses [23, 14].

In the previous chapter, satellite navigation systems' performance has been shown during the most significant Kp events in 2012. The degradation of GNSS positioning performance was measurable, although it was not significantly pronounced regarding the level of disturbance which took place. In case of severe geomagnetic disturbances, satellite navigation can be degraded for days,

together with other radio systems affected [18], including re-routing of flights operating at higher latitudes. Although inevitably linked with other types of space weather manifestation, geomagnetic disturbances can degrade the GNSS performance on global basis, leading to ranging errors and signal fade out due to satellite outages. Positioning and navigational solutions may be completely lost [23]. For example, during one of the solar events which occurred on December 2006, GNSS positioning errors reached values up to 20 meters in horizontal, and more than 60 meters in vertical directions. In addition, significant number of satellites was unavailable for more than 5 minutes [4]. As described in previous chapters, satellite navigation systems are used for wide spectrum of applications, and are nowadays embedded in the national infrastructure. According to [1], it is estimated that, already, 6–7% of GDP in Western countries is dependent on satellite radio navigation.

7 CONCLUSION

Geomagnetic activity has been elaborated in the paper. The year 2012 has been taken for analysis and, between existing parameters describing state and disturbances of the Earth's magnetic field, Kp index was chosen. Potential risks on technology arising from severe and extreme geomagnetic disturbances have been listed; however space weather effects other than geomagnetic disturbances were generally described. The study showed that 2012 was characterized with relatively quiet geomagnetic conditions, although there were several events with increased geomagnetic activity. These specific events were further processed and the geomagnetic activity was compared with GNSS positioning performance in times of geomagnetic disturbances. The results showed that there was measurable degradation of positioning performance during increased geomagnetic disturbances, although geomagnetic activity in 2012 was not significantly expressed.

ACKNOWLEDGMENTS

Research activities presented in this paper were conducted under the research project "Research into the correlation of maritime-transport elements in maritime traffic" supported by the Ministry of Science, Education and Sports, Republic of Croatia. Authors appreciate the development of RTKLIB© open-source program package for GNSS positioning, and the availability of open access data used for the study.

REFERENCES

[1] American Meteorological Society (AMS) (2011). *Satellite Navigation and Space Weather: Understanding the vulnerability & Building Resilience*. Policy Workshop Report. Boston, MA, USA.

[2] Baker, D. N. (2005). Introduction to Space Weather. Lecture Notes in Physics. 656: 3–20. Springer-Verlag Berlin Heidelberg, Germany.

[3] Brčić, D. (2012). Ensuring sustainability through utilisation of satellite navigation technology. *Proc. 15th International Conference of Transport Science*. Portorož, Slovenia.

[4] Carrano, C.S., Bridgwood, C.T. & Groves, K.M. (2008). Impacts of the December 2006 Solar Radio Bursts on GPS operations. AMS's 88th annual meeting. New Orleans, LA, USA.

[5] Cohen N. & Davies, K. (1994). *Space Environment Topics: Radio Wave Propagation*. NOAA Space Environment Laboratory. Boulder, CO, USA.

[6] Australian Government, Bureau of Meteorology: Radio and Space Weather Services (IPS) (2013). Communications and Space Weather. Available at: http://bit.ly/1eDxcnr, accessed on 20.02.2013.

[7] European Commission (2011). *Mid-term review of the European satellite radio navigation programmes*. Report from the Commission to the European Parliament and the Council. Brussels, Belgium.

[8] Filjar, R. (2008). A Study of Direct Severe Space Weather Effects on GPS Ionospheric Delay. *The Journal of Navigation*, **61**(1), pp. 115–128.

[9] Goodman J.M. (2005). *Space Weather and Telecommunications*. The Kluwer International Series in Engineering and Computer Science. Springer Science and Business Media. New York, NY, USA.

[10] International GNSS Service (IGS) (2012). GPS pseudorange observables in RINEX format. Available at: http://1.usa.gov/9K6tRn, accessed on 10.01.2013.

[11] Kintner P.M. & Ledvina B.M. (2004). The Ionosphere, Radio Navigation and Global Navigation Satellite Systems. *Proc 7th Latin-American Conference on Geophysics*. Sao Jose dos Campos, Brasil.

[12] Koons, H. C., J. E. Mazur, R. S. Selesnick, B. J. B, J. F. Fennell, J. L. Roeder, and P. C. Anderson (1999). The Impact of the Space Environment on Space Systems. Rep.TR-99 (1670)-1. Aerospace Corporation. El Segundo, CA, USA.

[13] McMorrow, D. (2011). *Impacts of Severe Space Weather on the Electric Grid*. Report JSR-11-320. The MITRE Corporation. McLean, VA, USA.

[14] National Aeronautics and Space Administration (2013). Available at: http://1.usa.gov/1duwngr, accessed on 21.03.2013.

[15] National Oceanic and Atmospheric Administration, Space Weather Prediction Center (NOAA SWPC) (2013): Explanation of Real-Time Solar Wind data dials. Available at: http://1.usa.gov/9bXiHG, accessed on 01.04.2013.

[16] National Oceanic and Atmospheric Administration, Space Weather Prediction Center (NOAA SWPC) (2012): 2012 Kp index. Available at: http://1.usa.gov/1dck33u, accessed on 01.02.2013.

[17] National Oceanic and Atmospheric Administration, Space Weather Prediction Center (NOAA SWPC) (2011): The K-index. Available at: http://1.usa.gov/HAWF9, accessed on 02.01.2013.

[18] National Oceanic and Atmospheric Administration (NOAA) (2005): NOAA Space Weather Scales. Available at: http://1.usa.gov/anwGOB, accessed on 01.10.2012.

[19] Poppe, B.B. & Jorden, K.P. (2006). *Sentinels of the Sun*. Johnson Books. Boulder, CO, USA.

[20] Russel, C. (2008). The Interplanetary Magnetic Field. Available at: http://bit.ly/9VP035, accessed on 12.03.2013.

[21] Schlegel K. (2005). *Space Weather Effects in the Upper Atmosphere: High Latitudes*. Lecture Notes in Physics. 656: 215 – 238. Springer-Verlag Berlin Heidelberg, Germany.

[22] Space Physics Research Group (SPRG) (2005). University of California, Berkeley. Available at: bit.ly/GLVgJd, accessed on 21.03.2013.

[23] The Royal Academy of Engineering (RAENG) (2013). *Extreme space weather: impacts on engineered systems and infrastructure.* London, UK.

[24] The Royal Academy of Engineering (RAENG) (2011). *Global Navigation Space Systems: reliance and vulnerabilities.* London, UK.

[25] Valtonen E. (2005). Space Weather Effects on Technology. Lecture Notes in Physics. 656: 241–273. Springer-Verlag Berlin Heidelberg, Germany.

[26] Warmuth A. & Mann G. (2005). *The Application of Radio Diagnostics to the Study of the Solar Drivers of Space Weather*. Lecture Notes in Physics. 656: 51–70. Springer-Verlag Berlin Heidelberg, Germany.

Faculty of Maritime Studies
University of Rijeka, Croatia

Royal Institute of Navigation
Science Technology Practice

7th GNSS
Vulnerabilities and Solutions Conference

eLORAN – THE ROUTE TO RESILIENCE

Paul Williams, Chris Hargreaves, David Last, Nick Ward

The General Lighthouse Authorities of the United Kingdom and Ireland
E-mail: paul.williams@thls.org

ABSTRACT. *The General Lighthouse Authorities of the United Kingdom and Ireland (GLA) provide marine aids-to-navigation (AtoNs) for the benefit and safety of all mariners within their waters. These AtoNs include traditional lighthouses, buoys and various radionavigation systems.*

Visual signalling by lights and buoys has for centuries played a crucial role in marine navigation close to danger. Its role remains vital in the future world of e-Navigation, a concept driven by the International Maritime Organisation (IMO) to harmonise, integrate and exchange maritime information, to enhance berth-to-berth navigation. However, GNSS (effectively GPS) has become the primary Aid-to-Navigation (AtoN) used by all professional and most other mariners. The vulnerability of GNSS to space weather and interference (unintentional and criminal jamming) means that a backup system is needed to achieve resilient Position Navigation and Timing (PNT) for e-Navigation. Though the probability of losing GNSS may be low, the consequential impact could be very high and maintaining an appropriate balance of physical and radionavigation AtoNs is vital for e-Navigation.

Enhanced Loran (eLoran) is the latest in the longstanding and proven series of low frequency, **LO***ng-***RA***nge* **N***avigation systems. eLoran evolved from Loran-C in response to the 2001 Volpe Report on GPS vulnerability. It vastly improves upon previous Loran systems with updated equipment, signals, and operating procedures. The improvements allow eLoran to provide better performance and additional services when compared to Loran-C. In recent years the GLA have been pioneering the introduction of eLoran in Europe.*

eLoran is an independent, dissimilar and complementary backup to GNSS and is the only credible and cost-effective option that, in the time available, can deliver eNavigation's urgently needed benefits of safety and security at

sea and protection of the marine environment through the provision of resilient PNT information, taking over seamlessly when GNSS fails.

The GLA have deployed a new eLoran transmitter station at Anthorn in Northwest England; conducted successful GPS jamming and eLoran trials; and continues to work with International colleagues to promote eLoran's maritime and nonmaritime benefits. The GLA's eLoran strategy is to extend their current trials; to continue building a European consensus in favour of eLoran; and to move towards UK eLoran Initial Operating Capability (IOC) in limited UK waters by mid-2014.

eLoran IOC will comprise Port Approach accuracy (10m 95%) level eLoran at several major ports on the east coast of the United Kingdom. This will include one upgrade of the already existing prototype service at Harwich/ Felixstowe and up to six new installations; Dover, the Thames Estuary to Tilbury, Humber (Immingham and Hull), Middlesbrough, Firth of Forth (to Grangemouth) and Aberdeen.

The work of installing IOC level eLoran includes performing surveys of Additional Secondary Factor (ASF) data within each desired coverage area and the installation of a DifferentialLoran (DLoran) Reference Station in the locality of each port. DLoran corrections will be broadcast using the Loran Data Channel – employing the Eurofix modulation scheme – implemented on the UK eLoran transmitter at Anthorn.

IOC will also include a DLoran Reference Station Monitoring and Control Centre based in Harwich. As of the time of writing a European tender process has almost been completed for the Operational Level DLoran Reference Stations and Monitor/Control Station.

IOC eLoran will provide areas for demonstrations and trials so that mariners can gain experience in using the service and allow them to understand the benefits that eLoran can bring to the resilience and integrity of their operations. It is the aim of the GLA to complete IOC installation by the end of 2014.

This paper describes the work done by the GLA in installing IOC level eLoran at the Port of Dover and the northern part of the Traffic Separation Scheme (TSS) within the Dover Strait; a vital sea traffic pinch point allowing access to and egress from the North Sea Region via the English Channel.

Technical background is presented on the technology required for implementing eLoran in and around port approach areas. The overall architecture of the IOC level DLoran system is presented. We then focus on the implementation of eLoran in the Port of Dover approaches and the northern part of the Dover Strait TSS. The planning and performance of the Dover ASF survey is highlighted. Accuracy of the eLoran implementation is assessed through validation runs using a vessel passing through the region covered by the ASF map and served by the Dover DLoran reference station. The processes outlined in this paper will be repeated at each of the other candidate eLoran IOC ports, and the results of ASF surveys in approaches to the River Thames and River Humber are also briefly discussed.

1 INTRODUCTION

The General Lighthouse Authorities of the United Kingdom and Ireland (GLAs) comprise Trinity House, The Commissioners of Irish Lights and The Northern Lighthouse Board. Between them, they have the statutory responsibility to provide marine Aids-to-Navigation (AtoNs) around the coast of England and Wales, all of Ireland and Scotland, respectively. AtoNs take many forms, from the more traditional lighthouse to radio navigation systems, including the use of new GNSS when they become available.

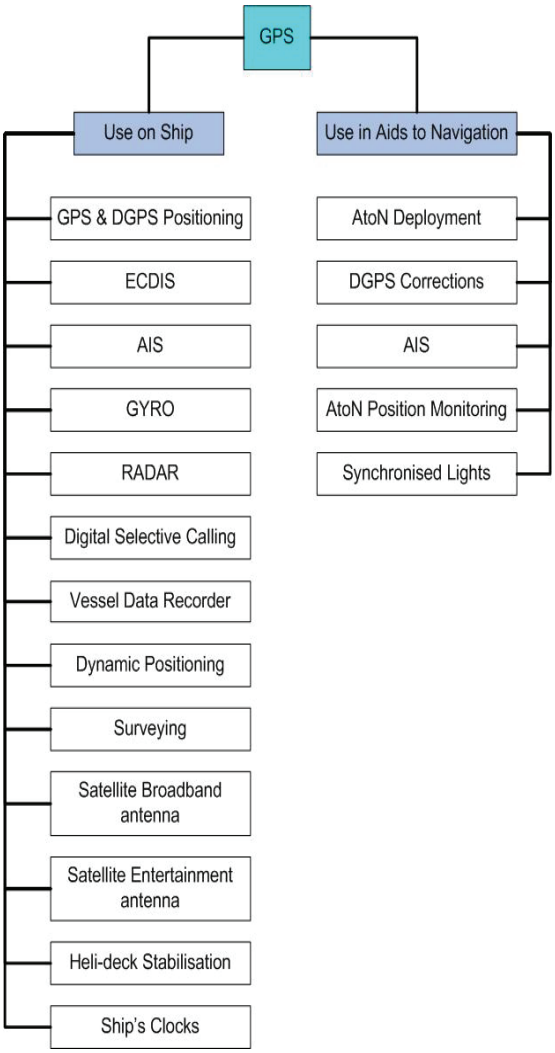

Figure 1 GPS is used in many ship's systems.

It is recognised that GPS, or more generally Global Navigation Satellite Systems (GNSS) have become the primary means of obtaining Position, Navigation and Timing (PNT) information at sea, and there is no doubt that GNSS will form the primary source of PNT for eNavigation.

An aim of the International Maritime Organisation is to develop a strategic vision for e-Navigation, integrating existing and new navigational tools in an all-embracing system, contributing to enhanced navigational safety and environmental protection, while reducing the burden on the navigator. One of IMO's requirements for eNavigation is that it should be resilient – robust, reliable and dependable [1]. Requirements for redundancy, say the IMO, particularly in relation to position fixing systems, should be considered.

GPS/GNSS IS EVERYWHERE!

But GPS is vulnerable to intentional and unintentional interference [2, 3], while at the same time it is used in many ship's systems, as shown in Figure 1.

Its output is displayed on the ECDIS; is transmitted to other vessels using AIS; is used to calibrate the gyro compass; in the RADAR; connected to the digital selective calling (DSC), its reported position transmitted at the push of the emergency button for search and rescue; the vessel data recorder; the dynamic positioning system; surveying equipment; the ship's entertainment system for aiming the satellite dish and it even synchronises the ship's clocks!

GNSS is also used in Aid-to-Navigation (AtoN) provision, for deploying buoys and lights, AIS transponders, AtoN position monitoring, and its precise timing capabilities are used to synchronise the lights along an approach channel to improve conspicuity [4].

2 THE SOLUTION?

In 2010 we followed the UK Treasury methods to produce the GLA' eLoran Business Case [5, 6]. This comprehensive document presented and analysed various options for providing 'Resilient PNT' in UK and Irish waters. It was clear that if the GLA chose to implement eLoran it could rationalise its physical AtoN infrastructure, removing some lights and other physical aids, and on balance actually reduce costs by implementing eLoran. Indeed, compared to other possible resilient PNT options such as GNSS hardening, radar absolute positioning, increasing physical AtoN provision, eLoran would save the GLA £25.6M over a nominal system lifespan of 10 years from the introduction of eNavigation services in 2018 to 2028.

3 BUT LORAN IS OLD FASHIONED ISN'T IT?

What's the difference between shiny new eLoran and the old, outdated, Loran-C system? Well, the core signal of eLoran is pretty much the same as Loran-C but tolerances have been tightened up. Things like carrier zero crossing points, half-cycle peaks, ECDs, transmission timing, signal power, signal availability, power supply resilience have all been upgraded taking advantage of improvements in technology allowing us to better appease the "four horsemen" of navigation: Accuracy, Availability, Continuity and Integrity.

SAM control is a thing of the past and eLoran transmitters are synchronised directly to UTC – this means that their times of transmission can be predicted. Having stations independently synchronised to UTC means that the mariner no longer has to rely on old fashioned hyperbolic navigation. Charts with hyperbolic lines of position on them are a thing of the past. A modern eLoran receiver works just like a GPS receiver, employing signals from all available transmitters in its position solution. With GPS those transmitters are moving in space, in eLoran the transmitters are fixed onto the surface of the earth.

Modern receivers are small (Figure 2), they use off the shelf, high performance processors; the receiver is written in software allowing a lot of flexibility.

Three transmitters are sufficient to give you position, 4 or preferably 5 signals are better for integrity. But for timing and frequency applications you only need one transmitter. The Anthorn station in the UK can cover the entire UK and Ireland with a radio signal that has stability enough to satisfy the Stratum 1 frequency source requirement for steering the clocks of telecom networks; and Anthorn has not even been upgraded to full eLoran standard yet!

Figure 2 Reelektronika LORADD receiver – this receiver is just 3cm tall.

Source: Picture courtesy of *Reelektronika*.

One of the MAJOR differences between Loran-C and eLoran is that eLoran now has a data channel. Some of the Loran pulses of each pulse group are modulated so that data can be sent over the 100kHz signal. This allows service providers to send integrity alerts, and application specific data, like UTC time, and differential-Loran and DGPS corrections. In Europe this is implemented by the already internationally standardised Eurofix system [7]. A parallel can be drawn with GPS signals, which contain a navigation component (pseudorandom noise code and/or carrier phase) and modulated data. Some options for data channel technology are still evolving with 1500 bits per second demonstrated, and 3000bps possible. That may not sound very much to salt of the earth communications engineers, but for Loran it's pretty impressive, especially when you consider prototype attempts at Loran data communications in the past have been limited to 30 to 250 bps.

4 MARITIME APPLICATION SERVICES

So, how do we apply eLoran to something like the maritime application of port approach? To do this it is important to remember that the receiver operates by measuring how long it takes a groundwave radio signal to travel over the surface of the earth. An eLoran receiver assumes that the world is made entirely of seawater, for which it has a very accurate propagation model built-in. The receiver does not, and indeed cannot, know about any land along the propagation path; and land slows the signal down, perhaps by as much as a few microseconds over typical propagation distances.

So the service provider must survey the effects of the land masses in the area of coverage, the Additional Secondary Factors (ASFs) of all the stations, across the proposed service area are mapped. The ASF survey is a onceandforall task but it needs to be done, and the ASFs published. In the old days, hyperbolic lines would be "grid warped", or tables would be published on paper for the navigator to enter values manually. But with modern eLoran receivers containing large amounts of memory, quite detailed ASF maps can be stored in the mariner's receiver.

ASFs depend on the electrical conductivity of the surface over which the eLoran signal travels. The conductivity changes with the constitution and moisture content of the earth. This means that the ASF along a path varies over a period of time – perhaps by as much as a few hundred nanoseconds over a year. Of course because the ASFs stored in a receiver are fixed a method is needed to correct for this *temporal* ASF variation. In order to monitor this variation, a reference station is installed close to the harbour, or point of use of the eLoran service.

This differential-Loran (DLoran) reference station measures the temporal changes in the signals' arrival times due to changing ASFs, transmitter variations and weather effects. The DLoran reference station performs the same task as a differential GPS reference station. Now, the phrase "reference station" conjures up images of expensive buildings, amenities, and hordes of personnel and associated support services. However, a DLoran reference station is a small box sitting in the corner of a room connected to a small eLoran receive antenna on the roof, and to the Internet. It sends differential corrections over the Internet to an eLoran transmitter, which then broadcasts them to the mariner's receiver over the Loran Data Channel.

Note that a DLoran reference station does not transmit a radio signal, it does not need a transmitter itself, it uses the Internet and the eLoran signal to disseminate its real time data. The mariner uses the same eLoran receiver to receive both the navigation signal AND the differential corrections.

So the process is: map ASFs once; run a reference station; and broadcast corrections. With good Signal to noise ratio and transmitter geometry 10m or better accuracy can be obtained.

5 MEASURING ASFS

The GLA have had the ability to measure ASFs for a number of years using a combination of commercial hardware (Figure 3) and bespoke software (Figure 4).

The software, written in Matlab™, shows a real-time plot of the survey as it progresses. The ASF values are colour coded according to magnitude. The software can also process the ASF data once it has been measured, to get the best performance out of it. The real time capabilities of the software allow the determination of the quality of the data while aboard the ship, rather than having to wait until back in the laboratory. Statistical analysis of the data can also show where the ship should go to gather more data in a particular area.

Once the survey is complete, the software can be used to generate interpolated grids of ASF data – the most convenient and accurate form of ASF data storage.

It is important with any scientific or engineering measurement to establish the error on that measurement. The same can be said of ASFs, and so the software can calculate the error bounds on ASF measurements. This "ASF error" data can again be published in grid form alongside the ASF database. This allows it to be used as one component of an Integrity Equation, implemented within the mariner's receiver, to calculate Horizontal Protection Levels (HPL).

Figure 3 Reelektronika ASF Measurement System.

Source: Picture courtesy *Reelektronika*.

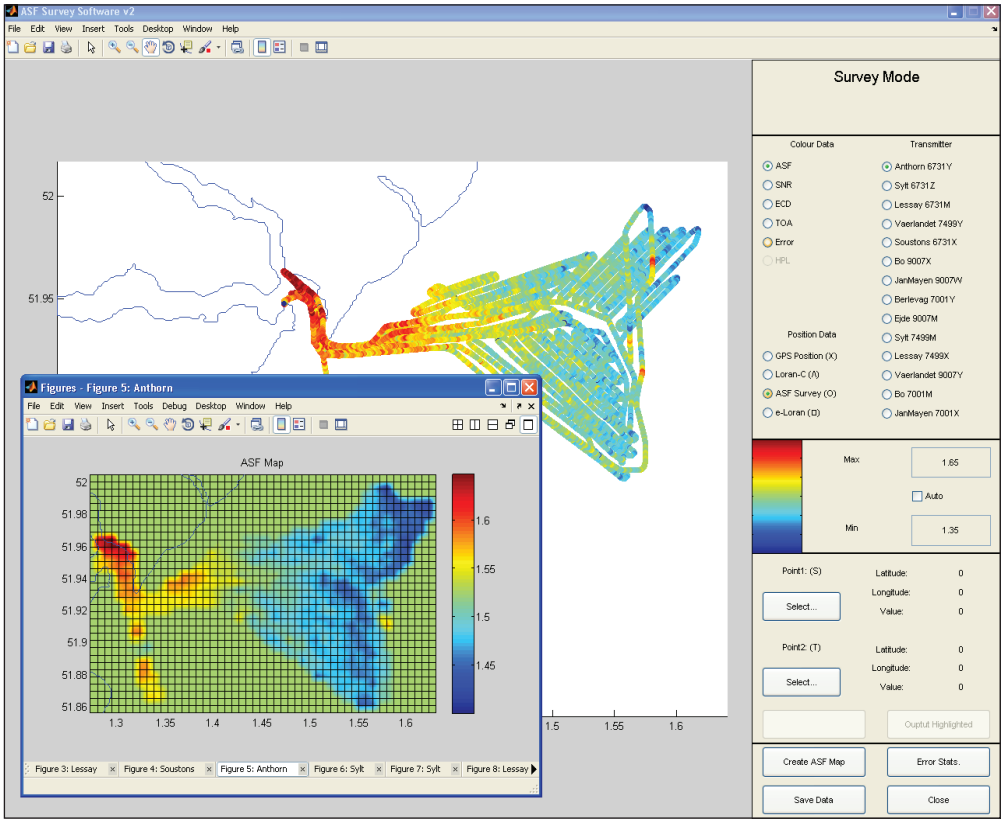

Figure 4 GLA produced software for ASF survey, processing and validation.

After processing the ASF data should be validated by performing a harbour approach or other manoeuvre that requires a particular positioning accuracy. For this, the software can be switched to "Validation" mode. Once the validation is

successful, the data can be output in a publication format (RTCM SC-127 format for example). [8].

The plot in Figure 4 shows an ASF database for Harwich and Felixstowe, major ports on the east coast of the UK. Using this data and differential-Loran in the Harwich and Felixstowe approach provides 10m (95%) positioning accuracy.

6 UK ELORAN PROTOTYPE

This prototype eLoran system works alongside GPS. It has been in operation 24 hours a day since about May 2010. It is "prototype" since it demonstrates the concept of eLoran using signals from existing Loran-C stations in Norway, the Faroe Islands, Germany and France plus the UK's station at Anthorn; see Figure 5.

Figure 5 Relevant European Loran-C stations for prototype eLoran.

These stations, together with ASF measurements and DLoran, can deliver a high-precision eLoran service in ports where 10-20 metre accuracy is needed, across the area enclosed by the green contour in Figure 6.

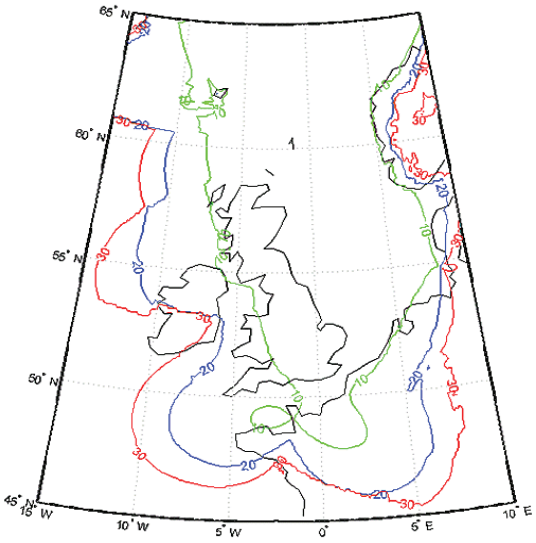

Figure 6 Coverage of prototype eLoran over the UK and Ireland.

It is very impressive, yet the full availability and accuracy benefits of eLoran are still to come as these stations are eventually upgraded to full eLoran capability. And for the last year or so the GLA has begun to move beyond the confines of the Harwich and Felixstowe approaches and implement initial eLoran services in other regions around the GLA service area.

The GLA aim to do this in two stages. In the first stage **Initial Operational Capability** (IOC) service will be installed by end-2014, with the second stage **Full Operational Capability** (FOC) service covering all major ports in the UK and Ireland, plus Traffic Separation Schemes, installed by 2019 in time for e-Navigation.

7 INITIAL OPERATIONAL CAPABILITY

IOC involves upgrading the installation at Harwich and Felixstowe and installations in the approaches to another six of the busiest ports in the UK; Aberdeen, Grangemouth, Middlesbrough, Immingham, Tilbury and Dover. For each of these areas an ASF survey and a differential Loran reference station will be required.

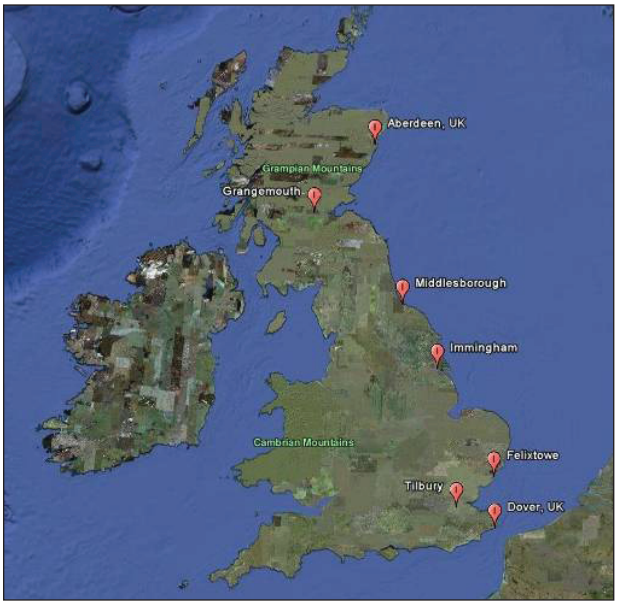

Figure 7 eLoran Initial Operational Capability will be installed in the approaches to seven of the busiest ports in the UK.

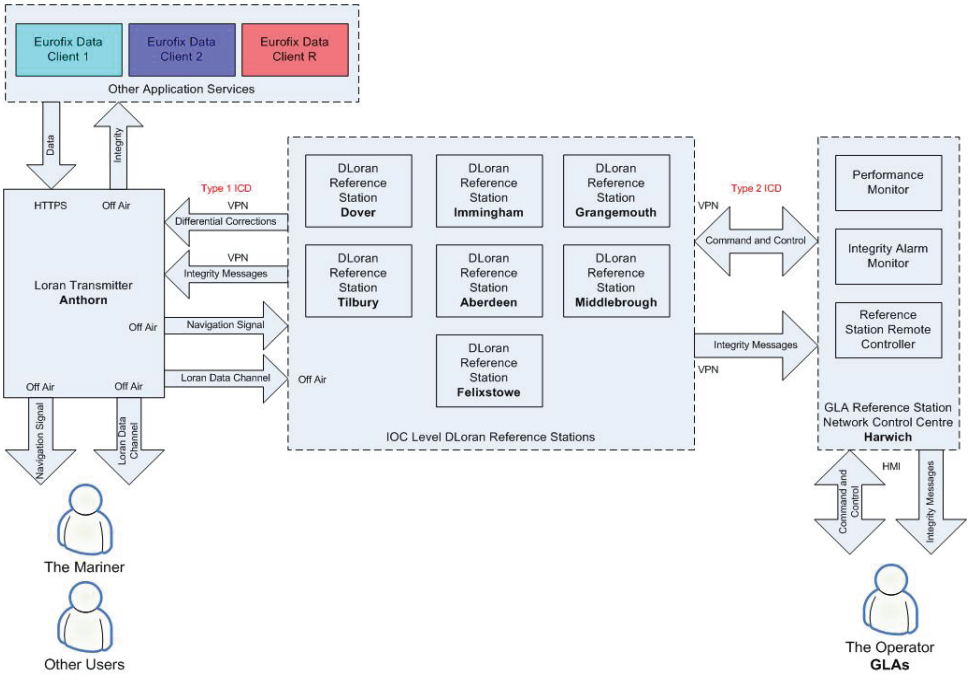

Figure 8 The Architecture of the UK GLA' eLoran Initial Operational Capability.

The corrections for these reference stations will be broadcast using the Anthorn Loran Data Channel. There is also the need for a Monitoring and Control System for the network of DLoran Reference Stations and it is envisaged that this will be based in Harwich. Figure 8 illustrates the architecture of the Initial Operational Capability system. The diagram shows the major components; eLoran transmitter; DLoran reference station network; monitor and control system. Also shown are the interfaces between the components, which provide not only operational data but also include the ability to monitor the integrity of the system. Also note that the Loran Data Channel is capable of supporting third party messaging applications using a client "logon" facility. This is already being done at Anthorn.

The European tender process for seven operational reference stations has been completed and equipment should be installed before the end of 2014.

The aim of IOC is to provide areas for demonstrations and trials, so that the mariner can gain experience of the system and its capabilities and provide feedback to the GLA on its performance.

8 eLORAN AT THE PORT OF DOVER

In the absence of the final operational reference stations it was decided by the GLA to perform an early implementation using prototype equipment that was already available at the GLA.

Figure 9 Port of Dover and the northern part of the Dover Strait.

The choice for this early implementation was obvious, the iconic Port of Dover, a major port on the southeast coast of the UK, and the Dover Strait, is one of the busiest sea ways in the world – some 500 plus vessels travel through there each day on their way to or from the North Sea Region; Figure 10.

An ASF survey and a differential-Loran reference station would be required.

The GLA has, with the agreement of Port of Dover Operations, installed a prototype differential-Loran Reference Station within the port's Terminal Control building. The roof of the building is an ideal location for the reference station receiver antenna as the location demonstrates low noise in the eLoran band, has easy access to mains power, cable runs, antenna mounts and Internet access.

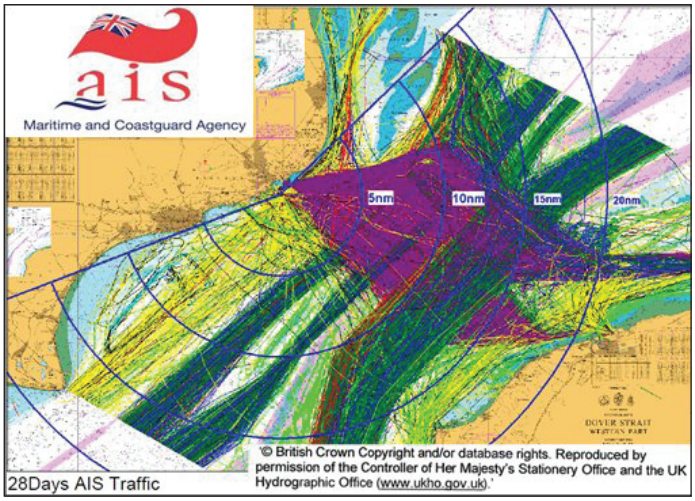

Figure 10 28 days' worth of historic AIS data for Dover.

The ASF survey took place during the week of 19th March 2012 aboard the Trinity House Vessel 'Alert'; Figure 11

Figure 11 Trinity House Vessel 'Alert' was used for the ASF survey of Port of Dover approach.

9 PORT OF DOVER ASF SURVEY

Planning the ASF survey started with a traffic analysis. Referring again to Figure 10, this is 28 days worth of historic AIS data in the Dover Strait, and the major traffic concentration areas can clearly be seen.

The next step is to prioritise the regions within that zone and estimate how much ship time will be required to perform the survey; Figure 12. For this early implementation interest was limited to the ferries travelling within this purple region, and the cargo and tankers travelling up and down the main parts of the channel. So the ferry routes, the harbour approach and the northern part of the traffic separation scheme (TSS) would be covered for IOC.

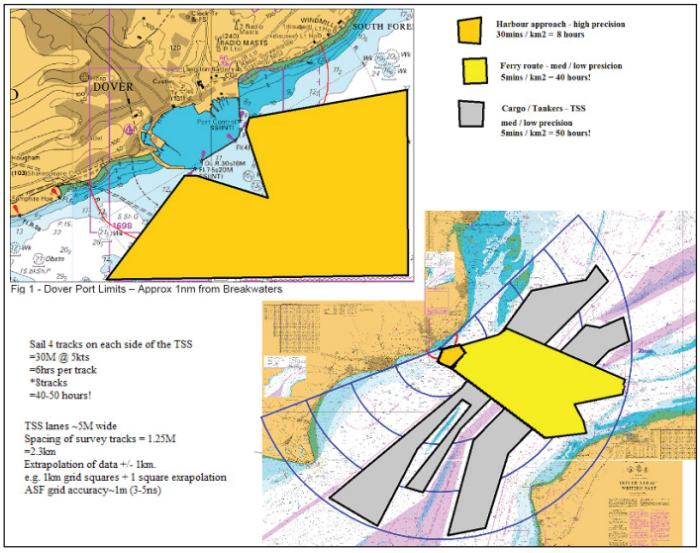

Figure 12 Prioritising areas and calculating ship time.

The next thing is to work out where to sail the survey ship. In order to make efficient use of ship time it is possible use knowledge of the physics of Low Frequency radio propagation and the expected spatial variations of the ASFs. So, for example, it was realized that the vessel could sail around the outer limits of the coverage area measuring raw data; see Figure 13. The middle of the area can be "filled in" by interpolating the measured data. This is possible in the region of the Dover Strait because the land surrounding the area and along the propagation paths from the Loran transmitters is relatively flat and smooth and, therefore it is likely the ASF values also vary smoothly.

It is possible to obtain land-path data using an electronic coastline database. The amount of land along the propagation paths from the transmitters to the prospective locations of the ASF measurement system can be used to gain an estimate of the amount of surveying required. For example, in an area where the ASF value is expected to be flat over a wide region, the vessel perhaps only needs to visit one point within that area. On the other hand in a region of complex coastline variations like the west coast of Scotland or Norway, the spatial ASF variation is expected to be much greater and so more concentrated ASF surveying would be required. As the GLA moves towards Fully Operational Capability, effort will be put into resurrecting ASF computer modelling work [X], as the need for efficiency would become greater when implementing over a much larger area.

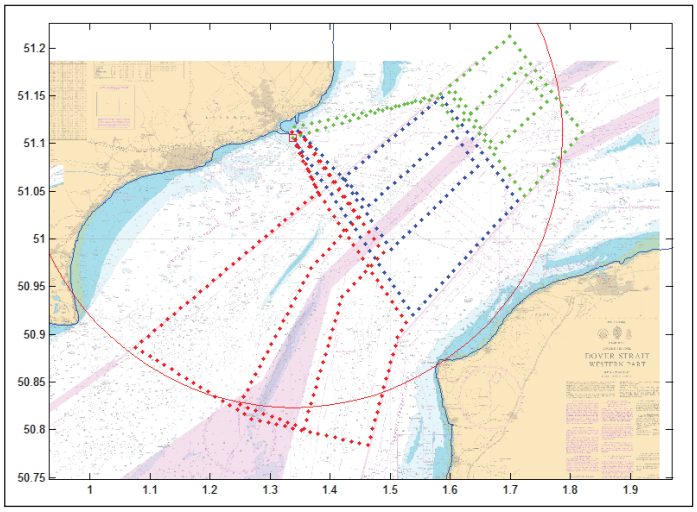

Figure 13 Proposed sailing routes for Port of Dover Approach ASF Survey.

Figure 14 shows the full set of ASF data the GLA collected for Anthorn. The ASF value varies from about 1.6μs in the north, to about 2.3μs in the southern part of this section of the Dover Strait. If ASFs were not used for Anthorn in this region, the mariner would experience a position error of about half a nautical mile or so.

ASF data is available for all of the transmitters likely to be used in the area; Anthorn, Lessay, Sylt and Soustons (see Figure 5).

The ASFs for Lessay, for example, are shown in Figure 15. They exhibit lower values than Anthorn because there is less land in the propagation paths from the transmitter at Lessay to Dover than there is for the paths from Anthorn to the area (of course the "type" of land also affects the ASF value, manifested by its electrical ground conductivity).

As a last example, Sylt's ASFs are shown in Figure 16.

Of course this is raw measured data. It was mentioned earlier that interpolation is employed to fill in the gaps within the ASF measurement tracks. Those tracks were designed to make the best use of ship time, taking into account the expected variations in the data and the knowledge that interpolation is possible.

The data therefore needs to be processed before it can be published and disseminated for use within eLoran receivers.

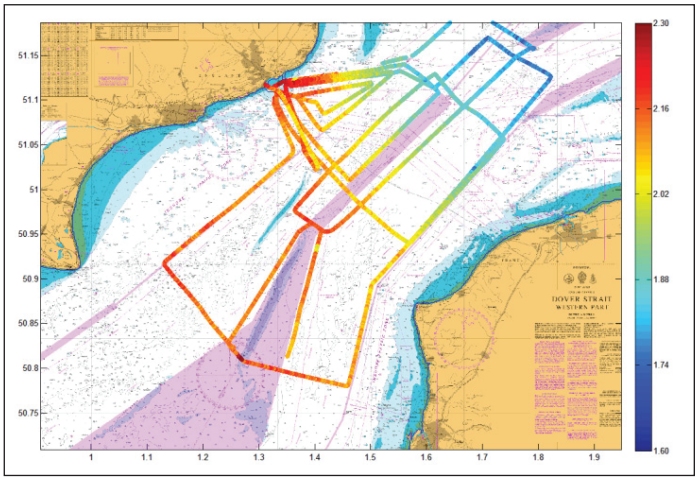

Figure 14 Raw measured ASF data for Anthorn.

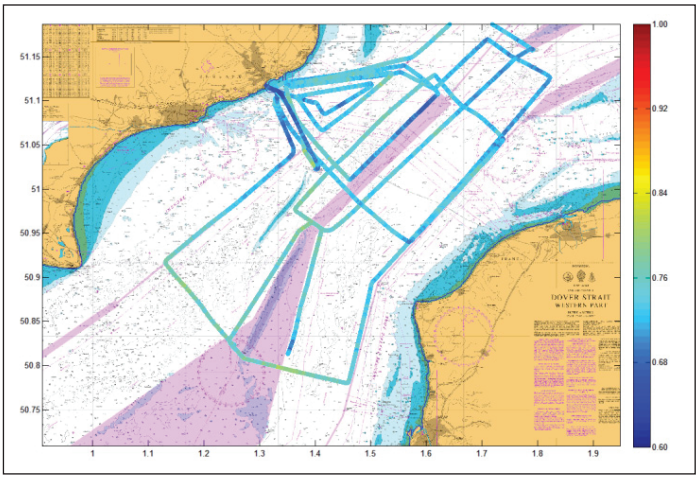

Figure 15 Raw measured ASF data for Lessay.

Figure 16 shows the results of applying interpolation and extrapolation, to the raw measured ASF data of Anthorn shown in Figure 14. This produced a convenient uniform grid of data.

The interpolation and extrapolation method used is not a simple linear interpolation, however, as that would likely result in inaccurate data. An interpolation method is required that takes into account the physics of Low Frequency radio signal propagation and the statistics of the measured data.

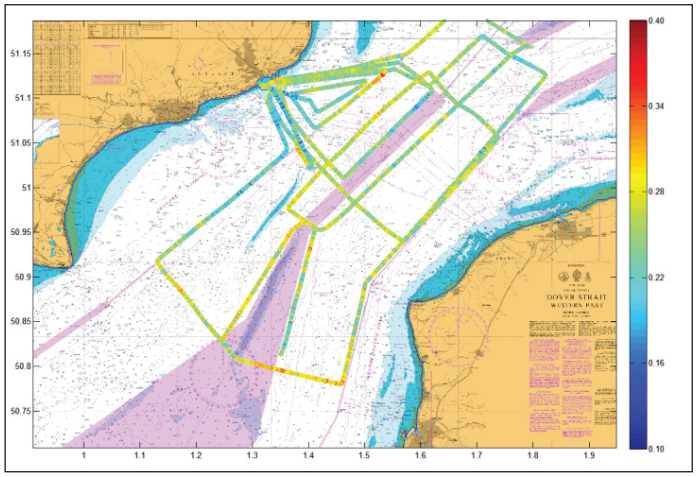

Figure 16 Raw measured ASF data for Lessay.

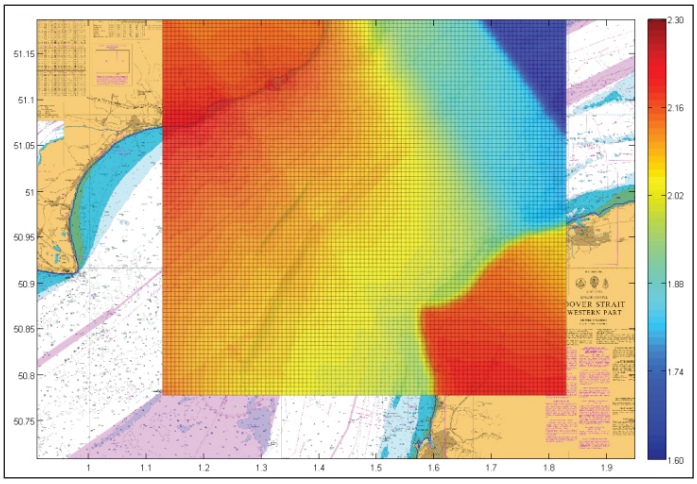

Figure 17 Anthorn ASF map or grid.

Several forms of interpolation were investigated, but the GLA settled on the so called "radial filter method" as providing the best accuracy performance (at least in this particular region). The method employs a "radial" filter, an example of which is shown in Figure 18. This filter is convolved with the raw measured data along a radial direction from the transmitter across the ASF measurement area.

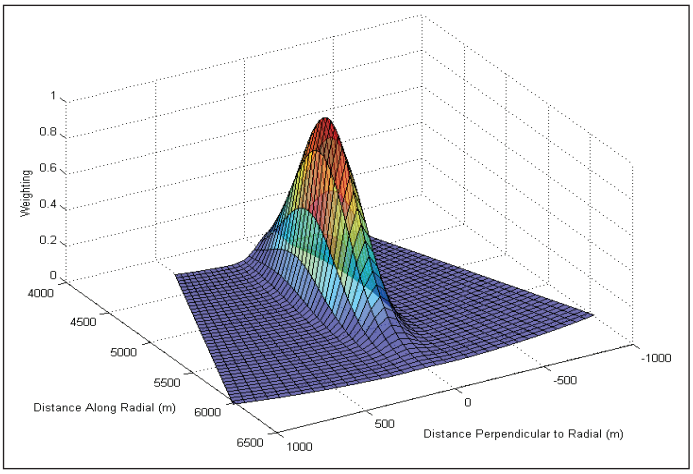

Figure 18 A radial filter is convolved with the raw measured data resulting in interpolated and extrapolated data.

Figure 19 Outer region of measured ASF data within which we expect to see 10 m positioning accuracy.

The filter has the effect of weighting strongly the ASF data that appears along a radial propagation path from the transmitter and less strongly the data appearing on parallel radial paths. This interpolation works very well and we would expect positioning accuracy on the order of 10m within the yellow region shown in Figure 19.

Extrapolation of data occurs outside the measurement tracks (yellow polygon), but it should be borne in mind that extrapolation is inherently more error prone than interpolation because there is less information available to 'bound' the resulting values. However, even extrapolated ASF data can provide better positioning accuracy than no ASF data at all, at least up to certain limits!

Despite the issues with extrapolated data it is still desirable to publish any two-dimensional data set in a friendly, uniform format rather than an odd polygonal shape such as that shown in Figure 19. It is much better to publish uniform, rectangular grids of data.

It is possible however to satisfy both the seemingly contradictory requirements of extrapolated data and uniform grids. The service provider is encouraged to advise the mariner about the ASF measurement error associated with each region of the grid. For example, anywhere within the yellow polygon of Figure 19 we expect a certain amount of measurement error. Anywhere outside the polygon, but still within the rectangular ASF grid we can reasonably expect that measurement error to be higher; but not as high as that error which would be observed outside the rectangular ASF grid.

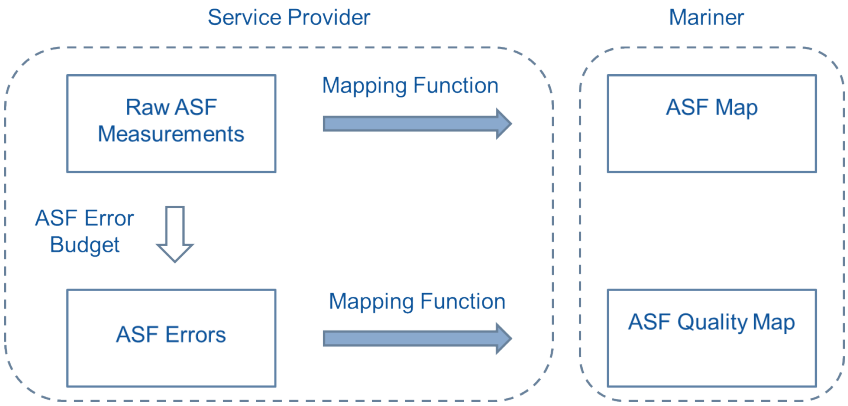

Figure 20 The principle of an "ASF Quality Map".

The GLA propose therefore that as well as an ASF map, an "ASF Quality Map" should also be published; see Figure 20. It is published at the same time, and in

exactly the same format, as the ASF data, and it contains an error estimate on the ASF measurement at each grid location. So receiver manufacturers would need to provide twice the small amount of memory required for each ASF map.

The ASF Quality Map can be employed as a component of an integrity equation implemented within the mariner's receiver. The aim of an integrity equation is to take into account the error budget for positioning and provide the mariner with an alarm (or several levels of alarm) should a computed Horizontal Protection Level (HPL) breach a preset Horizontal Alert Limit (HAL).

10 ACCURACY PERFORMANCE VALIDATION

Once the ASFs had been measured and the prototype reference station installed the performance needed to be tested. This was accomplished through a validation run of the vessel through the area.

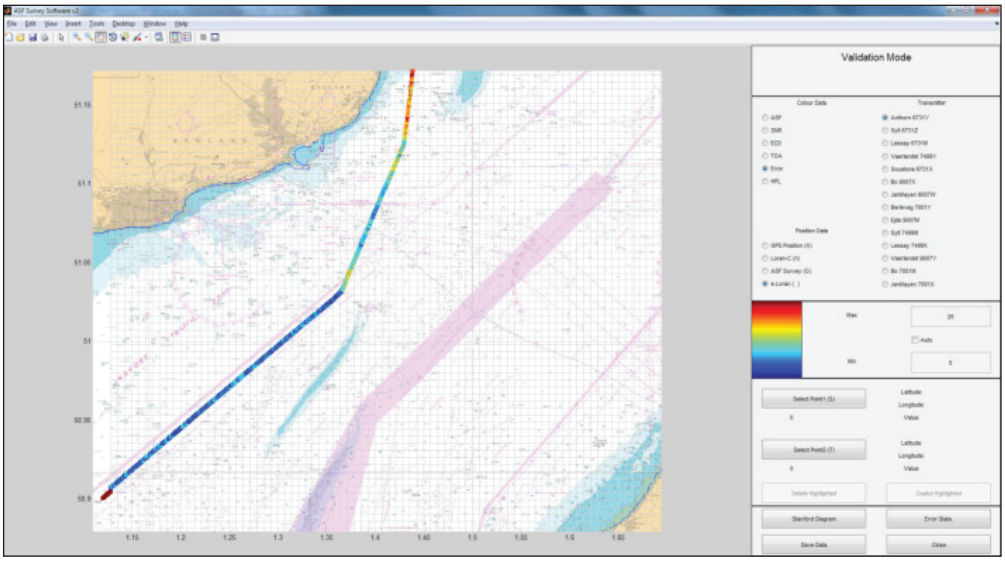

Figure 21 Screenshot of GLA ASF Measurement software running in validation mode.

Figure 21 shows a screenshot of the GLA ASF Measurement software running in validation mode. The coloured track shows the path of the vessel, with the colour indicating the positioning error compared to differential-GPS. The vessel travels through an area of **extrapolated** and **interpolated** ASF data, so the positioning error at the northern end of the track is higher than the lower end of the track.

Figure 22 shows a comparison of eLoran positioning against DGPS positioning along the route as a scatter plot. The associated Cumulative Distribution Function (CDF) is shown on the right of the diagram. From this it can be seen that the positioning accuracy obtained along this particular route was 12.5 m (95%).

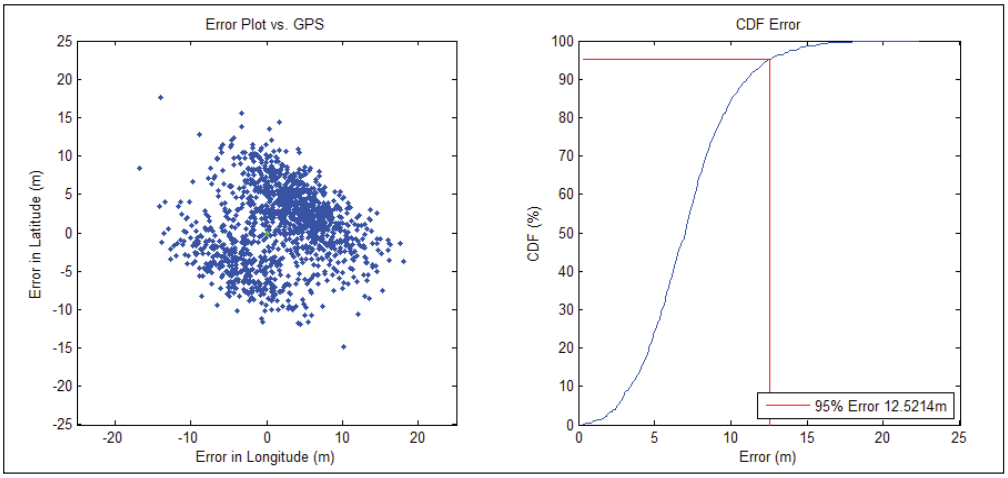

Figure 22 eLoran positioning accuracy scatter plot and Cumulative Distribution Function of positioning error. Accuracy: 12.5 m (95%)

11 DOVER TO CALAIS FERRY INSTALLATION

Further validation and demonstrations will take place aboard a cross Channel ferry. The GLA has made an agreement with P&O Ferries in the UK to install a receiver aboard their £157M vessel, "The Spirit of Britain". This relatively new vessel is one of the largest passenger ships to operate along the iconic Dover to Calais route. Data will be collected data and feedback obtained on the eLoran service's performance over the coming months.

12 OTHER AREAS

The GLA continue their work towards IOC level eLoran. Dover is the first port of call for the GLA' eLoran Initial Operational Capability – the ASFs have been mapped and a prototype differential-Loran reference station has been installed. The final operational DLoran reference stations should be available this time next year.

The next area the GLA has concentrated upon is the Thames Estuary up to Tilbury. Although the GLA has not yet installed a permanent DLoran reference station, the ASF survey was performed in November 2012 using a temporary reference station installed at Medway in the River Thames estuary. Along the route shown in Figure 23, a validation trial demonstrated 8.3 m (95%) accuracy; Figure 24.

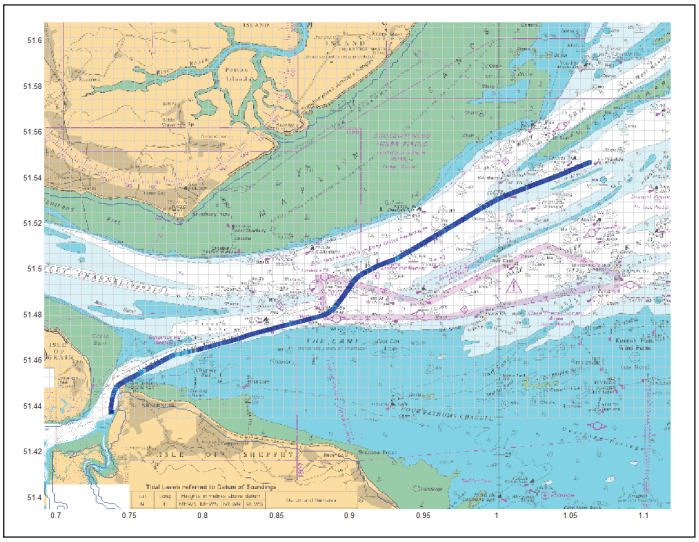

Figure 23 ASF map validation route from the port of Medway heading out of the River Thames estuary.

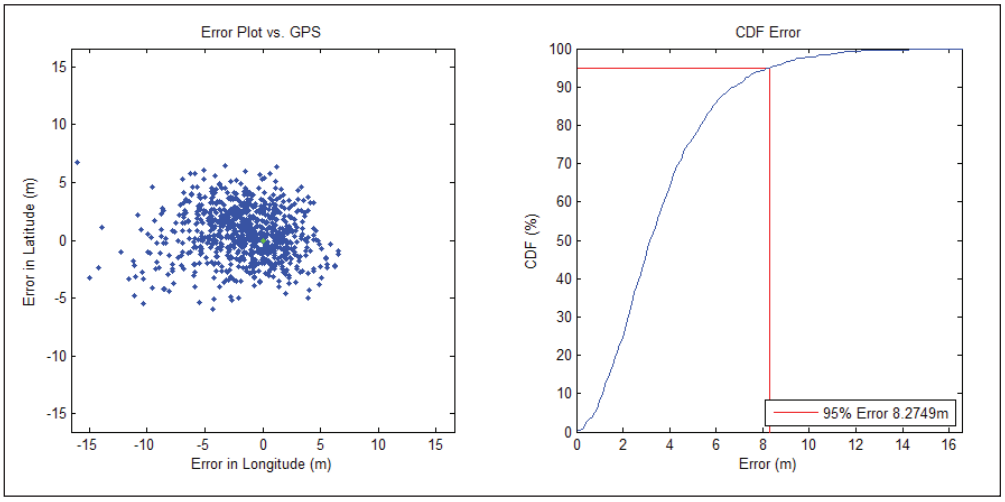

Figure 24 eLoran positioning accuracy scatter plot and Cumulative Distribution Function of positioning error. Accuracy: 8.3 m (95%).

The Humber Estuary and its approaches has also been surveyed. The ASF survey was performed in February 2013 using a temporary reference station installed at a coastal radar tower at Stone Creek on the shores of the River Humber opposite to the port of Immingham. Along the route shown in Figure 25, a validation trial demonstrated 7.9 m (95%) accuracy; Figure 26.

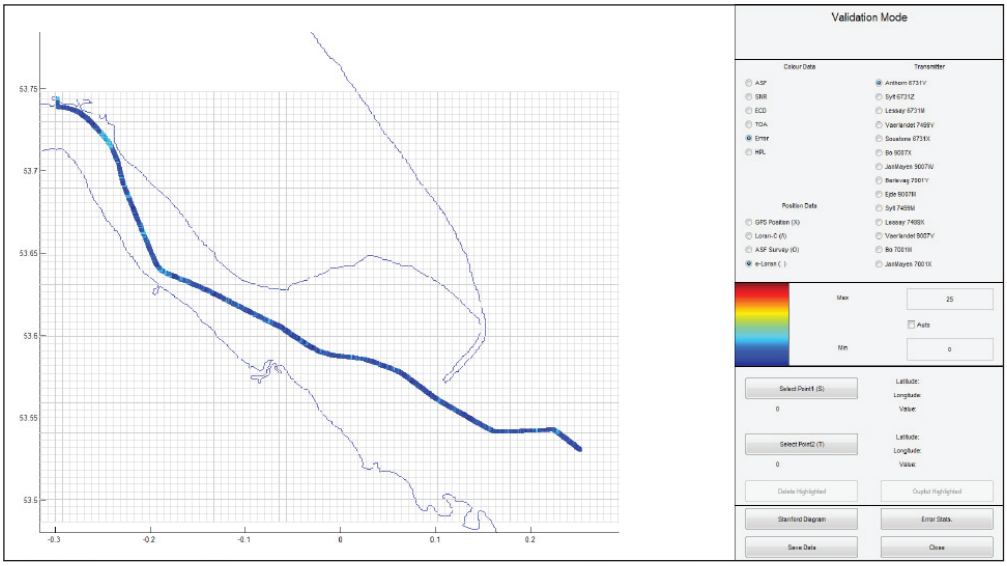

Figure 25 ASF map validation route from the port of Hull heading out of the Humber Estuary.

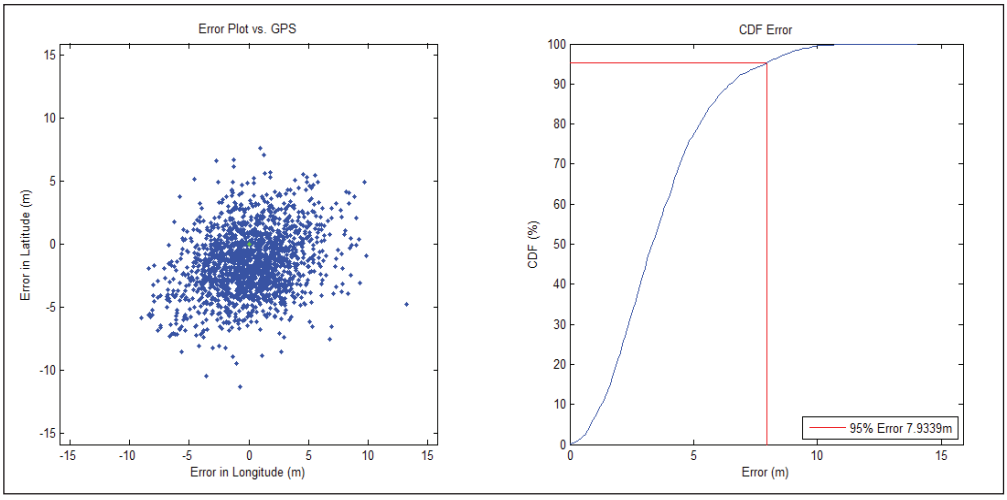

Figure 26 eLoran positioning accuracy scatter plot and Cumulative Distribution Function of positioning error. Accuracy: 7.9 m (95%).

13 CROSS SECTOR ELORAN AND E-NAVIGATION

eLoran has the potential to be a critical international asset benefiting more than just the maritime sector. There is also a desire to share the costs of running the service between the maritime sector and other potential user groups. That is why the GLA are interested in promoting the cross sector use of eLoran. The transmitter at Anthorn can already provide 50ns timing and Stratum 1 frequency, and it has not yet been fully upgraded to a final eLoran specification! So the GLA have been involved in projects like GAARDIAN and SENTINEL looking at GNSS and eLoran service quality for such applications as timing and GNSS interference detection on land.

The GLA have opened up the Loran Data Channel to interested third parties. One client is using the transmitter at Anthorn to transmit secure, scheduled messages over the Loran Data Channel. So the signal is not purely being used for PNT, **P**osition, **N**avigation and **T**iming), but also for D – **D**ata.

The GLA are leading a consortium of several interested partners who are interested in developing an eLoran land mobile demonstrator – using eLoran for land vehicle tracking.

Finally, returning to the maritime sector, the GLA are the lead partners in the European, INTERREG funded ACCSEAS project, which is looking at establishing an e-navigation test-bed in the North Sea Region. Resilient PNT will form a vital support component of future enavigation services in the North Sea and beyond.

14 STATUS SUMMARY AND NEXT STEPS

For the GLA and the UK, however, the next steps are to continue the implementation of IOC eLoran at the remaining port approaches. It is the aim that all ASF surveys will have been performed by the middle of 2014 in readiness for the installation of the operational differential-Loran reference stations at each candidate port. Licence agreements are being established with the various port authorities involved in order to allow this.

All ports that have been approached are positive and are keen to assist the GLA in their eLoran implementations. Locations for all DLoran reference stations have been found.

The Port of Dover has prototype eLoran up and running and so far has demonstrated 12.5m (95%) accuracy during the limited validation performed so far, however further validation continues aboard the ‘Spirit of Britain’ ferry.

An ASF survey has been performed along the River Thames to Tilbury and its approaches and 8.3m (95%) accuracy has been demonstrated in the area. The River Humber and approaches to Hull have also been surveyed with validation demonstrating 7.9m (95%) there.

IOC level DLoran reference stations should be available mid-2014 ready for installation.

The methods and processes employed during the progress of this work will be proposed for inclusion within the next version of the eLoran receiver Minimum Performance Specification as determined by Radio technical Commission for Maritime Services (RTCM) Special Committee (SC) – 127. These include the techniques and algorithms used for ASF measurement processing, the preferred ASF file format, and guidelines on the usage of ASF data.

The GLA continue to explore cross-sector applications of eLoran to derive potential funding streams and are exploring the wider international implementation of eLoran demonstration services with our European partners.

ACKNOWLEDGMENTS

The GLA acknowledge the assistance of the crew of 'THV Alert', the Dover Harbour Board, Peel Ports (Medway), Associated British Ports (Humber), Aberdeen Harbour Authority, Forth Ports, PD Ports (Middlesbrough).

REFERENCES

[1] *Report of the Maritime Safety Committee on its 85th Session*, MSC 85/26/Add.1, 6 January 2009.

[2] Last D., Grant A., Ward N. *Demonstrating the Effects of GPS Jamming on Marine Navigation*. 3rd GNSS Vulnerabilities and Solutions Conference, 5-8 September 2010, Baška, Krk Island, Croatia.

[3] *Vulnerability Assessment of the Transportation Infrastructure Relying on the Global Positioning System*, John A. Volpe National Transportation Systems Center, Prepared for the Office of the Assistant Secretary for Transportation Policy, U.S. Department of Transportation, 29 August 2001.

[4] *Synchronisation of Lights*, IALA Guideline No. 1069, May 2009.

[5] *Business Case informing eLoran decision: Driving down the cost of GLA Aids-to-Navigation provision by delivering resilient Position, Navigation and Timing (PNT) within the context of e-Navigation*, The General Lighthouse Authorities of the United Kingdom and Ireland, September 2010.

[6] *The Green Book – Appraisal and Evaluation in Central Government,* HM Treasury, 2013.

[7] *International Telecommunications Union, Technical Characteristics Of Methods Of Data Transmission And Interference Protection For Radionavigation Services In The Frequency Bands Between 70 And 130 kHz*, ITU Recommendation 589-3.

[8] *Minimum Operational Performance Standards for eLoran Receiving Equipment*, RTCM SC-127, V2.0 Draft, 2013.

Faculty of Maritime Studies
University of Rijeka, Croatia

Royal Institute of Navigation
Science Technology Practice

7th GNSS
Vulnerabilities and Solutions Conference

GPS/GNSS BACKUP WITH AUTOMATIC RADAR POSITIONING

Helmut H. Lanziner, Harvey Russell

Russell Technologies Inc.
North Vancouver, BC Canada
E-mail: hlanziner@russelltechnologies.ca

ABSTRACT. *Position fixing is one of the eight identified key elements of e-navigation. The primary aim is to provide position, velocity, and time data (PVT) for navigators and navigational systems (ECDIS, Track Control Systems, AIS, and INS). While Global Navigation Satellite Systems (GNSS) will play a significant role, there are increasing concerns about relying solely on a satellite-based PVT. In this regard there is a need for resilient positioning in terms of reliability, accuracy, and integrity during critical phases of navigation. The provision of resilient PNT data relies on the exploitation of existing, modernized and future radio navigation systems, sensors and services.*

This concern was again expressed in a recent IALA (International Association of Marine Aids to Navigation and Lighthouse Authorities) bulletin relating to ACCSEAS (Accessibility for Shipping, Efficiency Advantages and Sustainability) in the context of E-Navigation.

"Susceptibility of GNSS to interference, demands that backup systems are put in place to provide resilience for seamless positioning during GNSS outages. Under interference conditions, GNSS can provide hazardously misleading information – errors in position that may go un-noticed by the mariner but that are large enough to compromise safety of navigation and with no alarm raised. The need for independent, dissimilar backup systems is recognised by the IMO (International Maritime Organization) architectural framework for e-Navigation."

This paper describes a precise radar positioning system that was originally developed for stand-alone operation in confined waters, but has evolved to become an interface to existing shipboard radars. Advanced software continuously computes range and bearing to known objects and derives a fix from their geometry. In addition, accurate heading information is achieved

that is not affected by gyrocompass lag or magnetic anomalies. Positioning accuracy of 2–5m (95%) can be achieved with more reliability than GPS during severe weather and electro-magnetic interference conditions. As a totally independent, low-cost, robust backup to GPS/GNSS, the system requires no additional navigation equipment or infrastructure external to the vessel.

1 INTRODUCTION

The implementation of GPS/GNSS has had a significant impact on precise positioning for maritime navigation. Highly accurate and reliable positioning is provided at a low cost to users throughout the world. Although GPS by itself may not always deliver the required performance, the application of differential corrections through DGPS or regional SBAS (Space-Based Augmentation Systems) brings this to horizontal position accuracies of better than 2m in major areas around the world. This is particularly important for ships navigating in harbor approaches and river/inland waterways, and during critical maneuvering and docking. It is the continuous availability of this kind of accuracy that enables the mariner to enter situations requiring a high degree of reliability.

While the use of and reliance upon GPS/GNSS has increased, so has the potential for disastrous consequences in the case of intentional or unintentional service interruption. Concerns about the vulnerability of a GPS-based transportation infrastructure have prompted a number of studies and conferences in recent years, together with recommendations for independent backup systems, including terrestrial options.

This paper briefly reviews these developments and describes a previously developed and tested – but little known -precise radar positioning system. With the awareness of similar developments underway in northern Europe, Russell Technologies Inc., together with the University of British Columbia and the original developers, is in the process of updating and porting this advanced pioneering technology to current hardware and software.

2 GPS/GNSS VULNERABILITY

As the majority of users rely increasingly on GPS/GNSS, the impact of an unintentional or intentional interruption of the service is becoming more apparent. This fact was emphasized in a report published as early as 2001 by the John A. Volpe National Transportation Systems Center, entitled: "*Vulnerability Assessment of the Transportation Infrastructure Relying on the Global Positioning System*." [1]

The Volpe Report was written in response to a directive (Executive Order 13010, 15 July 1996) from *The President's Commission on Critical Infrastructure Protection* (PCCIP), – a top level White House technical advisory group. US DOT and DOD were directed to undertake a thorough evaluation of the vulnerability of the national transportation infrastructure that relies on GPS, and to assess the risks resulting from the degradation or loss of the GPS signal. The findings of the study reported that unintentional or intentional GPS disruption could be reduced but not eliminated. GPS cannot serve as a sole source for position location for certain critical applications. Further, backups for positioning and precision timing are necessary for all GPS applications involving the potential for life-threatening situations or major economic or environmental impacts. The report also mentions that some of the backup options include a combination of: (1) terrestrial or space-based navigation; (2) on-board vehicle/vessel systems; and (3) operating procedures.

In addition to the concerns expressed in the Volpe Report, there have been many other warnings, meetings and reports about the issue of backup. Although GPS is a 24-hour a day system with world-wide coverage, its operational low power is easily disrupted. A presentation at the U.S. Coast Guard Navigation Center (NAVCEN) stated: "Jamming techniques are well known" and that "Many jammer models exist" and that "appropriate backup systems or procedures should be maintained."[2] It was further stated that "GPS will become an increasingly tempting target as its civil uses proliferate." Further, regarding Vulnerability Mitigation, one "must insure alternate sources of positioning information" are available. [3] **The U.S. *President's Commission on Critical Infrastructure Protection* described GPS navigation as the greatest single risk to America in the modern electronic era.** [4]

3 RADAR AS A BACKUP TO GPS

There are some who believed that there is no realistic backup for GPS other than inertial navigation or Loran-C, or a combination of the two. However, prior to GPS, there were a number of international efforts focused on coming up with a practical and economic solution for precise, highly-reliable, land-based positioning. In order to reduce the complexity and cost of these types of installations, a small company undertook development work on a system called *RadarFix.* The plan was to adapt standard marine radar to become a highly-accurate automatic positioning system by accurately determining range and bearing, and determining position by solving for geometry. With the integration of a personal computer and software to standard marine radar, *RadarFix* could extract measurements

from existing radar targets of different shapes in a sophisticated manner to yield accurate range and bearing information. Effectively, it can subject the geometric shape resulting from the combination of measured targets to a pattern-matching process with a previously established database. Detailed parameters about the size and shape of these targets are entered into this database, together with precisely surveyed coordinates. This allows the radar to work not only with isolated point sources, but to use information from larger structures, such as faces and corners of buildings, edges of docks, and line-ends evident on jetties. The resulting position accuracies are 2–5m (95%).

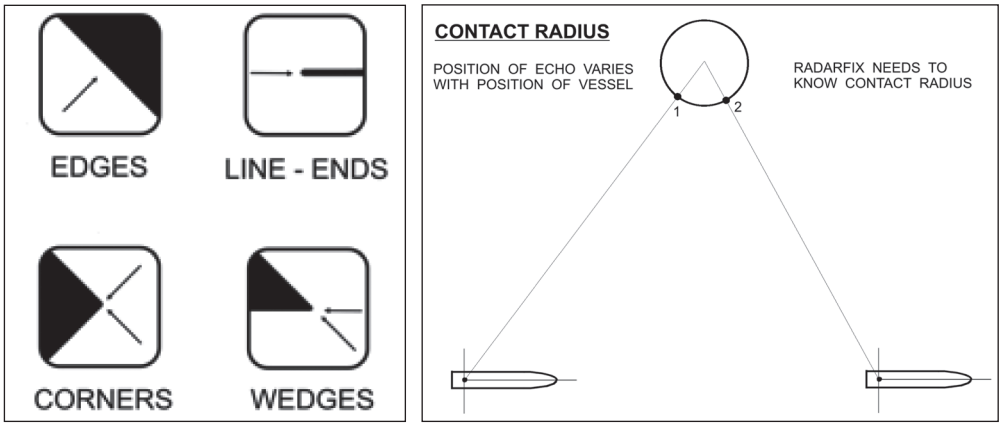

Figure 1

Although the system could analyze a number of radar images, it was clearly limited by the nature and complexity of the targets that the image was based on. When the radar target consisted of an isolated point source, such as a fixed light surrounded by water, it required little processing time, and measurements needed little refinement.

When the operating area consisted of a number of such targets, *RadarFix* quickly acquired those targets and "locked on" to provide reliable positioning information. In operating areas where targets were mostly complex, measurements took longer, resulting in a minor loss of position accuracy and reliability. In some cases, if it was a low-lying, open area, there were few targets to choose from. However, unless it was operating in open water, away from land, the system always found some targets to work with.

At the time, database creation required careful description and surveying of the radar targets to be used. Since most of the surveying was done with conventional

means (e.g., using optical instrumentation), there was a practical limit in the number of targets that could be surveyed. Tests and trials would then determine which targets were most suitable for positioning with respect to background clutter and proximity to other radar targets. This was not always a simple matter when faced with limited processing power, since attempts to differentiate an intended target from adjacent background clutter can take up a significant amount of the allotted processing time.

Figure 2 This RadarFix integrity monitoring display shows range/bearing residuals to three targets

Generally, the governing rule with *RadarFix* is that, as the number of measurements increases, the system becomes more accurate and more reliable. However, this could occasionally push the older processors to their limits. As part of the user interface, *RadarFix* continuously evaluates the reliability of its performance and displays a quality index.

RADARFIX R&D

At the same time that *RadarFix* was under development, a company in Vancouver, Canada was also looking at the possibility of using radar for positioning with electronic charting systems. It was interested in implementing radar image overlay onto an electronic chart display, as well as using the acquired radar data for positioning purposes. Recognizing that target-to-clutter discrimination was one of the major problems, they concentrated on the

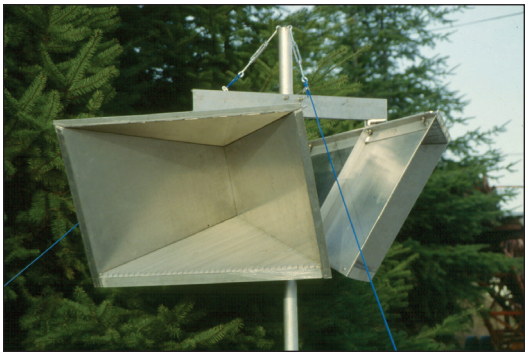

Figure 3 Modified reflector, as used at the time with RadarFix

development of a clutter suppression concept in conjunction with a new, inexpensive, passive reflector design.

Shaped differently than the conventional trihedral, these uniquely modified reflectors not only offer a greater radar cross-section overall, they also provide a wider response (beam width) horizontally, and a narrower response in the vertical.

It was decided to combine the two technologies and team up on some future projects. The compromise of using reflectors versus existing radar targets in difficult operating areas was made mainly to save surveying time during set up. Trihedral reflectors are a known quantity and they always respond as a point source. Alternatively, existing structures may not always perform as anticipated, which necessitates the survey of a larger number of existing potential targets than that required with the use of reflectors. The necessity of having to conduct conventional optical surveys in the pre-GPS days often limited the number of existing potential targets chosen for a given area.

PORT AUX BASQUES INSTALLATION

Although some *RadarFix* installations already existed, the first combined operational trials were conducted on the East Coast of Canada in 1989. Requirements called for a fully automated startup/operation where a single push of a button by the user was required to operate the system. With a combination of reflectors and existing targets at the northern terminus of Port aux Basques, Newfoundland, the system was installed on the 150 meter (492 ft) ferry *MV Atlantic Freighter*, operating between Newfoundland and Nova Scotia. Port aux Basques is notorious for its hazardous approach, high winds, snowstorms, and generally harsh environment.

Figure 4 MV *Joseph and Clara Smallwood* installation shows radar used with RadarFix (second from top of mast).

Following successful trials aboard *MV Atlantic Freighter*, systems were installed onboard two of North America's largest ferries, the *MV Caribou* and the *MV Joseph and Clara Smallwood.* Both of these vessels have a registered tonnage of 27,212 GRT and an overall length of 179 m (587 ft). Although *RadarFix* was employed during the entire voyage in all weather conditions, it was particularly relied upon during the harbor approach and docking (berthing) phases in periods of re-

stricted visibility. While outside of radar range, *RadarFix* was running mainly on Loran-C and other integrated sensors. Although Loran-C by itself will generally not provide an accurate position, *R*adar*Fix* opens up its "search windows" relative to predefined targets, in order to ensure target detection. During the approach, as soon as own-ship reaches a position that is within sight of selected targets or reflectors, *RadarFix* begins "locking on". Once the system has acquired most of its selected targets and reflectors, its integrity monitoring display indicates that it is performing with a high level of accuracy.

One of the more interesting aspects of *RadarFix* is that, while locked on, it is capable of providing much more accurate heading information than that available from the ship's gyrocompass. During the approach to the Port aux Basques dock, ferries rapidly reduce speed - from 18 knots to a halt, followed by a 180 degree turn before they back into the dock. This kind of maneuver causes significant gyrocompass errors, sometimes exceeding three to four degrees. The resulting own-ship presentation on the electronic chart shows the stern or the bow several meters up on the dock, since the display of own-ship is usually based on the input from the gyrocompass. *RadarFix* heading information is not affected by such maneuvers because it gets its orientation from the relationship to the shore-based network of targets/reflectors. Changing the heading input on the electronic charting system from the ship's gyrocompass to that of *RadarFix*, resulted in a correct orientation display of own-ship in relationship to the dock.

Another significant aspect of *RadarFix* is its ability to work in reverse. That is, it can determine or establish an accurate position for any additional new target once it is locked onto a network. For example, during the installation and after some trials at Port aux Basques, it was decided to add one more reflector at an isolated area on a hill. After the reflector installation, a surveyor was hired to determine the exact position. In order to find the reflector, he was given the coordinates established by *RadarFix* from own-ship sitting stationary at the dock. Upon completion of the survey, it turned out that the position determined by *RadarFix* only differed by 2.4 m in latitude and 1.85 m in longitude from that of the survey. This capability makes it possible to keep adding more targets once the system is up and running, while it was a major operation previously.

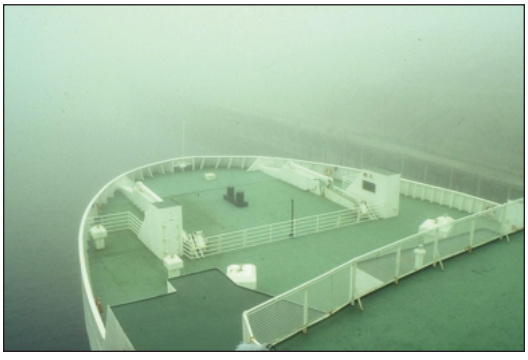

Figure 5 MV *Caribou* docking (berthing) with the use of RadarFix in heavy fog at Port aux Basques

Figure 6 Canadian Coast Guard survey vessel

CANADIAN COAST GUARD TRIALS

After several months of successful ferry operations in Port aux Basques, Newfoundland, the Canadian Coast Guard – Québec Region- expressed an interest in testing and evaluating *RadarFix*. Their test objectives included:

1.Evaluating the system in an operational environment

2. Comparing the accuracy of *RadarFix* and *Miniranger*[1] RPS (microwave positioning system)
3. Evaluating the system's operational and technical potential, including implementation and maintenance cost.

The Canadian Coast Guard – Québec Region, has its own surveying capability and extensive experience using precise positioning techniques. The *Miniranger* microwave positioning system had been in use for a number of years in this region in support of Coast Guard operations in confined waters. In particular, it was used onboard icebreakers (for river ice control and system management), buoy tenders, and sounding/dredging vessels. They also have access to external resources with extensive geodesic expertise from either private sector or university consultants.

Trials were conducted in the fall of 1991, with a final report publication in April 1992 [5].

A key aspect of the trials was to evaluate the dynamic positioning capability of *RadarFix*. However, to do so was not a trivial process. The positioning of a moving object on an open space of water, with the use of conventional survey equipment – even at low speeds – is challenging. For the *RadarFix* trials, two test areas were implemented along the St.-Lawrence River: The first one was on "Lac St.-Pierre," a 40 km long stretch of the river, which is wide and shallow, located between Montreal and Trois-Rivières. The second area is close to Québec City, where it extends beyond both Québec bridges that cross the river. Overall, twenty (20) reference sites were installed with modified trihedral reflectors. To complete the precision measurements, optical survey equipment was installed at four

[1] Motorola

shore-based survey stations[2]. Four survey teams established themselves at these stations on both sides of the riverbank, where they took simultaneous position fixes to a prism located on the test vessel at regular intervals, ranging from 30 to 45 seconds. Each one of these four readings was then subjected to geodetic corrections and a statistical analysis to define the value standard of these measurements. Finally, they were compared to *RadarFix* derived positions.

Figure 7 Canadian Coast Guard icebreaker, Québec City

As described in the Coast Guard report (translated from French):

> "In static mode, the system precision is about 1 m. The lack of data on static values does not allow a fine determination of its accuracy, but we can confirm with a sample of these results that the system precision will be kept below 5 m with 95% confidence without any difficulty under normal operational conditions, which would be representative of the buoy tending operational requirements."

RADARFIX DEVELOPMENT

There are some major differences in the functionality and performance of previous versions of *RadarFix* compared with the possibilities of today.

Target Selection

- One of the most time-consuming and complex aspects previously was setting up a *RadarFix* network. This included surveying the reflector/target sites and providing a detailed description of potential targets. Establishing survey control was costly, which normally resulted in the use of fewer targets than necessary for optimum results.
- With GPS/GNSS and accurate heading information, this is no longer the case. As an integrated input to *RadarFix*, these sensors provide a constant position and bearing reference for the acquisition of any number of targets. While target position determination used to be a one-time opportunity (i.e.,

[2] WILD Series 2000, Model DI-20

all measurements were made during the setup), it is now an ongoing process. The system can continuously check, verify, update and refine target positions. It will allow the addition of new targets on an ongoing basis, as well as further refinement of target shapes and positions through many hundred, or even thousands of radar observations from different perspectives, with the benefit of a continuous accurate position and heading reference of own-ship.

Computer Power

- Older personal computer processors could only process a limited number of targets.
- Today's computers have much greater processing power and memory at little additional cost. The number of targets that *RadarFix* can now process simultaneously has increased by orders of magnitude. Increasing targets enhances position accuracy and reliability.

Use of Existing Targets

- Many of the original *RadarFix* installations had specially designed radar reflectors to discriminate against a background clutter.
- Experiments and trials in some operational areas revealed that by utilizing the number of existing targets, it is possible to achieve the same level of accuracy and reliability as that accomplished using built-for-purpose reflectors. The result is that special reflectors are not always necessary and that the standard marine radar, as installed on the vessel, will deliver reliable positioning performance with *RadarFix*.

RADARFIX AS A BACKUP TO GPS/GNSS

The main weakness of GPS is in the low energy of its signals. There are a number of reported incidences of inadvertent GPS jamming. However, GPS/GNSS is also vulnerable to purposeful jamming or degradation. It is relatively easy and inexpensive to build a transmitter powerful enough to bury the GPS signals in noise and many jamming devices are now readily available on the Internet. Because radar uses wavelengths short enough to be directive, they are relatively immune to corruption. It is much more unlikely to find a noise generator powerful enough to inject a harmful signal into a rotating radar antenna.

RadarFix can serve as a totally independent, low-cost, and robust backup to GPS/GNSS, without the need for any additional navigation equipment or infrastructure external to own-ship. There are a number of reasons.

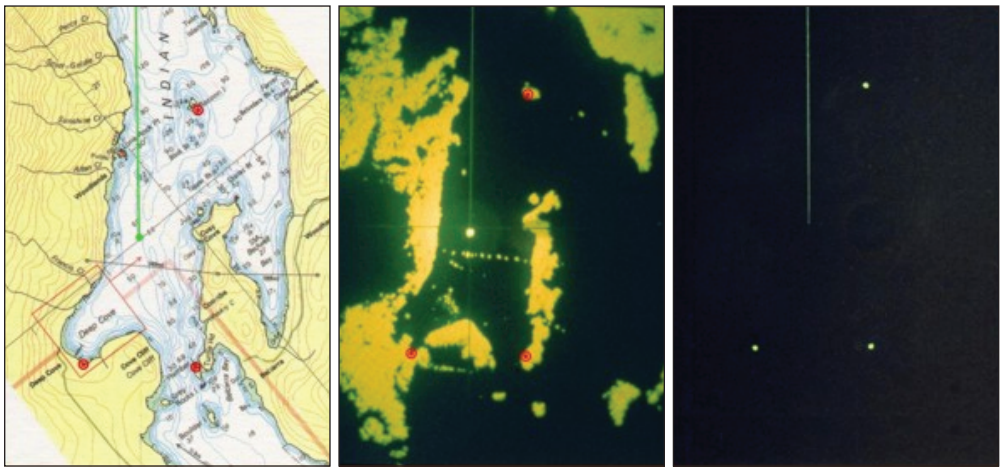

Figure 8 Red circles mark radar target positions on the radar display, which shows them completely buried in the radar shore clutter (centre). Radarfix quickly thresholds these targets (right side).

Radar signals are difficult to jam. What makes *RadarFix* particularly well-suited as a backup is the wavelength it operates at – that of the ship's radar -- is much more difficult to compromise than GPS/GNSS.

Shipboard radar systems are independent from, and work in a totally different way to, that of GPS or GNSS -- or any other satellite navigation system. Any intentional or unintentional service interruption to GPS will likely not affect *RadarFix* or other shipboard radar operations.

Since *RadarFix* works with existing radar installations on ships, all that is needed is a sensor interface between the radar and a computer, together with *RadarFix* software.

The shore-based infrastructure that *RadarFix* needs to perform in most operational areas (harbor and harbor approach) consists of existing radar targets. In difficult operating areas, reflectors can always be added as an augmentation to the system.

RadarFix, and radar operations in general, are highly localized in relationship to own-ship. The horizontal beam pattern of conventional marine radar is very narrow and of high-intensity, which makes it difficult for anyone to "jam" the continuously rotating antenna over a large area, or on a large scale. This is in contrast to a radionavigation systems like Loran-C, where shore based transmitters and towers can be damaged or destroyed, thereby affecting vessels in a wide area.

The *RadarFix* position output would be used as a standard position input for most navigation displays and charting systems, such as ECDIS, Track Control

Systems, AIS and INS. In case of primary sensor failure, integrated inputs would be switched automatically during the backup process, along with a status alert indicator to notify the user.

CONCLUSION

RadarFix is essentially a computer interfaced to the existing shipboard radar, which uses software to achieve precise positioning in confined waters. *RadarFix* continuously computes range and bearing to known objects and then derives a fix from their geometry. Additionally, accurate heading information is provided that is not affected by gyrocompass lag or magnetic anomalies. Although the initial installations and sea-trials included specially-designed radar reflectors, subsequent testing showed that this was no longer required in most applications. The positioning accuracy achieved is 2–5m (95%). *RadarFix* can serve as a totally independent, low-cost, and robust backup to GPS/GNSS, without the need for any additional navigation equipment or infrastructure external to own-ship.

REFERENCES

[1] Volpe National Transportation Systems Center. 2001. "Vulnerability Assessment of the Transportation Infrastructure Relying on the Global Positioning System, Final Report" Report to: Office of the Assistant Secretary for Transportation Policy, U.S. Department of Transportation, August 29, 2001.

[2] Carroll, J.D. 2001. "Vulnerability Assessment of the Transportation Infrastructure Relying on the Global Positioning System, DOT/OST Outreach Meeting", October 5, 2001. Available from: http://www.navcen.uscg.gov.

[3] Keane, CDR Peter Keane, 2004. " Protecting GPS Transportation Infrastructure, - Action Plan Status Report", March 10, 2004, Available from: http://www.navcen.uscg.gov

[4] Bond, Langhorne. 1998. "GPS Navigation and the Backup Issue: The Future of GPS: Commercial Opportunities", Published by White House Weekly, 18 June 1998.

[5] Marceau, G., M. Lachance and G. Bouchard. 1992. "Project RANAV – Tests de Precision – Rapport D'Evaluation," Canadian Coast Guard, 6 April 1992.

Faculty of Maritime Studies
University of Rijeka, Croatia

Royal Institute of Navigation
Science Technology Practice

7th GNSS
Vulnerabilities and Solutions Conference

GNSS INTERFERENCE DETECTION AND CHARACTERISATION USING A SOFTWARE RECEIVER: THE DETECTOR PROJECT

Kevin Sheridan, Yeqiu Ying, Timothy Whitworth

NSL, UK
Loxley House, Tottle Road, Nottingham, NG2 1RT, UK
E-mail: kevin.sheridan@nsl.eu.com

ABSTRACT. *Global Navigation Satellite System (GNSS) technology is being used in an increasing number of applications in various sectors, including those regarded to be critical as they concern safety and financial transactions. GNSS can provide flexible, accurate and reliable positioning at low-cost but there are some limitations which need to be understood and taken into account in the design and operation of products and services. One such limitation of GNSS is its vulnerability to signal interference and jamming, which can severely degrade the GNSS service and impact performance. Effects range from a loss of accuracy to complete denial of GNSS services.*

This paper describes the DETECTOR project, co-funded by the European GNSS Agency under the 7th Framework Programme and led by NSL, which has developed a low-cost device for detecting and characterising GNSS interference and jamming.

KEY WORDS: *Global Navigation Satellite System (GNSS), Radio Frequency Interference (RFI), Jamming, Detection and Characterization, Software Defined Radio (SDR)*

1 IMPACTS OF RADIO FREQUENCY INTERFERENCE

GNSS signals are very susceptible to noise, due to their extremely low power, which leads to a very widely documented vulnerability (e.g. Wildemeersch and Fortuny-Guasch, 2010; Bauernfeind et al., 2011; Thomas, 2011; Storm van Leeuwen, 2008; Kuusniemi, 2012). Any increase in the noise level at the receiver antenna will adversely affect the performance of GNSS receivers. If the interference level is so high that the receiver electronic components are saturated, the signals might well be unrecoverable. When extra noise is present at the front-end, the receiver will encounter the following situations:

1. Low noise will affect measurement accuracy;
2. Medium noise will cause problems with tracking, and make it harder to (re-)acquire satellite signals. Satellites at low elevation may be lost;
3. High noise can prevent a receiver acquiring or tracking enough signals to provide a position solution.

There are a variety of potential RF interference sources, both natural and man-made. Natural interference can be caused by geomagnetic and ionospheric activity. Solar activity influences the behaviour of charged particles in the ionosphere which delay GNSS signals passing from satellites to user receivers. Under normal circumstances this delay can be corrected in a standard GNSS solution, but there are a series of phenomena including solar radiation bursts and ionospheric scintillation which can severely disrupt GNSS signals over wide areas.

Man-made RF interference can be caused by a number of sources, ranging from television signals to mobile communication devices. Television broadcasts have the potential to interfere with GNSS through the harmonics of the primary frequency in the event of a system malfunction or changes to the broadcast that increase the power of the 2nd or 3rd harmonics. Similarly, there is the potential for TV antennas with internal pre-amplifiers to cause interference if the unit malfunctions. In Turin, Italy it has been documented that out-of-band interference from TV broadcasts is interfering with GNSS frequencies (Motella et al., 2008).

The principal focus in the DETECTOR project is the threat of disruption due to intentional interference or jamming. In recent years, intentional interference events have been experienced, detected and analyzed. The most widely reported case of RF interference caused significant disruption to a GNSS landing system at Newark Airport. After lengthy and costly investigation by multiple US government agencies, the source was found to be a low-cost (≈ $30) jammer in a truck on the nearby highway. Dedicated data collection campaigns triggered by

this case detected up to 25 separate interference events per day (Grabowski, 2012). The current extent of jammer use and the impacts it may have on GNSS services is not precisely known, but with the wide availability of low cost devices, easily accessible guides on how to "build your own jammer", and growing privacy concerns around tracking equipment, it is likely to be a growing problem.

For many applications a low level of drivers operating personal jammers could cause a nuisance for the operators of GNSS-based services and may impact operating efficiency, e.g. through the need to investigate On-Board Units (OBUs) which are not reporting position in a road tolling service. In many cases this would not be a significant or a new problem however, as these solutions already need to be designed to cope with intermittent GNSS signal loss. A similar argument applies in safety-related applications such as Advanced Driver Assistance Systems (ADAS) where designs must already ensure that there is not a total reliance on a single technology. The greater problem is likely to be caused to unrelated GNSS services near roads that are more susceptible to disruption. This could include power distribution facilities using GNSS for precise timing or construction sites using precise GNSS for machine guidance. Across multiple applications though, there is a need for better knowledge of the RFI threat and its potential impact on positioning equipment and services. The DETECTOR project is one step towards providing this information.

2 DETECTION AND CHARACTERIZATION METHODS

Measurements are available at many points in the GNSS receiver processing chain which can be used to detect the presence of RFI. One good indicator within the receiver is the gain value of the controllable gain amplifier before the analogue signals are fed into the analogue to digital converter (ADC). This is because the input signal to the ADC is required to be matched to the dynamic range of the ADC to guarantee the quantization accuracy. Therefore, within the GNSS receiver implementation an automatic gain control (AGC) circuit is normally implemented to adjust the gain value based on the output of the ADC. When the ADC input signal is higher than the nominal level due to the presence of excessive RFI, the AGC will try to lower the gain value of the adjustable gain amplifier, and vice versa.

The characteristics of the digital signals at the output of the ADC will be changed in the presence of different RFI. Since GNSS signals are below the noise floor when they arrive at the receiver, in the nominal scenario it will have the characteristics of the additive white Gaussian noise (AWGN). When excessive

RFI is present, these characteristics will be changed, allowing the digital signals at the output of ADC to be used to detect RFI.

The detection techniques used in this activity exploit the flexibility of software GNSS receiver concept, so that the above-mentioned measurements are accessible, some of which are not usually available from commercial off the shelf (COTS) receivers. The detection algorithms are composed of "pre-correlation" and "post-correlation" techniques. Pre-correlation algorithms make use of the digital signals at intermediate frequency (IF) that are available in the software receiver used within DETECTOR. The post-correlation algorithms can use signal to noise ratios (SNR) measurements either from our dedicated software receiver or from a COTS receiver.

The solution finally implemented in DETECTOR uses a combination of post-correlation and pre-correlation techniques to reach a detection decision. Using very distinct SNR drops across multiple satellites is an effective detection method for "strong" interference events and can be implemented simply based on existing (non-dedicated) sensors, e.g. standard GNSS receivers. However, it misses many weaker events which are not detectable with sufficient confidence to be flagged. Pre-correlation techniques are used in addition, helping to detect more jammer devices and to increase the confidence of any detections. A particular benefit of pre-correlation techniques is their ability to detect interference with a very narrow bandwidth. The overall jammer power may be low (so has little impact on SNR) put the power/frequency ratio may be very high so would have a significant impact on a receiver. Access to the digital samples also allows the interference signal to be analysed further to identify the nature of the interference source. Details of the algorithms used are provided in (Sheridan et al., 2012).

3 DETECTOR ARCHITECTURE

The DETECTOR system is composed of two major elements: networked DETECTOR field sensors or probes, and a DETECTOR server at the back-office for data storage, processing and analysis. This is illustrated Figure 1.

3.1 Field Sensor

The field sensor is composed of an embedded computer which hosts the software receivers, all the detection algorithms, as well as managing the internal and external communications. A software receiver front end called Stereo, which can be configured to cover all GNSS frequency bands, performs the GNSS receiver front end processing. A COTS hardware receiver is also included to provide redundancy of measurements. Ethernet and wireless communication modems sup-

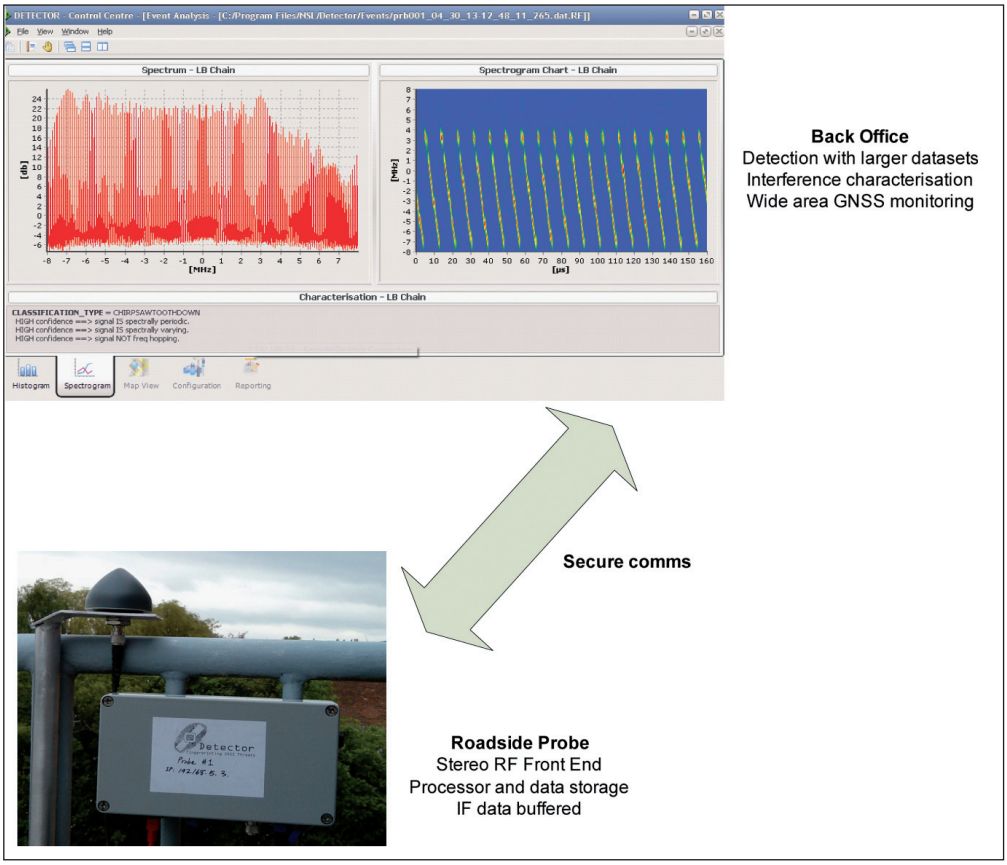

Figure 1 DETECTOR System Overview

port data communications. A sample of digital data is stored in a circular buffer. If an interference event is detected the samples are stored, otherwise the buffer is overwritten. All elements of the design are selected to be low-cost, allowing for a scalable solution with large numbers of sensors in future operation.

3.2 Back-office Server

The back-office collects transmitted digital samples and detection logs from the networked field sensors and performs more comprehensive interference detection and characterization analyses. It also makes use of additional information such as road databases and dynamic motion models to determine if multiple detection events are likely to be due to a single jammer. In addition, it monitors the state of the ionosphere to identify disturbances which could impact many receivers, and prevents this from incorrectly being attributed to intentional interference.

A database of jammer "signatures" will be built up to help develop effective countermeasures. Results can be interrogated to determine trends in the numbers, types and usage patterns of jammers over time.

4 RESULTS

4.1 Test at Targeted Site

DETECTOR algorithms have been tested in laboratories and in field trials using dedicated sensors, and also using data available from existing GNSS reference networks. The software can process RINEX and/or NMEA files, and perform post-correlation interference detection. In the UK, like many other countries, it is possible to obtain data from continuously operating GNSS reference stations which have been established to support land surveying and geodetic applications. Several of these are being continually monitored to check for potential interference events.

Preliminary tests identified a number of performance fluctuations which may have been caused by interference. Based on this, a location on an urban road close to an existing reference station was selected for collecting further data with DETECTOR equipment. Capturing digital samples in addition to more standard SNR data made it possible to use both post-correlation and pre-correlation detection and characterization techniques.

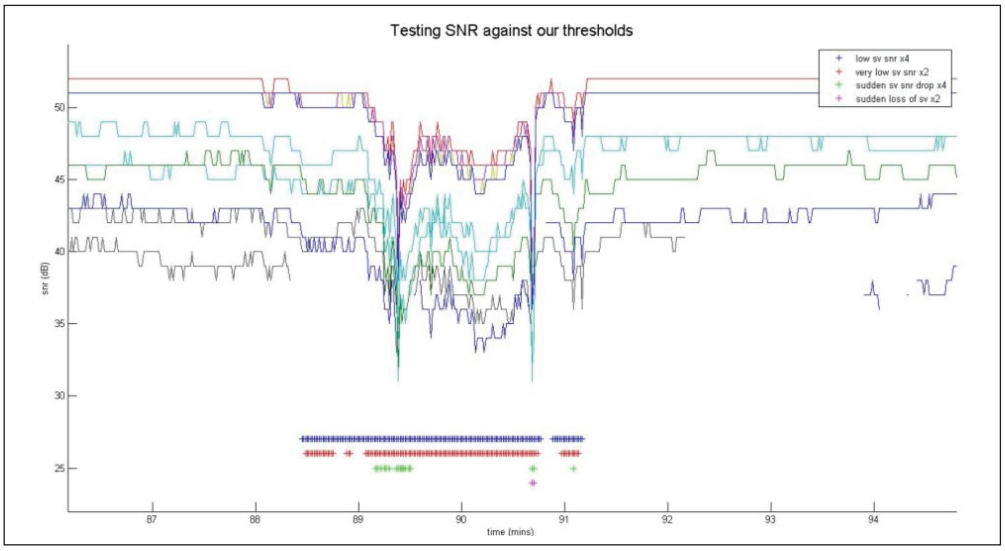

Figure 2 SNR values at reference site during interference event

Processing data SNR values from the permanent reference station, 5 or 6 possible events were identified over a 2-day period, including one which coincided with a 50m horizontal positioning error. Figure 2 shows the estimated SNR centred on a 3 minute period where there is an obvious drop in SNR.

Using a reference receiver with a high-grade rooftop antenna, there should be very little multipath (reflected signals) present, which can also reduce SNR, so this observed effect can be attributed to interference. In more obstructed environments, where multipath is more significant, it becomes increasingly difficult to identify the effects of interference using SNR alone. However, the pre-correlation methods are still very effective, and the sensitivity is much higher.

Figure 3 shows the change in received power over this three minute period. For each sample the upper image shows the received signal power in the frequency domain centred on the GPS L1 central frequency, with the blue trace showing the power recorded during a nominal calibration period and the red showing the received power during the test. The histogram below shows how this continuous signal is sampled to 2 bits in the ADC process. Initially no interference source is present and the power spectral density and histogram matches expected values for nominal conditions. Over time the impact of the interference signal on the receiver increases, with higher power leasing to more samples in the outer bins. This reaches a point at which the signal being evaluated has a digital power more than 5 times that of the nominal reference signal (labeled 1 in figure 3). The trend indicates that the jammer was mobile, and was moving towards our site. Most satellites could no longer be tracked at this time leading to degraded positioning. As the jammer moves away the interference level naturally drops. 50 seconds later though, it builds up again (to a peak labeled 2 in figure 3). This indicates that this is in fact two instances of jamming within a 3 minute window.

These were not the only events of interference. In the space of 41 hours more than twenty separate potential events were detected using these techniques, far more than the 5 or 6 which were observable simply using SNR values.

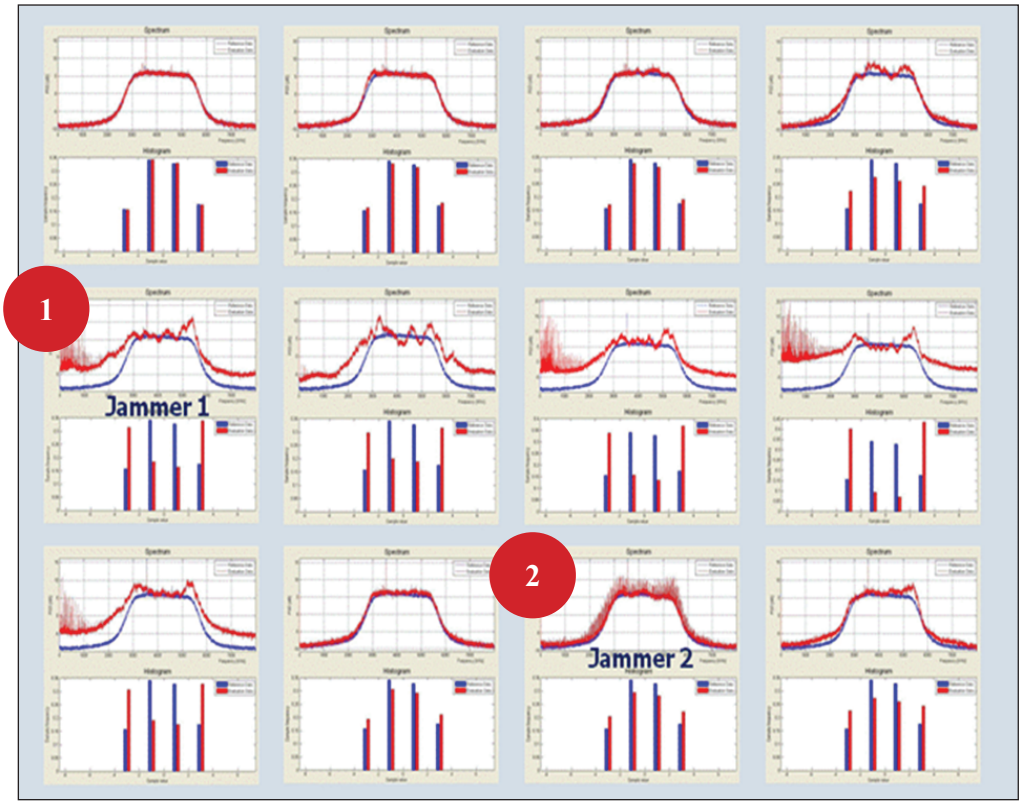

Figure 3 PSD & Histogram over 3 minute period

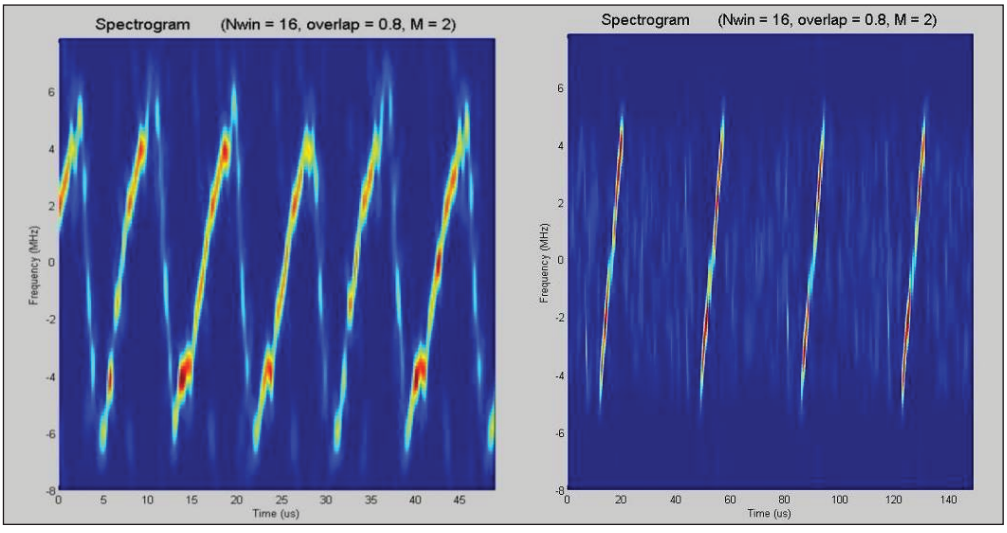

Figure 4 Spectrograms from the two jammers

The DETECTOR solution also characterizes the interference signals. This is a critical step in identifying the source of the interference, including differentiating between intentional and unintentional cases, and for providing evidence to support enforcement actions. Figure 4 shows the spectrogram for the two interference events. These plots show the interference to be of the "chirp" type – a continuous wave signal quickly swept through a wide frequency range. The two different signatures confirm that there are two jammers present, just a minute apart. Each of them is designed specifically to jam GNSS frequencies. Unintentional interference from badly tuned or malfunctioning equipment will not exhibit this behavior.

The DETECTOR software is able to characterize a signal automatically, based on; statistical periodicity, time periodicity, duty cycle, a swept signal test, a frequency hopping test, power, and bandwidth. In the case of the data here, the software correctly concludes that both the jammers are sawtooth (up) chirp, the first being continuous, the second pulsed. Note that in all likelihood the second signal will in fact be continuous, but the signal will travel outside the frequency of the pass-band of the receiver, i.e. it is the receiver hardware that is turning the signal from continuous to pulsed. DETECTOR identifies the type of interferer (classification) and also quantifies a set of attributes to describe the source (parameterization).

The other interference events characterized in this 41 hour data capture include several other chirp signals, some powerful single-tone signals, and a few narrowband signals. The majority of these look to be attributable to jammers but there are also a number of signatures which are more likely to be from unintentional man-made sources.

4.2 Tests at Field Jamming Trials

DETECTOR has been tested in a variety of scenarios where a known interference sources is introduced. In June 2012, NSL participated trials in Sennybridge, Wales, with the support of the Ministry of Defence and the Defence Science and Technology Laboratory (DSTL). In these trials, jammers with known and configurable characteristics were operated at a remote site. A variety of tests were performed with the jammers static and the detection equipment in a moving vehicle, then the situation was reversed with jammers moving and detection equipment static. In all cases the DETECTOR solution was able to detect and correctly characterize the jammer, and studying the results made it possible to determine the distance over which GNSS receiver performance will be degraded.

4.3 Laboratory Tests

DETECTOR has also been tested using the specialist laboratory facilities of the Institute for the Protection and Security of the Citizen (IPSC), one of the EC's Joint Research Centres, in Ispra, Italy. This facility allows jammers to be operated safely inside vehicles within an anechoic chamber (Figure 5 – left). A range of detection devices including high-grade spectrum analyzers can be used to sample the emitted RF signals. This allows the characteristics of the jammers to be analyzed in detail, identifying the emitted power and the frequency and periodicity of the signal. From this it is possible to determine both the likely disruption that each jammer could cause to GNSS services at various ranges, and also the distance over which the device could be effectively detected by monitoring equipment.

In initial tests a sample of commercially available jammers (Figure 5 – right) were operated in the anechoic chamber with the proposed DETECTOR equipment (Stereo RF Front End) and a more comprehensive spectrum analyzer recording and analyzing the signals.

Figure 5 Car being tested in anechoic chamber at IPSC, JRC (left). Sample of commercially available jammers tested (right).

DETECTOR was again able to reliably detect and characterize a range of typical jammers. Controlled testing provides an opportunity to better understand the jamming signals produced by various low-cost devices in a clean environment, which is a critical step in developing effective counter-measures. Figure 6 shows

the spectrogram of four of the jammers tested. It is interesting to note that many of the jammers tested will disrupt GNSS signals on multiple frequencies, including the proposed Galileo PRS side lobes on L1 in some cases.

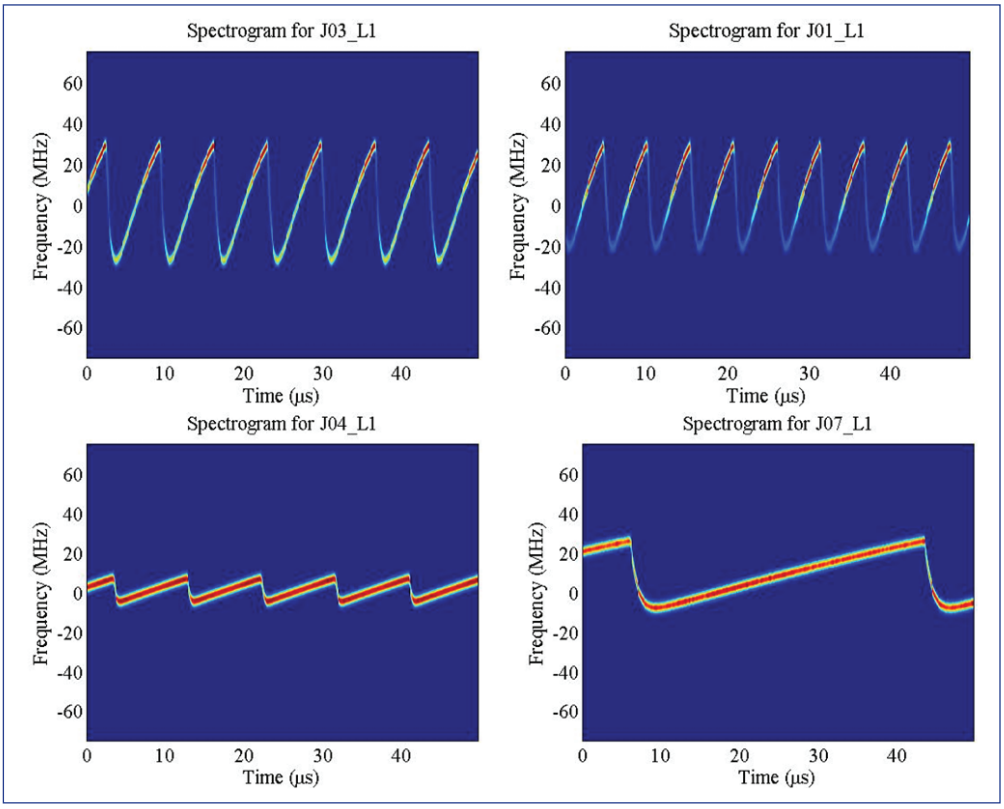

Figure 6 Spectrogram of jammers in laboratory testing.

Future multi-frequency GNSS equipment will add some robustness to interference, particularly from unintentional sources which are unlikely to disrupt widely distributed frequencies simultaneously. This provides improved mitigation but does not offer full protection given the presence of multi-frequency jammers.

Further tests were then carried out in which jammers were placed in different locations within two vehicles and the detecting antenna scanned over a complete hemisphere around the vehicles. The two vehicles used in these tests were a small hatchback (Fiat Panda) shown in figure 5 and a large van (Fiat Ducato). Transmitting antennas were placed on the dashboard, in the glove compartment and in the back of the vehicles to mimic different cases of concealment. In these tests a network analyzer was used to accurately evaluate the channel over a very

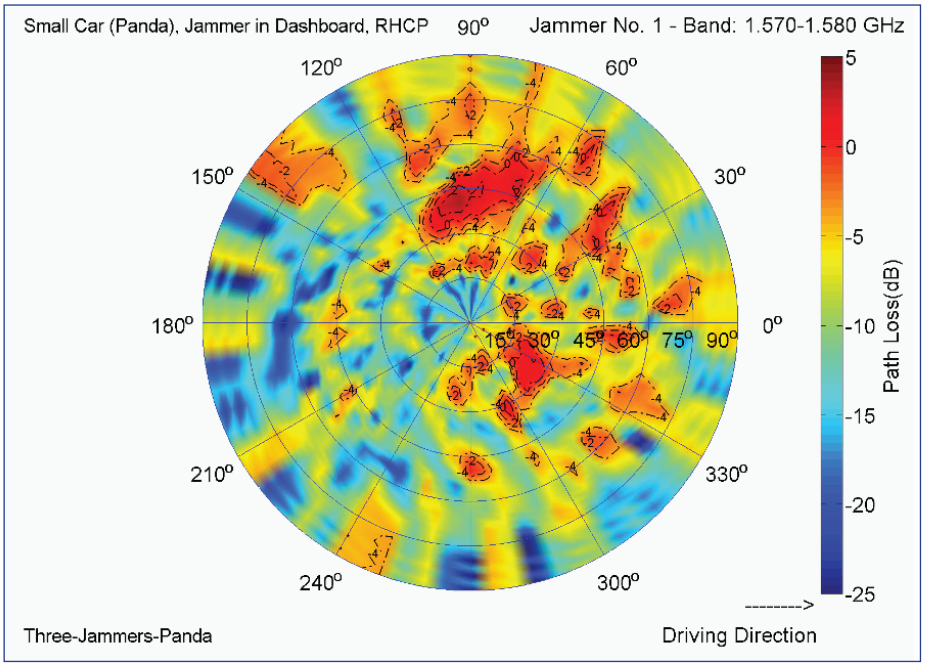

Figure 7 Path Loss with Jammer on dashboard of car

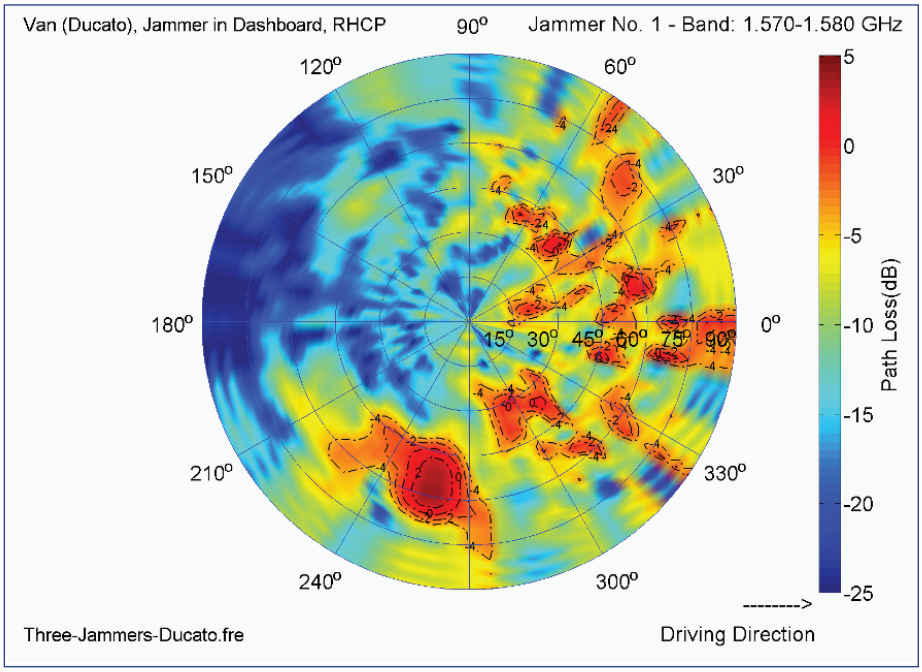

Figure 8 Path Loss with Jammer on dashboard of van

wide bandwidth. This made it possible to determine the path loss at each different GNSS band, and allowed samples to be taken at the receiving antenna from signals transmitted from each of the three antenna locations in the vehicle in turn.

These tests show how local obstructions influence the effective range of the jammers in different directions, so it is the differences in emissions which are of interest here rather than the absolute power of the interference signal. Figures 7 and 8 show the path loss from a transmitting antenna located on the dashboard of the small car, and the van respectively. The patterns clearly show the much stronger transmission of the signals through the windscreen and side windows. The metal back of the van provides an effective shield whereas the windows of the car allow the interference signal to propagate in all directions with a lesser reduction in received power.

The main conclusions of these tests are largely intuitive and predictable. Some of the more detailed analysis is important though, as it informs decisions of where to place detection devices (e.g. on an overhead gantry vs at the roadside) and also highlights some of the challenges in locating a jammer. A jammer in a vehicle cannot simply be treated as a point source uniformly emitting a signal in all directions. The signal profiles recorded in the lab have been combined to analyze the variation in signal strength as a function of the distance between a jammer and a detector placed on an overhead (figure 9).

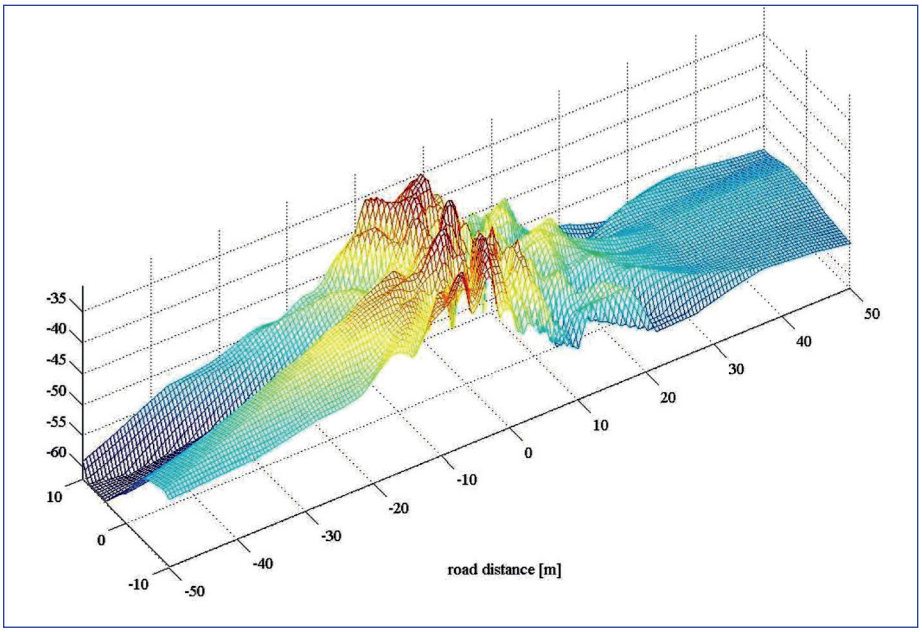

Figure 9 Jammer power variation vs distance from gantry

This indicates that it will be possible to locate a vehicle carrying a jammer with an accuracy of 10 to 15m based using a single probe, despite the non-uniform emission patterns.

Data collection and analysis has been used to support the development of an operational solution. The amount of digital data which is collected, analyzed, communicated and stored is an important design issue. These tests have helped identify the length of sample, bandwidth and quantization level (number of bits) required for reliable detection and characterization. The flexibility of the Stereo RF Front End makes it an ideal platform for performing these types of investigation. For example, by configuring the two available RF chains differently and using them simultaneously, it has been possible to directly compare results using a 2 bit quantization with 6 bits (3I, 3Q) on the other chain.

5 VALIDATION

The end-to-end prototype of the DETECTOR device was validated in May 2013 at the "AutomotiveGATE" in Germany . The Aldenhoven Testing Center (ATC) is a proving ground for positioning systems for road applications. Using this facility, jammers, receivers and detectors can be operated in a realistic road environment. The testbed includes road sections representative of urban, sub-urban and autobahn conditions. Jammers, receivers and interference detectors were installed on vehicles and on roadside gantries in various combinations. For example, the impact on a GNSS receiver from a brief exposure to a jammer which is being used in a vehicle travelling in the opposite direction could be assessed, as well as the ability to detect this jammer in slow and fast moving traffic.

Figure 10 shows an example where one detecting antenna is placed overhead and one at the roadside (highlighted in red circles). The jammer is operating in the car, which in this case is partially blocked by the truck. The effectiveness of detectors installed on overhead gantries rather than at the roadside was examined, taking into account alternative traffic conditions.

Figure 10 Testing at AutomotiveGATE (probe antennas highlighted)

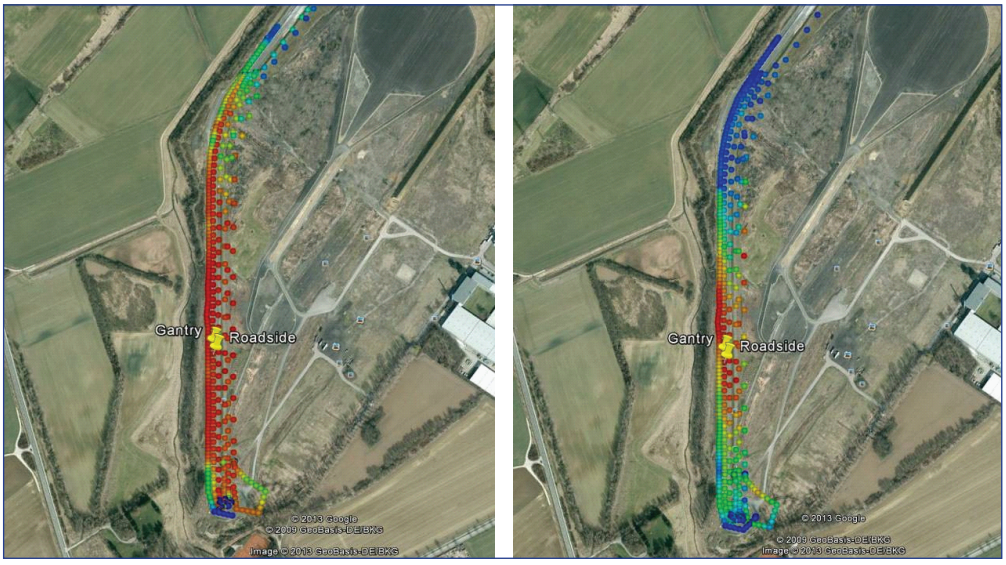

Figure 11 Jammer power profiles from a gantry (left) and roadside (right)

Figure 11 shows a map from tests in which the vehicle with a jammer passes the probes at a range of speeds. The power is represented by the colour, varying from blue (low power) through green (medium power) to red (high power). Re-

sults from successive runs are plotted with an incremental offset to the east, allowing them to be compared in a single image. This confirms that at high speeds (up to 165kmph) it is still possible to determine a power profile which follows the motion of the vehicle and can be used to identify it. It also demonstrates that with the same gain settings, a probe on an overhead gantry would provide a much coarser estimate of this profile – the received power is similarly high over a more than 100m here.

The validation tests confirmed that the DETECTOR system was able to automatically detect and classify jammers over a range of speeds, with different antenna placements, using different jammers, with obstructions, and also with the probe in a moving vehicle.

Figure 12 Sanef gantry for initial deployment of probes

6 DEPLOYMENT

Following the validation of the prototype will be installed at a Sanef operated site in northern France (Figure 12). The roadside equipment will detect interference, perform an initial characterization, and then transfer the data to a Back Office facility for storage and further analyses. Data and experience gained in deploying the system in an operational context will help assess the potential disruption to road operations from the use of jammers and will evaluate one mechanism to help address this threat.

7 CONCLUSIONS

DETECTOR has been developed to provide an effective, low-cost means to detect and characterize RF interference sources which degrade GNSS performance in road applications. Tests have demonstrated the potential of the system to reliably detect and characterize jammers in real-world conditions, controlled field tests and in the laboratory.

Pre-correlation techniques, which are made possible through the use of a flexible RF Front End and software receiver, have been able to detect events which would go undetected using only post-correlation (SNR) methods. Characterization allows the type of interference signal to be identified which gives a good indication of whether it is unintentional interference or a jammer. Knowing the signal characteristics helps understand the nature of the threat to GNSS services and to develop effective counter-measures.

ACKNOWLEDGMENTS

The work presented in this paper has been co-funded under the EC FP7 programme through the European GNSS Agency (GSA). This support is gratefully acknowledged. The project partners are Nottingham Scientific Ltd., Università di Bologna, Sanef, Black Holes B. V. and AGIT.

REFERENCES

1. Wildemeersch M., Fortuny-Guasch, J. (2010). RadioFrequency Interference Impact Assessment on Global Navigation Satellite Systems. *EC JRC Security Technology Assessment Unit, EUR 24242 EN*.
2. Bauernfeind R., Kraus ,T., Dotterbock, D., Eissfeller, B., Lohnert, E. and Wittmann, E. (2011). Car Jammers: Interference Analysis. *GPS World*, October 2011.

3. Thomas M. (2011). Global navigation space systems: reliance and vulnerabilities. *The Royal Academy of Engineering GNSS Vulnerability Report*.
4. Storm van Leeuwen S. (2008). Electromagnetic interference on low cost GPS receivers. *National Aerospace Laboratory Report.*
5. Kuusniemi H. (2012). Effects of GNSS Jammers on Consumer Grade Satellite Navigation Receivers. *Proceedings of the 2012 European Navigation Conference,* Gdańsk, Poland.
6. Motella B., Pini, M., and Dovis, F. (2008). Investigation on the effect of strong out-of-band signals on global navigation satellite systems receivers. *GPS Solutions,* Volume 12, Number 2, pp. 77–86.
7. Grabowski J. (2012). Field Observations of Personal Privacy Devices. *Proceedings of the 2012 Institute of Navigation International Technical Meeting,* Newport Beach, CA.
8. Sheridan, K., Ying, Y., and Whitworth, T. (2012). Pre- and Post-Correlation GNSS Interference Detection within Software Defined Radio. *Proceedings of ION GNSS 2012*, Nashville, TN.

Faculty of Maritime Studies
University of Rijeka, Croatia

Royal Institute of Navigation
Science Technology Practice

7th GNSS
Vulnerabilities and Solutions Conference

THE USE OF GNSS DATA IN ENVIRONMENTAL GOVERNANCE

Lidija Runko Luttenberger[1], **Leila Luttenberger**[2]

[1] Komunalac d.o.o. Opatija, Croatia
E-mail: lidija.luttenberger@komunalac-opatija.hr

[2] Faculty of Engineering, University of Rijeka, Rijeka, Croatia
E-mail: leila.luttenberger@riteh.hr

ABSTRACT. *Given the wide scope of possibilities that GNSS may provide in terms of environmental protection, the authors elaborate in particular the land use land cover (LULC) aspect in monitoring the state of the environment and for drawing up future physical plans that would safeguard the quality of living and that of the environment. Various stakeholders in the communities in vulnerable coastal karst regions or the mountains should be provided easy and non-costly access to detailed LULC data which could be processed and converted to quantifiable indicators of the degree of human intervention in the environment and its possible degradation. The availability of understandable indicators would ensure sound public participation and consultation in deciding on land use.*

KEY WORDS: *GNSS, environmental governance, LULC, karst*

1 SCOPE

Climate change, prognoses of sea-level rise and pollution present immeasurable threat to the planet, humanity, and all living communities. Authors contemplate the possibilities that GNSS may provide in terms of environmental protection through rendering possible the monitoring of state and changes of state of the environment , principally with regard to impervious surfaces and deforestation, through providing easy and non-costly public access to detailed land-use and land-cover (LULC) data which could be processed and converted to quantifiable indicators of the degree of human intervention in the environment and its possible degradation, and through observing vulnerable karst ecosystems, with the scope of drawing up physical plans that would safeguard the quality of living and of the environment.

2 INTEGRATED COASTAL ZONE MANAGEMENT

Coastal zone means the geomorphologic area either side of the seashore in which the interaction between the marine and land parts occurs in the form of complex ecological and resource systems made up of biotic and abiotic components coexisting and interacting with human communities and relevant socioeconomic activities. Integrated coastal zone management (ICZM) means a dynamic process for the sustainable management and use of coastal zones, taking into account at the same time the fragility of coastal ecosystems and landscapes, the diversity of activities and uses, their interactions, the maritime orientation of certain activities and uses and their impact on both the marine and land parts (Protocol on ICZM, 2009).

Coastal areas have been traditionally the source of wealth for many municipalities that were mainly dedicated to the fishing industry. At the end of the 19th century, tourism in Europe sprung forth, the beach acquiring great relevance as place for rest and leisure, and the coast being subjected to an intense exploitation aimed at offering progressively more demanding tourist services. It is however often forgotten that the coast is a very vulnerable environment, with the highest biological and geological values, that needs strong protective measures in order to be preserved. In this scenario, the diversity of uses and activities developed in the littoral area makes it necessary to seek the most suitable way to attain compatibility among them and, at the same time, preserve the environment. On the other hand, the threat of climatic change, and the prognoses of a sea-level rise that would flood coastal land, makes it necessary to elaborate coastal development scenarios that take into account all elements (Rodríguez et al., 2009).

Therefore the role of Global Navigation Satellite System (GNSS) in fulfilling two of main six principles of ICZM (EC, 2001): (1) that decisions are based on good data and information, which implies observation and processing, and (2) that all stakeholders and all relevant parts of the administration are involved, that entailing accessibility to the data.

3 LAND USE

Land use decisions are generally made at an individual landowner or local scale level; however, the impacts are often manifested cumulatively as change in spatial pattern on the landscape (O'Neill et al., 1988). As cities expand, bare ground, scrub and forest cover within and around urban areas are transformed to impervious surfaces like roads, driveways, parking lots, roof tops, sidewalks and other impermeable surfaces (Weng and Wilson, 2010). The increase in impervious cover lead to the increase in volume, duration and intensity of urban runoff (Weng, 2001), and additional avenue for the transportation of nonpoint source pollutants with consequences for water quality (Weng and Wilson, 2010), riparian, and marine habitats. Impervious surface has emerged not only as an indicator of the degree of urbanization, but also a major indicator of environmental quality (Arnold and Gibbons, 1996). It is a unifying theme for all participants at all watershed scales, including planners, engineers, landscape architects, scientists, social scientists, local officers, and others. Watersheds with large amounts of impervious cover may experience an overall decrease of groundwater recharge and baseflow and an increase of stormwater flow and flood frequency, while high areal extent and spatial occurrence of impervious surfaces may significantly influence urban climate (Weng, 2012).

The conversion of forest and agricultural land into urban built-up land thus contributes to increased land surface temperature. New developments of industrial zones in the outskirts of the cities are frequently located in high-quality agricultural land or forestland. In the past, agricultural or forest areas could provide a buffer zone between the urban and rural areas to absorb excess heat generated by automobiles and factories. Their conversion into urban built-up uses terminated this functionality, thus widening the temperature difference between the urban and the surrounding areas (Xiao and Weng, 2007).

The effects of deforestation itself are reduced biodiversity, release of greenhouse gas emissions, disrupted water cycles, increased soil erosion, and disrupted livelihoods (WWF, 2013). Deforestation is also a loss of green infrastructure which is defined as an interconnected network of green space that conserves natural ecosystem values and functions and provides associated benefits to human populations (Benedict and McMahon, 2001).

LULC change is therefore one of the most visible results of human modification of the terrestrial ecosystem. Changes in LULC can be largely attributed to population pressure on the land, rapidly growing economy, poor land use planning and the inconsistency in the governmental policies (Xiao and Weng, 2007).

Evaluating spatial scales is much easier in comparison with temporal ones because we can directly observe the present; however, evaluating changes through time is fundamental to predicting potential future conditions (Kepner, 2000). The European Environment Agency developed the method on land accounting, which analyses the stocks and flows (land cover changes) between two dates (Kleeschulte and Büttner, 2006). Satellite images have been used extensively to study temporal changes in LULC, but there have been few studies of LULC changes in karst areas, let alone the impact of these changes on the local environment (Xiao and Weng, 2007).

4 FRAGILITY AND COMPLEXITY OF KARST

Karst terrain accounts for about 15% of the world's land area and is home for about 1 billion people (17% of the world's population). One quarter of world's population is supplied largely or entirely by karst waters, including deep carbonate aquifers. Not only are studies of environmental change in karst areas important because of the large area and large population involved, they are also important because karst environments are extremely fragile, comparable with desert margins. Once damaged, their recovery can be slow and difficult. It takes 30-35 years for a karst environment to recover after deforestation, and recovery is longer than non-karst areas, and even impossible if the land is too badly damaged. It takes 2000-8000 years for weathering of carbonate rock to produce a 1 cm of soil in some karst areas, because very little insoluble material is left after dissolution (Xiao and Weng, 2007).

Karst areas are dynamic and environmentally sensitive. Potential adverse impacts on karst terranes greatly affect the man and of substantial interest financially (sinkholes, disruption of water flows). The geologic structure, solubility of the rocks involved, and the climatic conditions determine to a great degree how rapid these changes can take place. Rapid dynamic change can impact the hydrogeological history of an area, and brings about major environmental problems. Some of the examples are loss of civilization in Yucatan, major climatological impact in Guilin, China, impact on water supplies, transportation, energy pipelines, mining, communication, health, and loss of life in Shelby County, Alabama and also in South Africa, with condemnation of large areas of urban-agricultural land (LaMoreaux, 1991). There are methods available of remote sensing and GIS analysis to map, predict and explain the occurrence of caves in karst regions (Hung at al., 2002).

Karst is one of the most complex ecosystems. Basic characteristic of the karst are rocks prone to relatively quick dissolution. Karst landscape is a very active laboratory of quite simple but endless chemical processes. Dinaric karst itself is one of the two most precious karst phenomena in global terms. It is a home of at least twice the global average number of underground species. At least 1240 different species live in eternal darkness of its underground cavities. Dinaric karst is the greatest continuous karst area in Europe, encompassing north and eastern parts of the Adriatic from Udine in Italy to Skadar Lake at the border between Montenegro and Albania, and half of Adriatic Sea bed. Karst generally occupies much wider space than bare rocks which distinguish the landscape. It may be covered by pastures or forests, although porous character of its carbonate rocks is easily distinguishable by caves, funnel-like dolines or meagre fluvial network. The first recorded use of the world karst dates back to one tablet on the island of Krk of 30 December 1230 written in Glagolitic script (Lučić, 2012).

Presently karst does not fare well under the pressures of construction of mega-infrastructure, storage reservoirs, apartment building mania along the coast, etc. The majority of karst-related problems result from the perception in which nature is being reduced to its commercial functions. Karst underground is holding 90 pct. of Croatian water resources, of which 99 pct. are in tiny underground cracks. For instance, the aquifers like Ombla discharge water from cave passages in few days, but water from cracks is discharged for further 15 months. The variations between bottom and top levels of underground waters called ecotone in Dinaric karst may fluctuate up to 300 metres and constitute the most valuable feature of underground habitats and the generators of species (Lučić, 2012). Karst as specific form of relief occupies about 54% of territory. Karst phenomena and forms are particularly developed in limestones of highland and coastal Croatia and, as an isolated phenomenon, in the Sava- Drava River basin (EEA, 2013). Due to the uniqueness of the karst landscape, see figures 1, 2, and 3, especially the high fragmentation of land ownership, complex cultivation patterns, variable soil conditions and rapid overgrowing, it is difficult to distinguish some of the classes and more advanced methods need to be applied, e.g. post-classification. Land cover classification should be performed for smaller landscape units. The karst region demands a detailed research and accurate observation enabling historical comparisons (Kokalj and Oštir, 2007).

Figure 1 Aerial view of the area of the City of Krk, Island of Krk, Croatia
Source: Google Earth, 2013

Figure 2 Aerial view of Vrbnik area, Island of Krk, Croatia
Source: Google Earth, 2013

Figure 3 Aerial view of Baška area, Island of Krk, Croatia
Source: Google Earth, 2013

5 THE CASE OF CROATIA

In the period 1990-2000, a total of 4,738 ha of agricultural and forest land had its use permanently changed, and in the 2000-2006 period 8,050 ha. The main drivers of land take in both periods were building of settlements and roads and the expansion of industrial and commercial zones, and related setting up of construction sites and pits (EEA, 2013).

Corine[1] Land Cover (CLC) is a map of the European environmental landscape based on interpretation of satellite images which provides comparable digital maps of land cover available for most areas of Europe. CLC map for Croatia is shown in figure 4. The authors however hold that country CLC data used for national statistics purposes (AZO, 2010) does not necessary reveal local problems or may even fail to show the trends, which could all be misleading for local vulnerability analysis at the level of the municipality, the city, the county, watershed, forests, wetlands, or other ecosystems.

[1] Coordination of information on the environment

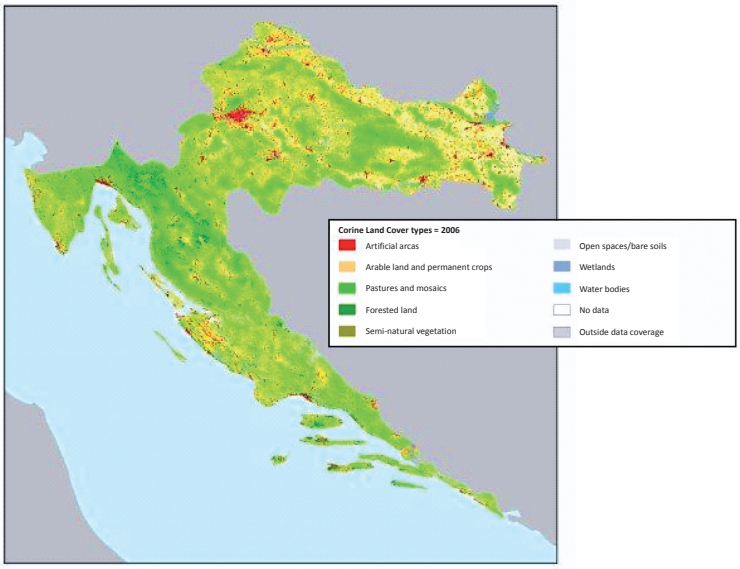

Figure 4 CLC map for Croatia (EEA, 2013)

For instance, CLC report for the Littoral-Mountain County (OIKON, 2011) states that "changes on the territory of the County are substantially less pronounced than on the territory of the Republic of Croatia….. changes which took place in county mainland, particularly in the corridor of main roads are much more pronounced than those in coastal part and on the islands".

The statement is simply too generalized, levelled out to average, and does not account for the fact that the county has exceptionally vulnerable ecosystems where minor land cover changes are significant.

Therefore, the spontaneous question arises as to whether the classification presented in table 1 is sufficient at all. Namely, the nomenclature which Croatia must comply with does not identify karst, meaning that it considers the use and cover regardless of this unique soil type. Karstic areas are accounted for in CLC headings 321 Natural grassland and 333 Sparsely vegetated areas (EEA, 2000), grouped with numerous reliefs that are quite different and characteristic of some other distant sites elsewhere. Limitations of the classification systems were also elaborated by (Villa et al., 2008), and also various other authors maintained that identification/description/quantification, rather than classification, should be applied in order to provide better understanding of the compositions and processes of heterogeneous landscapes such as urban areas, see (Melesse, 2007).

Therefore, remote sensing that would provide data of sufficient quality for adequate LULC monitoring requires more specific requirements on data providers.

On the other hand, as long as quality and detailed raw data are only available to companies and institutions holding monopoly on the use of satellite data, the quality of monitoring, measuring are interpretation of data might not be sufficient.

Table 1 CORINE land cover nomenclature (EEA, 1995)

Level 1	Level 2	Level 3
1. Artificial surfaces	1.1. Urban fabric	1.1.1. Continuous urban fabric 1.1.2. Discontinuous urban fabric
	1.2. Industrial, commercial and transport units	1.2.1. Industrial or commercial units 1.2.2. Road and rail networks and associated land 1.2.3. Port areas 1.2.4. Airports
	1.3. Mine, dump and construction sites	1.3.1. Mineral extraction sites 1.3.2. Dump sites 1.3.3. Construction sites
	1.4. Artificial non-agricultural vegetated areas	1.4.1. Green urban areas 1.4.2. Sport and leisure facilities
2. Agricultural areas	2.1.Arable land	2.1.1. Non-irrigated arable land 2.1.2. Permanently irrigated land 2.1.3. Rice fields
	2.2. Permanent crops	2.2.1. Vineyards 2.2.2. Fruit trees and berry plantations 2.2.3. Olive groves
	2.3. Pastures	2.3.1. Pastures
	2.4. Heterogeneous agricultural areas	2.4.1. Annual crops associated with permanent crops 2.4.2. Complex cultivation 2.4.3. Land principally occupied by agriculture, with significant areas of natural vegetation 2.4.4. Agro-forestry areas
3. Forests and semi-natural areas	3.1. Forests	3.1.1. Broad-leaved forest 3.1.2. Coniferous forest 3.1.3. Mixed forest
	3.2. Shrub and/or herbaceous vegetation association	3.2.1. Natural grassland 3.2.2. Moors and heathland 3.2.3. Sclerophyllous vegetation 3.2.4. Transitional woodland shrub
	3.3. Open spaces with little or no vegetation	3.3.1. Beaches, dunes, and sand plains 3.3.2. Bare rock 3.3.3. Sparsely vegetated areas 3.3.4. Burnt areas 3.3.5. Glaciers and perpetual snow
4. Wetlands	4.1. inland wetlands	4.1.1. Inland marshes 4.1.2.Peatbogs
	4.2. Coastal wetlands	4.2.1. Salt marshes 4.2.2. Salines 4.2.3. Intertidal flats

6 ACTING IN PUBLIC INTEREST AND DISSEMINATING THE INFORMATION

The European Union established the European Earth Monitoring Programme (GMES) and issued Regulation (EU) No 911/2010 relating to its initial operations. The GMES programme comprises the service component ensuring access to information in the area of land monitoring (besides atmosphere monitoring, climate change monitoring, emergency management, marine environment monitoring and security), the space component ensuring spaceborne observations, and the in situ component ensuring observations through airborne, seaborne and ground-based installations. The Commission shall manage the funds allocated to the activities under the Regulation. It shall ensure the complementarity and consistency of the GMES programme with other relevant Union policies, instruments and actions, relating in particular to competitiveness and innovation, cohesion, research, the European Global Navigation Satellite Systems (GNESS) programmes, data protection, the Shared Environmental Information System (SEIS), etc. The Commission shall ensure that service specifications match user needs (EU, 2011).

Many types of satellite imagery are readily available – low resolution for free online (Landsat, MODIS) and high resolution for purchase (World View, Quickbird) (UNEP, 2013).

In this private industry era for remote sensing which began at the end of the last millennium and beginning of this millennium and which consists of a number of innovations (Melesse, 2007), the power and reach of satellite technology have now been discovered by many non-profit groups, NGO's, government agencies, scientists, concerned citizens and indigenous peoples who are engaged in efforts to raise awareness and inspire action on a range of issues: environmental, humanitarian, cultural, educational and disaster relief/response, among others (Imaging Notes, 2007). Working with USGS, NASA, and TIME, Google reused a time series of images of Earth complied into an interactive time-lapse since 1970s using Google Earth Engine technology (Google, 2013). Authors are of the opinion that the concept should be further elaborated in two directions: 1) making the data more detailed and 2) making such detailed data available to the public. That would be a good starting point for developing realistic environmental indicators. Furthermore, it is necessary for educational institutes and universities to offer short-term and long-term programmes in remote sensing (UN, 2008).

On the other hand, there are many cases of government-financed technology that were commercialized and redounded to the benefit of the society. New technologies are invented by individual or corporate entrepreneurs, but it is government

action or support that transformed them into commercially viable technologies (Oreskes and Conway, 2010).

In fact, assets financed by public resources should be considered public assets and used for protecting nature. Just as one's use of a weather forecast does not subtract from the availability of that forecast to others, or one's consumption of public security does not reduce the general level of security available in a community (Ostrom, 1990), so is the case with remote sensing of the land cover.

Furthermore, people's science enables citizens to develop their own valid knowledge with their own resources. Local community in the form of citizen's groups provides the civic will and intelligence that animates scientific inquiry. Democratic science should therefore be fostered where scientific knowledge of experts is subordinated to a larger civic intelligence of the polity (Brown, 1998).

7 CONCLUSION

Apart from using GNSS for commercial purposes (mineral resources, agriculture), it should be put to use of preserving the nature locally. It could as well be complemented by remote sensing underground techniques, again not for the purpose of exploitation, but preservation, especially for monitoring the changes on karst landscape which represents the heritage of immeasurable value.

Processing the GNSS LULC data at national level for national statistics purposes does not necessary reveal local problems or may even fail to show the trends, which could all be misleading for local vulnerability analysis at the level of the municipality, the city, the county, watershed, forests, wetlands, or other ecosystems.

The availability of data and comprehensible indicators would ensure sound public participation and consultation in deciding on land use, thus preventing the monopoly on information by limited groups who then stake in the area. The authors point out that particular emphasis should be placed on GNSS use in monitoring the variations in size of impervious surfaces, compact and low-density greenfield developments, infill and redevelopment, the area of forests, shrubs and herbaceous vegetation, roads with or without walkways, the use of shorelines, intensity of road, rail, maritime and air transport and sources of pollution of the air, fresh water and the sea and soil. Such data should be sufficiently detailed, easily accessible, and ready for quantification, evaluation, and use as an input for models calculating the environmental threat.

Serving many users (local communities, schools, environmental NGOs) for an acceptable fee could ensure better care for environment. The investment in GNSS and coordination between various existing systems for obtaining an integrated picture are a matter of ultimate public interest.

REFERENCES

1. AZO. (2010). *Corine Land Cover: Pokrov i namjena korištenja zemljišta u Republici Hrvatskoj – stanje i trendovi*. Agencija za zaštitu okoliša, Zagreb.
2. Arnold, C.L., Jr., and Gibbons, C.J. (1996). Impervious surface coverage: The emergence of a key environmental indicator. *Journal of the American Planning Association*, 62, pp. 243–258.
3. Benedict, M.A., and McMahon, E.T. (2001). *Green Infrastructure: Smart Conservation for the 21st Century*. Sprawl Watch Clearninghouse Monograph Series, Washington.
4. Brown, R.H.(1998). *Toward a Democratic Science: Scientific Narration and Civic Communication*. Yale University Press.
5. EEA. (1995). *CORINE Land Cover*. http://eea.europe.eu. Accessed 8 March 2013.
6. EEA. (2000). *CORINE land cover technical guide – Addendum 2000*. Technical report No 40.
7. EEA. (2013) *Corine land cover 2006 by country*. http://www.eea.europa.eu/data-and-maps/figures/corine-land-cover-2006-by-country. Accessed 18 June 2013.
8. EU. (2011). *European Earth monitoring programme (GMES)*. http://europa.eu. Accessed 4 June 2013.
9. European Commission. (2001). *EU focus on coastal zones: Turning the tide for Europe's coastal zones*. Luxembourg: Office for Official Publications of the European Communities.
10. European Environment Agency. (2013). *Land use – State and impacts (Croatia),* http://www.eea.europa. Accessed 7 June 2013.
11. Google Official Blog. (2013). *A picture of Earth through time*. http://googleblog.blogspot.com. Posted on 9 May 2013. Accessed on 28 May 2013.
12. Hung, L.Q., Dingh, N.Q., Batelaan, O., Tam, V.T. and Lagrou, D., Remote sensing and GIS-based analysis of cave development in the Suoimuoi Catchment (Son La – NW Vietnam). *Journal of Cave and Karst Studies* 64(1), pp. 23–33.
13. Imaging Notes Magazine. (2007). *Raising Global Awareness with Google Earth*, 2(22), pp. 24–29.
14. Kepner, W. (2000). *Remote sensing and geographic information systems for decision analysis in public resource administration: Case study in a Southwestern watershed.* College of Urban Affairs, University of Nevada, Las Vegas.
15. Kleeschulte, S. and Büttner, G) (2006). European land cover maping – The Corine experience. *North American Land Cover Summit*, Washington, D.C. http://www.aag.org. Accessed 29 March 2013.
16. Kokalj, Ž. and Oštir, K. (1007). Land cover mapping using Landsat satellite image classification in the classical Karst-Kras region, *Acta Carsologica* 36(3), pp. 433–440.
17. LaMoreaux, P.E. (1991). *Proceedings of the International Conference on Environmental Changes in Karst Areas*. Quaderni del Dipartimento di Geografia n. 13, Università di Padova, pp. 215–229.
18. Lučić, I. (2012). Karst, major Croatian Dowry to the European Union. *Eurostorije*. Croatian Radio Third Programme, 21.5.2012.

19. Melesse, A.M., Weng, Q., Thenkabail, P.S., Senay, G.B. (2007). Remote Sensing Sensors and Applications in Environmental Resources Mapping and Modelling. *Sensors*, 7, pp. 3209–3241.
20. OIKON. (2011). *Pokrov i namjena korištenja zemljišta u Primorsko-goranskoj županiji – stanje i trendovi.*
21. O'Neill, R.V., Milne, B.T, Turner, M.G. and Gardner, R.H. (1988). Resource utilizitation scales and landscape pattern. *Landscape Ecology*, 2, pp. 63–69.
22. Oreskes, N. and Conway, E.M. (2020). *Merchants of doubt: How a Handful of Scientists Obscured the Truth on Issues from Tobacco Smoke to Global Warming*. Bloomsbury Press, New York.
23. Ostrom, E. (1990). *Governing the Commons*. Cambridge University Press, NY
24. Protocol on Integrated Costal Zone in the Mediterranean. (2009). *Official Journal of the European Union* L34, 4.2.2009, pp. 19–28.
25. Rodríguez, I., Montoya, I., Sánchez, M.J. and Carreño, F. (2009). Geographic Information Systems applied to Integrated Coastal Zone Management. *Geomorphology*, 107, pp. 100–105.
26. UN. (2008). *Report on the United Nation(/Saudi Arabia/United Nations Educational, Scientific and Cultural Organization International Conference on the Use of Space Technology for Water Management*, Riyadh, 12–16 April 2008.
27. UNEP. (2013). *Global Environmental Alert Service (GES)*, May 2013.
28. Villa, G, Valcarcel, N., Arozarena, A, Garcia-Ascensio, L., Caballero, M.E., Porcuna, A., Domenech, E. and Peces, J.J. (2008). Land cover classifications: an obsolete paradigm. *The International Archives of the Photogrammetry, Remote Sensing and Spatial Information Sciences*, Vol. XXXVII, Part B4.Beijing.
29. Weng, Q. (2001). Modeling urban growth effect on surface runoff with the integration of remote sensing and GIS. *Environmental Management*, 28, pp. 737–748.
30. Weng, Q. (2012). Remote sensing of impervious surfaces in the urgan areas: Requirements, methods, and trends. *Remote Sensing of Environment*, 117, pp. 34–49.
31. Weng, Q. and Wilson C. (2010). Assessing Surface Water Quality and Its Relation with Urban Land Cover Changes in the Lake Calumet Area, Greater Chicago. *Environmental Management*, 45(5), pp. 1096–1111.
32. World Wildlife Fund. (2013). *Deforestation*. http://wwf.panda.org.. Accessed 20 March 2013.
33. Xiao, H. and Weng, Q. (2007). The impact of land use and land cover changes on land surface temperture in a karst area of China. *Journal of Environmental Management*, 85, pp. 245–257.

Faculty of Maritime Studies
University of Rijeka, Croatia

Royal Institute of Navigation
Science Technology Practice

7th GNSS
Vulnerabilities and Solutions Conference

EFFECTS OF IONOSPHERIC ASYMMETRY ON ELECTRON DENSITY STANDARD INVERSION ALGORITHM: APPLICABLE TO RADIO OCCULTATION (RO) DATA USING BEST-SUITED IONOSPHERIC MODEL

Muhammad Mubasshir Shaikh[1], **Riccardo Notarpietro**[1], **Pavel Najman**[2], **Tomislav Kos**[2], **Bruno Nava**[3]

[1] Politecnico of Turin, Department of Electronics and Telecommunications, Torino, Italy
E-mail: muhammad.shaikh@polito.it

[2] University of Zagreb, Zagreb, Croatia

[3] The Abdus Salam International Centre for Theoretical Physics, Trieste, Italy

ABSTRACT. *The "Onion-peeling" algorithm is a very common technique used to invert Radio Occultation (RO) data in the ionosphere. Because of the implicit assumption of spherical symmetry for the electron density (Ne) distribution in the ionosphere, the standard Onion-peeling algorithm could give erroneous concentration values in the retrieved electron density vertical profile Ne(h). In particular, this happens when strong horizontal ionospheric electron density gradients are present, like for example in the Equatorial Ionization Anomaly (EIA) region during high solar activity periods. Using simulated RO Total Electron Content (TEC) data computed by means of the best-suited ionospheric model and ideal RO geometries, we evaluated the asymmetry level index for quasi-horizontal TEC observations. This asymmetry index is based on the Ne variations that a signal may experience*

along its ray-path (satellite to satellite link) during a RO event. The index is strictly dependent on RO geometry and azimuth of the occultation plane and is able to provide us indication of the errors (in particular those concerning the peak electron density NmF2 and the vertical TEC) expected in the retrieval of Ne(h) using standard Onion-peeling algorithm. On the basis of the outcomes of our work, and using best-suited ionospheric model, we will try to investigate the possibility to predict the ionospheric asymmetry expected for the particular RO geometry considered. We could also try to evaluate, in advance, its impact on the inverted electron density profile, providing an indication of the product quality.

KEY WORDS: *GNSS Radio Occultation, Ionospheric Asymmetry, Best-model Map*

1 INTRODUCTION

The Global Navigation Satellite Systems (GNSS) experience huge development during the last 10 years and it is predicted that GNSS market will grow even more in the future. Side by side with the GNSS advancement, demands on its services continuously increasing as well. Nowadays, satellite navigation has number of applications while some of them require high precision and accuracy. There are several factors which can introduce an error into the position solution. Since every navigation solution relies on the time between the transmission of the signal from the satellite to the reception of the signal by the receiver, any change of the signal's speed of trajectory resolves in error. One of the biggest errors is caused when a navigation signal passes the ionosphere. It is because the ionosphere contains such an amount of charged particles that mutual interaction between them and the propagating electromagnetic way can significantly change its trajectory and speed. This error is called "ionospheric error" and it depends on the amount of the charged particles which signal encounters on its way through the ionosphere. This particle amount is usually referred to as Total Electron Content (TEC).

The time delay caused by the ionosphere $\Delta\rho_{iono}$ can be calculated as:

$$\Delta\rho_{iono} = \frac{40.3}{f^2} TEC = \frac{40.3}{f^2} \int_l Ne(l)\mathrm{d}l,$$

where 'Ne' stands for electron density in a particular place along the signal path 'I'.

As it can be seen in Fig 1, the structure of the ionosphere is not simple. The structure significantly varies in time and space and strongly depends on Sun's activity.

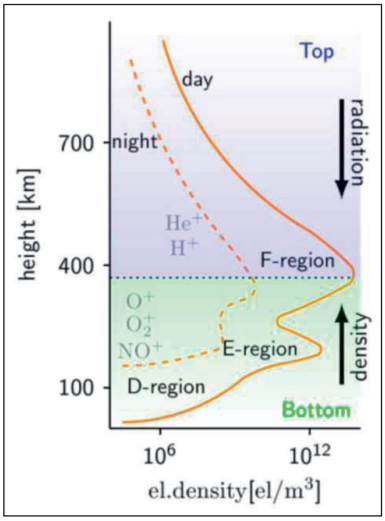

Figure 1 A typical electron density vertical profile of the ionosphere. The ionospheric layers for particular altitudes are shown. The electron density profile during day and night is represented by full and dashed line, respectively. The dotted line shows the average height of the electron density maximum. Made by the authors according to (Ya'acob N. et al. 2008).

In case of double frequency receiver, the major part of the ionospheric error can be easily compensated. However, most of the civil receivers are still single frequency receivers which need further assistance (Srinivas S. et.al. 2012). One possibility is to use an ionospheric model. Such a model predicts the current state of the ionosphere from given inputs and provides the value of the ionospheric error to the receiver. Ionospheric models are not used just for the ionospheric corrections but also for calibration and forecast improving purposes.

In our asymmetry assessment, we have used two ionospheric models NeQuick2 (Nava B. 2008) and IRI2012 (Bilitza D. 2008). NeQuick2 is able to characterize the electron concentration distribution in both bottom-side and topside of the ionosphere, and it is a quick-run model particularly tailored for trans-ionospheric propagation applications. Basic inputs for the NeQuick2 model are position, time (Universal Time) and value of $F_{10.7}$ solar flux; output is the electron concentration at the given location and time. IRI2012 is also a very well-known electron density model. The input for IRI2012 is position and time (year, day of year and UT). The solar flux calculation in IRI2012 is done by 12-month running

mean of the IG and RZ indices and the daily and 81-day running mean of $F_{10.7}$ solar flux values. A running mean of 81 days means that IRI2012 takes the average of daily values from 40 days before and 40 days after the day of interest. One of the main differences of the IRI2012 from the NeQuick2 is its limitation of height for vertical TEC (VTEC) calculations. With NeQuick2, it is possible to calculate VTEC from Earth's surface to the altitude of GPS satellite. IRI2012 limits this height up till 1500 Km above the Earth's surface. In this paper these models have been used to produce synthetic electron density data and to simulate corresponding L-TEC values given ideal geometry observations inside LEO orbit (R_{LEO} = 800 Km), in order to define test case scenarios that could be used to 'stress' the inversion procedure.

2 LIMB-TEC MEASUREMENT USING RADIO OCCULTATION

RO missions such as GPS/MET, CHAMP, COSMIC and METOP (Anthes et al. 2008, Gorbunov M.E. 2001, Hajj et al. 2002, Healy et al. 2002, Luntama et al. 2008) have been designed to sound the Earth's neutral atmosphere and ionosphere via radio link between a GPS navigation satellite and GPS receiver onboard Low Earth Orbit (LEO) satellites (Gorbunov, 1996). The U.S. GPS/MET experiment was the first mission which successfully applies Radio Occultation (RO) technique to the Earth atmosphere monitoring, using GPS signals. Fig 2 illustrates a view (not in scale) of the RO (or limb-sounding) geometry. Radio waves are refracted when passing through the Earth's atmosphere in the direct link between GPS and the occulted LEO satellite. The atmospheric refractivity changes mainly as a function of height and of geographical location. As a result, radio signals follow bent ray paths and experience significant propagation delay. The magnitude of such effects depends on geophysical conditions of the atmosphere. In neutral atmosphere, the bending of the signal is extracted and inverted into refractivity profiles through the Abel inversion (Kursinsky 1997, Ware et. al. 1996) whereas in the ionosphere, where bending is negligible, carrier phase measurement and corresponding limb-TEC observations (LTEC in what follows) are evaluated and inverted to extract electron density profiles, Ne(h). Ne(h) is defined in terms of ray perigee's location of each ray path between LEO and GPS.

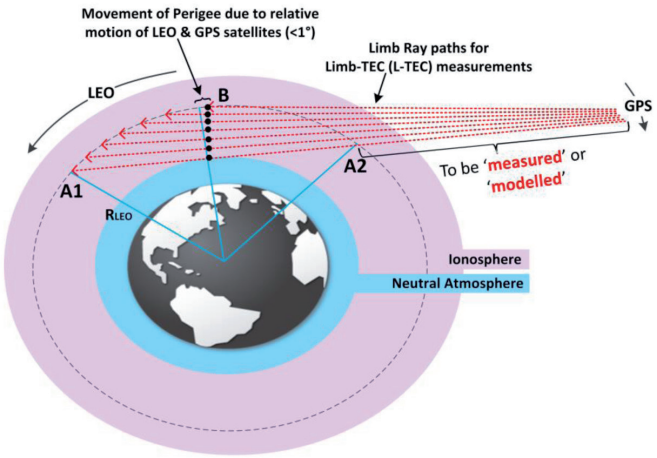

Figure 2 Limb TEC (L-TEC) measurement in the ionosphere using radio occultation technique. Sides A1 and A2 are two edges of the LEO orbit bisected by ray perigees. Ray perigee movement (black dots) is visible due to the relative movement of LEO and GPS satellites. TEC calculated between sides A1 and A2 is considered as internal orbit L-TEC (Shaikh M. M. et al. 2013).

Input for Ne(h) retrieval algorithm is internal orbit LTEC time-series (from points A1 to A2 in Fig 2) observed from the same GPS satellite during an occultation event. External LTEC (TEC from GPS-to-B or GPS-to-A2 in Fig 2) should be removed (either by measuring or modelling) before starting the inversion procedure. For the COSMIC mission, such external LTEC measurements are generally available. Alternatively, it is possible to model the external LTEC with the help of 3D electron density distribution derived by using other approaches, like opting for some climatological models such as NeQuick2, IRI2012, or tomography (Austen et al. 1988), etc.

3 THE BEST MODEL MAP

NeQuick2 and IRI2012 can provide electron density calculations at any desired resolution in the ionosphere. Based on their input parameter, both models model the ionosphere in quite different way. In order to produce background ionosphere using any of these models, careful consideration needs to be taken into account. As radio occultation geometry spread over a large area, it is possible that both models may be used in part to calculate electron density along the ray path. In this paper, to ensure the best possible approximation to the real ionospheric condition, the so called 'best model map' was constructed.

3.1 Methodology

A single 'best model map' is a grid of indicators. The resolution of the grid is the same as the resolution of the reference to which the models are compared. Each grid point has an indicator which shows for which model is the absolute difference between the modeled VTEC and the reference VTEC the smallest in that particular location and time. We used CODE maps as the reference. The CODE maps have vertical TEC values grid with resolution of 5 degrees in longitude and 2.5 degrees in latitude and are produced every 2 hours. The NeQuick2 version 2 driven by solar flux data and the IRI version 2012 driven by its default drivers were used to produce global TEC maps with the same time and spatial resolution. In this case, the NeQuick2 is not driven by its typical monthly averaged solar flux value to demonstrate difference between a model driven by monthly averaged and daily value. Maps created by the models were then compared with the reference CODE maps.

4 ONION-PEELING INVERSION

Onion-peeling technique is widely used to invert L-TEC measurements observed by a RO instrument capable of acquiring data also for ionospheric characterization, for Ne(h) profile retrieval. In reality, these profiles are not exactly vertical since, during an occultation event, the ray perigee moves slightly away from the vertical due to the relative motion of GPS and LEO satellites as shown in an exaggerated view of RO scenario in Fig 2. In this work, we applied standard Onion-peeling algorithm to invert simulated radio occultation data under a constraint of using ideal geometries (LEO-LEO occulted ray paths, fixed occultation plane and vertically distributed ray perigees). Rationale behind the use of this so called 'ideal geometry' is to focus the dependency of retrieval errors on the inversion approach only, avoiding taking into account inaccuracies due to geometry. For a given occultation event, the L-TEC relates to LEO-LEO ray path 'i' can be evaluated considering a set of spherical shells (identified by peel 'j') like 'onion shells' (Leitinger et al. 1997, Hernandez-Pajarez et al., 2000), characterized by a constant electron density (the mean radius of each shell is the impact parameter of the ray). Analytically, the L-TEC associated to the ith ray can be defined as:

$$LTEC_i = \sum_{j=i+1}^{N} 2L_{ij}\, Ne_j + L_{ii} Ne_i \quad --- \tag{1}$$

Where,

'L_{ij}'	is the length of the segment 'i' of the ray 'i' related to the electron density characterizing shell 'j'
'Ne_j'	is the electron density charactering the 'jth' shell
'$LTEC_j$'	is the limb-TEC value related to the 'ith' ray path of the ray (GPS to LEO) crossing all the shells from the most external to the 'ith' one
'N'	is total number of shells

Considering this definition, the L-TEC may be easily inverted to extract the Ne characterizing each shell Nej, starting from the most external ray path. This way, we can invert L-TEC to extract an Ne(h) profile. The matrix in Eq. (1) describing the linear system of equations is triangular, and therefore it can be easily solved from top to bottom for LTEC inversion to extract Ne(h) profile.

But this approach faces two major issues. Firstly, having defined "spherical" shells, this technique is based on spherical symmetry hypothesis, i.e., the Ne depends only on height. Secondly, as it is clear from the mathematical expression given in eq. (1), electron density in each shell is evaluated from electron densities characterizing all the layers above it. That is, if the calculation of Ne for one shell (at a particular height) is wrong because of any reason, the computed value, other than affecting electron density of that shell, adds an error contribution to the calculation of the electron densities for all the layers below it. Both these causes may impact the Ne profile retrieval, in particular considering cases of large horizontal Ne gradients which cause Ne distributions to diverge from the spherical symmetry assumption. With the current Onion-peeling implementation (without the help of external information like e.g. ground-based TEC data as suggested by (Hernandez-Pajares et al. 2000), there is no simple way to predict or compensate for this error.

In this paper our attention has been primarily devoted to test how much the ionospheric asymmetry evaluated through a background may impact electron density retrieval in particular considering high solar activity conditions. The results are formulated by comparing the Onion-peeling derived profiles derived inverting L-TEC data obtained by inversion of modelled TEC data (considering NeQuick2 and IRI2012 as background ionosphere) to the corresponding geographically co-located 'truth' profiles. With this approach the results produced by the standard Onion-peeling inversion can be quantitatively assessed in a simulated environment. In this work, particular attention has been given to the Equatorial Ionospheric Anomaly (EIA) to understand the effects of strong electron density gradients usually present in EIA.

5 IONOSPHERIC ASYMMETRY ASSESSMENT

We showed in our assessment study (Shaikh M.M. et al. 2012) that due to the strong spherical symmetry hypothesis, standard Onion-peeling can be successfully applied where GNSS signals cross ionospheric regions characterized by small horizontal gradients of electron density. In some cases, where the ionospheric conditions along the ray path differ greatly from the spherical symmetry assumptions like in the EIA region, the algorithm may lead to erroneous electron density profiles. In order to analyse such errors, we created test case scenarios under controlled and simple occultation geometries. Corresponding LTEC observables were simulated under high solar activity conditions.

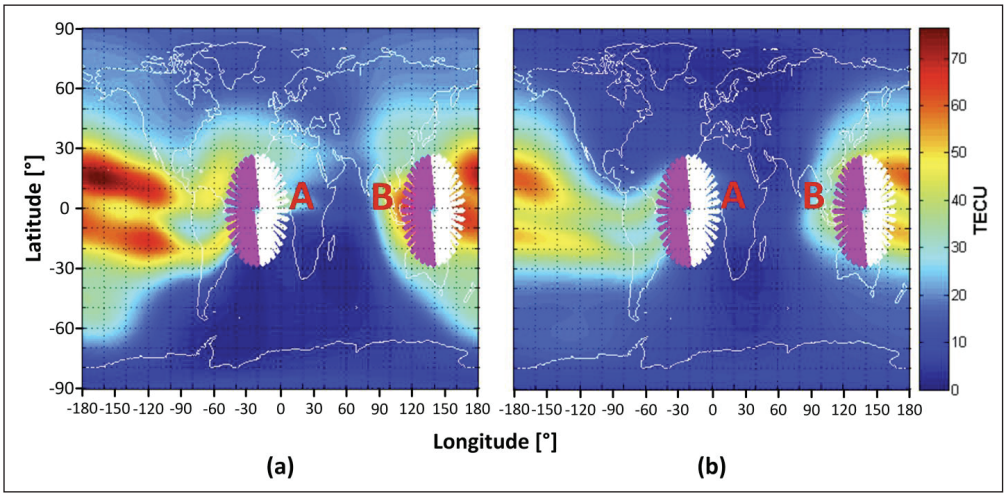

Figure 3 Global VTEC Distribution evaluated using (a) NeQuick2 and (b) IRI2012 superimposed with the footprints of RO events for 2 positions used in this work (as defined in table 1(a))

In this work, we have tried to define, mathematically, an asymmetry level index in order to quantify the impact of asymmetry on Onion-peeling retrieval errors considering N(e) variation along the limb-sounding ray path. We performed our analysis considering two occultation positions (A and B) shown in Fig 3. The positions are selected considering different background ionosphere; modelled using NeQuick2 and IRI2012. A brief summary of each RO event considered in Fig 3 is given in table 1. For each case, we have rotated the azimuth of the RO plane (i.e. rotation of RO plane around the vertical axis) by 180°. For each azimuth of occultation plane, errors between the Onion-peeling inversion and the co-located true ones have been evaluated. Errors taken into account are

Vertical TEC (VTEC) and the peak electron density value (NmF2) (see section 5.2 for their definition).

Table 1 (a) and (b) show a summary of various parameters for the radio occultation events considered in this study as shown in Fig 3. (a) contains parameters which are specific to each event while (b) shows the parameters which are generally applicable to all simulations throughout this work

a)

RO Event	Region	Perigee Position (Lat/Long)	Time
A	Equatorial	0° N/20° W	Night
B	Equatorial	0° N/140° E	Day

b)

NeQuick2		
Solar activity		High
Solar Flux value		190 sfu
UT		0100
Azimuth of RO Plane	Range	0° to 180°
	Step size	10°

IRI2012		
Solar activity		High
Day of Year/ Year		288/2003
UT		0100
Azimuth of RO Plane	Range	0° to 180°
	Step size	10°

5.1 Mathematical Formulation for Asymmetry Assessment

We define the asymmetry level of the ionosphere considering the degree of dissimilarity of electron density distribution along the two half parts of a ray path which crosses the ionosphere at a certain height. Electron density at each point along the ray path can be computed with NeQuick2 and IRI2012 by knowing the geographical position of that point (latitude, longitude and height), UT, $F_{10.7}$ solar flux value (for NeQuick2) and day of year/year (for IRI2012). Latitude and longitude values used in following equations depend on the spatial sampling of the ray path. For simplicity, we divided the complete ray path in 100 equal segments and then the electron density along the ray path was evaluated at the end point of each ray segment. Corresponding L-TEC value can be obtained by integrating Ne values along the ray path as follows:

$$TEC_{Ray\,path} = \int_0^{RayLength} Ne_{NeQuick2}\, dl \quad - - - \tag{2}$$

Fig 4a and 4b show example of electron density distribution along the ray path (azimuth 0° RO sounding of case A depicted in Fig 3) for NeQuick2 and

IRI2012, respectively. Top subplots represent how the ray paths experience the gradients of electron density.

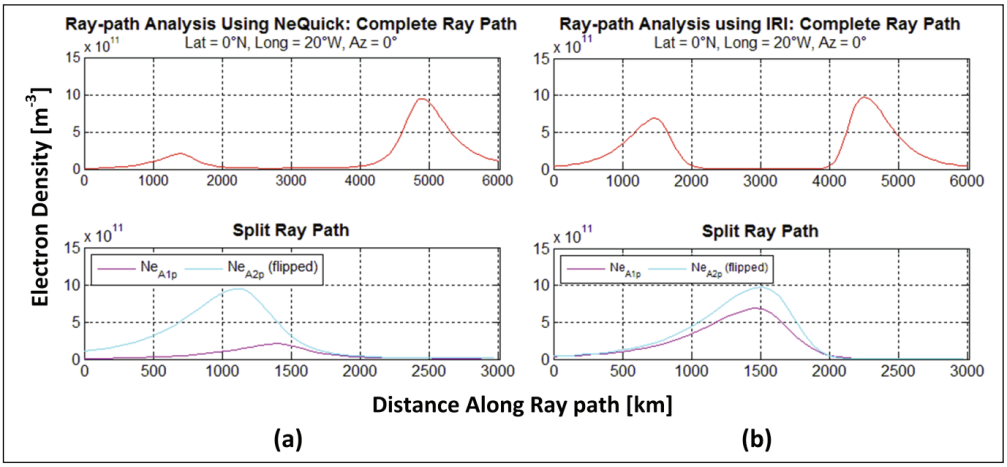

Figure 4 (a) and (b) show Ne along occulted ray paths calculated using NeQuick2 and IRI2012 at 0° azimuth of occultation plane, respectively. Top subplots show the Ne variation along full (LEO-LEO) ray path. In bottom subplots, magenta curve shows Ne variation along the ray path from point 'A1' to ray perigee 'p' and cyan curve shows Ne variation along the ray path from point 'A2' to 'p'. (See Fig 2 for details of points A1, A2 and p)

In the bottom subplots, the same electron density values are illustrated splitting the rays in two parts, from A1 to ray perigee p (pink) and from A2 to the same ray perigee p (cyan). A1, A2 and p are the points defined in Fig 2. Asymmetry is then calculated by considering the integral of the absolute value of the Ne differences evaluated along the two halves of the occulted ray path bisected by ray perigee i.e. the area between cyan and magenta lines:

$$\text{Asymmetry}_{\text{Iono}} = \int_0^{\text{half RayLength}} |\text{Ne}_{\text{NeQuick,A1p}} - \text{Ne}_{\text{NeQuick,A2p}}| \text{dl} \quad --- (3)$$

In order to normalize our asymmetry values, we divided the AsymmetryIono value (eq. (3)) by the TEC along ray path (eq. (2)). The asymmetry index for the ionosphere is therefore defined as:

$$\text{Asymmetry Index}_{\text{Iono}} = \frac{\text{Asymmetry}_{\text{Iono}}}{\text{TEC}_{\text{Ray path}}} \quad --- \quad (4)$$

This asymmetry index range between 0 (perfectly symmetric ionosphere) to 1 (completely asymmetric ionosphere). The former may be experienced when the two half curves (cyan and magenta curves shown in Fig 4) completely overlap each other exhibiting two sides of the ray around the ray perigee with identically the same Ne distribution. The latter may be experienced when one of the two half curves completely vanishes (Ne = 0) exhibiting largest possible difference in the Ne distribution present at the two sides of ray path w.r.t. ray perigee. Given certain occultation geometry (simulated or realistic) and a background three dimensional Ne distribution derived by a model, this index could provide an indication of the asymmetry level expected for that particular occultation event, giving in advance an idea of how misleading the spherical symmetry assumption is.

5.2 Onion-peeling Related Errors

After having qualitatively shown the impact of ionospheric asymmetry on retrieved product, we will demonstrate quantitatively the correlation between the observed errors and the asymmetry level. Therefore, second step of our assessment, is the definition of the errors/observables we will use to evaluate the impact of ionospheric asymmetry. Basically, for each simulated occultation evaluated with an ideal geometry, we have inverted the LTEC values to vertical Ne(h) by means of the Onion-peeling algorithm. The retrieved electron density profiles are then compared with the collocated NeQuick2 and IRI2012 'true' vertical Ne(h) profile in terms of difference on VTEC and NmF2 values. Analytically speaking, the two error indicators can be respectively defined as:

$$\Delta\mathrm{VTEC} = \int_{h^*}^{h_{\mathrm{LEO}}} \mathrm{Ne}_{\mathrm{Onion-peeling}}\,\mathrm{dh} - \int_{h^*}^{h_{\mathrm{LEO}}} \mathrm{Ne}_{\mathrm{NeQuick}}\,\mathrm{dh} \quad --- \tag{5}$$

$$\Delta\mathrm{NmF2} = \left|\mathrm{NmF2}_{\mathrm{Onion-peeling}} - \mathrm{NmF2}_{\mathrm{NeQuick}}\right| \quad --- \tag{6}$$

6 RESULTS AND DISCUSSION

6.1 Used data

We chose 24th of October 2003 for our analyses in particular 0 and 2 hours Universal Time (UT). The measured noon value of observed solar flux for this day was 190 solar flux units (sfu). Therefore, the NeQuick2 map was created using this solar flux value as the input (Figure 5 (a)). In case of the IRI2012, we

created the map particularly for 24th of October 2013 without any changes in default input allowing the IRI2012 to use the indices stored in its own database (Figure 5 (b)). The reference CODE maps for the 24th of October 2003 were downloaded at the CODE webpage (ftp://ftp.unibe.ch/aiub/CODE/2003/).

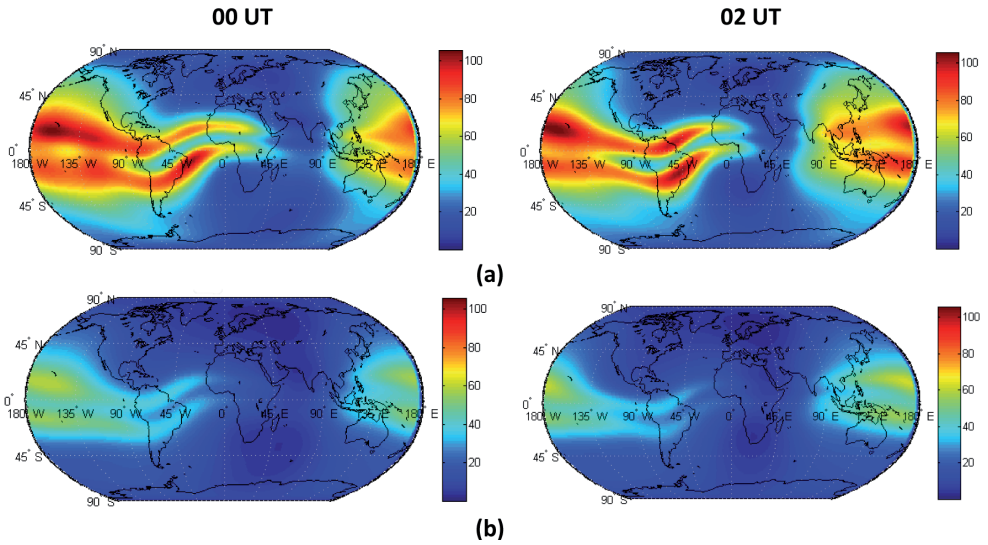

Figure 5 Ionospheric maps of 24th October 2003 constructed by the NeQuick2 (a) and IRI2012 (b). The NeQuick2 was driven by solar flux value of 190 sfu while IRI2012 was driven by it default values.

It can be seen that the maps produced by the NeQuick2 reach much higher TEC values then the one by the IRI2012. This is caused by the fact that the NeQuick2 was driven by the noon solar flux value while the IRI2012 maps were produced with its default averaged settings. Both models successfully model the shape of the equatorial anomaly along the geomagnetic equator.

6.2 The best model map

Fig 6 shows the best model maps for 24th October 2003 for 0 and 2 UT. It can be seen that for this particular time, the NeQuick2 performs better at equatorial region. On the other hand the IRI2012 shows better similarity to reference at mid latitude regions where the NeQuick2 overestimates electron content probably due to the manually input of solar flux value.

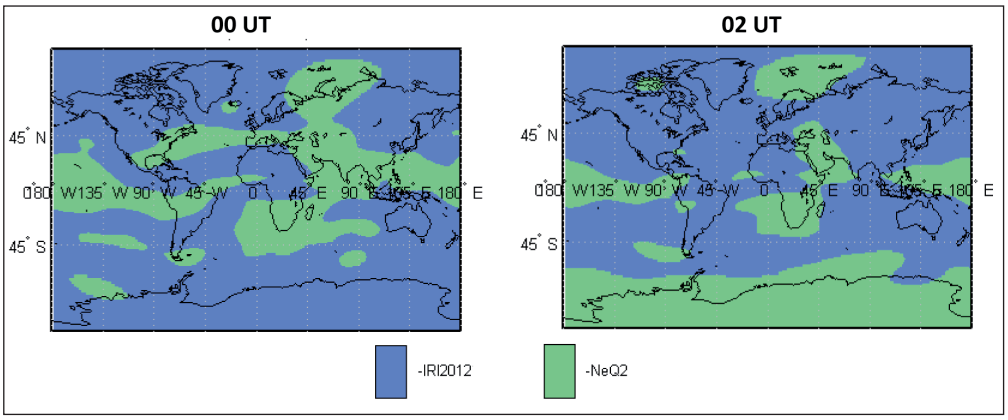

Figure 6 Best model maps of the 24th October 2003. The green colour indicates that the NeQuick2 was more simillar to the reference data while the blua indicates higher similarity for the IRI2012.

6.3 Reconstruction results and Analysis

Figs 7 and 8 show the asymmetry evaluation and corresponding Onion-peeling related errors. Fig 7 shows the results of case A for both NeQuick2 and IRI2012.

For case **A**, we found a very good correlation between the asymmetry evaluation and the corresponding Onion-peeling related errors for NeQuick2. As for IRI2012, in case A, the results are not much correlated. Specifically, ΔTEC and ΔNmF2 seem completely uncorrelated with asymmetry index values. However, a very good correlation exists between the two error curves for IRI2012.

In case **B** (shown in Fig 8), the situation seems very much flipped. Errors evaluated using IRI2012 background seems very well correlated with the corresponding asymmetry values. At the other end, NeQuick2 results are very much less correlated. Specifically, errors are negatively correlated with corresponding asymmetry values from 80° to 110° of the azimuth of occultation plane. However, the correlation elsewhere is quite good.

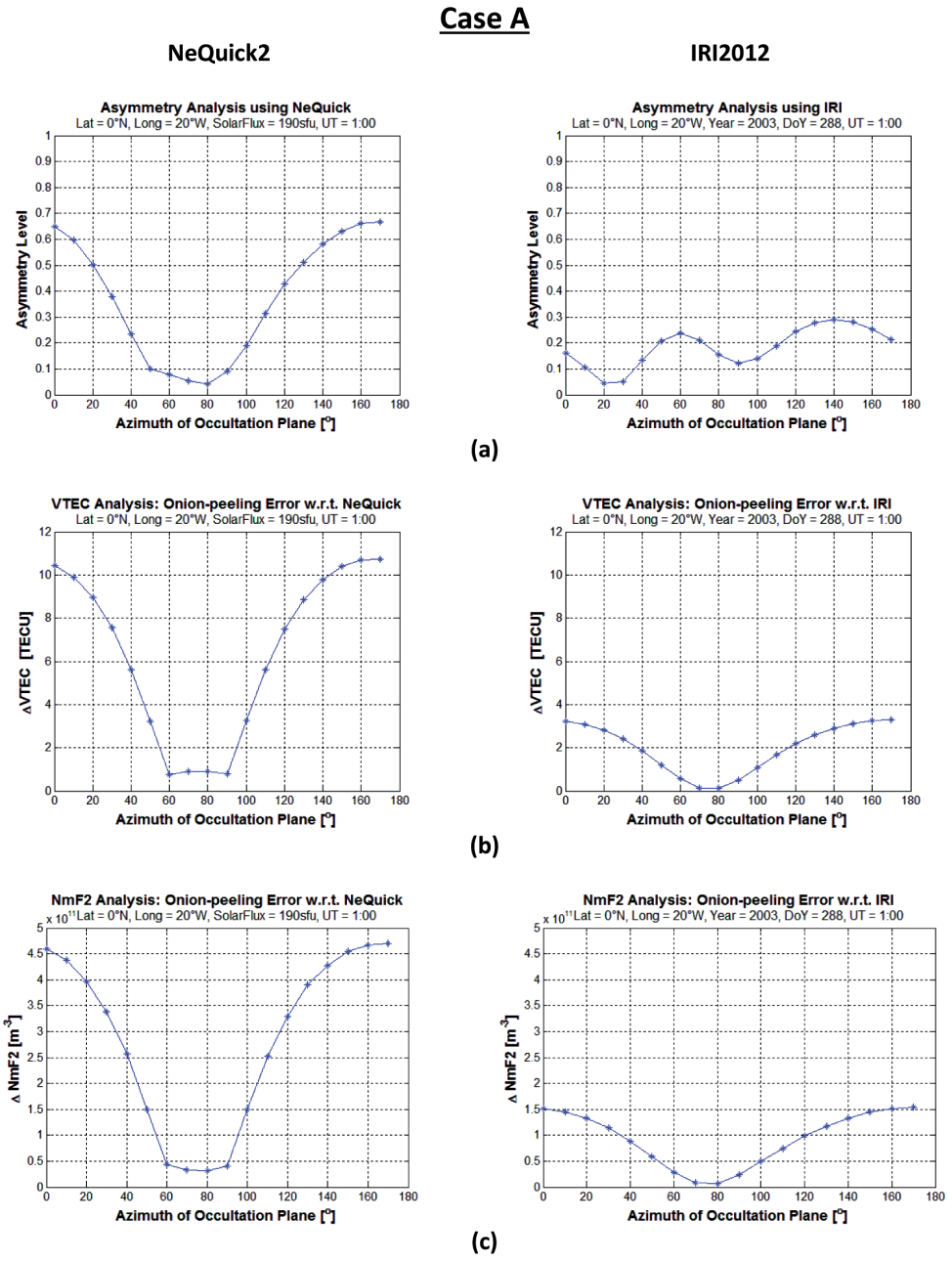

Figure 7 (a), (b) and (c) show asymmetry, ΔVTEC and ΔNmF2 calculations along occulted ray paths calculated using NeQuick2 and IRI2012 w.r.t. varying azimuth of occultation plane at 0°N/20°W, respectively. Left column show NeQuick2 based calculations and the right column shows IRI2012 based calculations.

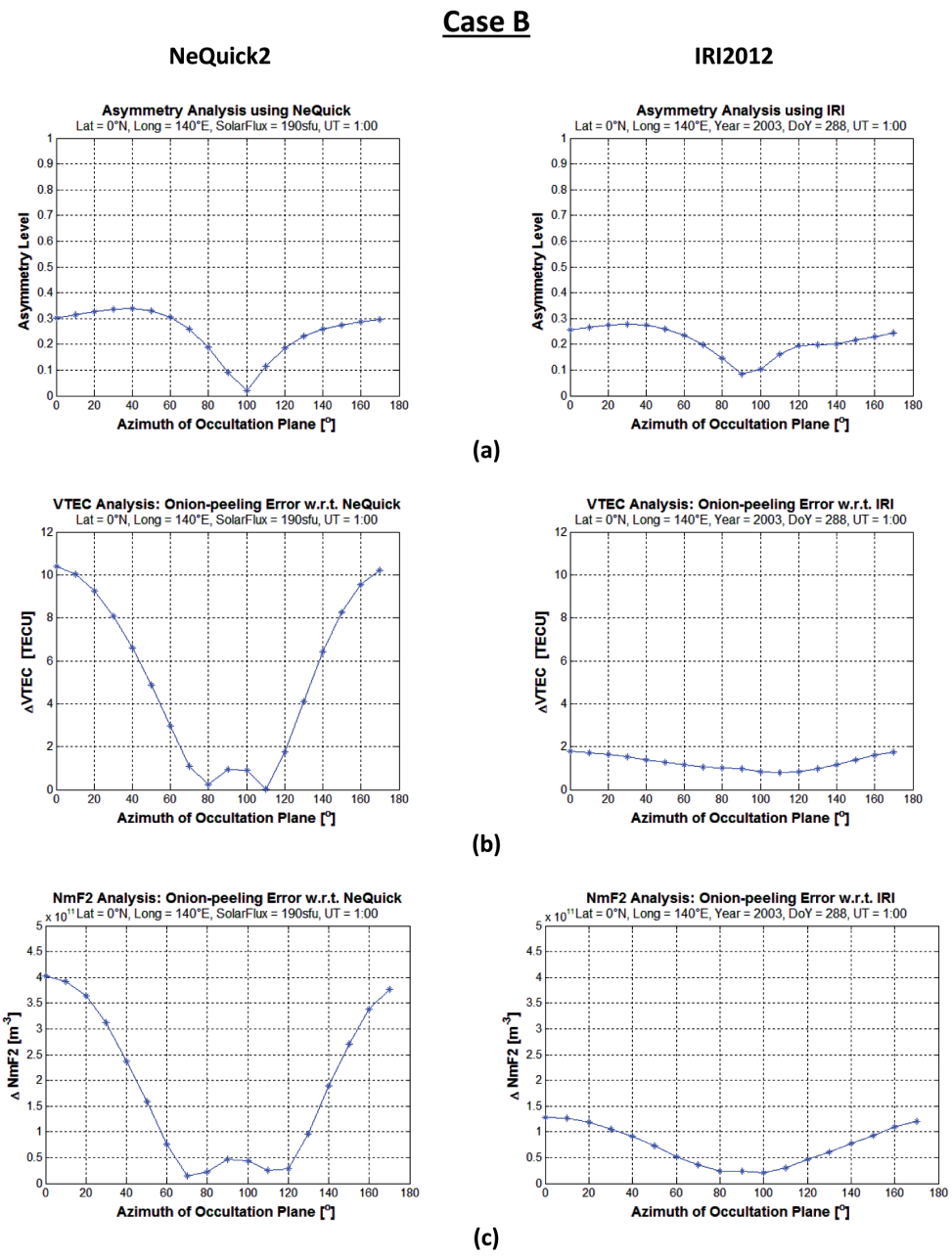

Figure 8 (a), (b) and (c) show asymmetry, ΔTEC and ΔNmF2 calculations along occulted ray paths calculated using NeQuick2 and IRI2012 w.r.t. varying azimuth of occultation plane at 0°N/140°E, respectively. Left column show NeQuick2 based calculations and the right column shows IRI2012 based calculations.

It can be clearly observed that our asymmetry index produce reliable results irrespective of the background ionosphere used to evaluate asymmetry values. However, we have different results for different electron density models at the same geographical location, UT and similar solar activity conditions. This may be because NeQuick2 and IRI2012 treat electron density calculations differently in spite of the fact that both models use same solar indices recommended by ITU.

7 CONCLUSION AND FUTURE WORK

In this work, we tried to evaluate ionospheric asymmetry using radio occultation technique with the help of 'best-model map'. Our initial results show that our asymmetry index is a good indicator of Onion-peeling retrieval errors. A good correlation has been found between our asymmetry evaluation and Onion-peeling retrieval errors considering two different background ionospheric models. It was observed that the results obtained using both models are significantly different in spite of the fact that they were simulated at the same location, UT and solar activity conditions. This may be because both electron density models evaluation electron density in quite different way which in turn provide a different background ionosphere for same parametric set. Therefore, the identification of the model which best suits the particular solar activity conditions is important to be identified before being used as background ionospheric model. This led us to use the concept of 'best model maps' in this paper. These so called best model maps show, w.r.t. to a geographical location and UT, which model performs better than the other. It has been observed that the careful consideration of background ionospheric model may help improving the results significantly in evaluating asymmetry in the ionosphere for a particular case study. In this work, we have been limited to only two cases based on their different background ionospheric conditions. In future, we will try to evaluate the ionospheric asymmetry using combination of different models with the help of the best model maps at a larger scale over the globe. Moreover, it is also foreseen, in our ionospheric asymmetry assessment, to include other 3D electron density models such as Multi-Instruement Data Analysis System (MIDAS) (Mitchell C. N. et al. 2002).

ACKNOWLEDGMENT

This research work is undertaken under the framework of the TRANSMIT ITN (www.transmitionosphere.net), funded by the Research Executive Agency within the 7th Framework Program of the European Commission, People Program, Initial Training Network, Marie Curie Actions - GA no. 264476.

REFERENCES

1. Anthes R. A., Ector, D., Hunt D. C., Kuo Y-H., Rocken C., Schreiner W. S., Sokolovskiy S. V., Syndergaard S., Wee T-K., Zeng Z. P., Bernhardt A., Dymond K. F., Chen Y., Liu H., Manning K., Randel W. J., Trenberth K. E., Cucurull L., Healy S.B., Ho S-P., McCormick C.T., Meehan K., Thompson D.C. & Yen N.L. (2008). The COSMIC/FORMOSAT-3 Mission: Early Results. *Bulletin of the American Meteorological Society.* Vol. 89, pp. 313–333, doi: 10.1175/BAMS-89-3-313.
2. Austen J. R., Franke S. J., Liu C.H. (1988). Ionospheric imaging using computerized tomography. *Radio Science,* Vol. 23, No. 3, pp. 299–307.
3. Bilitza, D., Reinisch B.W. (2008). International Reference Ionosphere 2007: Improvements and new parameters. *Advances in Space Research.* 42(2008), pp. 599–609.
4. Gorbunov M.E. (1996). Three-dimensional satellite refractive tomography of the atmosphere: A numerical simulation. *Radio Science.* Vol. 31, pp. 95–104.
5. Gorbunov, M.E. (2001). Analysis and validation of GPS/MET radio occultation data. *Journal of Geophysical Research.* Vol. 106, No. D15, pp. 17, 161–17, 169.
6. Hajj G.A., Kursinski E. R., Romans L.J., Bertiger W.I., Leroy S.S. (2002). A technical description of atmospheric sounding by GPs occultation. *Journal of Atmospheric and Solar-Terrestrial Physics.* 64 (2002), pp. 451–469.
7. Healy S.B., Haase J., Lesne O. (2002). Abel transform inversion of radio occultation measurements made with a receiver inside the Earth's atmosphere. *Annales Geophysicae.* 20, pp. 1253–1256.
8. Hernandez-Pajares M., Juan J. M., Sanz J. (2000). Improving the Abel inversion by adding ground GPS data to LEO radio occultation in ionosphere sounding. *Geophysical research letters.* Vol. 27, no. 16, pp. 2473–2476.
9. Kursinsky E.R. (1997). Observing Earth's atmosphere with Radio Occultation measurements using the Global Positioning System. *Journal of Geophysical Research.* Vol. 102, No. D19, pp. 23, 429–23, 465, October 20.
10. Leitinger R., Ladreiter H.P., Kirchengast G. (1997). Ionosphere tomography with data from satellite reception of GNSS signals and ground reception of NNSS signals. *Radio Science.* 32(4), pp. 1657–1669.
11. Luntama J-P., Kirchengast G., Borsche M., Foelsche U., Steiner A., Healy S., Von Engeln A, O'Clerigh E. & Marquardt C. (2008). Prospects of the EPS GRAS Mission For Operational Atmospheric Applications. *Bulletin of the American Meteorological Society.* Vol. 89, pp. 1863–1875, doi: 10.1175/2008BAMS2399.1
12. Mitchell C. N., Cannon P.S., Spencer P.S.J. (2002). Multi-Instrument Data Analysis System (MIDAS) Imaging of the Ionosphere. *Report for the United States Air Force European Office of Aerospace Research and Development.*
13. Nava B., Coisson P., Radicella S.M. (2008). A new version of the NeQuick ionosphere electron density model. *Journal of Atmospheric and Solar Terrestrial Physics.* 70 (2008), pp. 1856–1862.
14. Satya Srinivas V., Sarma, A.D., Swamy K.C.T., Satyanarayana, K., Performance evaluation of IRI-2007 at equatorial latitudes and its Matlab version for GNSS Applications, *Advances in Space Research,* In press, 2013.

15. Shaikh M.M., Notarpietro R., Nava B. (2013). The impact of spherical symmetry assumption on radio occultation data inversion in the ionosphere: An assessment study. *J. Adv. Space Res.* (2013), http://dx.doi.org/10.1016/j~.asr.2013.10.025
16. Shaikh M.M., Notarpietro R., Nava B. (2012). GNSS Radio Occultation: Identification of Criticism in electron density profile retrieval during moderate/high solar activity. *Proceedings of 6th GNSS Vulnerabilities and Solutions Conference 2012.*
17. Ware R.H., Exner M., Feng D., Gorbunov M., Hardy K.R., Herman B., Kuo Y.H., Meehan T.K., Melbourne W.G., Rocken C., Schreiner W., Sokolovskiy S.V., Solheim F., Zou X., Anthes R., Businger S. & Trenberth K. (1996). GPS Sounding of the Atmosphere from Low Earth Orbit: Preliminary Results. *Bulletin of the American Meteorological Society.* Vol. 77, pp. 19–40.
18. Ya'acob N., Abdullah M., Ismail M., Bahari S. A., Ismail M. K. (2008). Ionospheric Mapping Function for Total Electron Content (TEC) Using Global Positioning System (GPS) Data in Malaysia. *IEEE International RF and Microwave Conference Proceedings,* 978-1-42442867-0/08, pp. 386–390.

Faculty of Maritime Studies
University of Rijeka, Croatia

Royal Institute of Navigation
Science Technology Practice

7th GNSS
Vulnerabilities and Solutions Conference

UTILIZATION OF GPS IN PT PERFORMANCE EVALUATION

Marko Matulin, Štefica Mrvelj, Niko Jelušić, Hrvoje Gold

Fakultet prometnih znanosti
Borongajska cesta 83A, 10000 Zagreb, Croatia
E-mail: mmatulin@fpz.hr

ABSTRACT. *The focus of this paper is to demonstrate how Global Positioning System (GPS) can be utilized in order to conduct comprehensive data collection process and analysis of public transport (PT) performances. During CIVITAS ELAN project, GPS receivers were installed in trams in order to evaluate the impact of different project measures. We show how detailed analysis of obtained GPS data enabled us to conduct the evaluation of PT network performances on micro and macro level. The data was also used to define PT priority schemes which were implemented at 3 signalized intersections as a part of the project. Although valuable data was obtained, the paper also points out several disadvantages of this data collection methodology, which can be useful for future research endeavours.*

KEY WORDS: *Public transport performances, Data collection, Evaluation*

1 INTRODUCTION

In the variety of public services offered to the citizens of major cities, public transport (PT) service is certainly one of the main ones. In the European context, the PT is often referred as 'the backbone of the cities'. However, nowadays there are several challenges which PT operators are facing. The main two are: a) the operators are continuously struggling with the need to reduce operational costs and b) they have to keep up with the increasing passenger' requirements in terms of the quality of delivered service. It is clear that these two challenges are somewhat in collision with each other. On one side there are passengers who demand fast and reliable service which has to be provided in the state-of-the art PT vehicles, while on the other side PT operators are often dealing with the reduction of public funding, increasing energy prices and competition on the transportation market.

From 2008 to 2013 City of Zagreb implemented the CIVITAS ELAN project - large scale collaborative project which is a part of CIVITAS Initiative, (Anon., n.d.). One of the main project objectives was to optimize PT service by implementing various measures which, in turn, raised the quality of PT service for the end users. Specifically, new PT vehicles were introduced in operation (buses and trams) with better operational characteristics, intermodal conditions were improved as well as safety and security conditions, and PT priority system for trams was installed. These measures had to ensure that PT stayed one of the main transport modes in the city and that PT service becomes fast and reliable.

From the traffic engineering point of view the last abovementioned project activity (introduction of PT priority system) was especially interesting, because it imposed the need for detailed data analysis of traffic and PT network. The project measures were implemented in a predefined demonstration area within the city (approx. 10 km^2 around the city centre area). This corridor covered only one part of the total length of specific tram lines. This meant that improvements, achieved with the PT priority system, would occur only on specific network segments, while there would be no changes in other parts of the PT network. Moreover, due to technical issues which arose, the project team decided to implement the priority system on 3 intersections. It was, therefore, necessary to investigate tram network performances per specific segment of a line, in order to enable us to draw evaluation conclusions per specific intersection if necessary. In turn, this required very detailed set of data which describe the performances of PT network.

The first question which arose was *what where the common indicators of tram network performances?* By reviewing the literature on this matter, we found that

PT performances are often expressed by a mix of quantitative and qualitative indicators. This lack of standardisation was indicated long ago by Pullen who argued for improved definition and clarification (Pullen, 1991). Owing to this fact, the quantitative indicators are sometimes only represented by the monetised values of network delay, operation time etc., which means that PT network performances are expressed from the perspective of economists and that kind of analyses do not necessarily give an insight into full impact of different measures (e.g. this is the case in Currie et al., 2005, Currie et al., 2007 or Vedagiri and Arasan, 2009).

In (Harrison et al., 1998) authors defined "hard" quality indicators as those which are more quantifiable (e.g. access time) and "soft" quality indicators as "non-journey time attributes" such as information provision, staff attitude and satisfaction. Prioni and Hensher grouped bus performance indicators into six quality dimensions, also deploying the concept of "hard" and "soft" indicators (Prioni and Hensher, 2000). In (Egmond et al., 2003) four levels of PT performances are defined: external, strategic, tactical and operational. Different levels are focusing on population attributes, population density, political interest and regulations, organisational and financial framework analysis, accessibility of different PT modes, intermodality, marketing and information. Some authors devote higher importance to the user perspective of PT performance and argue that "hardcore" performances are good indicator for service provider, but "true" performance can only be evaluated with customer satisfaction survey (e.g. Thompson and Schofield, 2007).

For the purpose of evaluating different impacts of PT priority system, we were focused exclusively on the operational performances of specific tram lines which traverse through the corridor. The vagueness of PT performance definitions encouraged us to define our own evaluation indicators which were then used for evaluation of the PT priority system in Zagreb. Defined indicators required detailed data sets so that evaluation of operational performances would be possible per specific segment of the line. For this purpose it was decided to use GPS tracking of trams over the period of two weeks before and two weeks after the implementation of the PT priority. Here, we bring the results of this analysis and point out several disadvantages of this data collection methodology.

The remainder of this paper is structured as follows: Section 2 describes our performance indicators used in evaluation, brief description of data collection methodology can be found in Section 3, Section 4 brings results and short discussion while Section 5 concludes.

2 DEFINITION OF PERFORMANCE INDICATORS

A single journey of a tram has two terminals (origin terminal A and destination terminal B) and a finite number of PT stops and signalised intersection in between (see Figure 1). The main impact of the PT priority system on the operational performance of trams is the reduction of intersection delay. This reduction should result in a decrease of travel times between adjacent PT stops and terminals of the same PT line, but sometimes this is not the case due to the various background impacts: mixed traffic conditions, number of PT users, number of PT vehicles in operation, time-gap between PT vehicles and partial implementation of PT priority system, (Matulin et al., 2010).

For instance, due to mixed traffic conditions, in the peak periods of the day, when transport demand is at its highest levels, queues of cars can be formed in front of signalised intersections, and block the tram tracks. The tram pathway can also be blocked by traffic accidents which results in further performance deterioration. In this case, positive impacts of giving priority to trams at signalised intersections can be easily cancelled out, because trams cannot reach the intersections. Sun et al. detected and described the complex interactions between PT vehicles and general traffic vehicles in such mixed traffic environments (Sun et al., 2008). In addition, possible increase of PT users could require more PT vehicles in order to satisfy the increased transport demand. More trams can increase the possibility of congestion. This means that the time-gap between two trams can become too small, so several trams may arrive at the same PT stop at the same time, which then negatively affects boarding and alighting times. In this case trams will spend more time at the PT stops, thus their round trip times and passenger travel times will increase as well, even though trams might get the priority at intersections.

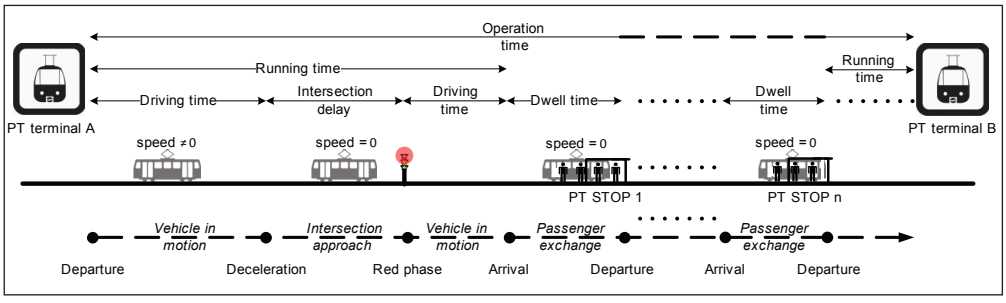

Figure 1 Operation time decomposition (Matulin et al., 2011)

Effects of the PT priority system could also be reduced if the system itself is partially implemented. This can happen in two cases:

1. If PT priority system is not implemented on all signalized intersections of the selected line/corridor (in this case PT vehicles could pass through one intersection and cause a blockage on the consecutive intersection).

2. If priority equipment is not installed in all PT vehicles which travel on the same line/corridor (in this case a vehicle which is not equipped with the priority equipment could disturb traffic flow of the PT vehicles which are equipped).

All of the above described background impacts affect the operational performance of trams. During the analysis of the possible benefits of a PT priority system, such impacts must not be ignored. In our case, when the PT priority system is implemented only on a part of the tram line, certain improvements which are achieved on a micro level (e.g. on specific intersection or between two adjacent PT stops) could remain undetected if operational performance of each line segment is not evaluated. Therefore, we decomposed tram operation time into smaller time segments and defined evaluation indicators (this is depicted in Figure 1 and described in Table 1).

Table 1 Indicator description (Matulin et al., 2011)

Level	Indicator	Description
Macro	Operation time	The time that elapses from the departure of a PT vehicle from a terminal to the arrival at the other terminal on the line.
	Operating speed	The average journey speed of PT vehicles between an origin and a destination terminal, including any delay arisen in the course of the journey.
Micro	Dwell time	The time which a vehicle spends on PT stop due to passenger exchange. The time needed for opening and closing the doors is also a part of dwell time.
	Intersection delay	The time that elapses from the arrival of a PT vehicle at an intersection approach to its passing through the intersection.
	Speed per segment	Vehicle speed for predefined segments of the line (a segment represents a part of PT line between two adjacent PT stops).
	Running time	The time that elapses from the departure of a PT vehicle from a stop to the arrival of a PT vehicle at the adjacent stop.
	Driving time	The time that a vehicle spends in motion.

Since we conducted the measurements in predefined demonstration area of the project (corridor), by the operation time we consider the time that elapses from the entering of a PT vehicle into the corridor to the exit from the corridor.

3 DATA COLLECTION

In order to collect the data about the operation time and its segments we decided to use GPS tracking of trams. Four GPS receivers were installed in four trams travelling on the same line. Measurements were conducted twice: before and after implementation of the PT priority system. Recordings took place in two week period (Monday to Sunday), each day from 6 a.m. to 10 p.m. Every GPS receiver recorded the vehicle position and actual speed each second. GPS data was extracted from the devices and imported in an Excel table for the analysis. Setting up the recording interval to one second provided us with the high resolution of the measurement which was important for the performance evaluation by defined indicators. Nevertheless, apart from good measurement resolution which was highly beneficial to us, this method also created some issues which had to be resolved in the process of data analysis.

The issues were manifested as a mismatch between geographical locations of the control points (PT stops or signalized intersections) and actual tram position recorded by GPS receiver as indicated on Figure 2a and Figure 2b (triangles on the GPS track represent tram in motion and rectangles represent that tram is stopped). GPS vehicle tracking method gives very accurate results for the tram operation time and average commercial speed. Nevertheless, when the tram speed is around 0 km/h, due to the GPS signal reflection, GPS tracks can be in offset to about 30-40 meters. Without map matching (Figure 2b.) it is impossible to determine actual vehicle position in a specific moment of time, which is important for calculation of different operation time segments.

In case when two trams arrive on the same stop in the same time, as it is depicted in Figure 3a, with the GPS vehicle tracking method it is not possible to determine the exact reason why tram B stopped. In this specific situation, geographical location of the PT stop and the position of tram B, when the speed v is 0 km/h, do not overlap. Knowing the GPS signal reflection problems, during the data processing it is hard to determine whether the tram B has reached the PT stop and started to alight/board passengers or another vehicle (tram or even individual vehicle) was occupying the PT stop at the time.

Furthermore, when the PT stop is located directly in front of signalized intersection and the “red” period is activated (Figure 3b), intersection delay and dwell time measurements are incomplete. This results in inaccurate calculation of driving time and speed per segment. While processing the GPS data it can be easily detected when the tram speed was 0 km/h, but in this case the difference between dwell time and intersection delay cannot be recognized.

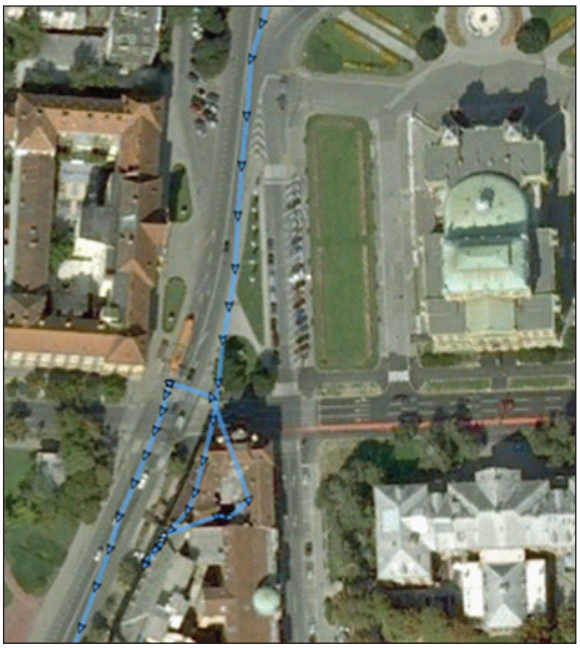

Figure 2a Recorded GPS track, (Jelušić et al., 2010)

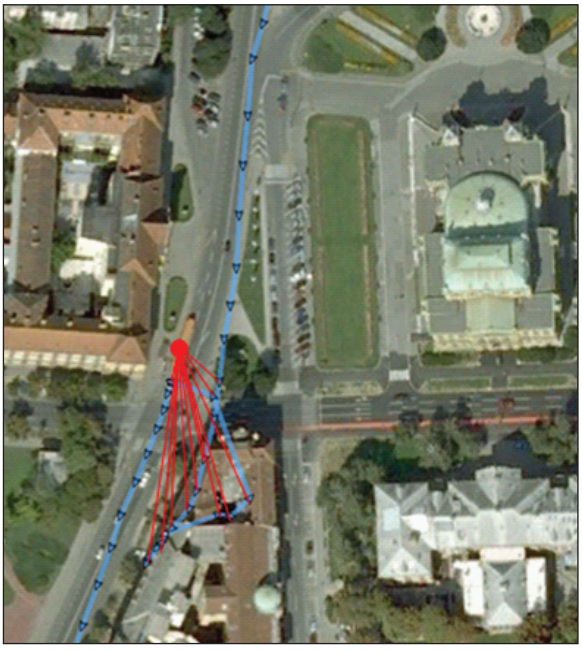

Figure 2b Recorded GPS track and actual PT vehicle position, (Jelušić et al., 2010)

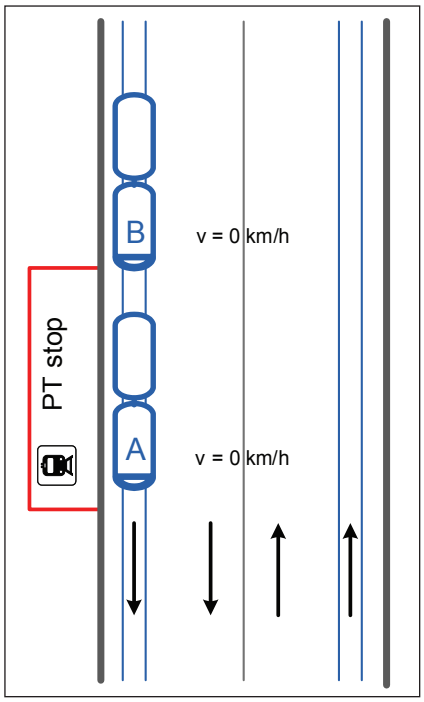

Figure 3a Arrival of two trams on the same PT stop, (Jelušić et al., 2010)

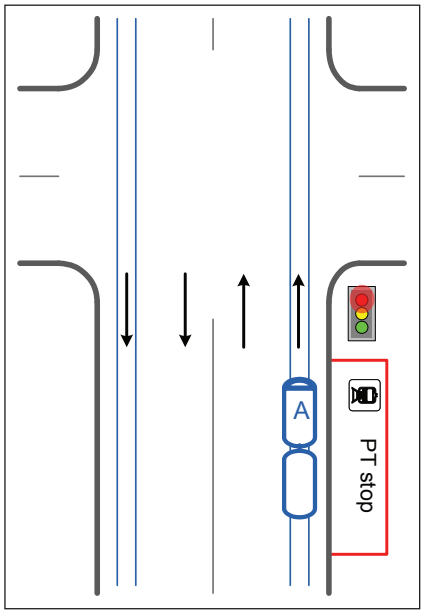

Figure 3b Specific geographical locations of PT stop, (Jelušić et al., 2010)

4 IMPACT OF PT PRIORITY SYSTEM

In Table 2 we present the results of the data analysis, i.e. the performance of the tram network in the demonstration corridor before and after the implementation of the PT priority system (only for one direction of travel). The gray coloured rows represent the location where PT priority equipment is installed.

Operation time is calculated by adding up tram running time and dwell time. Operating speed is then derived by dividing the corridor length (2,855 m) and operation time. Average running time and average driving time is presented between two consecutive PT stops; average dwell time is presented for each PT stop, while average intersection delay is presented for each intersection in the corridor.

Table 2 Results

Indicator	Before implementation		After implementation		Difference: After – Before	
Operation time [hh:mm:ss]	Average: 00:14:58		Average: 00:14:00		- 58 seconds, i.e. - 6.46%	
Operating speed	Average: 11.45 km/h		Average: 12.24 km/h		+ 0.79 km/h, i.e. + 6.9%	
Running time [hh:mm:ss]	PT stop_sequence number	Average running time between two stops	PT stop_sequence number	Average running time between two stops	PT stop_sequence number	Difference
	veslačka_1	0:01:05	veslačka_1	0:00:59	veslačka_1	- 6 seconds
	prisavlje_2	0:01:24	prisavlje_2	0:01:38	prisavlje_2	+ 14 seconds
	vjesnik_3	0:01:08	vjesnik_3	0:00:52	vjesnik_3	- 16 seconds
	učit_akademija_4	0:02:32	učit_akademija_4	0:02:17	učit_akademija_4	- 15 seconds
	zagrebčanka_5	0:00:56	zagrebčanka_5	0:00:57	zagrebčanka_5	+ 1 second
	stud_centar_6	0:01:29	stud_centar_6	0:01:27	stud_centar_6	- 2 seconds
	vodnikova_7	0:01:15	vodnikova_7	0:01:11	vodnikova_7	- 4 seconds
	trg_marš_tita_8		trg_marš_tita_8		trg_marš_tita_8	
	(PT priority)	0:01:49	*(PT priority)*	0:01:26	*(PT priority)*	- 23 seconds
	frankopanska_9		frankopanska_9		frankopanska_9	
	Cumulative:	**0:11:38**	**Cumulative:**	**0:10:47**	**Cumulative:**	**- 51 seconds - 7.3%**
	Average-average:	**0:01:27**	**Average-average:**	**0:01:21**	**Average-average:**	**- 6 seconds - 6.89%**

Indicator	Before implementation		After implementation		Difference: After – Before	
Driving time [hh:mm:ss]	PT stop_sequence number	Average driving time between two stops	PT stop_sequence number	Average driving time between two stops	PT stop_sequence number	Difference
	veslačka_1	0:00:54	veslačka_1	0:00:59	veslačka_1	+ 5 seconds
	prisavlje_2	0:01:03	prisavlje_2	0:01:13	prisavlje_2	+ 10 seconds
	vjesnik_3	0:01:06	vjesnik_3	0:00:52	vjesnik_3	- 14 seconds
	učit_akademija_4	0:01:25	učit_akademija_4	0:01:12	učit_akademija_4	- 13 seconds
	zagrebčanka_5	0:00:55	zagrebčanka_5	0:00:57	zagrebčanka_5	+ 2 seconds
	stud_centar_6	0:00:45	stud_centar_6	0:00:53	stud_centar_6	+ 8 seconds
	vodnikova_7	0:01:00	vodnikova_7	0:01:06	vodnikova_7	+ 6 seconds
	trg_marš_tita_8		trg_marš_tita_8		trg_marš_tita_8	
	(PT priority)	0:00:26	*(PT priority)*	0:00:22	*(PT priority)*	- 4 seconds
	frankopanska_9		frankopanska_9		frankopanska_9	
	Cumulative:	**0:07:34**	**Cumulative:**	**0:07:34**	**Cumulative:**	**0 0%**
	Average-average:	**0:00:57**	**Average-average:**	**0:00:57**	**Average-average:**	**0 0%**
Intersection delay [hh:mm:ss]	Name of the intersection	Average inter-section delay	Name of the intersection	Average inter-section delay	Name of the intersection	Difference
	Veslačka	0:00:01	Veslačka	0:00:00	Veslačka	- 1 second
	Prisavlje	0:00:11	Prisavlje	0:00:05	Prisavlje	- 6 seconds
	Slavonska	0:00:21	Slavonska	0:00:25	Slavonska	+ 4 seconds
	Gagarinov	0:00:02	Gagarinov	0:00:00	Gagarinov	- 2 seconds
	Vukovarska	0:01:07	Vukovarska	0:01:05	Vukovarska	- 2 seconds
	Koturaška	0:00:01	Koturaška	0:00:00	Koturaška	- 1 second
	Tratinska	0:00:33	Tratinska	0:00:28	Tratinska	- 5 seconds
	Vodnikova	0:00:11	Vodnikova	0:00:06	Vodnikova	- 5 seconds
	Kršnjavoga	0:00:14	Kršnjavoga	0:00:05	Kršnjavoga	- 9 seconds
	Perkovčeva	0:00:01	Perkovčeva	0:00:00	Perkovčeva	- 1 second
	Hebrangova	0:00:43	Hebrangova	0:00:49	Hebrangova	+ 6 seconds
	Deželićeva	0:00:25	Deželićeva	0:00:04	Deželićeva	- 21 seconds
	Varšavska	0:00:11	Varšavska	0:00:11	Varšavska	No change
	Cumulative:	**0:04:01**	**Cumulative:**	**0:03:18**	**Cumulative:**	**- 43 seconds - 17.84%**
	Average-average:	**0:00:19**	**Average-average:**	**0:00:15**	**Average-average:**	**- 4 seconds - 21.04%**

Indicator	Before implementation		After implementation		Difference: After – Before	
	PT stop_sequence number	Average dwell time	PT stop_sequence number	Average dwell time	PT stop_sequence number	Difference
Dwell time [hh:mm:ss]	veslačka_1	0:00:18	veslačka_1	0:00:16	veslačka_1	- 2 seconds
	prisavlje_2	0:00:19	prisavlje_2	0:00:15	prisavlje_2	- 4 seconds
	vjesnik_3	0:00:13	vjesnik_3	0:00:14	vjesnik_3	+ 1 second
	učit_akademija_4	0:00:14	učit_akademija_4	0:00:17	učit_akademija_4	+ 3 seconds
	zagrebčanka_5	0:00:14	zagrebčanka_5	0:00:18	zagrebčanka_5	+ 4 seconds
	stud_centar_6	0:00:44	stud_centar_6	0:00:28	stud_centar_6	- 16 seconds
	vodnikova_7	0:00:16	vodnikova_7	0:00:20	vodnikova_7	+ 4 seconds
	trg_marš_tita_8	0:00:44	trg_marš_tita_8	0:00:45	trg_marš_tita_8	+ 1 second
	frankopanska_9	0:00:18	frankopanska_9	0:00:20	frankopanska_9	+ 2 seconds
	Cumulative:	**0:03:20**	**Cumulative:**	**0:03:13**	**Cumulative:**	**- 7 seconds - 3.5%**
	Average-average:	**0:00:22**	**Average-average:**	**0:00:21**	**Average-average:**	**- 1 seconds - 4.55%**

As it can be seen from the table, GPS vehicle tracking provided us with enough data to be able to conduct very detailed evaluation of network performances. It made evaluation possible on a micro level, i.e. evaluation per specific intersection, and on the macro level, i.e. for the whole corridor.

The data shows that average tram operation time was decreased by 58 seconds or 6.46%, while operating speed is increased by 6.9%. The largest share of these 58 seconds comes from the reduction of intersection delay on Deželićeva intersection (indicated by the gray rows). The average delay on that intersection alone is reduced by 21 seconds. Cumulative intersection delay in the corridor was reduced by 43 seconds or 17.84%. Furthermore, cumulative running time was also decreased by 51 seconds or 7.3% which was expected due to the reductions of intersection delay. However, it must be noted that cumulative dwell time was reduced by 7 seconds which also contributed to these improvements.

On a micro level we can see that average running time on the part of the line where the priority is introduced shows that between PT stops trg_marš_tita_8 and frankopanska_9 it was reduced by significant 23 seconds. Of course this is due to the already mentioned reduction of intersection delay at Deželićeva intersection by 21 seconds.

5 CONCLUSION

The introduction of PT priority system imposed different research requirements in all phases of its implementation and evaluation. In this paper we were focused only on the last phase, i.e. evaluation, for which we defined several evaluation

indicators. Due to specific implementation conditions and restraints (various background impacts and partial implementation of the system) it was recognized that only full data sets will suffice if we want to be able to conduct detailed performance evaluation of the tram network. The ability to record tram speed and position each second was very much appreciated, thus GPS vehicle tracking method was selected.

As it can be seen from the presented results, this data collection method made evaluation possible on a micro level, i.e. evaluation per specific intersection, and on the macro level, i.e. for the whole corridor. This ability was crucial for the project evaluation and we believe that this can be highly beneficial for future investigations of PT network performances.

Nevertheless, we were also able to identify few drawbacks of this methodology. Two main ones were: a) mismatch between geographical locations of the control points (PT stops and intersections) and actual tram position recorded by GPS receiver which requires additional attention in the data analysis process, and b) inability to distinguish dwell time and intersection delay if the PT stop is located directly in front of signalized intersection.

Based on these findings we can conclude that GPS vehicle tracking method provides enough data for very detailed evaluation, however, it is wise to supplement it with other methods (e.g. on-sight measuring, video image analysis etc.) in order to avoid abovementioned drawbacks.

ACKNOWLEDGMENTS

This paper is inspired by the research undertaken in the CIVITAS ELAN project (Grant Agreement No.: ELAN TREN/FP7TR/218954/"ELAN"). We wish to thank all project partners, especially Zagreb's public transport company (ZET) for enabling us to conduct the measurements.

REFERENCES

1. Anon., n.d. *CIVITAS Initiative*. [Online] Available at: http://www.civitas-initiative.eu [accessed 2012].
2. Currie, G., Sarvi, M. and Young, B. (2005). Road space allocation for public transport priority. *Proceedings of the AITPM National Conference*, Brisbane.
3. Currie, G., Sarvi, M. and Young, B. (2007). A new approach to evaluating on-road public transport priority projects: balancing the demand for limited road space. *Transportation*, **34**, pp. 413–428.
4. Egmond, P., Nijkamp, P. and Vindigni, G. (2003). *A comparative analysis of the performance of urban public transport systems in Europe*. Oxford: Blackwell Publishing Ltd.

5. Harrison, S., Henderson, G., Humphreys, E. and Smyth, A. (1998). Quality bus corridors and green routes: can they achieve a public perception of 'permanence' of bus services? *Proceedings of the European Transport Conference, PTRC*, London.
6. Jelušić, N., Mrvelj, Š. and Matulin, M. (2010). Data collection method analysis for evaluation of public transport system performances. *Proceeding of the 17th World ITS Congress*, Busan.
7. Matulin, M., Mrvelj, Š. and Gold, H. (2010). Evaluating the public transport priority system – Identifying background data impact. *Proceedings of the 17th ITS World Congress*, Busan.
8. Matulin, M., Mrvelj, Š. and Jelušić, N. (2011). Two-level evaluation of public transport system performances. *Promet – Traffic & Transportation, Scientific Journal on Traffic and Transportation Research*, **23**(5), pp. 329–411.
9. Prioni, P. and Hensher, D. A. (2000). Measuring service quality in scheduled bus services. *Journal of Public Transportation*, **2**(3), pp. 51–74.
10. Pullen, W. T. (1991). *The measurement of the quality of local bus services with respect to the effects of bus deregulation in Scotland*. Newcastle: University of Newcastle upon Tyne. Ph.D. thesis.
11. Sun, H., Si, B. and Wu, J. (2008). Combined model for flow assignment and mode split in two-modes traffic network. *Journal of Transportation System Engineering & IT*, **8**(4), pp. 77–82.
12. Thompson, K. and Schofield, P. (2007). An investigation of the relationship between public transport performance and destination satisfaction. *Journal of Transport Geography*, **15**, pp. 135–144.
13. Vedagiri, P. and Arasan, V. (2009). Estimating modal shift of car travelers to bus on introduction of bus priority system. *Journal of Transport System Engineering and Information Technology*, **9**, pp. 120–129.

Faculty of Maritime Studies
University of Rijeka, Croatia

Royal Institute of Navigation
Science Technology Practice

7th GNSS
Vulnerabilities and Solutions Conference

TRAM ELECTRIC GRID INFLUENCE ON GPS RECEPTION

Marko Ševrović[1], Mario Miller[2], Bojan Jovanović[3]

[1] University of Zagreb, Faculty of Transport and Traffic Sciences, Zagreb, Croatia
E-mail: marko.sevrovic@fpz.hr

[2] University of Zagreb, Faculty of Geodesy, Zagreb, Croatia
E-mail: mmiler@geof.hr

[3] E-mail: bobofpz@gmail.com

ABSTRACT. *In this article we tested the statistical hypothesis that tram electric power lines have significant influence on the quality of the low cost GPS signal reception in urban areas. In order to determine the impact of tram power lines on the quality of GPS signal reception, we have conducted two measurements on the Borongaj tram turnaround in the city of Zagreb. In order to gather the necessary data, we used two GPS receivers that were set up on a tripod at a height of 1.5 m from the ground. GPS receivers were thereby placed at two predefined reference sites with precisely defined geographic coordinates. The first GPS receiver was located near the tram tracks, while the other was located in the parking about 80 meters from the tram turnaround. Information about the location of GPS receivers were recorded every second over a period of 60 and 90 min respectively.*

KEY WORDS: *GPS applications in the transport system, measuring the quality of GPS signal reception, the impact of tram traffic, precision of locating GPS receivers in urban areas*

1 INTRODUCTION

The first part of the article considers the various types of satellite positioning system applications in the road transport system, and analyzes the advantages and disadvantages of its implementation in urban areas. The potential applications of GPS systems in a variety of ITS applications are also considered. This part of the article specifically deals with the problems of GPS signal degradation in urban areas.

The second part of this paper describes the methodology of data collection which includes the process of determining location of reference sites and the method of recording GPS receiver location. The technical characteristics of the applied GPS receivers as well as the characteristics of the research area are also described.

In the third part of the paper a statistical analysis of the data collected was conducted in order to determine the degree of influence of tram traffic on the quality of GPS signal reception. We have conducted a comparison between the values of the geographic coordinates which were measured by consumer grade GPS receiver and exactly determined geographic coordinates on survey and control point. Statistical analysis was conducted to determine the accuracy and precision measures of GPS receivers as well as median and standard deviation of the measured geographic coordinates. The values of Root Mean Squared Error and Circular Error probability for the observed statistical sample are also determined. Based on the collected data we tested the hypothesis about the impact of tram traffic on the quality of GPS signals.

The fourth part of the paper presents and explains the results of conducted research. In the last part of the paper we discussed the possibilities and suggestions for further research related to the issue of the impact of tram traffic on the quality of the GPS signal reception in urban areas.

2 APPLICATION OF GPS SYSTEM IN URBAN AREAS

Satellite positioning systems (Spilker 1996) are increasingly being applied in different areas of the transport system. Application of the GPS system is particularly important in determination of the current position and velocity of individual transport entities in the road network. Based on the collected data about the current coordinates and speed of individual vehicles, it is possible to determine the trajectories of individual vehicles in the traffic stream (Dadić et al. 2006). This enables the real time measurement of the relevant parameters of traffic flow, and determination of the intensity of traffic flow intersection at

certain points of the observed road network (I. Dadić, D. Škaro, K. Vidović, M. Ševrović, M. Šoštaric, D. Jeremić 2012). Based on the GPS system it is possible to optimize the movement of traffic entities in the transport network by finding the shortest path between the defined positions of origin and destination points. GPS systems are also applied in a fleet management system for the monitoring of individual transport and commercial vehicles and for optimization of the entire transport process.

Accurate positioning systems also allow efficient tracking of goods, which significantly increases the level of safety and reduces costs in the transport process and storage of goods. GPS systems are also increasingly being applied in Road User Charging systems. Based on the detected position of the vehicle in the road network the amount of compensation for the road infrastructure usage is determined (European Commission 2011). Satellite positioning systems can also be applied in a variety of ITS applications such as the systems for automatic detection of traffic accidents occurrence in which it is necessary to minimize the response time of emergency services.

Certain positioning and navigation systems can tolerate relatively greater deviations of the measured longitude and latitude values from the actual geographic position of the vehicle. On the other hand, systems that are more vulnerable in terms of positional accuracy such as the Road User Charging systems and emergency systems, require increased precision in determining the location of GPS receiver. More accurate differential GPS systems are used in order to improve accuracy in determining the location of the vehicle. Hihger positional accuracy can be achieved by relative positioning with control station located at precisely defined geographical coordinates. (Witte & Wilson 2005)

From the accuracy point of view, even basic consumer-grade receivers can achieve uncorrected positional accuracies within approximately 5 m of the true position in open sky environments and 20 m in urban areas (Arnold & Zandbergen 2011) (Lehtinen et al. 2008). Therefore, the average positional accuracy of consumer grade GPS receiver is between 5 and 15 meters.

Using the GPS system in ideal conditions of the full visibility of the sky, the GPS horizontal error falls below 5 m, providing an excellent framework for development of numerous applications for Intelligent Transport Systems. Several sources of positioning errors (the space weather and ionospheric disturbances, in particular) (Spilker 1996; Filjar 2008; Filjar et al. 2009; Thomas 2011; American Meteorological Society 2011) may temporarily affect the GPS positioning performance (Volpe 2001; Filjar & Huljenic 2012; Spilker 1996), but it still remains at acceptable levels of positioning errors. However, the situation deteriorates considerably in urban positioning environments, where significant

reduction of sky visibility, increased multipath effects and sudden ionospheric disturbances either separately or combined produce more frequent and notable deteriorations of GPS positioning performance (R. Filjar, M. Ševrović, I. Dadić 2012) (Dadić et al. 2012). The multipath effect of the reflection of satellite signals on objects (e.g. large buildings, land obstacles or walls, lake surfaces, hoods of cars, etc.) also encompasses position calculations. Instead of a direct signal, the receiver can detect a reflected signal or multiple reflected signals, which take a longer time to reach the receiver than a direct signal. The surrounding buildings generate a multipath effect for the receiver, which makes accurate positioning more difficult.

3 DETERMINATION OF REFERENCE POINTS AND DATA COLLECTION

In order to evaluate positional accuracy, collected data must be compared to a referece point. The location of reference points is determined with a system of higher accuracy than the receivers being used during the measurement (Trimble R8 Survay Grade GPS). The reference point is the ‘‘true’’ location of the point in question. Measurement was conducted by two identical GPS receivers (GeoChron GPS Data Logger) mounted on a tripod, which were placed directly over the reference points. The height from the control point to the antenna was measured, and accounted for when calculating observed height. Units were on average 1.5 m above the control point. Control and survey points were located in the area with no significant additional obstacles to the reception of GPS signal (Elevation mask was 10°).

The first measurement was conducted on March 13, 2013. in the morning period from 10:00 to 11:30 h, while the other measurement was carried out on April 03, 2013. in the afternoon period between 13:15 and 14:15 h. The geographic coordinates of two reference points were recorded by GPS receivers for every second during the time period of 60 min and 90 min respectively.

Trimble R8 Survay Grade GPS receiver was applied for determining the exact values of the geographic coordinates on the survey and control point in the research area. Survey point was located on the Borongaj tram turnaround directly adjacent to tram tracks, while the control point was located in the parking lot located about 80 m from the tram turnaround. During the first measurement, on the survey point a total of 6319 pairs of coordinates were recorded, while on the control point 6021 pairs of coordinates were collected during a period of 90 min. In the second measurement, a total of 4359 pairs of coordinates were recorded on the survey point, while on the control point 4406 pairs of coordinates were

recorded during the period of 60 min. During the first measurement a total of 12340 individual pairs of location coordinates were recorded on both observed locations, while in the second measurement a total of 8765 individual pairs of coordinates were collected.

Figure 1 Data collection on survey point located on the Borongaj tram turnaround directly adjacent to tram tracks.

For data collection, two GeoChron GPS loggers were used. The GeoChron GPS Data Logger incorporates an EM408 GPS receiver from GlobalSat, with a high-sensitivity SiRF Star III GPS chipset at its core. Moreover, it provides quite a high functioning autonomy, as the rechargeable built-in 1000 mAh Li-Polymer provides a continuous functioning time of around 7.4 hours and a stand-by time of around 500 hours. The device allows users to select the exact time between records, and also choose between the several available log sentences (RMC, GGA, GSA, and GSV). Moreover, the GPS logger contains a tri-color status LED, which indicates the current activity the device is carrying out. The major disadvantage of device is the lack of built-in memory.

The GeoChron GPS Data Logger relies exclusively on the external SD card (the device supports storage capacities of up to 2 GB).

GPS data logger recorded data about current date, time, as well as the longitude and latitude in the NMEA format in 4 sentences. $GPGGA sentence (Global Positioning System Fix Data) records information about the current time, latitude, longitude, altitude, number of satellites in view, the height of the geoid above the WGS84 ellipsoid, the time of the last update of the DGPS system, DGPS station ID number, and other required control information. $GPGSA sentence (GPS DOP and active satellites) records information about operation mode and the available data about active satellites. $GPRMC sentence (Recommended minimum specific GPS /Transit data) records information about the current time, latitude, longitude, speed, magnetic variation in degrees of GPS receiver, and other required control information. $GPGSV sentence (GPS Satellites in view) records information about the current number of visible satellites, altitude and azimuth, and information about the characteristics of the visible satellites.

After data were collected, data points from the GPS receivers were downloaded and stored on a computer and converted into the appropriate format suitable for statistical analysis. For all unit types, data were set to transfer in geographic coordinate system WGS to avoid any automatic datum transformations. WGS is the native reference system used in GPS.

The used coordinate system of the point data was HTRS (EPSG 3765) with no datum transformation. The receivers outputted the raw position data in NMEA format. Recorded longitude and latitude coordinates are then converted using the Python Script programming language from NMEA format to CSV format suitable for further data processing.

4 STATISTICAL ANALYSIS OF COLLECTED DATA

Based on the recorded geographic coordinates of the GPS receivers locations, it is possible to determine the impact of tram traffic on the GPS receiver positioning accuracy. The degree of impact of tram traffic on the reduction of GPS receiver positioning precision can be determined based on the deviation of the measured coordinates from exactly defined geographic location on survey and control point.

Based on the conducted statistical analysis the values of Longitude and Latitude Error (Ex, Ey), Positioning Distance Error (DE), Longitude and Latitude mean and standard deviation, distance root mean squared values (DRMS, 2DMRS) and Circular Error Probability value (CEP) were determined.

Longitude and Latitude Error are determined by the following equations:

$$E_x = x_i - x_T; \quad E_x = y_i - y_T \tag{1}$$

Where:

E_x, E_y – Longitude and Latitude Error

x_i, y_i – measured Longitude and Latitude coordinates

x_T, y_T – the actual geographic coordinates of survey and control point

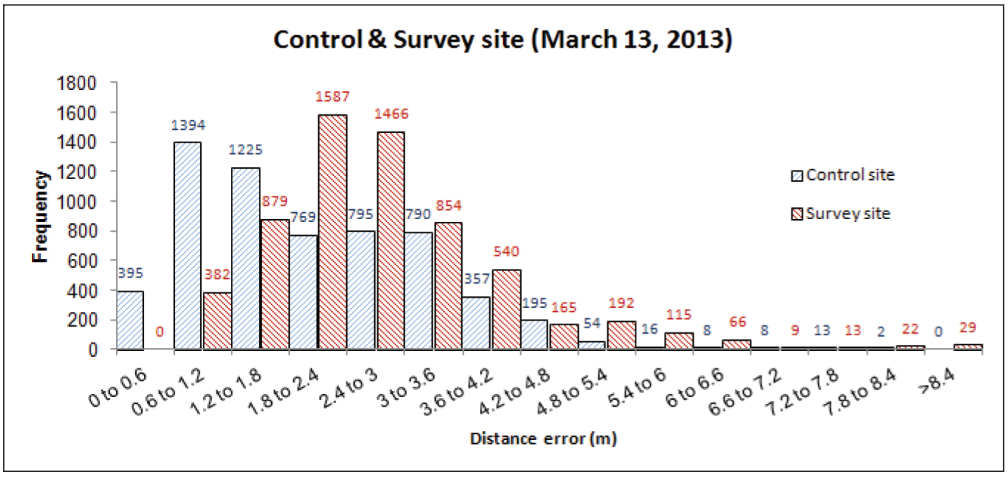

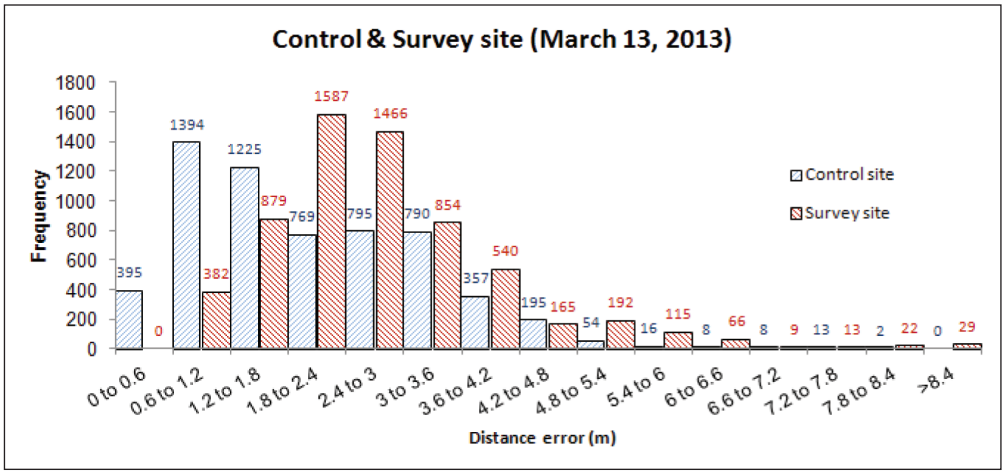

Figure 2 Comparation of Distance error absolute frequencies on Control and Survey site during the first and second measurement.

Positioning Distance Error can be determined using the following expression:

$$D_E = \sqrt{E_x^2 + E_y^2} \tag{2}$$

Where:

D_E – Positioning Distance Error

E_x, E_y – Longitude and Latitude Error

Comparation of Distance Error absolute frequencies on Control and Survey site during the first and second measurement are shown in Figure 2. Determined Distance Error values on the survey and control site indicate slightly larger deviations of the measured coordinates on survey point during both measurements. Scatter diagram of determined coordinates on Survey and Control site during the first and second measurement are shown in Figure 3.

Accuracy and precision measures are used to describe how good is the position acquired by GPS receiver. A distinction should be made between accuracy and precision. Accuracy is the degree of closeness of an estimate to its true, but unknown value and the precision is the degree of closeness of observations to their means.

When GPS positions are logged over time, the positions are scattered over an area due to measurement errors. This dispersion of points is called a scatter plot, which GPS manufacturers use to characterize their equipments accuracy. The area within which the measurements or estimated parameters are likely to be is called the confidence region. The confidence region is then analyzed to quantify the GPS performance statistically. The confidence region with a radius describes the probability that the solution will be within the specified accuracy.

From the coordinates of each point in the 60-min and 90-min span respectively, the median, 75th percentile, 95th percentile, sa well as accuracy and precision measures are determined for horizontal (x, y) dimensions. Additionally, the positional accuracy in averaged x and y is computed. Measurement point averaging involves taking multiple coordinate readings at a single location with a goal of creating an average coordinate pair that is closer to the true location. The average positional accuracy for the x and y dimensions for each position fix is determined using the mean formula:

$$\bar{x} = \frac{1}{n}\sum_{i=1}^{n} x_i; \qquad \bar{y} = \frac{1}{n}\sum_{i=1}^{n} y_i; \tag{3}$$

Where:

$\bar{x}$ – Longitude mean value

$\bar{y}$ – Latitude mean value

x_i, y_i – measured Longitude and Latitude coordinates

n – number of observed values

Standard deviation is a measure of the variability in the same dimension as the observed variable (measured latitude and longitude coordinates) and it represents average deviation of a variable from its mean value (Fratrović et al. 2008). It is also defined as the mean square deviation from the mean value, and it is calculated according to the following equations:

$$\sigma_x = \sqrt{\frac{1}{n-1}\sum_{i=1}^{k}(x_i - \bar{x})^2 f_i}\,; \qquad \sigma_y = \sqrt{\frac{1}{n-1}\sum_{i=1}^{k}(y_i - \bar{y})^2 f_i}\,; \tag{4}$$

Where:

fi – absolute frequencies of individual statistical classes

$\bar{x}$ – Longitude mean value

$\bar{y}$ – Latitude mean value

x_i, y_i – measured Longitude and Latitude coordinates

n – number of observed values

Root Mean Squared Error is than determined using the following expression:

$$RMSE = \sqrt{\bar{x} = \frac{1}{n}\sum_{i=1}^{n} E_i^2}; \tag{5}$$

Where:

RMSE – Root Mean Squared Error

$\bar{x}$ – Longitude mean value

E_i – the positional error in each unique GPS position fix

n – number of observed values

For each set of data collected, the average positional accuracy in x and y was tested against zero to determine if bias is present. Mean values were tested against aknown value to assess bias. For each set of data collected at a given

control points, the median, 75th percentile, 95th percentile, and RMSE were calculated and compared to determine if there is any influence of tram traffic on GPS data. A distance error was calculated between the GPS measurements and the known coordinates of the test points by deriving the straight-line distance between coordinate locations.

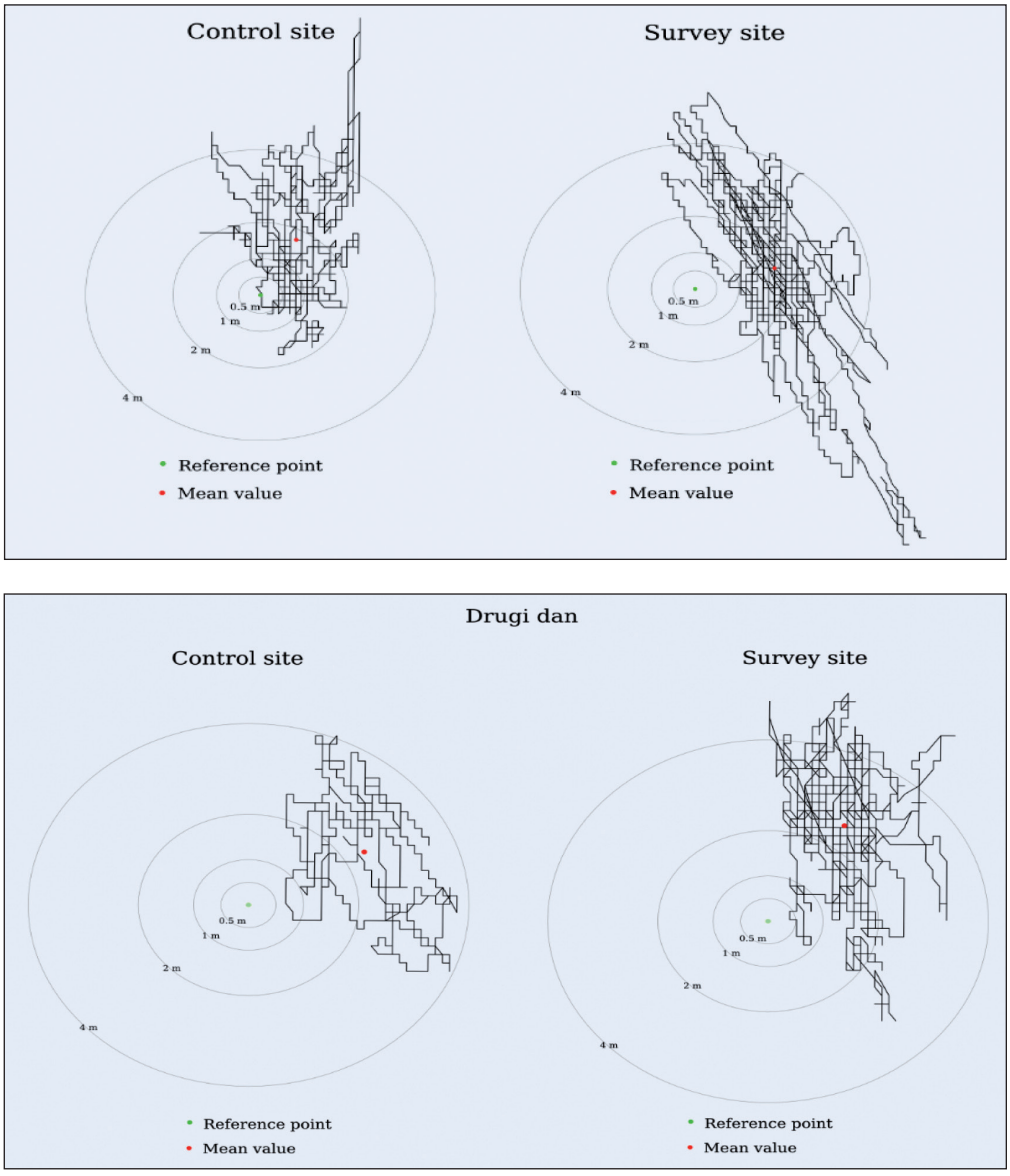

Figure 3 Scatter diagram of determined coordinates on Survey and Control site during the first and second measurement.

DRMS is a single number that expresses 2D accuracy. In order to compute the DRMS of horizontal position errors, the standard errors (σ) from the known position in the directions of the coordinate axis are required. DRMS is the square root of the average of the square errors which is defined as follows:

$$\mathrm{DRMS} = \sqrt{\sigma_x{}^2 + \sigma_y{}^2} \tag{6}$$

Where:

DRMS – Distance Root Mean Squared

σ_x^2, σ_y^2 – the standard errors from the actual position of survey and control point

Standard errors (σ) of estimated coordinates (*x, y*) of each point being positioned can be predicted from the corresponding variances on the diagonal of the covariance matrix.

CEP refers to the radius of a circle in which 50% of the values occur, i.e. if a CEP of 5 meters is quoted then 50% of horizontal point positions should be within 5 meters of the true position. The radius of the 95% is often quoted and the term R95 used. R95 is CEP with the radius of the 95% probability circle. Circular Error Probability is determined by following expression:

$$\mathrm{CEP} = 0.62 \cdot \sigma_y + 0.56 \cdot \sigma_x \tag{7}$$

Where:

CEP – Circular Error Probability

σ_x^2, σ_y^2 – the standard errors from the actual position of survey and control point

5 CONCLUSION AND RECOMMENDATIONS

Impact of tram lines on the quality of GPS signal reception in the city of Zagreb was determined based on two measurements which were conducted on the Borongaj tram turnaround in the city of Zagreb. Based on collected data we tested the statistical hypothesis that tram traffic has a significant impact on the quality of the car GPS signal reception in urban areas. In order to evaluate positional accuracy of GPS receivers, collected data were compared to a referece point. The location of reference points was determined with a system of higher accuracy than the receivers being used during the measurement (Trimble R8 Survay Grade GPS). Meas-

urement was conducted by two identical GPS receivers (GeoChron GPS Data Logger) mounted on a tripod, which were placed directly over the reference points.

The degree of impact of tram traffic on the reduction of GPS receiver positioning precision was determined based on the deviation of the measured coordinates from exactly defined geographic location on survey and control point. Based on the conducted statistical analysis the values of Longitude and Latitude Error (Ex, Ey), Positioning Distance Error (DE), Longitude and Latitude mean and standard deviation, distance root mean squared values (DRMS, 2DMRS) and Circular Error Probability value (CEP) were determined. Determined Distance Error values on the survey and control site indicate slightly larger deviations of the measured coordinates on survey point during both measurements.

Since the deviations of the measured coordinates only slightly differs on survey and control point, it can be concluded that there is no significant impact of tram lines on the quality of GPS signal reception in urban areas. In order to confirm obtained results future research should be conducted in other areas of the city of Zagreb and other cities in the Republic of Croatia.

REFERENCES

1. American Meteorological Society, 2011. *Understanding the Vulnerability & Building Resilience*, Washington D.C.
2. Arnold, L.L. & Zandbergen, P. a., 2011. Positional accuracy of the Wide Area Augmentation System in consumer-grade GPS units. *Computers & Geosciences*, 37(7), pp. 883–892. Available at: http://linkinghub.elsevier.com/retrieve/pii/S0098300411001063 [Accessed March 15, 2013].
3. Dadić, I. et al., 2012. Problems and solutions in logging of traffic accidents location data. In *XI International Symposium "ROAD ACCIDENTS PREVENTION 2012"*. Novi Sad, pp. 67–75.
4. Dadić, I. et al., 2006. Satellite navigation in the function of managing traffic flows in the future. In *ISEP 2006 proceedings.* Ljubljana.
5. European Commission, 2011. *The European Electronic Toll Service (EETS)*, Bruxelles, Belgium.
6. Filjar, R., 2008. A Study of Direct Severe Space Weather Effects on GPS Ionospheric Delay. *Journal of Navigation*, 61, pp.115–128.
7. Filjar, R. & Huljenic, D., 2012. The importance of mitigation of GNSS vulnerabilities and risks. *Coordinates*, 8(5), pp.14–15.
8. Filjar, R., Kos, T. & Kos, S., 2009. Klobuchar-Like Local Model of Quiet Space Weather GPS Ionospheric Delay for Northern Adriatic. *Journal of Navigation*, 62, pp. 543–554.
9. Fratrović, T., Ivanković, B. & Striko, K., 2008. *Vjerojatnost i statistika*, Sveučilište u Zagrebu, Fakultet prometnih znanosti, Zagreb.

10. I. Dadić, D. Škaro, K. Vidović, M. Ševrović, M. Šoštaric, D. Jeremić, 2012. Advanced method of detection of unnecessary conflicts of traffic flows. *Intelligent Transportation Systems (ITSC), 15th International IEEE Conference*, pp. 178–181.
11. Lehtinen, M., Happonen, A. & Ikonen, J., 2008. Accuracy and time to first fix using consumer-grade GPS receivers. *2008 16th International Conference on Software, Telecommunications and Computer Networks*, pp.334–340. Available at: http://ieeexplore.ieee.org/lpdocs/epic03/wrapper.htm?arnumber=4669506.
12. R. Filjar, M. Ševrović, I. Dadić, 2012. Impact assessment of urban GPS positioning error on intelligent transport system's road use charging service. *International conference on applied internet and information technologies, Zrenjanin*.
13. Spilker, J.J., 1996. *Global positioning system: theory and applications, Volume 1; Volume 163*, American Institute of Aeronautics and Astronautics.
14. Thomas, M., 2011. *Global Navigation Space Systems: Reliance and Vulnerabilities*, Royal Academy of Engineering.
15. Volpe, J.A., 2001. *Vulnerability Assessment of the Transportation Infrastructure Relying on the Global Positioning System*.
16. Witte, T.H. & Wilson, a M., 2005. Accuracy of WAAS-enabled GPS for the determination of position and speed over ground. *Journal of biomechanics*, 38(8), pp. 1717–22. Available at: http://www.ncbi.nlm.nih.gov/pubmed/15958230 [Accessed March 15, 2013].

Faculty of Maritime Studies
University of Rijeka, Croatia

Royal Institute of Navigation
Science Technology Practice

7th GNSS
Vulnerabilities and Solutions Conference

CORRELATION BETWEEN IONOSPHERIC MODELS AND SPACE WEATHER INDICES FOR 2011

Pavel Najman[1], **Tomislav Kos**[1], **Mainul Hoque**[2]

[1] University of Zagreb, Faculty of Electrical Engineering and Computing, Zagreb, Croatia
E-mail: pavel.najman@fer.hr

[2] German Aerospace Center, Institute for Communication and Navigation, Germany

ABSTRACT. *Modelling of the ionosphere is used to mitigate ionospheric effects on single frequency satellite-receiver transmission as well as for background data input for data assimilation and for ionospheric forecasting. There are several empirical models of the ionosphere, all of them are based on different principles and using different inputs to compute electron density or Total Electron Content. However, their performance can strongly degrade especially under the disturbed conditions. The main cause of disruptions in the ionosphere is varying solar activity which can be described by number of space weather indices. Studying how the ionospheric models react on the changes of space weather indices is of great importance in order to signify which and how the indices should serve as an input to the models. In this paper, we show results of comparative studies for year 2011 among different ionosphere models such as the NeQuick 2, IRI 2012, Klobuchar and the NTCM model with Solar Spot Number (SSN), Solar Flux (SF) and geomagnetic activity indices Ap and AE. We used Space Weather Application Center Ionosphere (SWACI) data as reference to our comparisons. The correlation with SSN, SF is high while the correlation with Ap and AE is insignificant. Trend of linear regression of correlation between the reference with SSN and SF was the most similar to Klobuchar data.*

KEY WORDS: *IRI 2012, NeQuick2, Klobuchar, NTCM, Space Weather*

1 INTRODUCTION

Nowadays, the Global Navigation Satellite System (GNSS) is commonly used for satellite based positioning and navigation. The GNSS based services are used in maritime, aviation, agriculture, public transportation, geodetic survey and other applications. The position of a GNSS receiver is computed from travel times which the navigation signals need to travel from GNSS satellites to receivers (Daly, 1993). In ideal circumstances, the distance between the receiver and a particular satellite would be simply multiplication of the travel time by the signal propagation speed, speed of light. However, there are several factors which can significantly change the propagation time so that the measured time would not anymore represent the true distance between the satellite and the receiver. Consequently, it leads to an error into the final position solution.

One of the most severe errors is so called ionospheric error which is caused when a navigation signal passes through the ionosphere (Norsuzila et al., 2007). There are several techniques used to compensate the ionospheric effcts. First possibility is to use multi-frequency for communication which can eliminate about 95% of the error due to the dispersive nature of the ionosphere (Satya Srinivas et al., 2012). Second is usage of a network of reference stations which compute the ionospheric error and sent its value to a GNSS receiver. When neither of these techniques are available, an ionospheric model can be used to compute the ionospheric error. Furthermore, ionospheric models are also used for satellite and receiver inter-frequency bias estimations and TEC calibration techniques (Jakowski, Hoque and Mayer, 2011).

There are several empirical models of the ionosphere. The most common are the International Reference Ionosphere (IRI), the NeQuick and the Klobuchar model. Another empirical model we focused on is a relatively new model NTCM which was developed at DLR (Deuches Zentrum für Luft – und Raumfart) (Jakowski, Hoque and Mayer, 2011). All of them are based on different principles and use diffrent inputs to compute electron density or Total Electron Content (*TEC*). Nevertheless, they still do not perform sufficiently under all conditions. They show considerable degree of inaccuracy especially under the disturbed ionospheric conditions.

The main cause of disruptions in the ionosphere are changes in solar activity. The Sun, as the main source of ionization, can significantly change electron density of the ionosphere, especially when solar flare or coronal mass ejection (CME) occurs (Langley, 2000). Solar activity can be described by number of indices. The most common are solar flux of 10.7 cm wavelength (F10.7), sunspot number (SSN), indices which indicate changes in geomagnetic field as planetary

index (*Kp*) or auroral indices (e.g: AE). All of them describe different physical processes but all are related to the activity of the Sun and subsequent condition of the ionosphere. As the space weather indices are used as inputs into the ionospheric models, it is desirable to map their correlation with the models and with the real state of the ionosphere.

2 IONOSPHERE

The ionosphere is a part of the atmosphere which contains charged particles in such quantity that their reaction with a propagating electro-magnetic wave changes its propagation speed and trajectory (Barclay, 2003). The main parameter of the ionosphere is *electron density*. It depends on concentration of ionisable gas that reduces with the altitude, and on solar radiation which decreases with increasing penetration into the Earth's atmosphere from above due to absorption processes (heating and ionization). Thus, finally an ionization or electron density maximum is created at around 250 – 400 km depending on geographical location, local time and solar activity.

The typical vertical structure of the ionosphere is shown in Figure 1. The ionosphere is divided into several regions according to the different ionization and recombination principles.

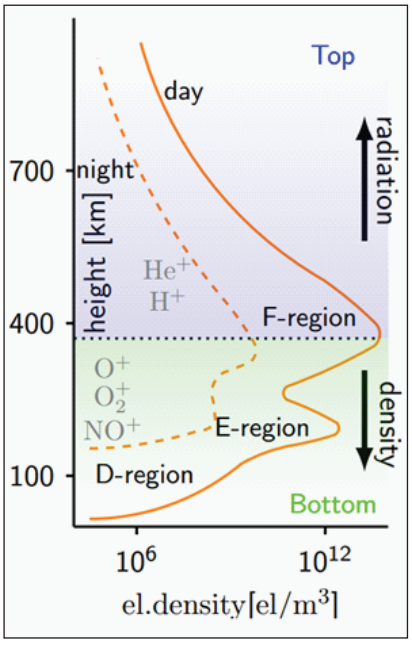

Figure 1 A typical electron density vertical profile of the ionosphere. The ionospheric layers for particular altitudes are shown. The electron density profile during day and night is represented by full and dashed line, respectively. The dotted line shows the average height of the electron density maximum; made by the authors according to (Ya'acob et al., 2008).

D region, 70-140 km, $10^8 - 10^{10}$ electrons/m^3
E region, 140-210 km, several 10^{12} electrons/m^3
F region, above 210 km, several 10^{12} electrons/m^3

3 TOTAL ELECTRON CONTENT

Ionospheric error of a single satellite – receiver link depends on the total amount of the electrons which the signal encounters on its way through the ionosphere. The error in meters ΔR can be expressed as:

$$\Delta R = \frac{40.3}{f^2} \int_S N_e \mathrm{d}S \tag{1}$$

where N_e is electron density in a particular part dS. TEC can be obtained by integration the N_e along the signal path S:

$$TEC = \int_S N_e \mathrm{d}S \tag{2}$$

There are two commonly used types of *TEC* values: *vertical* and *slant total* electron content. Vertical total electron content (*vTEC*) at a certain geographical point stands for total electron content in the direction of the zenith angle. *TEC* between a satellite and a receiver is usually referred to as the slant *TEC* (*sTEC*) that signifies that the *TEC* is at a different angle from the zenith angle. We can also say that *sTEC* is depended on geometry, whereas *vTEC* is not. The *TEC* is usually given in *TEC* Units (*TECU*) where 1 *TECU* = 10^{16} electrons/m^2.

4 SPACE WEATHER

The term *space weather* is used to describe physical processes in the vast space between the Earth and the Sun which are generated by solar radiation (Filjar, 2008). Space weather influences both the Earth's magnetosphere and the ionosphere. Therefore, in can significantly change amount of the ionospheric propagation error. Aside from the regular changes caused by the rotation of the Earth around its axis and around the Sun, substantial changes arise when the Sun burst a large amount of particles in the direction of the Earth. Such burst can be *coronal mass ejections* (*CME*) or *solar flares*. Duration of these anomalies can be from several hours to few days. The frequency of their occurrence depends on the current activity of the Sun. It has been observed that Sun's activity as well as the amount of the solar events changes periodically with 11 years cycles. The solar activity peak for the current solar cycle is anticipated this year (2013). The activity of the Sun is quantified by parameters such as Solar Spot Number (*SSN*) or Solar Radio Flux (*SF*). Geomagnetic indices such as *Kp*, *Dst* or *AE* are used for describing the effect of solar activity on the Earth's magnetosphere.

4.1 SSN

Sunspots are regions on the Sun's surface of diameter around 10 000 km with temperature about 2 000 °K lower than typical surface temperature (6 000 °K). A significant discovery was made by Schwave; he recorded the sunspot numbers continuously from the year 1826 for next 43 years continuously. He is the first one to report 11 years periodicity of their occurrence (Figure 2). From that moment the discussion about the possible relationship between the number of sunspots and solar and magnetic activity was began by Moldwin (2008). Later on, the sunspot numbers were introduced to measure the solar activity R

$$R = k(10g + f) \tag{3}$$

where f is the number of sunspots, g denotes the number of sunspot groups, k is a correction coefficients depended on the instruments used for the determination of the R. Despite the fact that today exist better methods to quantify the solar activity, the sunspot number are still used mainly due to the available data archive of sunspot numbers for last nearly 400 years (Hanslmeier, 2002).

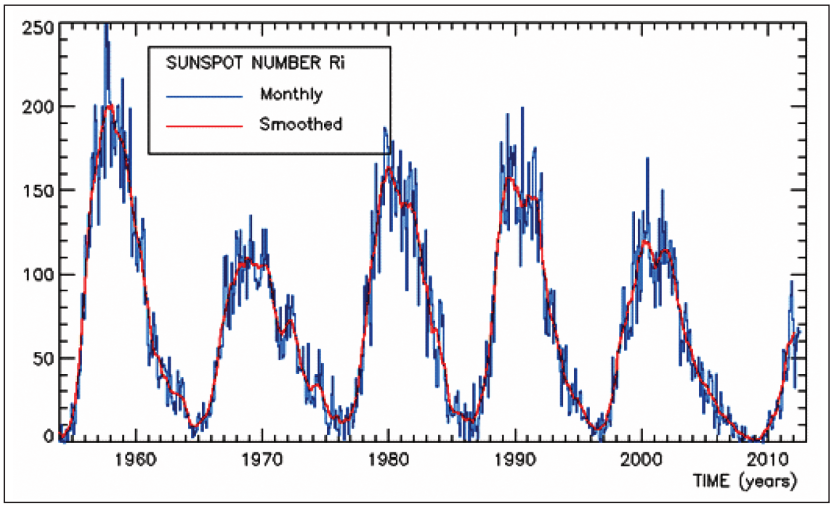

Figure 2 The monthly (blue) and monthly smoothed (red) sunspot numbers for the latest five cycles. (Solar Influences Data Analysis Center webpage, 09.08. 2012, http://sidc.oma.be/html/wolfmms.html)

4.2 Solar flux

The Sun emits radio energy with slowly varying intensity. This radio emission originates mainly from *Bremsstrahlung radiation* (Mehta and Vats, 2011) which comes from higher part of Sun's chromosphere and lower part of its corona.

The most longest and reliable data set is available for frequency 2800 MHz (λ = 10.7 cm) since at this frequency the radio emissions are found to be the most regular. 10.7 cm solar flux from the entire solar disc was continuously recorded by a radio telescope near Ottawa, Canada, since 1947 (Hanslmeier, 2002). Solar radio flux is given in units of $10^{-2}\,Js^{-1}\,m^{-2}\,Hz^{-1}$ also called solar flux units (*sfu*). The data are usually archive in two forms: *observed solar flux* which are measured values varying also due to the changing Earth-Sun distance and *adjusted solar flux* which is scaled to the standard distance of 1 astronomical unit i.e. average Earth-Sun distance.

4.3 *Kp, Ap*

Aside from observing the Sun or solar emissions, we can also measure how the Earth magnetosphere responses on the solar activity. *Kp* index is one of the most used index to interpret current condition of the geomagnetic field.

Geomagnetic disturbances are monitored by ground-based magnetic observatories recording the three magnetic field components. Each observatory site measures local magnetic activity and every 3 hours produces local *K*-index. Such value represents how the condition of the magnetic field changes relatively to the quiet day curve calculated for the local observatory. The global planetary *Kp* index is obtained as the mean value of the *K* indexes from 13 observatory stations around the Earth between 44 degrees and 60 degrees of latitude in both the south and the north hemisphere (Jusoh et al., 2008).

Kp index has scale from 0 to 9 expressed in thirds of a unit, e.g. 3-is 2+2/3 and 3+ is 3+1/3. Numbers up to 5- indicate quiet geomagnetic condition, whereas levels of 5 to 9 indicate geomagnetic storms. Since *Kp* scale is logarithmic, the *Ap* index was introduces as a linear representation of the geomagnetic activity. The *Ap* index has scale from 0 to 400 where each value of *Kp* index has its equivalent value of *Ap* (e.g. 0 is 0, 3- is 12, 6- is 67 and 9- is 300).

4.4 Auroral electrojets indices

Auroral indices describe jets of particles entering in the North polar region. Its parameters are derived from the measurements of about 12 stations positioned in the northern high latitudes. There are several electrojets indices: Auroral Upper (*AU*) index is a measure of the eastward auroral electronjet in the uppermost envelope of the superposed *H*-component perturbations at auroral latitudes; Auroral Lower (*AL*) is the measure of the westward auroral electrojets in the lowest envelope; *AO* index is defined as $AO = (AU + AL)/2$ and *AE* which is defined $AE = AU - AL$ which reflects the integrated effect of the different current systems.

5 IONOSPHERIC MODELS

As it was mentioned, ionospheric models are not used just for correction of the ionospheric error but also for calibration techniques and as a background for data assimilation or for improvement of ionospheric forecasting. In general, ionospheric models reflect our ability to understand the ionospheric mechanics or ability to describe the ionospheric effects.

5.1 NeQuick

The NeQuick is an empirical model based on the model introduced by Di Giovanni and Radicella. The NeQuick constructs electron density distribution of the ionosphere by sum of Epstein layers. It enables to calculate electron density in any given location in the ionosphere, and therefore also total electron content and electron density profile along the ray-path between any two given points (Radicella and Nava, 2010). The version 2 of the NeQuick used for the analysis was obtained the International Centre for Theoretical Physics in Trieste. The model is typically driven by averaged smoothed mean value of the solar flux F107. Aside from the averaged index, daily value of the observed solar flux was also used.

5.2 IRI2012

Another empirical model, which is often used for estimation of ionospheric parameters, is the International Reference Ionosphere (IRI). Its 2012 version is currently available on National Aeronautics and Space Administration (NASA) webpage (http://nssdcftp.gsfc.nasa.gov/models/ionospheric/iri/). The IRI is able to compute *TEC* and electron density profile in zenith angle. The integration height for electron density of the IRI is limited to 1500 km (Bilitza and Reinisch, 2008). The IRI uses variation of *Ap* and solar flux indices.

5.3 Klobuchar

The Klobuchar empirical model was developed by John A. Klobuchar at the Air Force Geophysics Laboratory, U.S. The algorithm was designed to correct ionospheric time-delay in GPS system for single frequency communication.

The Klobuchar model is very fast and simple. It models daytime course of ionospheric time delay as a half period of cosine function whose shape is determined by 8 ionospheric coefficients with function maximum at 14:00 local time. The night time ionospheric delay is set as a constant with value of 5 ns. Therefore, no integration of electron density is required since the model directly approximates time delay value (Klobuchar, 1987).

5.4 NTCM

GNSS-based ionospheric monitoring has been carried out at DLR (Deutsches Zentrum f˙ur Luft- und Raumfahrt) in Neustrelitz since 1995. Recently, they have developed the global empirical ionospheric model Neustrelitz TEC Model (NTCM) which should provide a simple way to obtain the value of vertical TEC at any given time and location. The core of the model are 12 coefficients which can be autonomously used for a full solar cycle. The driver of the NTCM is daily value of the solar radio flux. The model does not use any integration of electron density profiles and is therefore very simple and fast (Jakowski, Mayer, Hoque and Wilken, 2011). All the formulas of the code can be found in (Jakowski, Hoque and Mayer, 2011).

6 METHODOLOGY & DATA

Data of solar weather indices for 2011 were obtained from National Geophysical Data Center (NOAA) webpage (http://www.ngdc.noaa.gov/stp/). Reference SWACI (Space Weather Application Center – Ionosphere) maps for year 2011 were obtained at the DLR in Neustrelitz (http://swaciweb.dlr.de). SWACI is a research project of DLR. These maps are created by assimilation of measurements from IGS (International GNSS Service) stations into a background model.

Database of global *TEC* maps were created for each evaluated model: IRI2012, Klobuchar, NTCM and two for NeQuick (driven by monthly averaged and daily solar flux index). Maps were done for every hour for every day in the year 2011. Each global map has resolution of 5 degrees in longitude and 2.5 degrees in latitude which is the same as the SWACI maps.

A mean value of *vTEC* for particular value of a solar weather index was computed for every model according to:

$$vTEC = \frac{1}{p}\sum_{i=1}^{p}\left(\frac{1}{m}\sum_{l=1}^{m} vTEC_{i,l}\right) \tag{4}$$

where p is the number of hours included in computation and m is the number of grid *vTEC* map points. These values of each model were then put intocorrelation with the values of the solar indices. In case that one value of a index occurred in two or more days, the final *vTEC* value is computed as the mean value of all hours of all the days.

7 RESULTS

7.1 Space Weather Indices in year 2011

The year 2011 was two years before the peak of the 24th solar cycle. According to the data from NOAA, there were five R2 level and 6 R3 level Radio Blackouts, 16, 7 and 2 geomagnetic storms level G1, G2 and G3 respectively, 8 S1 level solar radiation storms and 27 10 cm electron emissions with maximum peak of 23000 sfu (7th March). Progress of solar weather indices over the period of year 2011 is shown on Figure 3. Their mean and limit values are included in the Table 1 and the their mutual correlation in the Table 2. As the correlation between adjusted and observed solar flux is nearly 1, further results will include data just for observed values. We did not include *Dst* index into the analyses as its beahaviour is very similar to Ap.

Table 1 Mean, minimum and maximum values of space weather indices for year 2011

	SF (obs)	**SF (adj)**	**SSN**	***Ap***	***Dst* (-)**	**AE**
max	190.4	191.6	136	45	76	525
min	79.2	76.7	0	0	17	0
mean	113.4	113	55.8	7.5	7.7	123.4

Table 2 Correlation between space weather indices for year 2011.

	AE	***Dst* (-)**	***Ap***	**SSN**	**SF (adj) SF (obs)**
SF (obs)	0.209	0.049	0	0.872	0.9952
SF(adj)	0.1825	0.0632	0	0.8839	
SNN	0.1345	0.04	0		
Ap	0.404	0.6154			
Dst	0.1187				

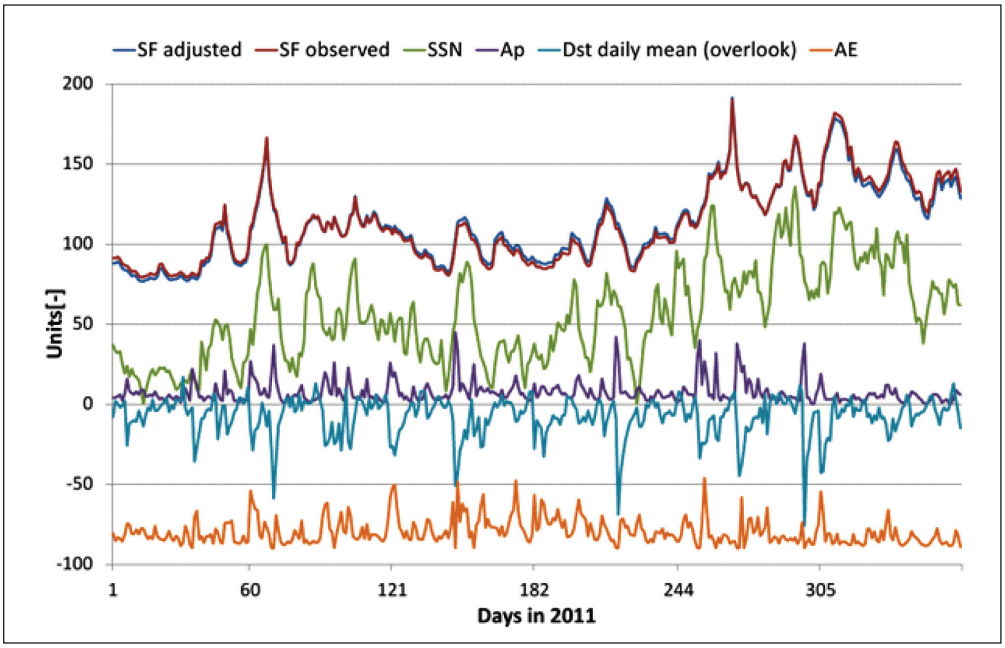

Figure 3 Solar weather indices of year 2011.

7.2 Correlations with models

Figure 4 shows correlation between the solar spot number and the mean daily *vTEC* values from ionospheric models and SWACI, Figure 5 shows correlation with the observed solar flux, and Figure 6 and Figure 7 show correlation with the *Ap* index and *AE* index respectively. The coefficients of determination of linear regression are shown in the Table 3.

Table 3 Correlation coefficients R between space weather indices and ionospheric data

	SF (obs)	**SSN**	***Ap***	***AE***
NeQuick (monthly)	0.856	0.891	0.042	-0.151
IRI 2012	0.874	0.909	0.093	-0.209
NeQuick (daily)	0.978	0.957	0.131	-0.218
NTCM	0.977	0.929	0.118	-0.227
Klobuchar	0.903	0.904	-0.093	-0.218
SWACI	0.856	0.888	-0.317	-0.277

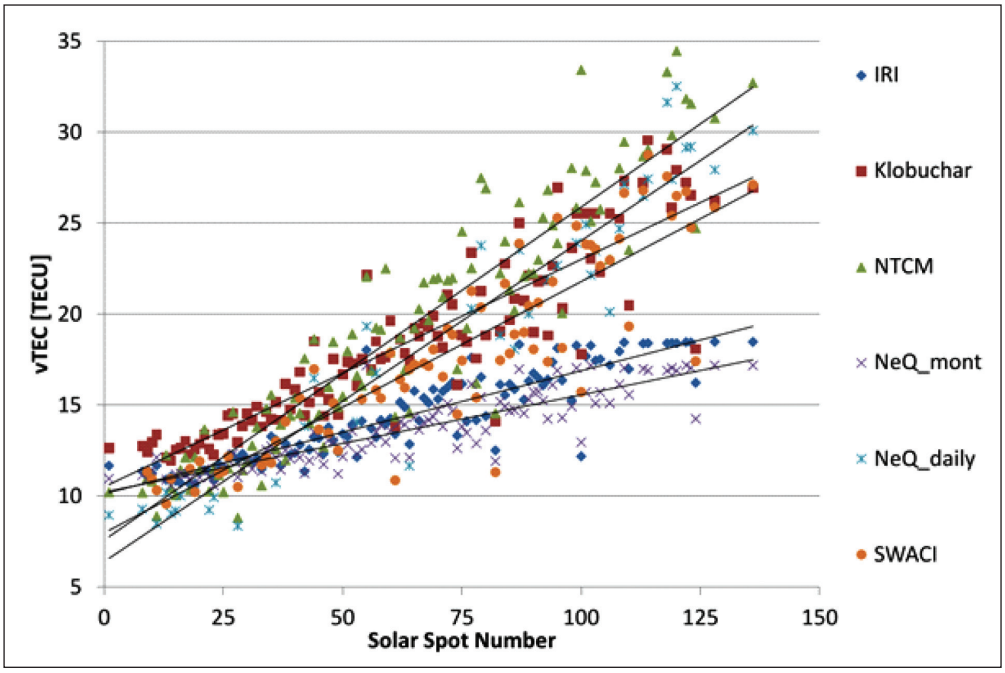

Figure 4 Correlation between mean *vTEC* values and Solar Spot Number.

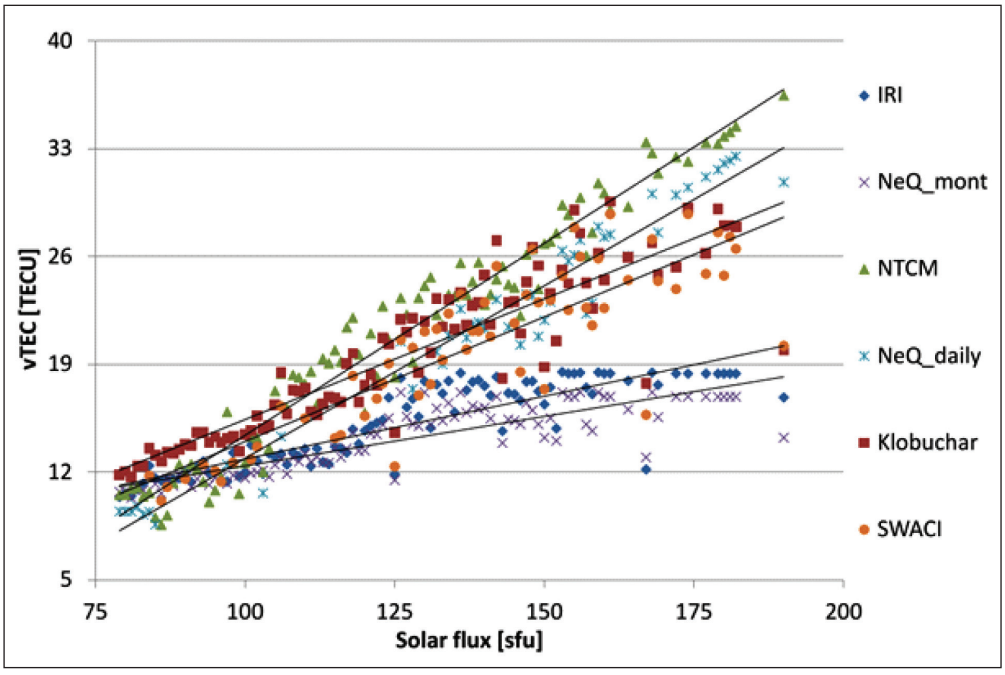

Figure 5 Correlation between mean *vTEC* values and Solar Flux.

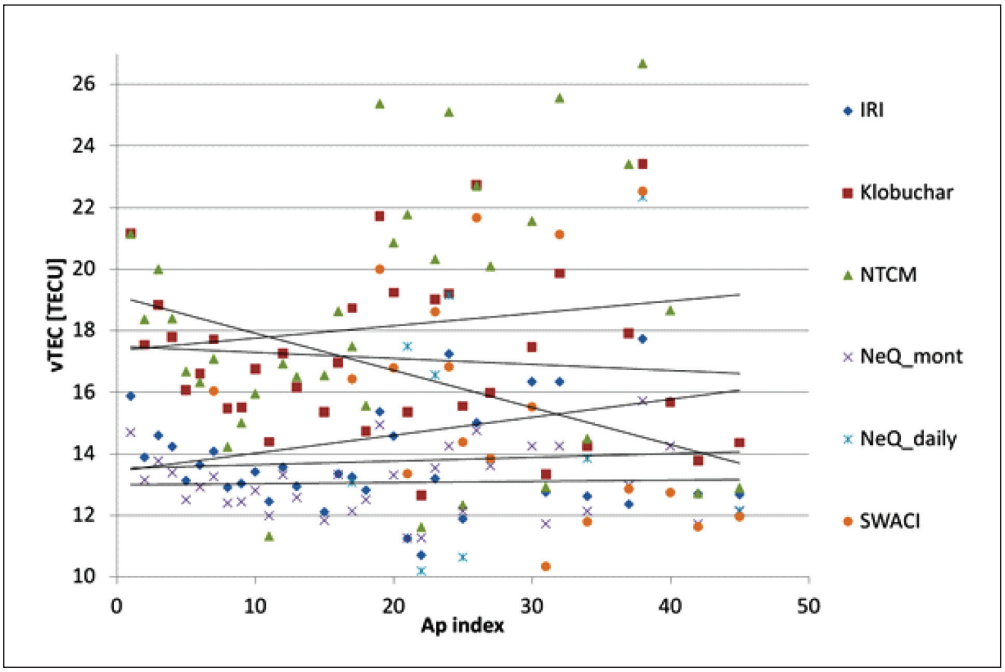

Figure 6 Correlation between mean *vTEC* values and *Ap* index.

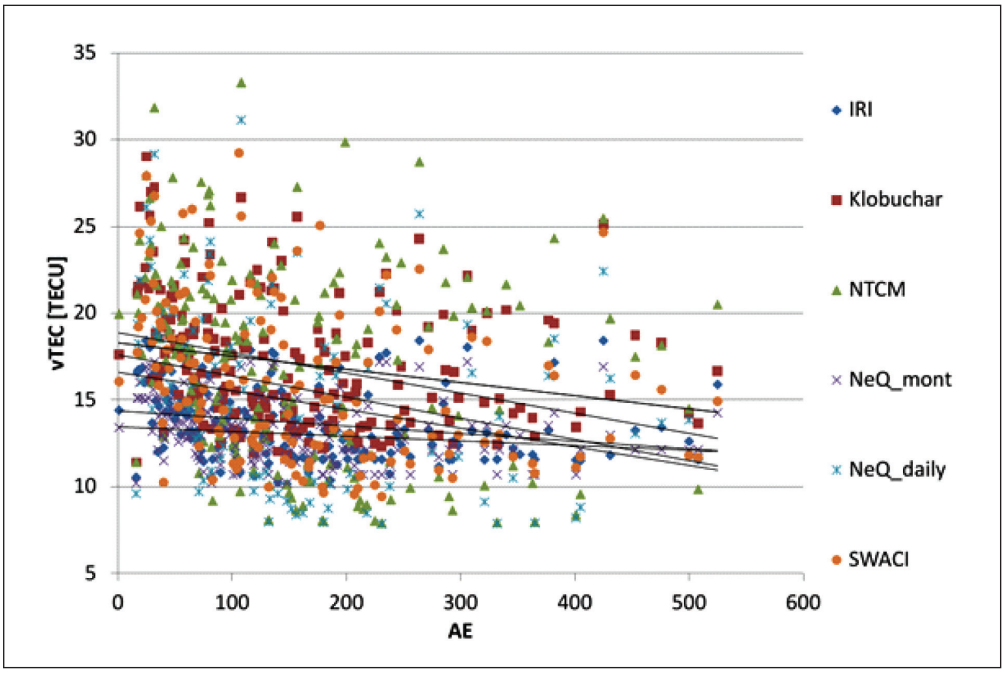

Figure 7 Correlation between mean *vTEC* values and *AE* index.

8 CONCLUSION AND FUTURE WORK

The correlation between SSN and SF is very high. Thus, it can be said that SSN and SF can be interchangeable to some extent. On the other hand, zero correlation between *Ap* index with other space weather indices suggests that even though the *Ap* index is frequently used to quantify solar events, it should not be used in the same way as others when referring to the electron content. The correlation between SF and SSN with both modelled and reference ionospheric data is very high. The highest correlation is for the NeQuick driven by daily value and NTCM. This is not surprising as in both cases daily SF value was used as an input. Correlation with data modelled by the IRI and the NeQuick driven by monthly value is diminish by the fact that both models are seasonal and they do not reach high values of *TEC* as they are unable to react on one day peaks in solar activity. This can be seen on the Figure 4 and 5 where both models show a kind of saturation around 18 *TECU*. The most similar trend to reference data is shown by Klobuchar model which suggests that despite the simplicity of the model it can represent behavior of the ionosphere with respect to changes in space weather indices very well. For both *Ap* and *AE* index the correlations are insignificant which shows that connection between them and global ionospheric *TEC* is very limited. In future work, we would like to focus on other indices and measurements, not just the most common, and we would like to perform analyses for different regions.

ACKNOWLEDGMENT

Pavel Najman's research work is undertaken in the scope of the TRANSMIT ITN (www.transmit-ionosphere.net), funded by the Research Executive Agency within the 7th Framework Program of the European Commission, People Program, Initial Training Network, Marie Curie Actions – GA no 264476.

REFERENCES

1. Barclay, L. (2003), *Propagation of Radiowaves*, 2nd ed edn, The Institution of Engineering and Technology, London.
2. Bilitza, D. and Reinisch, B. (2008), 'International Reference Ionosphere 2007: Improvements and new parameters', *Advances in Space Research* **42**(4), pp. 599–609.
3. Daly, P. (1993), 'Navstar GPS and GLONASS: global satellite navigation systems', *Electronics & Communication Engineering Journal* (December 1993), pp. 349–357.
4. Filjar, R. (2008), 'A Study of Direct Servere Space Weather Effects on GPS Ionospheric Delay', *The Journal of Navigation* **61**(1), pp. 115–128.

5. Hanslmeier, A. (2002), *The Sun and Space Weather*, Kluwer Academic Publishers, Dordrecht.
6. INGV (2013), 'INVG – Roma2 Department'. URL: http://roma2.rm.ingv.it/en/themes/23/geomagnetic_indices/27/dst index.
7. Jakowski, N., Hoque, M. M. and Mayer, C. (2011), 'A new global TEC model for estimating transionospheric radio wave propagation errors', *Journal of Geodesy* **85**(12), pp. 965–974.
8. Jakowski, N., Mayer, C., Hoque, M. M. and Wilken, V. (2011), 'Total electron content models and their use in ionosphere monitoring', *Radio Science* **46**(5), pp. 1–11.
9. Jusoh, M. H., Bakar, F. N. A., Sulaiman, A. A., Baba, N. H., Awang, R. A. and Khan, Z. I. (2008), 'Determination of traveling ionospheric disturbances of geomagnetic storm by using dual frequency GPS data', 2008 *IEEE International RF and Microwave Conference* pp. 361–366.
10. Klobuchar, J. A. (1987), 'Ionospheric Time-Delay Algorithm for Single- Frequency GPS Users', *IEEE Transactions on Antennas and propagation* **AES-23**(3), pp. 325–331.
11. Langley, R. B. (2000), 'GPS , the Ionosphere, and the Space Weather', *GPS World* **July**, pp. 44–49.
12. Mehta, M. and Vats, H. O. (2011), 'Rotational characteristics of solar radio emissions and IMF: A comparative study', *Audio, Transactions of the IRE Professional Group* **18**(11–12), pp. 5–7.
13. Moldwin, M. (2008), *An introduction to Space Weather*, Cambridge University Press.
14. Norsuzila, Y., Ismail, M. and Abdullah, M. (2007), Investigation of the GPS signals ionospheric correction: Ionospheric TEC prediction over equatorial, *in* '2007 IEEE International Conference on Telecommunications and Malaysia International Conference on Communications', Ieee, pp. 294–298.
15. Radicella, S. M. and Nava, B. (2010), NeQuick model: Origin and evolution, *in* 'Proceedings of the 9th International Symposium on Antennas, Propagation and EM Theory', Ieee, pp. 422–425.
16. Satya Srinivas, V., Sarma, A., Swamy, K. and Satyanarayana, K. (2012), 'Performance evaluation of IRI-2007 at equatorial latitudes and its Matlab version for GNSS applications', *Advances in Space Research* **December** (In Press).
17. Ya'acob, N., Abdullah, M., Ismail, M., Bahari, S. A. and Ismail, M. K. (2008), 'Ionospheric mapping function for total electron content (TEC) using global positioning system (GPS) data in Malaysia', *2008 IEEE International RF and Microwave Conference,* pp. 386–390.

Faculty of Maritime Studies
University of Rijeka, Croatia

Royal Institute of Navigation
Science Technology Practice

7th GNSS
Vulnerabilities and Solutions Conference

ON GENESIS OF GPS IONOSPHERIC MODEL

Renato Filjar

Faculty of Maritime Studies, University of Rijeka
Studentska 2, 51000 Rijeka, Croatia
E-mail: renato.filjar@gmail.com

ABSTRACT. *Mitigation of GPS ionospheric delay plays the fundamental role in maintaining required level of GPS positioning, navigation and timing (PNT) performance. The role of the ionosphere in GPS positioning performance was identified in the early days of satellite navigation development, retaining its importance. Here the results of research into development of understanding of GPS ionospheric delay, and development of GPS ionospheric model are presented, emphasising the seminal works in the field and charting the orientation of future developments.*

KEY WORDS: *Fleet management, Agriculture, Sustainable development*

1 INTRODUCTION

The GPS ionospheric delay is the single most influential cause of GPS positioning performance deterioration. Identified as a source of risk for sustained GPS positioning performance, the GPS ionospheric delay became and remains an attractive research topic. Advancements in the field do not only develop understanding of GNSS risks, but also help in understanding of the genesis and nature of ionospheric dynamics.

Here the development of understanding of both ionospheric dynamics and GPS ionospheric delay were presented through the historical landmark achievements that combines atmospheric physics, signal processing, time series analysis and forecasting and satellite navigation.

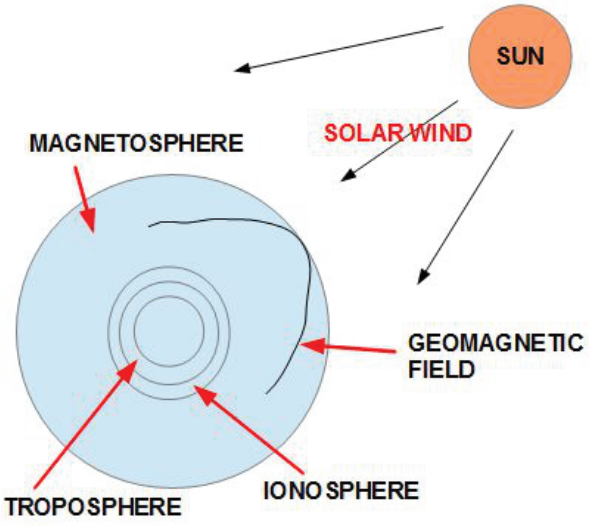

Figure 1 Processes in Sun-Earth system generate the Earth's ionospheric dynamics

2 ORIGINS OF THE IONOSPHERIC EFFECTS ON GPS PERFORMANCE

The ionospheric processes result from a more complex dynamics in energy and particle transfer in the Sun-Earth system, as depicted in Fig 1.

Driven by solar thermonuclear reactions, a huge amount of energy and charged particles is continuously expelled from the Sun in an uneven manner. The portion reaching the Earth affects the status of the Earth's magnetic (geomagnetic)

field, and drives the ionising processes in the upper layers of the Earth's atmosphere (ionosphere).

The ionosphere embraces the space with the height borders at around 50 km and 2000 km, respectively, above the Earth's surface. The region is sparsely populated by particles, and inhomogeneous from the perspective of the electron density. The ionosphere comprises several local maxima of the electron density, historically called the ionospheric layers and having various appearances depending on factors such as the time within the day, thus forming the so-called vertical ionospheric profile, as shown in Fig 2. The F2 layer holds the largest concentration of free electrons.

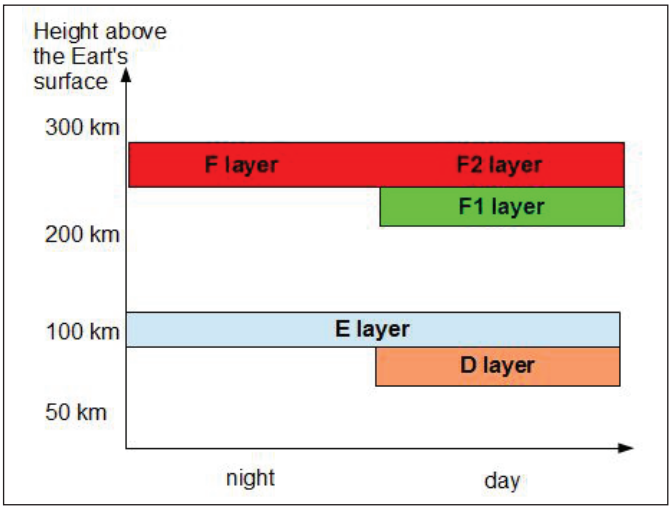

Figure 2 Characteristics of ionospheric layers

The ionospheric layers affect the propagation characteristics of GPS signals, causing the variations of the refractive index *n*. The refractive index n can be determined from the Appleton – Hartree formula (1).

$$n^2 = 1 - \frac{X}{1 - i \cdot Z - \frac{Y_T}{1 - X - i \cdot Z} \pm \left[\frac{Y_T^4}{4 \cdot (1 - X - i \cdot Z)^2}\right]^{0.5}} \qquad (1)$$

After imposing the restrictions that characterise the radio propagation in the related environment, the GPS single-frequency ionospheric delay may be understood the group delay of a satellite signal, and expressed as shown in (2).

$$d_{GPS}[m] = K \cdot \int_0^H N(h) \cdot dh \tag{2}$$

The integral form in (2) presents the total number of electrons encountered by satellite signal on its path from satellite to user aerial. Measured in number of electrons per m^2, this parameter is dubbed the Total Electron Content (TEC), as defined in (3).

$$TEC = \int_0^H N(h) \cdot dh \tag{3}$$

Consideration of (2) and (3) reveals that the equivalent GPS ionospheric time delay is directly proportional with TEC value, proving that the vertical ionospheric profile affects pseudorange determination and GPS-based position estimation.

Ionospheric layers express rather erratic behaviour, when certain patterns of dynamics can be identified in relation to the time of the day (daily patterns, Fig 3), a season (seasonal patterns), a geographical region (geographical patterns), and solar activity. Still, temporal variation in the ionosphere of natural and artificial origins can account for a large part of the un-corrected GPS ionospheric delay.

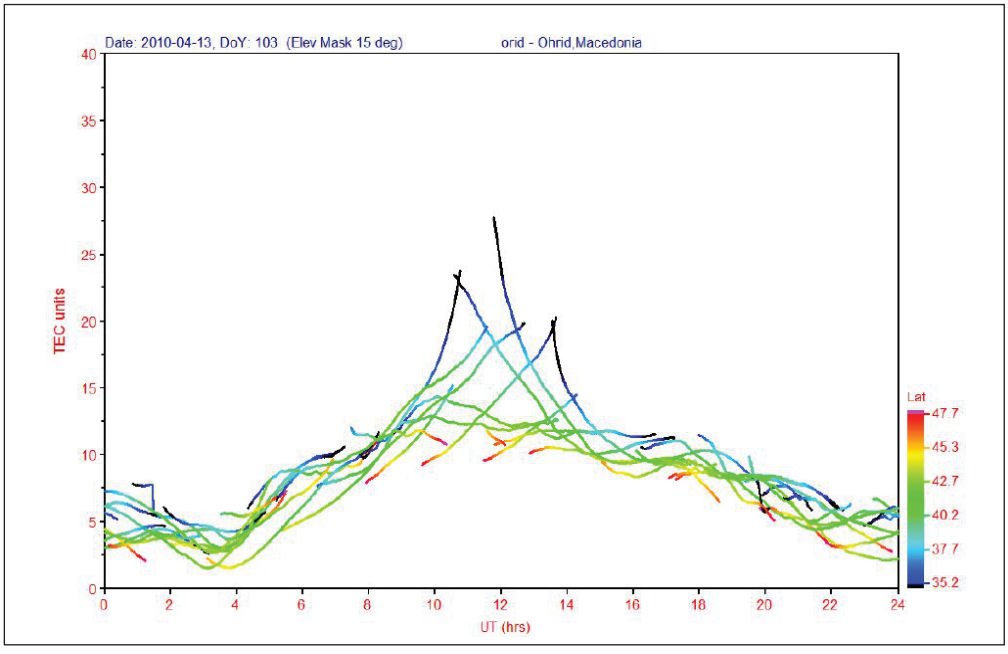

Figure 3 Daily pattern of TEC and GPS ionospheric delay dynamics

3 CATEGORIES OF IONOSPHERIC MODELS

Analytical modelling of the ionospheric vertical profile is essential for either complete or partial correction of the GPS ionospheric delay with the aim to improve the quality (accuracy) of the GPS-based position estimation.

Three essential approaches have been developed in order to tackle GPS ionospheric delay through understanding of the ionospheric dynamics, as follows:

- simple layer ionospheric models,
- numerical maps,
- composite models.

Simple layer ionospheric models rely upon a successful reconstruction of the geometry of ionospheric layers assumed to provide noticeable contribution to GPS ionospheric delay. Such models take into account the solar activity status, as well as real-time observables of geomagnetic field component values and the ionospheric parameters.

$$\Omega(\varphi,\ \lambda,\ t) = a_0(\varphi,\lambda) + \sum_{j=1}^{N} [a_j(\varphi,\ \lambda)\cdot\cos(j\cdot T) + b_j(\varphi,\ \lambda)\cdot\sin(j\cdot T)] \qquad (4)$$

Numerical maps forecast GPS ionospheric delay using numerical models of spatial distribution of free electrons, based on experience (previously catalogued patterns of ionospheric behaviour in relation to solar and geomagnetic activity), as expressed in (4).

Finally, the composite models integrates simple layer and numerical map models in order to provide more complex, but at the same time more accurate description of the ionospheric vertical profile behaviour. Improved estimation of the GPS ionospheric delay is achieved by exploiting the the advantages of simpler models.

4 BENT MODEL

Rodney B Bent and collaborators analysed historical observations of daily ionospheric dynamics taken world-wide in mid- and low-latitude regions in order to establish a model of ionospheric dynamics. Bent model uses geometrical approach in describing the vertical profile of the ionospheric layers, and to fine-tune it to observed daily, solar dynamics and seasonal observations.

Bent and his team conducted the research with the partial intention to use it in then-developing GPS system. The team identified the determination of the critical frequency of F2 layer *f0F2* and the height of F2 layer as the critical points in the GPS ionospheric delay model.

5 KLOBUCHAR MODEL

Klobuchar model is an approximation of the daily dynamics of GPS ionospheric delay and TEC, based on experimental observation. The model was derived from previously presented Bent model by John A Klobuchar, and established as the standard GPS ionospheric correction model.

Klobuchar model assumes two fundamental components contribute to the total GPS ionospheric delay: a constant nightly value, and a half-cosine component expressing the daily variations of GPS ionospheric delay.

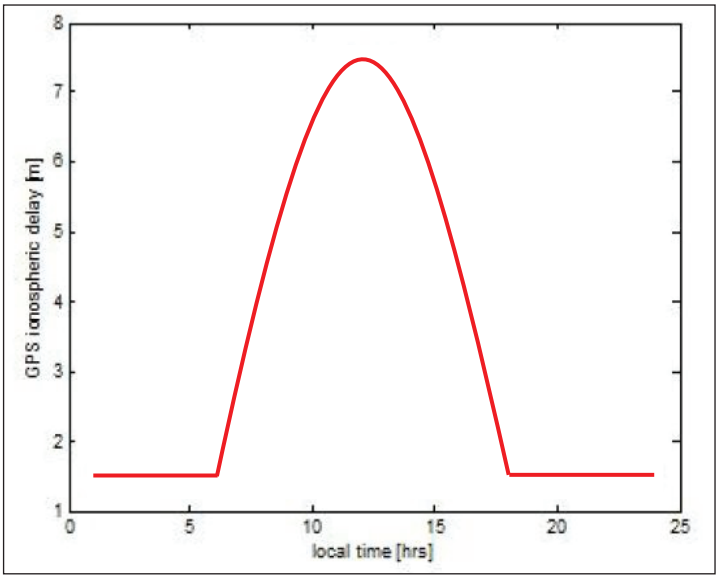

Figure 4 Klobuchar model definition

$$\Delta t_{slant} = m(el) \cdot \Delta t_{VTEC}$$
$$\Delta t_{VTEC} = t_{night-time} + A(\varphi, \lambda, Ap) \cdot \cos\left[\frac{2 \cdot \pi \cdot (t - t_0)}{P}(\varphi, \lambda, Ap)\right] \quad (5)$$

Day-time component enters into operation at dawn and ceases at dusk, reaching its maximum around 1400 local time. The amplitude and period of the half-cosine daily component of GPS ionospheric delay are determined by the level of solar and geomagnetic activity, and by components of position (geomagnetic longitude and latitude) of the so-called pierce-point (point at which satellite signals intersects imagined Earth-centred sphere extending to the height of 350 km above the Earth's surface).

6 VALIDATION OF KLOBUCHAR MODEL

In the strict pursuit of the highest scientific standards, which can also be seen as an educational contribution, Klobuchar and his team conducted numerous validation field campaigns world-wide aimed at assessment of Klobuchar model performance.

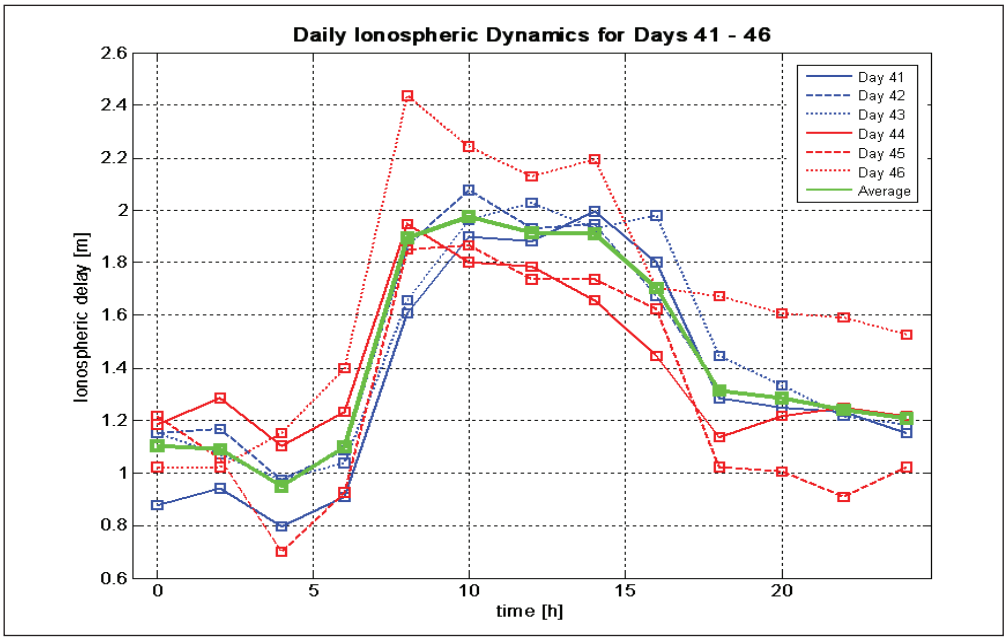

Figure 5 Unusual local GPS ionospheric delay dynamics is observed in Northern Adriatic area

Initial assessments reveal the model's capability to correct up to 70% of the total GPS ionospheric delay for single-frequency receivers. Later research validated this capability for periods of quiet space weather. Furthermore, Klobuchar model

is incapable of correcting local ionospheric disturbances due to its approach in determination of the daily component parameters based on world-wide-averaged ionospheric dynamics.

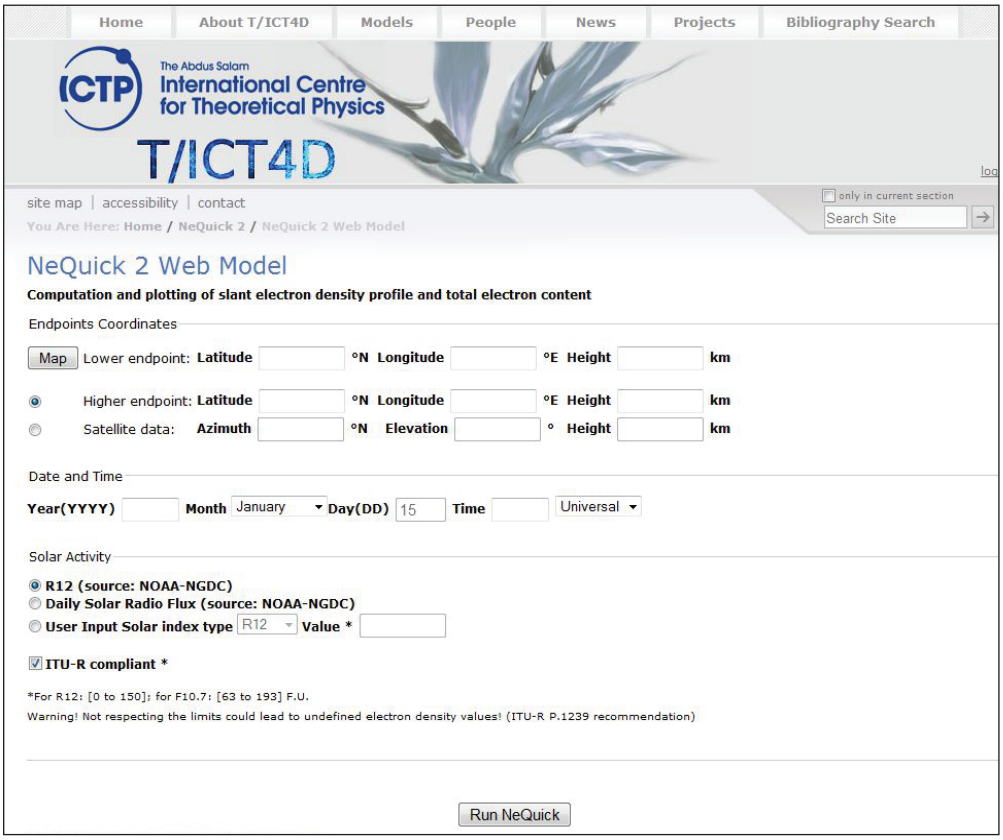

Figure 6 A web-based tool is provided for the independent NeQuick model assessment

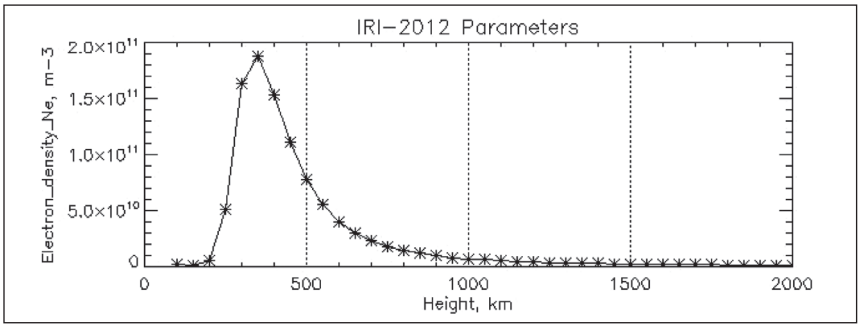

Figure 7 A result of an IRI web-based ionospheric modelling

7 RECENT ADVANCEMENTS IN GNSS IONOSPHERIC MODELLING

Independent research has been conducted in order to allow for more accurate description of ionospheric dynamics world-wide, with occasional side-effects on determination of GPS ionospheric delay.

A team led by Sandro M Radicella developed the NeQuick ionospheric model, accepted for utilisation as a standard ionospheric correction model for the European satellite navigation system Galileo. NeQuick model uses the common approach in attempting to model the vertical profile geometry of ionospheric layers. Its foundations lay in the extensive catalogue of ionosonde-based screening of the ionosphere at the various sites world-wide.

At the same time, an international co-operation, led by Dieter Bilitza and Bodo Reinisch, has collaborated on development of the physics-based International Reference Ionosphere (IRI) model. Considering the details of ionospheric layers formation and taking into account the plasmasphere effects, often neglected in simplifying models, the IRI aims at providing the detailed and complex description of the ionospheric dynamics.

Mitigation of the GNSS ionospheric effects has taken other approaches. One of the most effective mitigation techniques was the utilisation of FDMA signals for Russian satellite navigation system Glonass, thus removing the need to deploy any ionospheric correction model.

8 CONCLUSION

The ionospheric effects on GPS performance were recognised from the early beginnings of GPS development. The extensive field research conducted during 1950s and 1960s, and continued world-wide in uninterrupted fashion, resulted in a number of standardised and independent models aimed at description of the ionospheric dynamics and its effects on GPS performance.

Early achievements of Bent and Klobuchar have established a completely new discipline, combining atmospheric physics, signal processing, time series modelling, forecasting end estimation with satellite navigation.

While the traditional models attempted at describing the ionospheric effects on GPS in a global fashion, recent advancements focus on identification of sources of local ionospheric disturbances and the mechanisms of their transfer to surrounding regions.

More detailed insight into the nature of the GPS ionospheric delay dynamics allows for reverse engineering, and utilisation of GPS/GNSS receivers as ambient sensors of space weather and ionospheric conditions.

REFERENCES

1. Allain, D J, and Mitchell, C N. (2009). Ionospheric delay corrections for single-frequency GPS receivers over Europe using tomographic mapping. *GPS Solutions*, **13**, pp. 141–151.
2. Bent, R B, Llewellyn, S K, and Walloch, M K. (1972). Description and Evaluation of the Bent Ionospheric Model. DBA Systems, Inc. Melbourne, FL.
3. Bilitza, D et al. (2012). Measurements and IRI model predictions during the recent solar minimum. *J of Atmospheric and Solar-Terrestrial Physics*, **86**, pp. 99–106.
4. Bilitza, D et al. (2010). The international reference ionosphere today and in the future. *J Geod*, **85**, pp. 909–920.
5. Davis, K. (1990). Ionospheric Radio. Peter Peregrinus Ltd. London, UK.
6. Filjar, R, Kos, T, and Kos, S. (2009). Klobuchar-Like Local Model of Quiet Space Weather GPS Ionospheric Delay for Northern Adriatic. *J of Navigation*, **62**, pp. 543–554.
7. Kintner, P M, and Ledvina, B M. (2005). The ionosphere, radio navigation, and global navigation satellite systems, *Adv Space Res*, **35**(5), pp. 788–811.
8. Klobuchar, J A et al. (1973). Total Electron Content Studies of the Ionosphere. AF Surveys in Geophysics, No. 257. Hanscom, MA.
9. Klobuchar, J A. (1975). A First-Order, Worldwide, Ionospheric, Time-Delay Algorithm. AF Surveys in Geophysics, No. 324. Hanscom, MA.
10. Klobuchar, J A. (1983). Ionospheric Effects on Earth-Space Propagation. Environmental Research Papers No. 866. Hanscom, MA.
11. Klobuchar, J A. (1987). Ionospheric Time-Delay Algorithm for Single-Frequency GPS Users. *IEEE Trans on AES*, 3, pp. 325–331.
12. Klobuchar, J A et al. (1987). Measurements of Trans-Ionospheric Propagation Parameters in the Polar Cap Ionosphere. Environmental Research Papers, No. 973. Hanscom, MA.
13. Van Dierendonck, A J, Klobuchar J A, and Hua, Q. (1989). Ionospheric Scintillation Monitoring Using Commercial Single Frequency C/A Code Receivers. *Proc of ION GPS-94: 7th International Technical Meeting of the Satellite Division of the Institute of Navigation* (10 pages). Salt Lake City, UT.
14. Klobuchar, J A. (1991). Present Status and Future Prospects for Ionospheric Propagation Corrections for Precise Time Transfer Using GPS. *23rd Annual Precise Time and Time Interval Applications and Planning Meeting*, Pasadena, CA.
15. Parkinson, B W, and Spilker Jr., J J. (editors). (1996). Global Positioning System: Theory and Applications (Vol. I.). AIAA. Washington, DC.
16. Petrovski, I G, and Tsujii, T. (2012). Digital Satellite Navigation and Geophysics: A Practical Guide with GNSS Signal Simulator and Receiver Laboratory. Cambridge University Press. Cambridge, UK.
17. Radicella, S M. (2009). The NeQuick model genesis, uses and evolution. *Annals of Geophysics*, **52**, pp. 417–422.

Faculty of Maritime Studies
University of Rijeka, Croatia

Royal Institute of Navigation
Science Technology Practice

7th GNSS
Vulnerabilities and Solutions Conference

GNSS RADIO OCCULTATION: Identification of Criticisms in Electron Density Profile Retrieval During Moderate/high Solar Activity

Muhammad Mubasshir Shaikh[1], **Riccardo Notarpietro**[1], **Bruno Nava**[2]

[1] Politecnico of Turin, Department of Electronics and Telecommunications, Torino, Italy
E-mail: muhammad.shaikh@polito.it

[2] The Abdus Salam International Centre for Theoretical Physics, Trieste, Italy

ABSTRACT. *NeQuick2 is a quick-run ionospheric electron density model designed for trans-ionospheric propagation applications with improved profile representation of the entire ionosphere (bottom and top side). In this work, NeQuick2 has been used to produce synthetic electron density data in order to define test case scenarios that have been used to study the ionospheric effects on Radio Occultation (RO) signals. Such data will be used to identify possible criticalities both in the standard retrieval algorithms and in the standard ionospheric compensation procedures. As far as the RO data inversion technique in the ionosphere is concerned, the onion-peeling algorithm is the one commonly used. In the framework of this work, it has been implemented and it has been used to extract electron density profiles from the limb sounding total electron content (TEC) measurements (limb TEC in what follows) simulated within the controlled environment generated using NeQuick2. Because of the implicit assumption of electron density spherical symmetry distribution, the onion-peeling algorithm could give erroneous results (e.g. in the retrieved peak electron density) when strong horizontal ionospheric electron density gradients are present, as it could happen in the Equatorial Ionization Anomaly (EIA) region. Indeed, this contribution mainly aims to point out the impact of the solar activity on the electron density profiles retrieval, considering limb sounding observation strategy.*

KEY WORDS: *GNSS Radio Occultation, NeQuick2, Onion-peeling, Moderate/High Solar Activity*

1 INTRODUCTION

TRANSMIT (Training Research & Application Network to Support the Mitigation of Ionospheric Threats) project deals to suggest solutions to the effects of the ionosphere on Global Navigation Satellite Systems (GNSS). These effects will become significant as we approach the next solar maximum, predicted for the year 2013. The main aim of the project is to develop a set of integrated real-time state-of-the-art tools capable to mitigate ionospheric threats on GNSS signals and receivers in areas such as civil aviation, marine navigation and land transportation. TRANSMIT is divided in 13 sub-projects (ESR1 to ESR13). One of these (ESR4 sub-project, entitled: "Radio Occultation for Ionospheric Monitoring – Impact & Mitigation of High Solar Activity Effects") will be focused on the development of improved algorithms for RO data processing, both for the electron density profile retrieval and for ionospheric compensation strategies; the latter one is necessary for a better retrieval of neutral atmospheric products. Basically, the RO technique allows us to transform phase observations performed on a limb sounding geometry from a Low Earth Orbit receiver, into atmospheric profiles (electron density in ionosphere, temperature, pressure and water vapour in the troposphere).

This sub-project will be focused on the development of improved GNSS – RO inversion algorithms for a better characterization of ionospheric profiles and on the development of improved ionospheric compensation algorithms to be applied when neutral atmospheric profiles are extracted from RO data. Assimilation of RO – derived data into imaging and forecasting algorithms will be attempted exploiting strong collaborations with the Abdus Salam ICTP (International Centre for Theoretical Physics), ISC (Institute of Complex Sciences), UoB (University of Bath) and other partners of the network.

1.1 Radio Occultation

RO missions such as GPS/MET, CHAMP, COSMIC and METOP [Anthes et al. 2008, Gorbunov M.E. 2001, Hajj et al. 2001, Healy et al. 2002, Luntama et al. 2008] have been designed to sound the Earth's neutral atmosphere and ionosphere via a radio link between a GPS navigation satellite and GPS receiver onboard Low Earth Orbit (LEO) satellites [Gorbunov, 1996]. The U.S. GPS/MET experiment was the first mission which successfully applies radio occultation technique to the Earth using GPS signals. Figure 1.1 illustrates a view (not in scale) of the RO or limb sounding geometry. Radio waves are refracted when passing through the Earth's atmosphere in the direct communication between GPS and the occulted LEO satellite. As a result, they follow bent ray-paths and

experience significant propagation delays. The magnitude of such effects depends on the nature of the atmosphere. In neutral atmosphere, the bending of the signal is extracted and inverted into refractivity profiles through the Abel inversion [Kursinsky 1997, Ware et al. 1996] whereas in the ionosphere, where bending could be neglected, excess phase measurement, and corresponding limb TECs, are evaluated and used to extract electron density profiles.

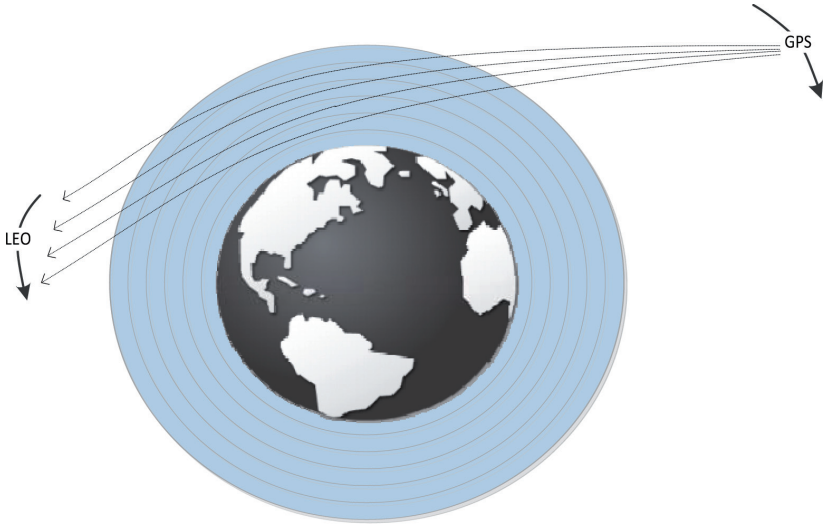

Figure 1.1 A typical RO scenario between LEO and GPS satellites in Earth's atmosphere

In the ionosphere, the inversion method for RO data is based on an assumption of a local spherical symmetry for the electron density (where locally means up to a few thousand kilometres radius around the tangent point of the GPS-to-LEO ray-path). This assumption cannot always be valid, even for moderate solar activity, since it ignores the physical presence of horizontal density gradients. The retrieved electron density profile may have errors in cases when ionospheric conditions differ greatly from the assumptions; e.g. in the EIA region. It is understood that during high solar activity periods, the increased electron density gradients may lead to increased errors in the electron density profiles retrieved by TEC inversion. This issue, which is the main focus of this work, has been discussed in details in the latter part of this paper.

1.2 Electron Density profile Retrieval

Limb TEC derived measurements between LEO and GPS satellites are necessary for subsequent electron density profile (Ne(h)) retrieval. The profile is defined in

terms of the locations of the ray perigees of each ray-paths between LEO and GPS. Input for Ne(h) retrieval algorithm are internal orbit TEC-time series (from A1 to A2 points in figure 1.2) observed from the same GPS satellite during the occultation event. External TEC (TEC from GPS-to-B or GPS-to-A2) should be removed before starting the inversion procedure. With current RO missions, except for the COSMIC case, it is only possible to perform TEC measurements at the highest point of LEO orbit (point B in Figure 1.2). For the COSMIC case, TEC measurements from GPS to A2 are also available. If none of the measurements are available, we need to model the 'external' TEC (from GPS to B or GPS to A2) using climatological models, tomography, or following other strategies. The Onion-peeling algorithm is a good technique to invert TEC data to electron density profiles. Unfortunately, the major drawback of this technique is that it assumes a spherical symmetric distributed ionospheric electron density (more details on this aspect will be given in the next section). The onion-peeling is very effective in case of small horizontal gradients in the ionosphere electron density (then, particularly during low solar activity periods). But, for moderate to high solar activity periods, large electron density gradients can be experienced. In this case, the onion-peeling algorithm may fail, giving in output erroneous Ne(h) profiles.

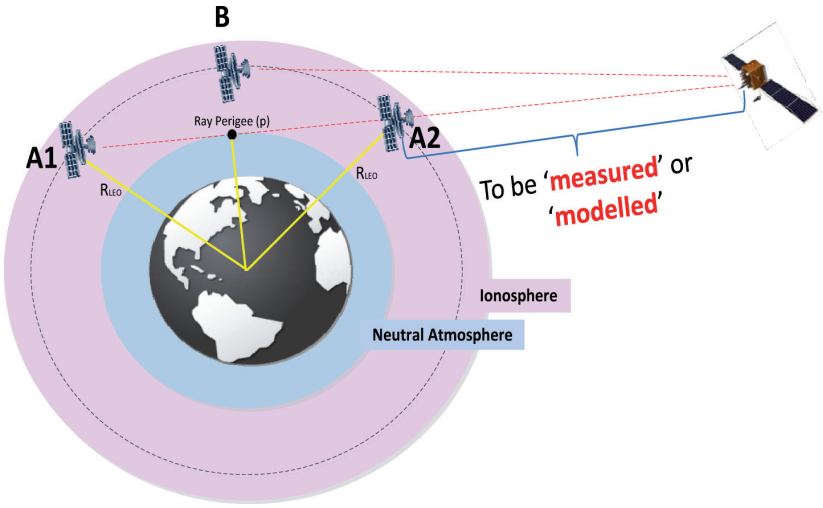

Figure 1.2 Limb TEC measurement in a RO Scenario

2 ONION-PEELING

In the ionosphere, inversion techniques are based on the assumption that the LEO-GPS ray bending angle is negligible. The inversion we applied is the onion-peeling method. It is an inversion algorithm which is widely used to invert the limb TEC measurements for RO events in order to obtain vertical electron density profiles. These profiles are not exactly vertical as, during an occultation event, the ray perigee moves slightly away from the vertical due to the relative motion of the GPS and LEO satellites.

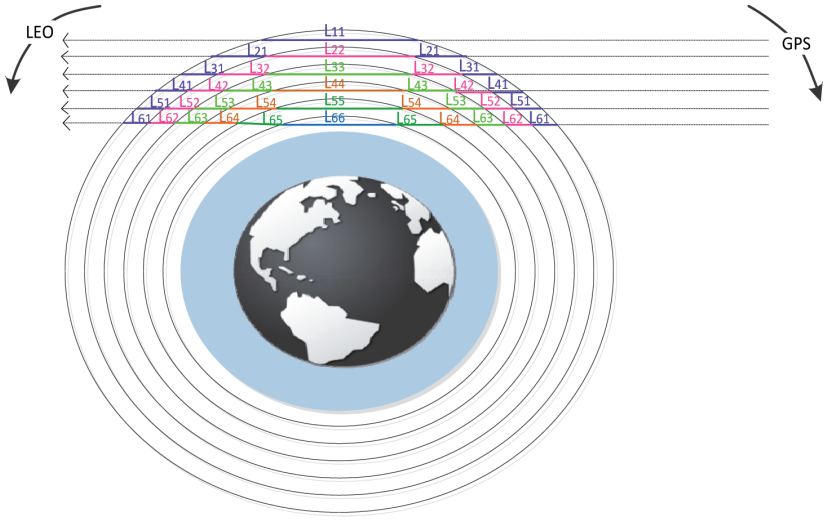

Figure 2.1 Onion-peeling Scenario with shells in the Ionosphere

Since the movement of GPS satellite is very small during an occultation event, the displacement of the ray perigee towards GPS satellite is also very small. But these movements should not be ignored and should always be taken into account. In the framework of this work, the onion-peeling has been implemented and it has been used to extract electron density profiles from the limb TEC measurements simulated within a controlled environment. For a given occultation event we can write the limb TEC of each ray 'i' as a set of spherical shells like 'onion rings' [Leitinger et al. 1997, Hernandez-Pajarez et al, 2000], where the mean radius of the shell is the impact parameter of the ray. Figure 2.1 is a simplified illustration of onion-peeling technique.

Using onion-peeling technique, the STEC may be inverted to extract the electron density profile Ne(h) as follows:

$$STEC_i = \sum_{j=1, j\neq i}^{\#\ Ne\ Shells} 2L_{ij}\, Ne_j + L_{ii} Ne_i$$

$$\begin{bmatrix} TEC_1 \\ TEC_2 \\ TEC_3 \\ TEC_4 \\ TEC_5 \\ TEC_6 \end{bmatrix} = \begin{bmatrix} L_{11} & 0 & 0 & 0 & 0 & 0 \\ L_{21} & L_{21} & 0 & 0 & 0 & 0 \\ L_{31} & L_{31} & L_{31} & 0 & 0 & 0 \\ L_{41} & L_{41} & L_{41} & L_{41} & 0 & 0 \\ L_{51} & L_{51} & L_{51} & L_{51} & L_{51} & 0 \\ L_{61} & L_{61} & L_{61} & L_{61} & L_{61} & L_{61} \end{bmatrix} \cdot \begin{bmatrix} Ne_1 \\ Ne_2 \\ Ne_3 \\ Ne_4 \\ Ne_5 \\ Ne_6 \end{bmatrix}$$

$$\overline{STEC} = \bar{\bar{L}} \cdot \overline{Ne}$$

$$\overline{Ne} = \overline{\bar{L}^{-1}} \cdot \overline{TEC}$$

where,

'L_{ij}' is the length of the segment used to calculate the electron density (N_{ej}) in 'j_{th}' shell

'N_{ej}' is the calculated electron density for 'jth' shell/shell

'TEC_j' is the limb TEC value of the ray (GPS to LEO) crossing all the shells at the height of 'jth' shell

This approach faces two major issues. Firstly, this technique is based on spherical symmetry hypothesis, namely, the electron density distribution is assumed to have a spherical symmetry (the electron density depends only on height). Secondly, as it is clear from the mathematical expression given above, electron density in each ionospheric layer is calculated from all the electron densities evaluated above it. That is, if the calculation of electron density for one shell (at a particular height) is wrong because of any reason, the calculated value not only affects that shell's calculated electron density, but it could also add an error contribution in the calculation of the electron densities for the layers below it. Both these causes may impact the right electron density profile retrieval, above all in the case of large horizontal electron density gradients. With the current implementation (namely without the help of external information like e.g. ground-based TEC data as suggested by [Hernàndez-Pajares et al. 2000]), there is no way to predict or correct this error.

3 NEQUICK2

As mentioned by [B. Nava et al. 2008 and references therein], NeQuick2 is an ionospheric electron density model developed at the Aeronomy and Radio-

propagation Laboratory of The Abdus Salam International Centre for Theoretical Physics (ICTP), Trieste, Italy. Historically the NeQuick (version 1) has to be considered as an evolution of the DGR profiler proposed by [Di Giovanni and Radicella 1990], and subsequently modified by [Radicella and Zhang 1995]. The first version of the model has been used by the European Space Agency (ESA) European Geostationary Navigation Overlay Service (EGNOS) project for assessment analysis and has been adopted for single-frequency positioning applications in the framework of the European Galileo project. It has also been adopted by the International Telecommunication Union, Radio-communication Sector (ITU-R) as a suitable method for total electron content (TEC) modelling [ITU, 2003]. In addition, the NeQuick has been implemented in the simulation toolkit developed in Australia to conduct a qualitative assessment of the performance characteristics of the future GNSS infrastructure [Seynat et al., 2004] and it has been adapted by the Rutherford-Appleton Laboratory of the UK to forecast vertical TEC from forecasted values of foF2 and MUF(3000)F2 [Cander, 2003].

In the scope of this sub-project, NeQuick-2 has been used to produce synthetic electron density data and to simulate corresponding limb TEC observations in order to define test case scenarios that could be used to 'stress' the onion-peeling algorithm. The NeQuick2 is able to characterize the electron concentration distribution in both the bottomside and topside of the ionosphere, and it is a quick-run model particularly tailored for trans-ionospheric propagation applications. The basic inputs of the NeQuick2 model are position, time (UT) and solar flux (or sunspot number); the output is the electron concentration at the given location and time. The mathematical expression implemented on NeQuick for the day time and night time electron densities are different as the E-layer normally disappears during night time. During day time, when all the ionospheric layers are present, the electron density profile can be calculated as:

$$N(h) = N_E(\mathrm{h}) + N_{F1}(\mathrm{h}) + N_{F2}(h)$$

$$N_E(h) = \frac{4N_m \cdot E}{(1 + exp^{(\frac{h - h_{mE}}{BE}\xi(h))})^2 \cdot exp^{(\frac{h - h_{mE}}{BE}\xi(h))}}$$

$$N_{F1}(h) = \frac{4N_m \cdot F1}{(1 + exp^{(\frac{h - h_{mF1}}{B1}\xi(h))})^2 \cdot exp^{(\frac{h - h_{mF1}}{B1}\xi(h))}}$$

$$N_{F2}(h) = \frac{4N_m \cdot F2}{(1 + exp^{(\frac{h - h_{mF2}}{B2}\xi(h))})^2 \cdot exp^{(\frac{h - h_{mF2}}{B2}\xi(h))}}$$

with,

$$\begin{cases} N_m \cdot E = N_m E - N_{F1}(h_m E) - N_{F2}(h_m E) \\ N_m \cdot F1 = N_m F1 - N_E(h_m F1) - N_{F2}(h_m F1) \\ \xi(h) = exp^{\left(\frac{10}{1+1|h-h_m F2|}\right)} \end{cases}$$

where,

'$\xi(h)$' Function that ensures a "fadeout" of the E and $F1$ layers near the *F2 layer peak in order to avoid secondary maxima around* $h_m F2$

'$N_m E, N_m F1, N_m F2$' Layer peak electron densities for E, $F1$ and $F2$ (expressed in '10^{11}/m^3')

'$h_m E, h_m F1, h_m F2$' Layer peak heights for *E, F1* and *F2* (expressed in 'km')

'$BE, B1, F2$' Layer thickness parameters for *E, F1* and *F2* (expressed in 'km')

4 METHODOLOGY

This paper is mainly focused on analysing the impact of the spherical symmetry hypothesis on the onion-peeling algorithm when it is used to invert limb TEC data into electron density profiles. The attention has been mainly devoted to test whether the ionospheric spherical symmetry hypothesis of onion-peeling algorithm can be applied with valid results in moderate/high solar activity conditions. The initial results during this work are obtained by preliminary (and standard) implementation of the onion-peeling algorithm. During this TRANSMIT subproject, this algorithm will be tentatively improved with the help of ionospheric models in order to verify if it is possible to overcome this main limitation.

During this work, in order to better understand the effects of electron density asymmetry, we have used NeQuick2 to simulate the ionosphere behaviour for the month of July during a moderate and a high solar activity period. The solar flux values used as NeQuick input were 128 and 180 solar flux unit (sfu[1]). The occultation events have been simulated also in EIA region to understand the effects of the strong electron density gradients present in this region. This work has only been done by taking into account 2D geometry of the RO events.

[1] 1 sfu = 10^{-22} watt/m^2/Hz

4.1 Simulation Results

In order to formulate the scenario for the simulation, a global VTEC grid has been evaluated using NeQuick2. This was achieved by running NeQuick2 for a 1° X 1° grid of latitude and longitude. In this way, a complete VTEC grid of 180° (90° N to 90° S) by 360° (180° W to 180° E) has been evaluated at UT 0100 for a solar flux equals to 128 sfu. This map is shown in figure 4.1. In the VTEC grid shown in figure 4.1 the white/magenta lines show the projection on Earth's surface of the GPS-to-LEO links (internal to the LEO orbit). The simulated occultation events occur for simple 2D geometries at constant longitudes of 170° W and 10° W. The white part is the projection from the ray perigee point (p) to the (A1) side of the LEO orbit whereas magenta is used for the projected ray-path from ray perigee (p) to (A2) point (see figure 1.1).

The choice of these two longitudes is made because at each longitudinal line the ionosphere exhibits different VTEC values and consequently, different electron density gradients. In addition, for each longitude, five geometrical configuration have been defined (by shifting the occultation plan for a certain number of degrees in latitude) in order to put in evidence the effects of spherical symmetry assumptions. As it is shown in figure 4.1, the simulated occultation events at 170° W cross a well-developed EIA region in contrast to what is happening at 10° W. The results are formulated by comparing the onion-peeling inverted profiles to the 'truth' profiles (generated by NeQuick2 in correspondence to the geographical position of all the ray perigees of the simulated occultation event at the same location, UT and solar flux value). This is done to observe how the onion-peeling algorithm is impacted by asymmetry in electron densities present in the ionosphere. Also, this will help us to qualitatively evaluate how truthfully we can rely on the results produced by the onion-peeling inversion in presence of electron density gradients observed in different locations or time of the day and different solar activities.

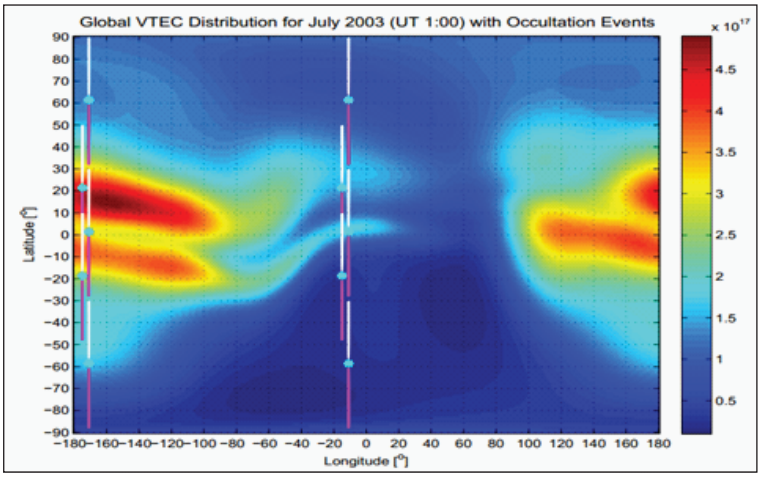

Figure 4.1 Global VTEC Distribution calculated using NeQuick2; solar flux = 128 sfu. Superimposed are the projections on Earth's surface of the GPS-LEO links

Several simulation results have been obtained during this experiment by considering several RO events and then extracting electron density profiles following the described approach. To support the idea presented in the paper in a better way, we only selected simulation results evaluated with the set of parameters listed in table 4.1 below.

Table 4.1 Parameter set for simulation

Solar activity type	Moderate/high
Solar Flux value	128 and 180 sfu
Month	July
UT	0100
Longitude	10° W and 170° W
Latitude	90° N to 90° S

Figure 4.2 summarizes the results concerning the RO events evaluated at longitude 10° W and 170° W. In figure 4.2a, plots showing results of the RO event evaluated at 10° W and 170° W longitudes with the ray perigees lying at around 60° N in latitude. As shown in the VTEC distribution (evaluated for a solar flux value of 128), both RO events are observed in relatively low gradients of TEC, since simulated trajectories lie outside the equatorial anomaly region. This is evident in the extraction of electron density profiles, where the inverted profiles (blue lines) and their simulated truth (red line) are in a good agreement.

The last two plots of figure 4.2a show the electron density profile meridian distributions (electron density "cross-sections" at longitude of 170° W and 10° W). The height of the maximum electron density (F2 layer peak height) is indicated by a thin green line and the traces of all the ray-paths between LEO and GPS satellites characterizing the simulated occultation events (for ray perigees height varying from 1 km to 900 km above Earth's surface) can be found. The thick green line represents the trace of the ray-path between LEO and GPS satellites at F2 layer peak height. It can be observed that, for both cases, the B to A1 and B to A2 ray-paths cross low (and rather symmetric) electron density gradients. Therefore a good agreement between onion-peeling retrieved electron density profile and corresponding NeQuick2 truth is expected.

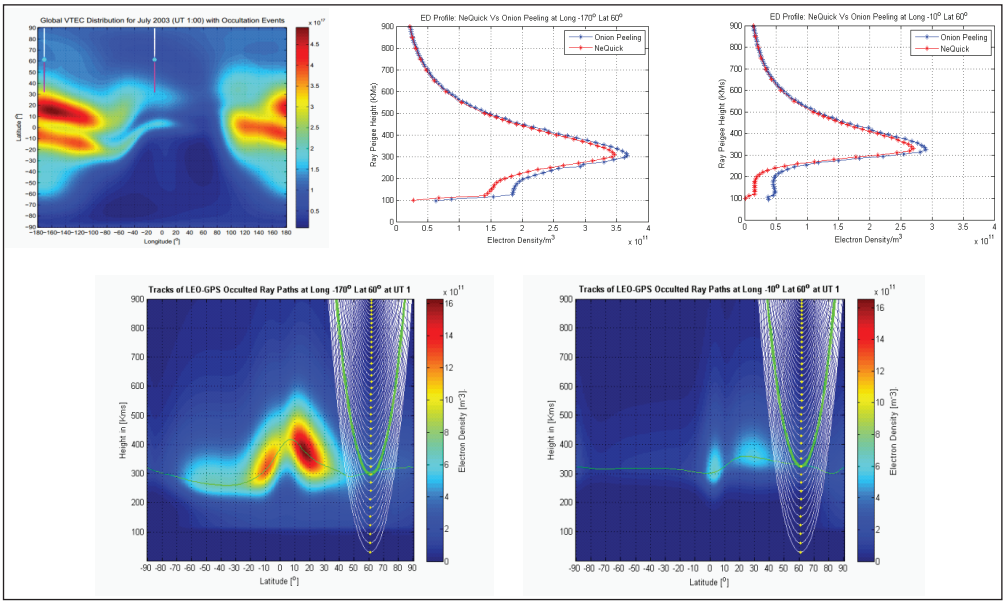

Figure 4.2a Comparison between onion-peeling inversion and simulated truth (NeQuick2; solar flux = 128 sfu) at Lat 60°

In case of figure 4.2b, the occultation plan is shifted in a way that the ray perigees lie at and around 20° N in latitude. It is evident that the behaviour of the ionosphere in this case is significantly different. In this situation, the ray-paths of both the simulated RO events lie in the EIA, where larger electron density gradients are present. The situation is mainly highlighted in the 170° W longitude case, because of the used local time (0100 UT). At 10° W, the inverted profile and the reference one are in good agreement as the VTEC values show much smaller variations in the 10° W meridian plane than in the 170° W plane. In the plots of electron density

profiles comparison large differences between 170° W and 10° W longitudes' electron density profiles can be observed, with differences reaching about one order of magnitude. This is also visualized in the electron density "cross-sections" (figure 4.2, bottom). In case of 170° W, the peak of F2 (thick green line in the middle of the ray-path traces) crosses the equatorial anomaly in presence of very high gradients, whereas at 10° W the ionization seems to be less pronounced.

Last examples are those shown in figures 4.2c and 4.2d, where occultation plans are shifted to evaluate ray perigees at 0° and 20° S in latitude respectively. In figure 4.2c it is clearly shown how the onion-peeling could produce some misleading results due to the invalid spherical symmetry hypothesis. In this case even a negative electron density at 10° W is obtained by the inversion procedure.

In both cases (170° W and 10° W) the ray-paths followed by the signals seem to cross the highest electron density gradients (see figure 4.c, bottom). At 170° W longitude, the ground 'truth' and the onion-peeling-derived electron density profiles seem to be in much better agreement at F2-peak level, whereas the discrepancy increases at lower heights. This because the ray-paths are sensing essentially a symmetric electron density from the top of the orbit down to the F2 peak height, while below this height strong departures from the spherical symmetry are evident. This effect is more clear in the 10° W example, where the ray-paths start to detect remarkable departures from the spherical symmetry at higher heights and the error is accumulated down to 100km producing even negative electron density values.

In the case shown in figure 4.2d, at 10° W the onion-peeling-derived electron density profiles have larger differences with respect to the simulated truth than the onion-peeling-derived and the corresponding true profiles at 170° W. This is an opposite case with respect the one shown in figure 4.2c. By observing the traces of ray-paths for the 10° W case (figure 4.2d, bottom, right) we can see that almost all the shells above the maximum electron density height did not lead to the error propagation as they experience an ionosphere with low gradients. But, the ray-paths closer to the Earth's surface produced these errors, since they experience larger gradients of TEC on one side only. NeQuick2 profile is then evaluated for the geographical position of the ray perigee, which is placed in a less ionized region.

At the other end, at 170° W longitude the retrieved electron density profiles seem to be in much better agreement with the truth one. This is a particular case since, as highlighted in figure 4.2d (bottom, left) the distribution of electron density seems to be (qualitatively) an odd function of the angular distance between the considered point and tangent point, the ray perigee, of each ray-path (considering in particular those trajectories crossing regions near to the F2 peak height). Gradients have opposite "signs" in both sides of the ray-paths, causing the opposite gradient

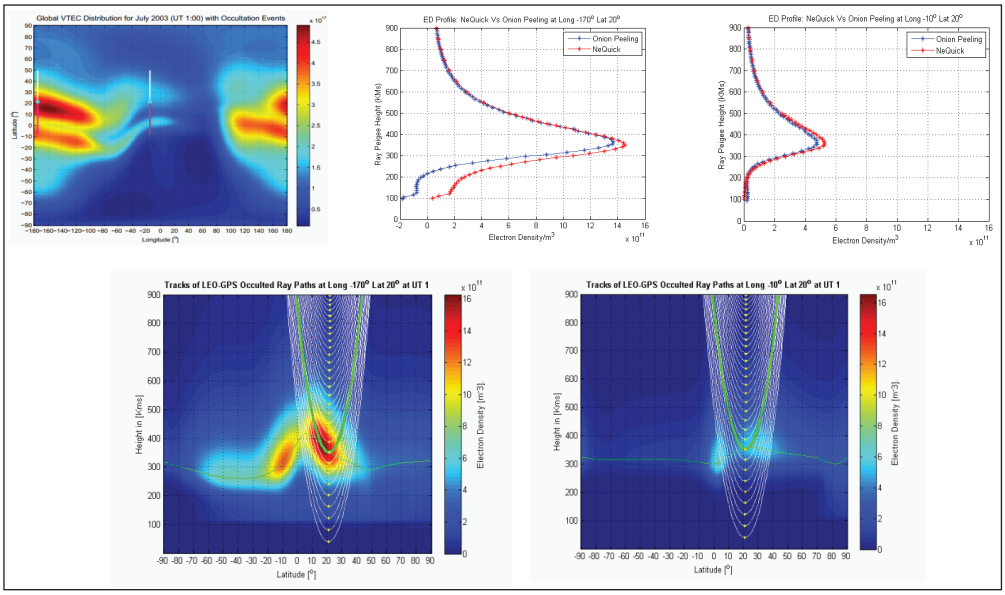

Figure 4.2b Comparison between onion-peeling inversion and simulated truth (NeQuick2; solar flux = 128 sfu) at Lat 20°

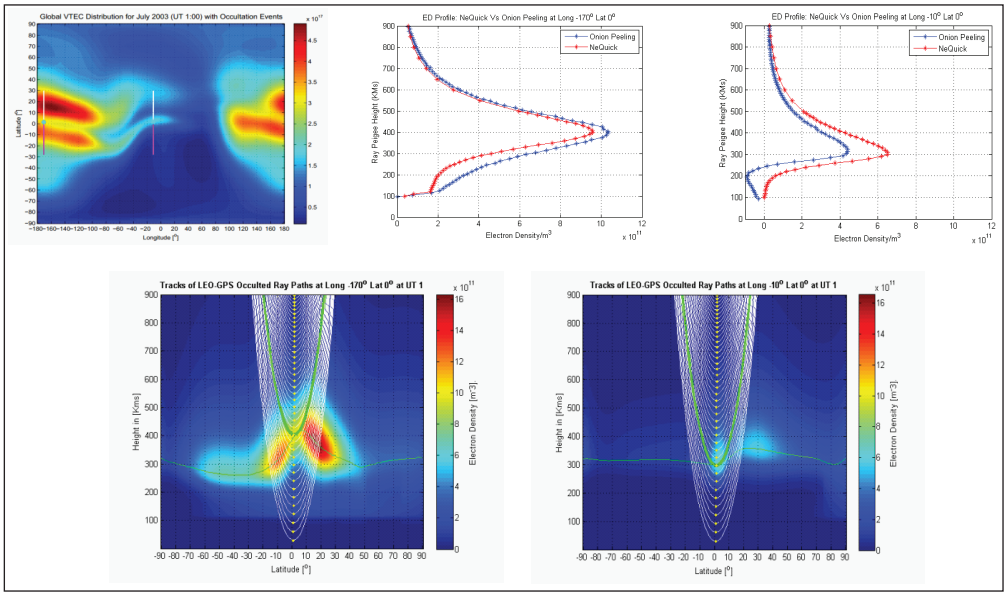

Figure 4.2c Comparison between onion-peeling inversion and simulated truth (NeQuick2; solar flux = 128 sfu) at Lat 0°

effects to cancel out (Hochegger et al. 2001) in the proximity of the ray perigees (where the inverted profile is compared with the truth one).

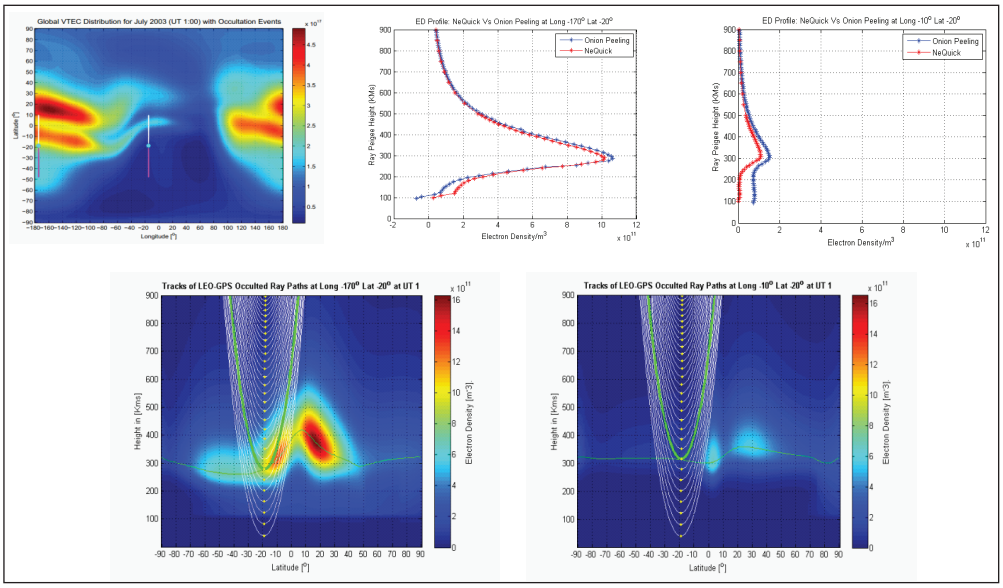

Figure 4.2d Comparison between onion-peeling inversion and simulated truth (NeQuick2; solar flux = 128 sfu) at Lat -20°

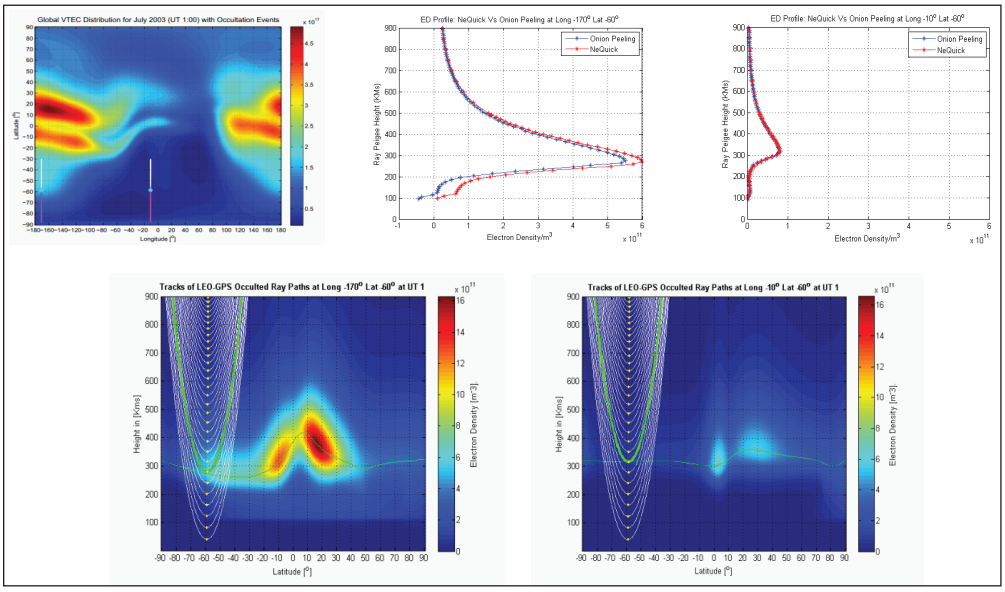

Figure 4.2e Comparison between onion-peeling inversion and simulated truth (NeQuick2; solar flux = 128 sfu) at Lat -60°

Finally, figure 4.2e shows the example of what can may be regarded as the "spherically symmetric ionosphere" case (see the 10° W longitude case, where the ray-paths are experiencing very small horizontal gradients). The agreement between inverted electron density profile and truth profiles is the evidence of that. For the 170° W case, we have a typical behaviour where half of the ray-paths are experiencing large ionospheric gradients whereas the other half is crossing lower electron density gradients, producing differences between the inverted and the corresponding "ground truth" electron density profile.

In order to evaluate the influence of solar activity on the possible retrieval errors related to the onion-peeling-derived profiles, the same kinds of simulations have been performed with a solar flux = 180 sfu. In the case of high solar activity, as expected, the results are qualitatively similar to the results obtained for moderate solar activity, but the differences between the onion-peeling-derived and the ground truth profiles is bigger than in the corresponding case of moderate solar activity.

As a summary, figure 4.3 shows an overall comparison considering all the cases described before. In particular, the electron density profile 'errors' (i.e. differences) between inverted profile values and the corresponding truth (NeQuick2) profile values, evaluated at ray perigee heights, are plotted. The largest errors are expected for 170° W case are evaluated where the simulated ray perigees are those around 20° N latitude crossing F2 peaks in the region of largest TEC (and electron density gradients) values. The same effects are experienced for the 10° W case around the equator. In extreme cases, remarkable departures (in terms of electron density) from the spherical symmetry may also lead to large inversion errors and negative electron densities could be retrieved.

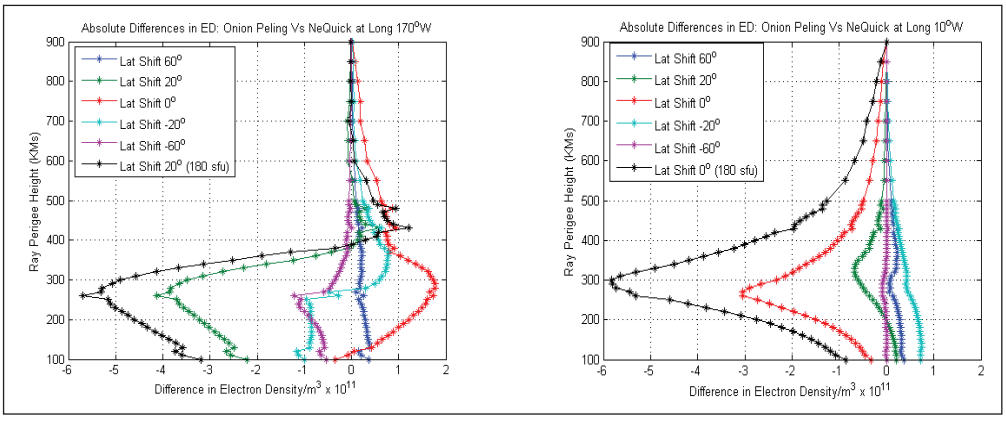

Figure 4.3 Differences between onion-peeling-derived and the corresponding "truth" profile for ray-perigees at different latitudes at longitude 170° W & 10° W

The black lines shown in figure 4.3 (a and b) are related to simulations performed during a high solar activity period (i.e. 180 sfu). They clearly confirm that the retrieved electron density profile errors follow the same trend observed in the case of moderate solar activity period (the occultation geometry being the same), but with larger absolute differences, depending on the longitude or local time considered.

5 CONCLUSION & FUTURE WORK

In this work we tried to evaluate how the large electron density gradients present in the ionosphere may be a source of error for the techniques/algorithms usually adopted for the retrieval of electron density profiles considering GNSS RO measurements. To achieve this, we created test case scenarios which are expected to give an idea of the behaviour of the phenomenon we are studying. The paper represents an assessment study concerning the assumption of spherical symmetry of the ionosphere while inverting RO data. 'Onion-peeling', which is an accepted algorithm to invert the limb TEC data into electron density profiles has been implemented and thoroughly tested. It has been found that the onion-peeling, which is based on spherical symmetry hypothesis, can be successfully applied, above all where GNSS signal experience small gradients of electron density along their propagation paths. In some cases, where the ionospheric conditions differ greatly from the spherical symmetry assumptions, like e.g. in the EIA region, the algorithm may lead to erroneous electron density profiles.

Based on ITU recommendations, NeQuick2, the background ionospheric model used in this work, already has a limit for $F_{10.7}$ solar flux input. It is not possible to do TEC calculation using NeQuick2 above 193 sfu (NeQuick Source[2]). The model doesn't produce any data for any value of $F_{10.7}$ solar flux input greater than 193 sfu. However in this work, we didn't use such a high number. The two $F_{10.7}$ solar flux values used in this work are 128 sfu (for moderate solar activity) and 180 sfu (for high solar activity) for comparative analysis. Indeed it has been shown that, during high solar activity periods, where larger electron density gradients in the ionosphere are present, increased errors in the electron density profile retrieved by TEC inversion could be expected. Based on the solar activity input, the NeQuick2 produces TEC values which are well within the limits of the electron density gradients present in reality. In fact, the TEC values in a very high solar activity period may be much higher than what has been shown in the work as high solar activity; which will lead to even greater values of errors

[2] http://www.itu.int/ITU-R/index.asp?category=documents&link=rsg3&lang=en

compare to the ones shown in figure 4.3b. It is important to mention here that the 'observed' $F_{10.7}$ solar flux value can vary from as low as 70 sfu to greater than 260 sfu (Space Weather Canada[3]).

The work done up to now has been limited to the use of NeQuick2 model as a source for producing a 'synthetic' ionosphere and only space-based TEC data have been considered. In the future, other ionospheric models (like IRI) or diverse kind of data (e.g. ground-based TEC data; Hernàndez-Pajares 2000) will be taken into account. In addition ionospheric electron density 3D distributions (obtained using tomographic software) will be used to produce 3D electron density maps (and VTEC maps) which, in turn, can be used to simulate limb TEC observations necessary for the onion-peeling algorithm inversion. For example MIDAS is a tool available at one of the partner institutes of TRANSMIT project (University of Bath) which is able to produce realistic electron density maps of the ionosphere. Moreover, this work is the starting point for the development of an 'onion-peeling' model aided. In this case we will try to introduce some suitable strategies into such algorithm, in order to overcome the limitations created by the spherical symmetry hypothesis.

ACKNOWLEDGEMENT

This research work is undertaken under the framework of the TRANSMIT ITN (www.transmitionosphere.net), funded by the Research Executive Agency within the 7th Framework Program of the European Commission, People Program, Initial Training Network, Marie Curie Actions – GA no. 264476.

REFERENCES

1. Anthes R. A., Ector, D., Hunt D. C., Kuo Y-H., Rocken C., Schreiner W. S., Sokolovskiy S. V., Syndergaard S., Wee T-K., Zeng Z. P., Bernhardt A., Dymond K. F., Chen Y., Liu H., Manning K., Randel W. J., Trenberth K. E., Cucurull L., Healy S.B., Ho S-P., McCormick C.T., Meehan K., Thompson D.C. & Yen N.L. (2008), "The COSMIC/FORMOSAT-3 Mission: Early Results. Bulletin of the American Meteorological Society", Vol. 89, pp. 313–333, doi: 10.1175/BAMS-89-3-313.
2. Cander, Lj.R., 2003. Towards forecasting and mapping ionospheric space weather under COST actions. Advances in Space Research 31 (4), 957–964.
3. Di Giovanni, G., Radicella, S.M., 1990. An analytical model of the electron density profile in the ionosphere. Advances in Space Research 10 (11), pp. 27–30.
4. Gorbunov M.E., "Three-dimensional satellite refractive tomography of the atmosphere: A numerical simulation", Radio Science, vol. 31, pp. 95–104 (1996).

[3] http://www.spaceweather.gc.ca/data-donnee/sol_flux/sx-5-mavg-eng.php

5. Gorbunov, M.E., “Analysis and validation of GPS/MET radio occultation data”, Journal of Geophysical Research, vol. 106, No. D15, pages 17, 161–17, 169, August 16, 2001.
6. Hajj G.A., Kursinski E. R., Romans L.J., Bertiger W.I., Leroy S.S., “A technical description of atmospheric sounding by GPs occultation”, Journal of Atmospheric and Solar-Terrestrial Physics 2001.
7. Healy S.B., Haase J., Lesne O., “Abel transform inversion of radio occultation measurements made with a receiver inside the Earth’s atmosphere”, Annales Geophysicae (2002) 20: pp. 1253–1256 c European Geophysical Society 2002.
8. Hernàndez-Pajares M., Juan J. M., Sanz J., “Improving the Abel inversion by adding ground GPS data to LEO radio occultations in ionosphere sounding”, Geophysical research letters, vol. 27, no. 16, pp. 2473–2476, 2000.
9. Hochegger G., R. Leitinger, “Model assisted inversion of GNSS occultation data”, Physics and Chemistry of the Earth, Part C: Solar, Terrestrial & Planetary Science, Vol. 26, No 5, pp. 325–330, 2001.
10. ITU, 2003. Ionospheric propagation data and prediction methods required for the design of satellite services and systems. Recom-mendation P. 531–7, Geneva.
11. Kursinsky E.R., “Observing Earth’s atmosphere with Radio Occultation measurements using the Global Positioning System”, Hournal of Geophysical Research, Vol. 102, No. D19, pp. 23, 429–23, 465, October 20, 1997.
12. Leitinger R., H.P. Ladreiter, G.Kirchengast, “Ionosphere tomography with data from satellite reception of GNSS signals and ground reception of NNSS signals”, Radio Sci., 32(4), pp. 1657–1669, 1997.
13. Luntama J-P., Kirchengast G., Borsche M., Foelsche U., Steiner A., Healy S., Von Engeln A, O’Clerigh E. & Marquardt C. (2008), “Prospects of the EPS GRAS Mission For Operational Atmospheric Applications. Bulletin of the American Meteorological Society”. Vol. 89, pp. 1863–1875, doi: 10.1175/2008BAMS2399.1
14. Nava B., Coisson P., Radicella S.M., “A new version of the NeQuick ionosphere electron density model”, Journal of Atmospheric and Solar-Terrestrial Physics 70 (2008), pp. 1856–1862.
15. Radicella, S.M., Zhang, M.L., 1995. The improved DGR analytical model of electron density height profile and total electron content in the ionosphere. Annali di Geofisica XXXVIII (1), pp. 35–41.
16. Seynat, C., Kealy, A., Zhang, K., 2004. A performance analysis of future global navigation satellite systems. Journal of Global Positioning Systems 3 (1–2), pp. 232–241.
17. Ware R.H., Exner M., Feng D., Gorbunov M., Hardy K.R., Herman B., Kuo Y.H., Meehan T.K., Melbourne W.G., Rocken C., Schreiner W., Sokolovskiy S.V., Solheim F., Zou X., Anthes R., Businger S. & Trenberth K. (1996), “GPS Sounding of the Atmosphere from Low Earth Orbit: Preliminary Results”, Bull. Am. Meteorol. Soc., Vol. 77, pp. 19–40.

Faculty of Maritime Studies
University of Rijeka, Croatia

Royal Institute of Navigation
Science Technology Practice

7th GNSS
Vulnerabilities and Solutions Conference

LOCAL NEQUICK 2 MODEL ADAPTATION

Josip Vuković, Tomislav Kos

University of Zagreb, Faculty of Electrical Engineering and Computing
Department of Wireless Communications
Unska 3, 10000 Zagreb, Croatia
E-mail: josip.vukovic@fer.hr

ABSTRACT. *Ionosphere causes the largest error in single-frequency satellite positioning. Dual-frequency Global Positioning System (GPS) receivers can measure actual state of the ionosphere in the area above them. Such measurements could be used to generate Satellite Based Augmentation System (SBAS) corrections. In the areas with no SBAS available and no differential positioning providers operating, ionospheric models are the only instrument that could be used for estimation of ionospheric error. The Klobuchar model used in GPS and the NeQuick model implemented in Galileo system are both relying on global data input, which is why they cannot account for sudden ionospheric changes and local anomalies. This paper describes the process of data ingestion into the NeQuick 2 model. Calibrated Total Electron Content (TEC) derived from dual frequency GPS station's measurements is used as a reference and NeQuick 2 is fitted to match that value at the output, e.g. locally adapted. Data from Dubrovnik station in days of quiet and disturbed ionosphere were observed.*

KEY WORDS: *NeQuick 2, GPS data calibration, local ionospheric model*

1 INTRODUCTION

Ionosphere is a layer of charged particles situated between 100 km and 2000 km above the Earth. It is affected by solar conditions and Earth's magnetic field. Electromagnetic signals generated by navigation satellites are affected by the ionosphere, which slows them down while passing through. As the position of the receiver is calculated measuring the signal propagation time from the satellite and transforming it into distance, the propagation speed changes cause positioning errors. In the ionospheric model implemented in GPS, a thin shell ionosphere representation is used. As the ionosphere has the highest electron density at about 350 km above the Earth, the whole ionosphere is represented with an imaginary, infinitesimally thin layer at that height. The signal from a satellite to a receiver passes through the ionosphere and length of a path through the ionosphere depends on the elevation of the satellite. The path is the shortest if the satellite is in zenith with regard to the receiver position and gets longer as the satellite's elevation angle gets lower. As TEC is the number of electrons along a path with cross section of 1 m^2 between two points, longer path causes higher TEC on the path, which leads to higher signal delay. TEC is given in TEC units (TECU), equal to 10^{16} electrons per square meter. In GPS, the ionosphere is modelled by the Klobuchar model, which estimates vertical TEC (VTEC). If a satellite is not in the zenith position, a mapping function is applied to convert VTEC into slant TEC (STEC). The mapping function input is VTEC at an Ionosphere Pierce Point (IPP), the point where the signal from the satellite to the receiver passes through the 350 km layer.

2 NEQUICK 2 MODEL

NeQuick 2 is a global model able to compute ionospheric density between two points in the atmosphere. It was designed for simple and fast execution and one of the earlier versions is implemented in European Galileo system. It is also used for assessment and analysis of the European Geostationary and Overlay System EGNOS. It was chosen in this research because International Telecommunication Union, Radiocommunication sector (ITU-R) Recommendation P.531-7 finds it suitable for TEC modelling, including both bottom side and top side ionosphere. The bottom side, reaching height from about 100 km above the Earth up to F_2 layer peak, in this model consists of five semi-Epstein layers with modelled thickness parameters. The top side ionosphere, above the F_2 layer peak, is described by a semi-Epstein layer with a height dependant thickness parameter empirically determined (Radicella, 2010).

The model inputs are latitude, longitude and height of the observed points, the epoch (month and universal time) and the amount of solar activity presented either by the monthly average solar flux at the wavelength of 10.7 cm ($F_{10.7}$) or by the twelve-month smoothed relative sunspot number (R_{12}). Those averaged values can be converted by the following expression (ITU-R P.371-8, 1999):

$$F_{10.7} = 63.7 + 0.728R_{12} + 8.9 \cdot 10^{-4} \cdot R_{12}^2 \quad (1)$$

Those are only global indications of the solar activity, which is the reason why local ionospheric conditions cannot be modelled. $F_{10.7}$ being monthly average makes it impossible to adapt to sudden ionospheric changes. The NeQuick 2 model can be locally adapted if one of its input parameters describes those local ionospheric conditions (Nava, 2006). Thus the local ionization level *Az* was used as a model input instead of the global solar flux. If the referent TEC is available at some point, it is possible to change *Az* and use it by NeQuick 2 to recalculate TEC until it matches the referent value. Such a process results with ionization level fitted to actual ionospheric conditions at that point. The same *Az* can then be used for local or regional surrounding area as input into the NeQuick 2 model instead of global $F_{10.7}$. Performance of the model would deteriorate moving away from the data ingestion point.

3 REFERENT TOTAL ELECTRON CONTENT

Different augmentation systems cover only small portions of the globe, leaving large areas without proper assistance that could increase single-frequency GPS receiver's accuracy in either real time or post processing (Figure 1). Even though there is no SBAS in southern hemisphere and most of the Asia, referent GPS stations can be found in those areas.

International GNSS Service (IGS) stations are well distributed around the world (Figure 2), but besides them, there are several other networks with dozens of GPS stations. All of them produce Receiver Independent Exchange Format (RINEX) files containing data created from the Global Navigation Satellite System (GNSS) navigation messages.

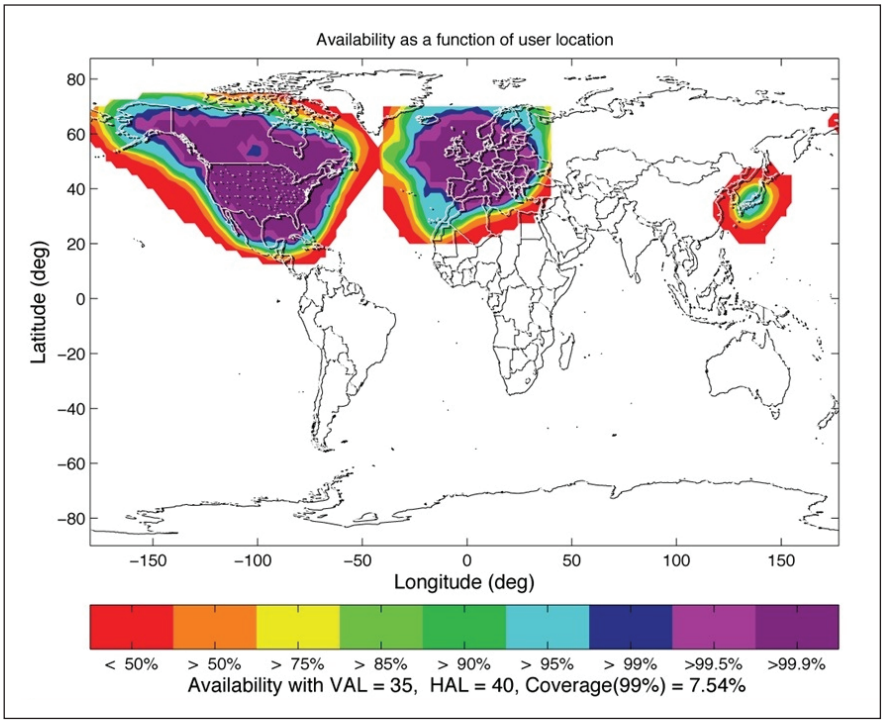

Figure 1 Currently available SBAS systems (ESA, 15 March 2013)

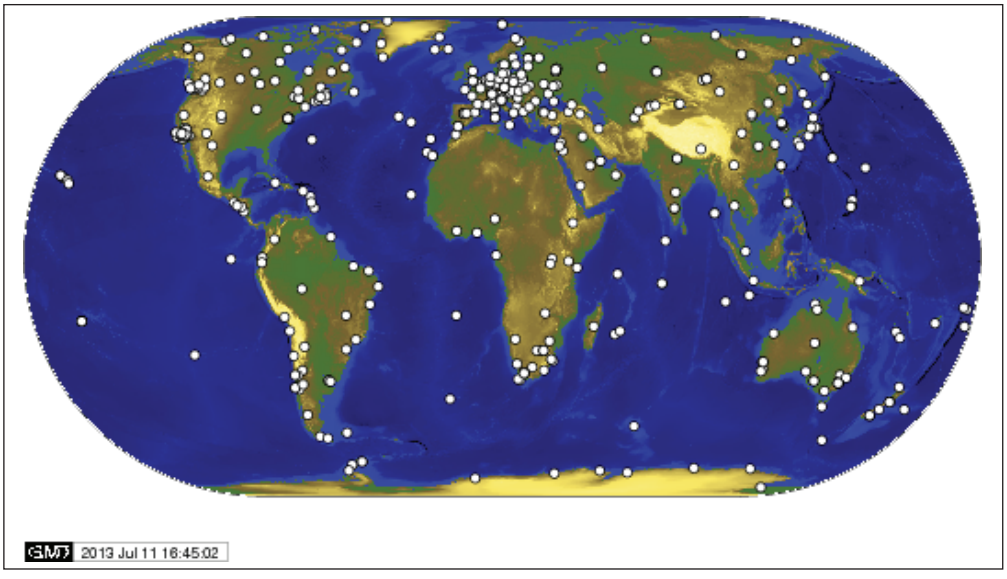

Figure 2 IGS Tracking Network (IGS, 19 July 2013)

RINEX observation files made by dual-frequency receivers contain carrier-phase and code-delay GPS observables. Those data can be used to calculate TEC between the receiver and satellites, but the calculation is affected by inter--frequency biases (IFB). IFB can be produced by the receiver and by the satellites. To calibrate TEC, it is necessary to estimate and eliminate IFB present in levelling carrier-phase to code-delay ionospheric observable (Sardon, 1994). The levelling process is used to reduce carrier-phase ambiguities. Even though receiver IFB can vary significantly, up to 8.8 TECU in a one-day period (Ciraolo, 2007), those variations were not considered in this paper as only widely adapted Differential Code Bias (DCB) files were used for data calibration (CODE, 14 December 2012). DCB files contain monthly values of differential code biases for satellites (GPS and GLONASS) and receivers of the IGS network. Only satellites with an elevation angle of 20 degrees or more were considered.

4 RESULTS

In this research, a day of 2003 Halloween solar storm was observed and compared to the day with quiet ionospheric conditions which took place 40 days before. Both days were in the period of 11-year high solar activity. An IGS station in Dubrovnik, Croatia with four-digit code DUBR, latitude of 42.65000° N, longitude of 18.11044° E and height of 468.85 m was observed. DUBR observation RINEX files and BRDC navigation RINEX files were used as the input into GPS-TEC analysis application developed by G. K. Seemala. The GPS-TEC application was used to download necessary .DCB files and calibrate STEC values for all satellites above the elevation cut-off angle. An inverse GPS mapping function was applied in order to convert STEC into VTEC at the IPP.

Table 1 and Table 2 show calibrated TEC data for Dubrovnik station in time of non-disturbed solar conditions. The first one represents the low, night-time period, while the second one shows values calculated at a diurnal peak. Global NeQuick 2 model for September 2003 uses $F_{10.7}$ of 110.2, which at the station's coordinates in the night-time gives VTEC of 4.69 TECU. Measured average VTEC over the station area is 6.29 TECU. In order to produce such an output from the NeQuick 2 model, *Az* has to be equal to 133. At 2:00 p.m. NeQuick 2 driven by its original input calculated VTEC of 18.81 TECU, while the real VTEC was 21.63 TEC. *Az* of 122 has to be used in order to get that level of VTEC.

Table 1 Calibrated TEC at DUBR station, 27 September 2003, 3:00 a.m.

PRN	Azim [°]	Elev [°]	IPP Lat [° N]	IPP Lon [° E]	STEC [TECU]	VTEC [TECU]
1	200.52	10.42	32.47	13.66	15.80	5.71
3	169.71	7.17	30.14	20.71	19.22	6.53
7	321.91	10.33	50.73	7.56	10.64	3.84
11	308.11	77.56	43.05	17.40	6.90	6.76
14	49.65	34.26	45.26	22.61	8.91	5.54
20	265.51	45.94	42.37	14.31	9.34	7.03
23	63.06	9.96	46.78	32.52	14.58	5.22
25	114.82	16.84	38.89	27.47	17.98	7.56
31	189.93	32.50	38.30	17.14	13.96	8.38

Table 2 Calibrated TEC at DUBR station, 27 September 2003, 2:00 p.m.

PRN	Azim [°]	Elev [°]	IPP Lat [° N]	IPP Lon [° E]	STEC [TECU]	VTEC [TECU]
5	247.33	26.54	40.35	11.50	43.68	23.14
7	74.78	46.60	43.32	21.77	27.73	21.04
9	310.07	59.09	43.77	16.24	22.55	19.70
18	280.25	18.84	43.53	8.09	48.35	21.35
23	320.83	9.98	50.71	7.13	51.21	18.35
26	186.62	56.18	40.69	17.81	27.77	23.59
28	56.21	19.42	46.34	26.78	45.22	20.26
29	172.02	38.43	39.07	18.76	38.23	25.60

Table 3 and Figure 3 show calibrated TEC data for the same station in day of highly disturbed ionosphere, for the same time of day as before. At 3:00 a.m., for $F_{10.7}$ of 107.8, NeQuick 2 calculated VTEC equal to 3.66 TECU. The real value was 5.97 TECU, which requires *Az* as high as 181. At the diurnal peak, NeQuick calculated VTEC equal to 20.93 TECU, while the measurement has shown that the actual value was 37.96 TECU. To achieve that, NeQuick 2 needs Az of 153 at the input. Figure 3 also depicts spatial VTEC distribution with lower values on north-east and higher values on south-west of Dubrovnik station, marked with a blue dot. It also shows that in time of disturbed ionosphere the difference between VTEC on IPPs visible from one station can exceed 10 TECU.

Table 3 Calibrated TEC at DUBR station, 4 November 2003, 3:00 a.m.

PRN	Azim [°]	Elev [°]	IPP Lat [° N]	IPP Lon [° E]	STEC [TECU]	VTEC [TECU]
1	259.61	82.20	42.58	17.57	6.18	6.13
4	311.82	31.18	45.63	13.18	7.10	4.15
7	260.42	19.36	41.06	8.66	15.68	7.02
11	162.03	27.74	37.66	20.14	13.20	7.18
13	239.23	48.15	41.27	15.12	9.31	7.21
20	70.11	63.76	43.13	19.99	6.33	5.75
25	47.85	23.49	46.57	24.71	8.76	4.33

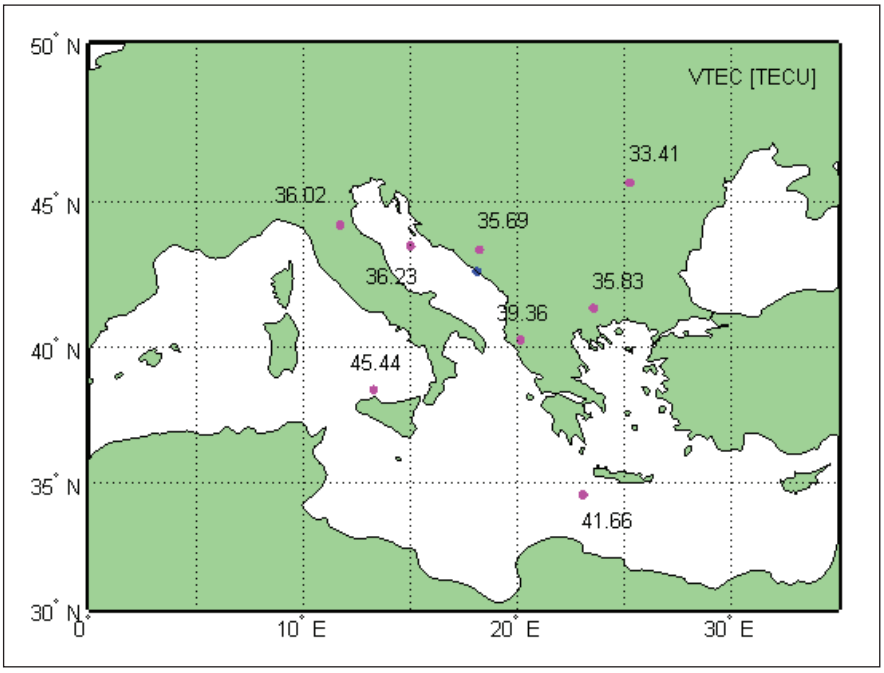

Figure 3 Calibrated VTEC at DUBR station, 4 November 2003, 2:00 p.m.

5 CONCLUSION

In this paper the process of adaptation of the NeQuick 2 model to local ionospheric conditions was described. The NeQuick 2, usually driven by global monthly average $F_{10.7}$ index, used ionization level instead. *Az* was based on calibrated VTEC which was calculated from Dubrovnik station RINEX files.

Results have shown that real VTEC differs from VTEC calculated by the global NeQuick 2 model. In quiet ionospheric conditions the difference was about 25% at the night-time and about 10% at diurnal TEC peak. In the day of disturbed ionosphere, the difference was much higher, reaching over 65% in the night-time and 80% at 2 p.m. These results clearly indicate that global ionospheric models, like NeQuick 2, cannot efficiently eliminate ionospheric error specific for observed location, especially if the ionosphere is disturbed. Locally adapted NeQuick 2 model solves that problem and can be used in the geographic area surrounding the point where referent data were obtained. Its usage is currently limited to post processing because calibrated VTEC from RINEX files is not available in real time.

ACKNOWLEDGEMENT

The work described in this paper was conducted under the research project: "Environment for Satellite Positioning" (036-0361630-1634), supported by the Ministry of Science, Education and Sport of the Republic of Croatia. NeQuick 2 model was provided by T/ICT4D Laboratory of the Abdus Salam International Centre for Theoretical Physics (ICTP) in Trieste, Italy.

REFERENCES

1. Radicella S. M., Nava B., (2010). NeQuick model: Origin and evolution, Proceedings of the 9th International Symposium on Antennas, Propagation and EM Theory, 2, pp. 422–425.
2. International Telecommunication Union, Radiocommunication sector, (1999). Choice of indices for long-term ionospheric predictions, Recommendation ITU-R, pp. 371–8.
3. Nava B. et al., (2006). A near real time model assisted ionosphere electron density retrieval method", Radio Science, 41, No. 6.
4. ESA, Space in Images, Current combined SBAS coverage, http://spaceinimages.esa.int/Images/2012/01/Current_combined_SBAS_coverage, accessed on 15 March 2013.
5. IGS Tracking Network, http://igscb.jpl.nasa.gov/network/netindex.html, accessed on 19 July 2013.
6. Sardon E., Rius A., Zarraoa N., (1994). Estimation of the transmitter and receiver differential biases and the ionospheric total electron content from Global Positioning System observations, Radio Science, 29, Number 3, pp. 577–586.
7. Ciraolo L. et al, (2007). Calibration errors on experimental slant total electron content (TEC) determined with GPS, Journal of Geodesy, 81, Issue 2, pp. 111–120.
8. Center for Orbit Determination in Europe CODE, (2003). ftp://ftp.unibe.ch/aiub/CODE/2003/, accessed on 14 December 2012.

Faculty of Maritime Studies
University of Rijeka, Croatia

Royal Institute of Navigation
Science Technology Practice

7th GNSS
Vulnerabilities and Solutions Conference

SINGLE WINDOW RIS APPLICATION

Darko Herak[1], **Damir Obad**[1], **Neven Grubišić**[2]

[1] RGO Communication Ltd., Kuzminečka 53, 10000 Zagreb, Croatia
E-mail: obad@rgo.hr

[2] University of Rijeka, Faculty of Maritime Studies, Rijeka, Croatia
Studentska 2, 51000 Rijeka, Croatia

ABSTRACT. *River Information Services (RIS) are Cross-European platform for development of vessel tracking and tracing system in Inland navigation. Existing subsystems, namely AIS, Notices to Skippers, Electronic Reporting International, Hull Database and Data Gateway exist as standalone causing difficulties in communication protocols. In this article we propose integration of different subsystems through the unique single window RIS application. The idea is to use already available services to get the required data and import it into the ECDIS Viewer application. The single window ECDIS viewer application enables the authorized users to open a vessel information window which contains a customized view for several different user types. That means that the vessel information window will give the user a personalized overview of all the most important data available from different sources.*

KEY WORDS: *River Information Services, Inland ECDIS, Inland navigation, AIS base station*

1 INTRODUCTION

River Information Services (RIS) in Europe constitute of many standalone applications. In many cases issues arise when these subsystems are interconnected due to incompatible interfaces, while in other cases complications come up caused by numerous usernames and need to start several applications or web pages by the user. With a single window RIS application, users get an ultimate RIS application capable of delivering all the relevant data promptly and in a user friendly fashion. The benefits of having the Notices to Skippers, Hull Database, Electronic Reporting and Data Gateway data readily available and integrated within the ECDIS viewer are abundant.

2 VESSEL TRACKING AND TRACING

To unlock the full potential of a Single Window RIS application there is a need for a complete RIS system to be implemented and functional. The most important part, which enables vessel tracking and tracing, is of course an advanced AIS (*Automatic Identification System*) network which is used to distribute different navigation messages around the vessel's position, voyage and convoy data, which are sent via VHF. For increased safety and precision DGPS reference stations should be part of this AIS network to greatly increase the precision of received position data (Figure1).

All the data received at AIS base stations are then processed and distributed to the users depending on their user rights and displayed within this Single Window RIS application on an electronic navigational chart in compliance with the ECDIS (*Electronic Charts Display Information System*) standard. Vessel mounted AIS transponders receive all the messages within their range that are sent from other vessels and base stations and this AIS stream is then visualized again on the chart within the RIS Single Window application. Additional precision and safety is in this case achieved by usage of DGPS systems. DGPS corrections can be transmitted in various ways to the end users.

The AIS DGPS System uses the AIS Message 17 to broadcast corrections over the AIS network to the users. Several different configurations of AIS DGPS systems are possible considering the number of reference stations, relative location of the reference stations to AIS base stations and the way the correction data is transmitted to the AIS base station from the reference station. Some of the possible configurations of the DGPS system are:

Alternative A – the information is transferred to the AIS base station via any telecommunication or radio communication network (Figure 2).

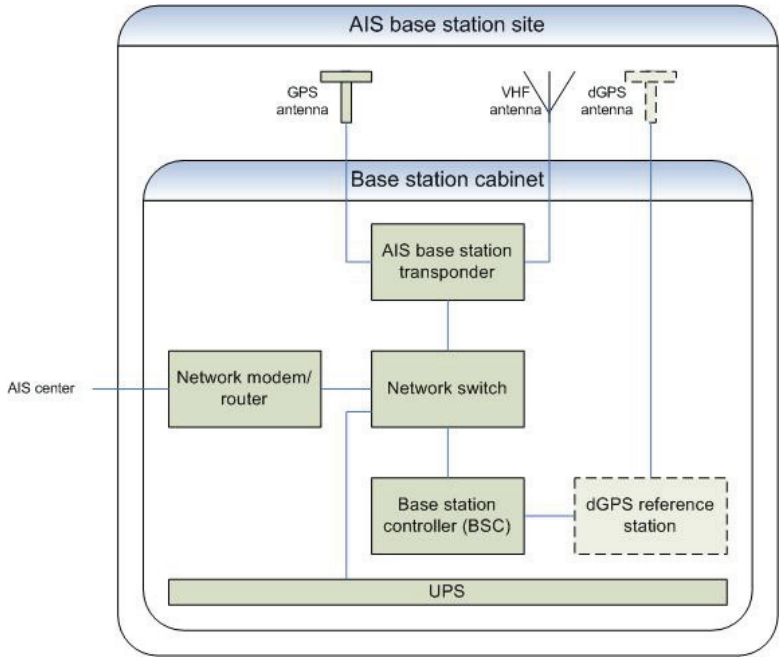

Figure 1 AIS Base station components

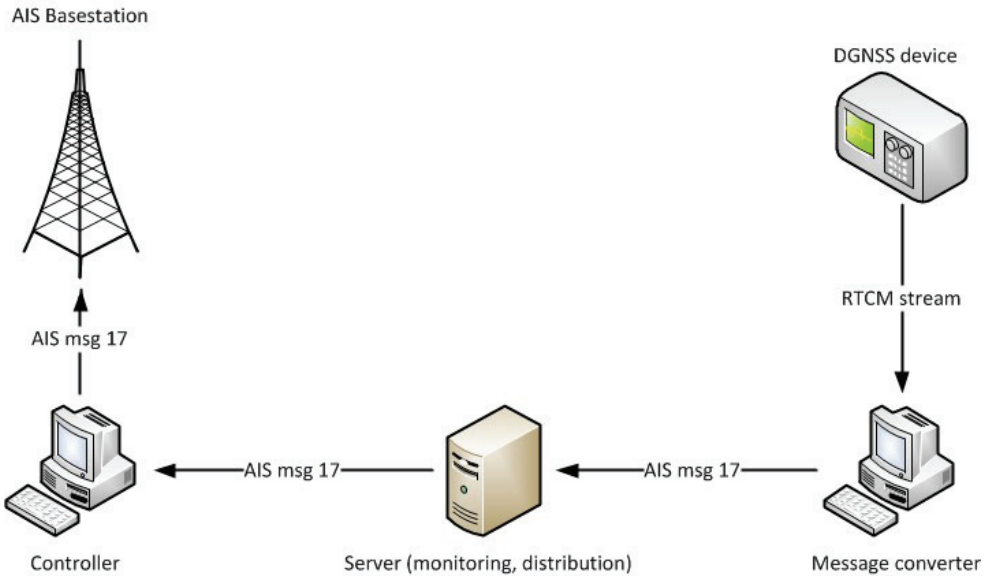

Figure 2 Configuration of the AIS-DGPS system – Alternative A

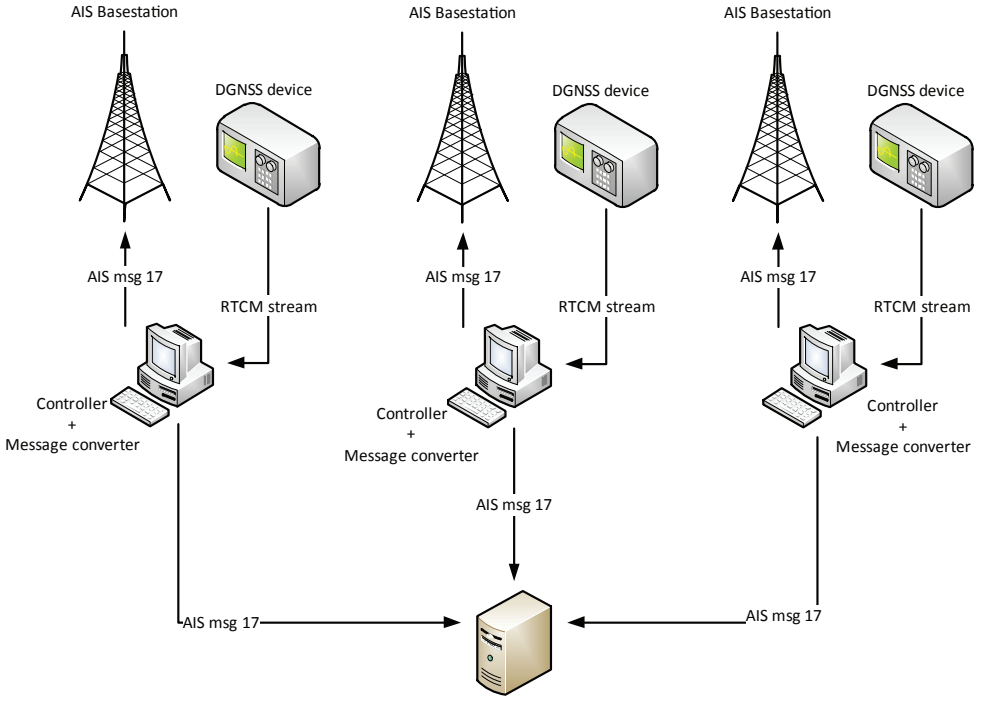

Figure 3 Configuration of the AIS-DGPS system – Alternative B

Alternative B – the corrections are generated locally by a local reference station at the AIS base station (Figure 3).

Alternative C – technically, there is no obstacle to combine the mentioned alternatives in the final system so an AIS base station can have a DGNSS device on site, the controller can send the AIS message 17 to the server and then the server distributes the correction data to other AIS base stations which finally broadcast the correction data (Figure 4).

Once the correction data is delivered to the AIS base station they are broadcasted in form of AIS Message 17. These messages are then picked up by the vessel's transponder and taken into account during the visualization of targets within the RIS Single Window application. In case an IALA MF beacon is a part of the DGPS system it is possible to use this correction data if the ship or shore station is equipped with an appropriate receiver.

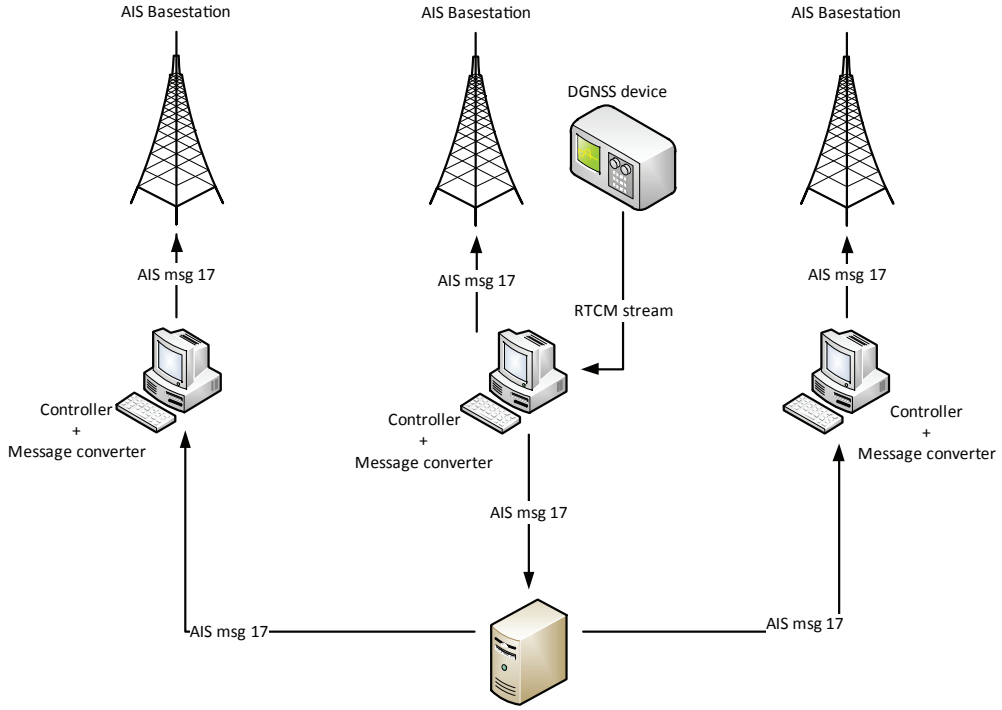

Figure 4 Configuration of the AIS-DGPS system – Alternative C

3 INTEGRATION WITH OTHER RIS SYSTEMS

To provide the skipper and various other users with interest in the current traffic situation on inland waterways (i.e. police, customs, lock operators, calamity and abatement services, etc.) with the full picture and even more safety related information other RIS sub-systems need to be implemented and fully functional, including the standardized web services for the following applications:

- NtS (Notices to Skippers) – important fairway and traffic related messages, weather and ice related messages as well as latest water level messages can be retrieved via a dedicated web service.
- ERI (Electronic Reporting International) – whole ERINOT messages containing accurate voyage, transport and cargo information is available in case a web service is implemented and can be retrieved and used within the RIS Single Window application.
- Hull Database – a minimum hull data set can be retrieved using the national Hull Database application's web service from both the national and European

Hull Database applications. This data set contains the basic information about the vessel like its identification numbers, dimensions, type, owner information and certificates.

- Data Gateway – a request can be sent to the national Data Gateway application in case the web service has been implemented and depending on the users access rights different types of data are returned in the response. In case of a foreign vessel the Data Gateway application will forward the request to an appropriate foreign Data Gateway and once it receives a response it will forward it to the requester.
- DGPS monitoring – information about the precision of current GPS signals, the DGPS corrections and statistical data in form of graphs and table with values over different periods of time are available to users as a nice overview of the quality of service they are getting.

Since these are web based services an internet connection is required. All the data gathered from available web services are then used within the RIS Single Window application and presented to the user where he needs it and when he needs it. The user always has the ability to review the notices, messages, reports and responses in their original form within this single application but more importantly the data is presented to him throughout the usage of the application in such a manner to improve his user experience, his efficiency and most importantly the safety on the waterways.

The important and relevant notices picked up from the NtS web service are visualized on the ECDIS chart in various ways. Fairway and traffic messages which relate to a fairway section or sections will have those parts of the fairway marked so the user immediately knows to which part of the river the notice is related. Notices with important safety related data can always mark relevant areas of the river to improve the situational awareness of the skipper while other notices would only be visualized when the user demands them. The user would also have access to a list of all notices which are relevant for the portion of the chart he is currently viewing as well as a list of all active notices for the charts he has loaded into the application. By selecting and opening a notice from those lists he would invoke a new window where the notice would be visualized with all its data.

Most ECDIS Viewer applications have a Ship Details window where available data about the vessel and convoy are displayed. The problem is that this data is taken from AIS which can unfortunately be incorrect in many cases and as such are unreliable. Even when the data is correct the amount of data is simply not sufficient. With the connection to other RIS subsystems the amount and precision of this data would improve significantly.

Even by just glancing over the ECDIS chart in front of the user he gets a good idea what data is available to him since indicators of available data from various systems are shown for each target. By selecting a target and opening the Ship Details window of the Single Window RIS application the user accesses more data, whenever appropriate subsystems are available. The contents of this window are different for different user types. Depending on the user and what is his role in inland navigation, different groups of data shall be presented in this overview. Skippers and customs officers do not have the same interests when it comes to ship details so for the skipper the data that is most relevant for him are presented like the identification, size of the vessel, its speed, heading and generally most of the AIS and Hull data with only the most crucial data from the ERI system like if the ship has any dangerous cargo on board. The customs officer on the other hand is more interested in the cargo data so besides the identification numbers and similar basic vessel data mostly cargo related data from ERI is displayed whenever available. However, all users with sufficient access rights can access complete hull data sets and ERI reports by clicking the appropriate buttons inside the Ship Details window.

By using these customized views (templates) for several different user types, users are not overloaded with information and data but are instead given the most relevant data with an option to view complete sets of data.

The existence of the Data Gateway interface allows the user of the Single Window RIS application to send requests to their national Data Gateway application and receive and view the responses inside of the application. Using this option, users can obtain valuable information about foreign vessels. The user sends a request to obtain data sets which are of interest to him to the Data Gateway application which then forwards the request to the relevant foreign Data Gateway and upon receiving a response it forwards it back to the user which requested the information (if he has sufficient access privileges). Received data is displayed within the Single Window RIS application where the user can review the received data. Besides requesting data based on ship identification, users authorized for sending requests to the Data Gateway application can also send requests based on port of destination and areas. Port authorities can retrieve vessels which are navigating on a particular river and have that port set as destination port.

RIS Single Window application provides users that have sufficient access rights with a nice overview of DGPS monitoring data. Upon the user's request the DGPS statistical data is retrieved via web service and displayed within the RIS Single Window application. An overview of all reference stations is given, including several parameters for each of them including the offset data, status of

the reference station and an indicator if the AIS transponder is working in High accuracy mode. Users can also access detailed reports for all reference stations which include detailed information about the offsets of the DGPS monitoring station and the DGPS AIS transponder, as well as charts which display the average, minimum and maximum offsets for each hour of the past day and a chart which displays visually the offsets including their direction represented as dots on a target. Under these charts there are tables for both the DGPS reference station's and DGPS AIS transponder's alarms with date and time of each alarm.

User's login data is managed within the application's preferences window where he can input credentials for each of the subsystems which will then be used to retrieve the data from the web services. This ensures that all the users of this application have access only to data which they are authorized to access so no privacy issues can arise.

4 CONCLUSION

To summarize, the Single Window RIS application provides an all-in-one solution for all participants in inland navigation. All users get an improved overview of the most relevant data in a personalized manner in a way depending on their role in inland navigation. Skippers get a precise strategic traffic image using GPS data received via AIS improved with DGPS corrections, notifications of dangerous cargo is possible even from ERI and not only via AIS, and details of nearby ships include some relevant hull data which is not present in the AIS messages. Skippers are also provided with another huge advantage in form of Notices to Skippers visualized over the ECDIS chart, giving them an overview of relevant valid notices for nearby areas. Other users, depending on their type get different combinations of AIS, NtS, ERI and Hull data tailored for their needs ensuring maximum efficiency of information transfer from the system to the user because in inland navigation more information means more safety.

REFERENCES

1. Chang, S.J. (2004). Development and analysis of AIS applications as an efficient tool for vessel traffic service. *Oceans '04. MTTS,* 4, pp. 2249–2253.
2. Grubisic, N. (2002). Informacijski sustav na unutarnjim plovnim putevima – RIS. *Pomorski zbornik*, 40, pp. 95–111.
3. Grubisic, N. (2011). Specifičnosti tehnoloških procesa u riječnom prometu. *Pomorski zbornik,* 46, pp. 11–37.
4. Gunnar Aarsæther, K. & Moan, T. (2009). Estimating Navigation Patterns from AIS. *The Journal of Navigation,* 62 (04), p. 587.

5. Jandrisits, M., De Mateo, J.C. & Abwerzger, G. (2005). EGNOS Terrestrial Regional Augmentation Networks Based on AIS for River Information Services. *GNSS 18th International Technical Meeting of the Satellite Division,* Long Beach, CA, pp. 827–832.
6. Lisaj, A. (2012). Navigation Data Transmission in the RIS System. *International Journal on Marine Navigation and Savety of Sea Transportation,* 6 (3), pp. 303–305.
7. Obad D. & Bosnjak-Cihlar, Z. (2004). Benefits of Automatic Identification System within framework of River Information Services. *Proceedings Elmar 46th,* Zadar, Croatia, pp. 143–147.
8. Ou, Z. & Zhu, J. (2008). AIS Database Powered by GIS Technology for Maritime Safety and Security. *The Journal of Navigation,* 61 (04), p. 655.
9. Pfliegl, R. (2001). Innovative Application for Dynamic Navigational Support and Transport Management on Inland Waterways: Experience from a Research Project on the Danube River. *Transportation Research Record,* 1763 (1), pp. 85–89.
10. Pfliegl, R. & Bäck, A. (2006). Increasing the Attractiveness of Inland Waterway Transport with E-Transport River Information Services. *Transportation Research Record,*.1963 (1), pp. 15–22.
11. Pfliegl, R et al. (2004). Introduction of EGNOS in River Information Services. *Proceedings Elmar 46th*, Zadar, Croatia, pp. 137–142.
12. PIANC (2011). *Guidelines and Recommendations for River Information Services – part III*, PIANC – Inland Navigation Commission, Report No. 125.

ISBN 978-953-165-113-4